Investigation of Coupled Processes in Argillite Rock: FY20 Progress

Spent Fuel and Waste Disposition

Prepared for
U.S. Department of Energy
Spent Fuel and Waste Science and Technology

Jonny Rutqvist, Yves Guglielmi, Hao Xu, Yuan Tian, Piotr Zarzycki, Hang Deng, Pei Li, Mengsu Hu, Peter Nico, Sharon Borglin, Patricia Fox, Tsubasa Sasaki, Jens Birkholzer

Lawrence Berkeley National Laboratory

May 22, 2020
LBNL-2001324
SFWD Working Document: External Release

Revision 0
05/22/2020

APPENDIX E

NTRD DOCUMENT COVER SHEET [1]

Name/Title of Deliverable/Milestone/Revision No.	Investigation of Coupled Processes in Argillite Rock: FY20 Progress M4SF-20LB010301031
Work Package Title and Number	Argillite Disposal R&D – LBNL/Argillite International Collaboration – LBNL
Work Package WBS Number	SF-20LB01030103 /SF-20LB01030107
Responsible Work Package Manager	Jonny Rutqvist (signature on file) (Name/Signature)

Date Submitted **5/22/2020**

Quality Rigor Level for Deliverable/Milestone[2]	☐ QRL-1 Nuclear Data	☐ QRL-2	☐ QRL-3	☒ QRL 4 Lab-specific [3]

This deliverable was prepared in accordance with Lawrence Berkeley National Laboratory (LBNL)
(Participant/National Laboratory Name)

QA program which meets the requirements of
☒ DOE Order 414.1 ☐ NQA-1 ☐ Other

This Deliverable was subjected to:

☐ Technical Review	☐ Peer Review
Technical Review (TR)	**Peer Review (PR)**
Review Documentation Provided	**Review Documentation Provided**
☐ Signed TR Report or,	☐ Signed PR Report or,
☐ Signed TR Concurrence Sheet or,	☐ Signed PR Concurrence Sheet or,
☒ Signature of TR Reviewer(s) below	☐ Signature of PR Reviewer(s) below
Name and Signature of Reviewers	**Name and Signature of Reviewers**
Pierre Jeanne: Sections 2, 3, 5, 6, 9, 10	Liange Zheng: Sections 1, 4, 8, 11, 12, 13, 14
(Signature on file)	(Signature on file)
Boris Faybishenko: All Sections	
(Signature on file)	

NOTE 1: *Appendix E should be filled out and submitted with each deliverable. Or, if the PICS:NE system permits, completely enter all applicable information in the PICS:NE Deliverable Form. The requirement is to ensure that all applicable information is entered either in the PICS:NE system or by using the FCT Document Cover Sheet.*

- *In some cases there may be a milestone where an item is being fabricated, maintenance is being performed on a facility, or a document is being issued through a formal document control process where it specifically calls out a formal review of the document. In these cases, documentation (e.g., inspection report, maintenance request, work planning package documentation or the documented review of the issued document through the document control process) of the completion of the activity, along with the Document Cover Sheet, is sufficient to demonstrate achieving the milestone.*

NOTE 2: *If QRL 1, 2, or 3 is not assigned, then the QRL 4 box must be checked, and the work is understood to be performed using laboratory specific QA requirements. This includes any deliverable developed in conformance with the respective National Laboratory / Participant, DOE or NNSA-approved QA Program*

NOTE 3: *If the lab has an NQA-1 program and the work to be conducted requires an NQA-1 program, then the QRL-1 box must be checked in the work Package and on the Appendix E cover sheet and the work must be performed in accordance with the Lab's NQA-1 program. The QRL-4 box should not be checked*

TABLE OF CONTENTS

LIST OF FIGURES

LIST OF TABLES

ACRONYMS

ALC	Micro-tunnel experiment at Bure
ANDRA	French National Radioactive Waste Management Agency
BBM	Barcelona Basic Model
BExM	Barcelona Expansive Clay Model
BGR	Bundesanstalt für Geowissenschaften und Rohstoffe
BGS	British Geological Survey
CDM	Continuum Damage Mechanics
CFD	Computed Fluid Dynamics
CIEMAT	Centro De Investigaciones Energéticas, Medio Ambientales Y Tecnológicas
COx	Callovo-Oxfordian Claystone
DECOVALEX	DEvelopment of COupled Models and their VAlidation against Experiments
DEM	Distinct Element Method
DFN	Discrete fracture network
DOE	U.S. Department of Energy
DRZ	Disturbed rock zone
DSID	Deviatoric Stress Induced Damage
EBS	Engineered barrier system
EDZ	Excavation damaged zone
EOS	Equation of State
FBG	Fiber Bragg gratings
FE	Full-scale emplacement
FEBEX	Full-scale Engineered Barrier Experiment
FEPs	Features, Events, and Processes
FLAC	Fast Lagrangian analysis of continua
FOP	Fault Opening Pressure
FY	Fiscal year
GDSA	Generic Disposal Systems Analysis
H1	Heater #1
H2	Heater #2
H3	Heater #3
HLW	High-Level Waste

HM	Hydro-mechanical
IRSN	Institut de Radioprotection et de Sûreté Nucléaire
KAERI	Korea Atomic Energy Research Institute
KBS	Kärnbränslesäkerhet/Nuclear Fuel Safety
LASGIT	Large Scale Gas Injection Test
LBM	Lattice Boltzmann method
LBNL	Lawrence Berkeley National Laboratory
MHM	Meuse/Haute-Marne
MPI	Message Passing Interface
MULES	Multidimensional universal limiter with explicit solution
NAGRA	National Cooperative for the Disposal of Radioactive Waste, Switzerland
NMM	Numerical manifold method
NWMO	The Nuclear Waste Management Organization, Canada
OpenFOAM	Open Field Operation and Manipulation
PA	Performance assessment
R&D	Research & Development
RBSN	Rigid-Body-Spring Network
REV	Representative Elementary Volume
RWM	Radioactive Waste Management Limited, Quintessa Ltd
SFWST	Spent Fuel and Waste Science and Technology
SIMFIP	Step-Rate Injection Method for Fracture In-situ Properties
STP	Standard temperature and pressure
SURF	Sanford Underground Research Facility
TED	Thermal Borehole Experiment at Bure
TH	Thermal-hydrological
THC	Thermo-hydro-chemical
THM	Thermo-hydro-mechanical
THMC	Thermal-hydrological-mechanical-chemical
TOUGH	Transport of Unsaturated Groundwater and Heat
TPHM	Two-part Hooke’s model
TSX	Tunnel Sealing Experiment
UFD	Used Fuel Disposition
UFDC	Used Fuel Disposition Campaign
UFZ	Helmholtz Centre for Environmental Research, Leipzig

UPC	Universitat Politècnica de Catalunya
URL	Underground Research Laboratory
VOF	Volume of fluid

This page is intentionally left blank.

1. INTRODUCTION

Shale and argillite geological formations have been considered as potential host rocks for geological disposal of high-level radioactive waste (HLW) throughout the world because of their low permeability, low diffusion coefficient, high retention capacity for radionuclides, and capability to self-seal fractures. Low permeability of shale and argillite is well-known in the hydrogeology community, because these rocks usually serve as aquitards that limit groundwater movement, and in petroleum industry, because they act as caprocks limiting the rise of buoyant petroleum fluids. While fractures can occur in argillite and shale, these formations often demonstrate the tendency to self-seal fractures, reducing the effects of fractures on bulk permeability. Other favorable characteristics of argillite/shale are the strong sorptive behavior for many radionuclides, reducing conditions because of the lack of oxygen transport from the surface, and chemical buffering the effects of materials introduced during repository construction, operation, and emplaced materials.

The focus of research within the Spent Fuel and Waste Science and Technology (SFWST), formerly called Used Fuel Disposal (UFD), Campaign is on repository-induced interactions of the host rock and an engineered barrier system (EBS) bentonite, which may affect the potential repository safety characteristics. The research is focused on investigations of thermal-hydrological-mechanical-chemical (THMC) processes that occur because of repository construction and waste emplacement. Some of the key questions addressed in this report include investigations of the formation of an excavation damaged zone (EDZ) near tunnels and the evolution of near field coupled thermo-hydro-mechanical (THM) processes after the waste emplacement.

Within the SFWST program, LBNL's work on argillite disposal research & development (R&D) started in 2010 by leveraging on previous experience on coupled THM processes modeling within domestic and international nuclear waste programs (Rutqvist et al., 2001; 2002; 2011). Much of this work has been dedicated to the development and validation of coupled THM simulators for modeling of near-field coupled processes. From a safety assessment perspective, near-field coupled processes are relatively short-lived, but could give rise to permanent changes, such as the formation of a thermally altered or a damaged zone around excavations, and which could provide a pathway for transport of radionuclides if released from a waste package (Figure 1-1). For a repository hosted in clay-rock, the mechanical evolution and swelling of the protective buffer surrounding the waste package (often bentonite) are imperative to its functions, such as to provide long-term mechanical support to seal the EDZ. At the same time, the mechanical evolution of the buffer is governed by complex coupled interactions of temperature and hydraulics, micro- and macro-structures of bentonite, as well as the host rock. Currently, more advanced constitutive mechanical models are being applied, but those require a large number of input parameters for describing processes at the different field scales. It is important to test and validate the models at a relevant field scale, in addition to verification and validation against independent analytical and numerical solutions and laboratory experiments.

Figure 1-2 illustrates a schematic of occurrence of coupled THM processes at the repository scale, such as activation of faults or fractures, creation of new fractures due to thermal stress, and thermal pressurization. Thermal pressurization is a process of pressure increase due to thermal expansion of pore-fluids being trapped because of low permeability of a porous argillite host rock. Another potential cause of near field coupled THM processes is gas generation within the waste package, as well as seismic motion from a distant earthquake. The potential implication for repository performance related to the activation of faults includes creation of (permeable) flow paths, induced seismicity and a potential shear load on a waste canister.

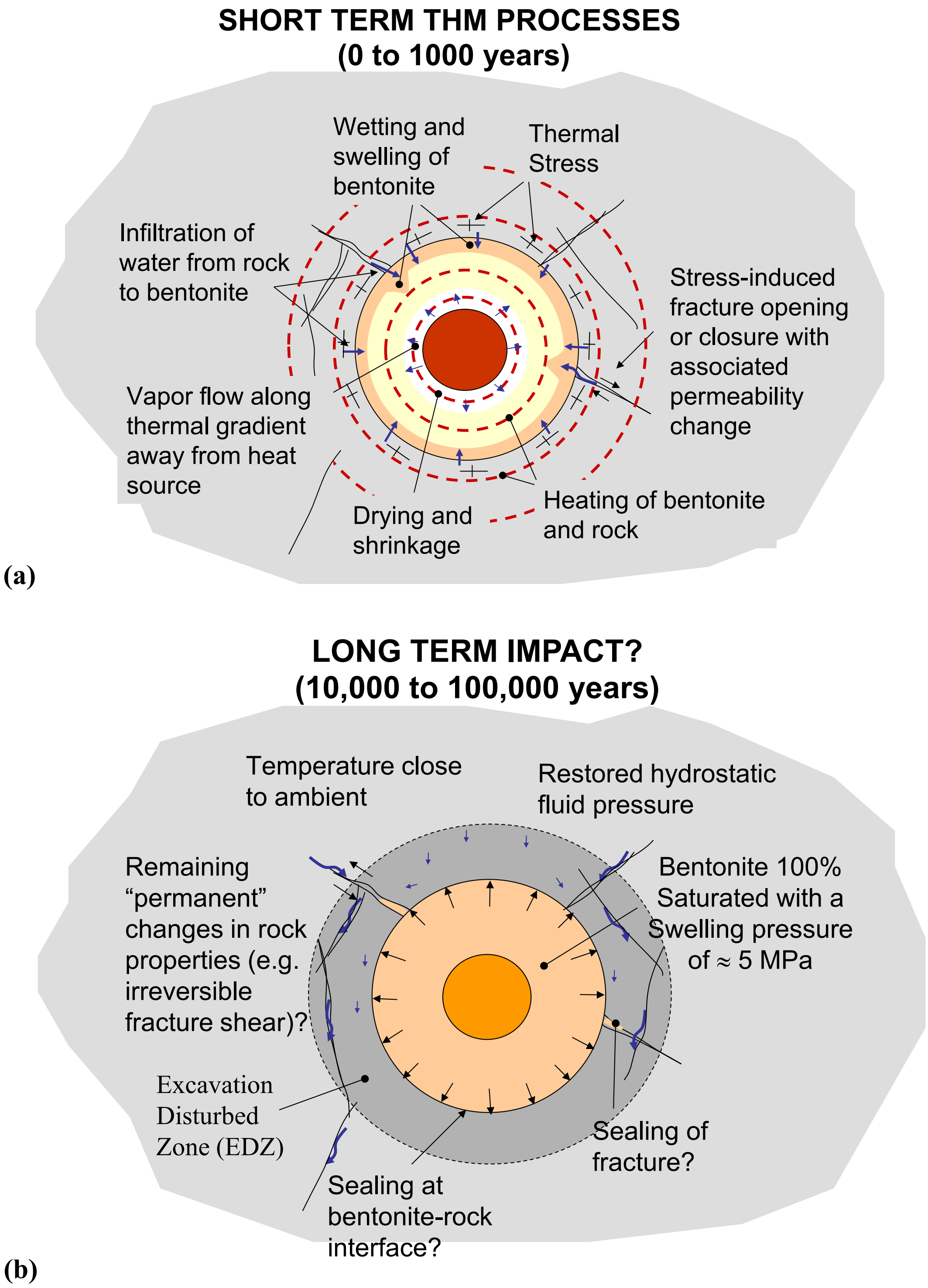

Figure 1-1. Schematic illustration of coupled THM processes driven by heat released from the waste package: (a) short-term THM processes, and (b) long-term impact of early time coupled THM processes.

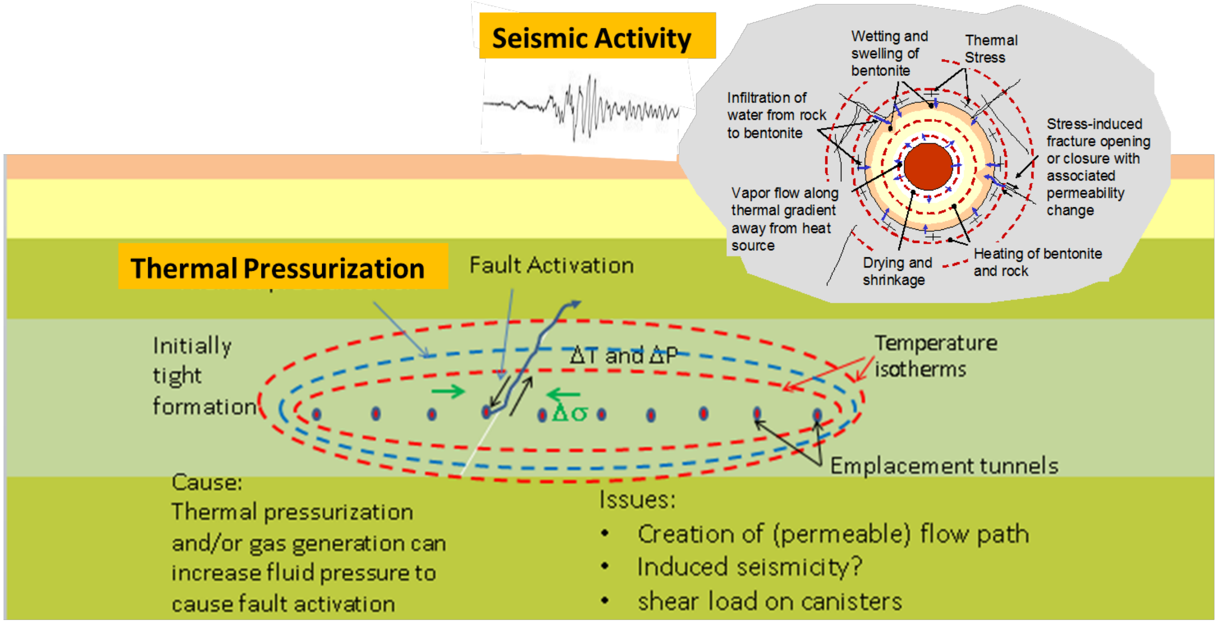

Figure 1-2. Schematic of coupled THM responses in a repository in the near field (upper right) and at the repository scale caused by heating, thermal pressurization and potential gas generation.

LBNL is developing two complementary coupled simulation approaches to model THM processes (Figure 1-3). TOUGH-FLAC, based on linking LBNL's TOUGH2 multiphase fluid flow simulator with the FLAC3D geomechanics code, provides an efficient continuum modeling approach with state-of-the-art constitutive models for bentonite and host rock (Rutqvist et al., 2002; Rutqvist 2011; 2017). The complementary TOUGH-RBSN simulator, based on linking the TOUGH2 simulator with the Rigid-Body-Spring Network (RBSN) model, enables for explicit modeling of discrete fractures and a fracturing process (Asahina et al. 2014; Kim et al., 2017). The TOUGH-RBSN is most suitable for detailed analysis of fracturing in laboratory samples, as well as within the EDZ. The TOUGH-FLAC enables modeling of the evolution of the EBS, EDZ, and surrounding host rock at a larger scale. TOUGH-FLAC with appropriate constitutive models is also used to calculate the evolution of permeability and transport properties in the EDZ, which can then be used as input to future safety assessment models and the Geologic Disposal Safety Analysis (GDSA).

In addition, the ongoing work is focused on modeling of the fault activation. This includes, for example, development of capabilities for modeling of fault slip, induced seismicity, and associated changes in fault permeability. Figure 1-4 presents one such model, involving the TOUGH-FLAC simulator, with a discrete representation of a fault plane, a slip weakening fault rupture model, and with the potential for modeling seismic wave propagation as available in the FLAC3D code. This model can also be applied for modeling of activation and creation of new flow paths resulting from the over pressure due to gas generation or thermal pressurization, as illustrated in Figure 1-2. In addition, 3DEC, a code based on the distinct element method is applied for modeling fault activation and fractured rock coupled processes.

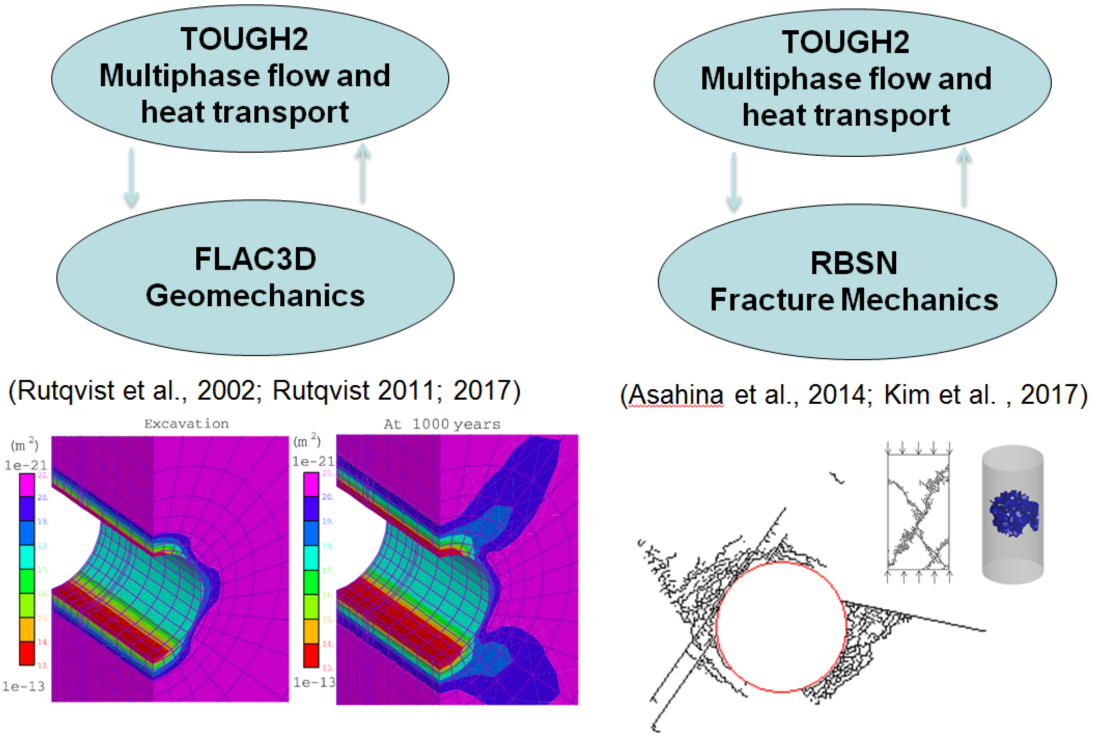

Figure 1-3. TOUGH-FLAC (left) and TOUGH-RBSN (right) models developed for coupled THM process analysis.

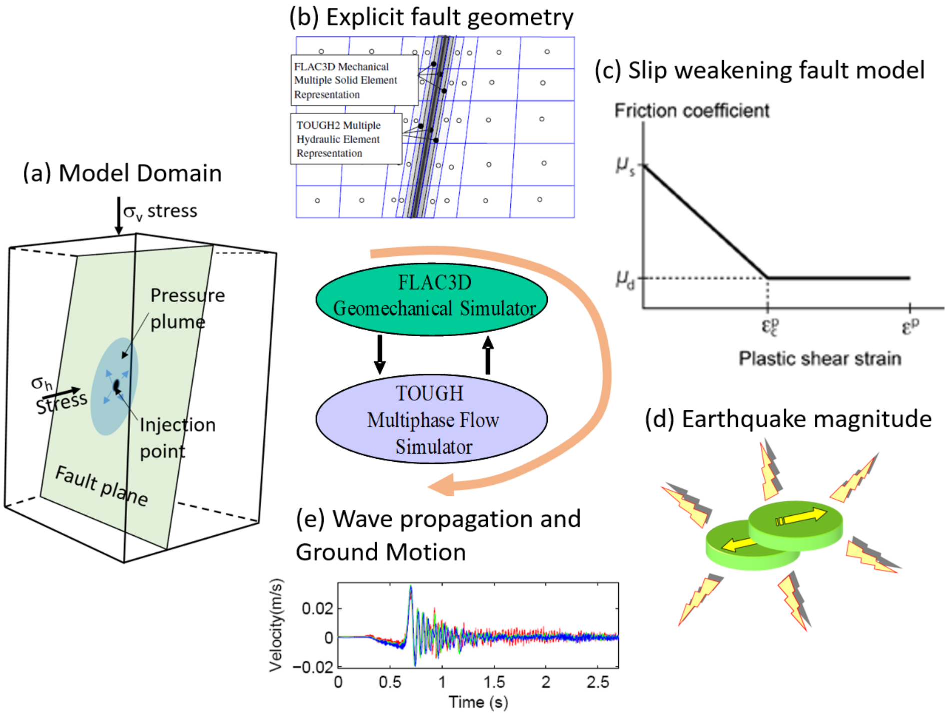

Figure 1-4. Fault activation modeling approach using TOUGH-FLAC (Rutqvist and Rinaldi, 2019).

In this report, we present our FY20 progress to date and plans for the rest of FY20 on these activities. The document delivers milestone M4SF-20LB010301031 "Investigation of Coupled Processes in Argillite Rock" in the LBNL Argillite R&D Work Package (SF-20LB01030103) with input from "LBNL FY20 Argillite International Collaboration" in the LBNL Argillite International Collaboration Work Package (Activity SF-20LB01030107). These activities address key Features, Events, and Processes (FEPs), which have been ranked in importance from medium to high, as listed in Table 7 of the Used Fuel Disposition Campaign Disposal Research and Development Roadmap (FCR&D-USED-2011-000065 REV 1) (Nutt, 2012). Specifically, they address FEP 2.2.01, Excavation Disturbed Zone, for clay/shale, by investigating how coupled processes affect EDZ evolution; FEP 2.2.05, Flow and Transport Pathways; and FEP 2.2.08, Hydrologic Processes, and FEP 2.2.07, Mechanical Processes, as well as FEP 2.2.12, Gas Sources and Effects.

The activities documented in this report also address a number of research topics identified in the R&D Plan for Used Fuel Disposition Campaign (UFDC) Natural System Evaluation and Tool Development (Wang,2011), including Topics S3, Disposal System Modeling – Natural System; P1, Development of Discrete Fracture Network (DFN) Model; P14, Technical Basis for Thermal Loading Limits; and P15, Modeling of Disturbed Rock Zone (DRZ) Evolution (Clay Repository).

In Sections 2 and 3 of this report, we present the current status of the TOUGH-FLAC and TOUGH-RBSN simulators for modeling coupled THM processes in argillite, including fracturing. Section 4 is dedicated to the improved THM bentonite modeling considering micro- and macro-structural changes. In Sections 5 and 6, we present the results of the validation of the TOUGH-FLAC model against *in situ* heater experiments at the Mont Terri Underground Research Laboratory (URL) in Switzerland and at the URL in Bure, France. The heater experiments modeled are the Mont Terri FE (Full-scale Emplacement) Experiment, conducted as part of the Mont Terri Project, and the TED and ALC experiments conducted in Callovo-Oxfordian claystone (COx) at the Meuse/Haute-Marne (MHM) URL in Bure, France. Modeling of the TED and ALC heater experiments have been conducted as part of a modeling task (Task E) of the international DECOVALEX-2019 project. DECOVALEX, which stands for DEvelopment of COupled Models and their VALidation against EXperiments, is an international collaborative activity, in which DOE and LBNL gain access to unique laboratory and field data defined as modeling test cases. DECOVALEX tasks are studied collectively among several international groups to better understand the processes and to improve numerical models, which could eventually be applied in the performance assessment for nuclear waste disposal in clay host rocks and bentonite backfill. Section 7 presents LBNL's activities focused on modeling gas migration in bentonite related to Task A of the international DECOVALEX project. Section 8 present modeling of multiphase flow in rough fractures. Sections 9 and 10 are related to field-scale fault slip experiments in Argillite including a DECOVALEX-2019 task. Section 11 presents research on coupled microbial-abiotic processes in EBS and host rock materials and Section 12 newly added work on molecular modeling of radionuclide retention by bentonite. Finally, in Section 13, we present thoughts on the integration of coupled THM processes models into the Geologic Disposal Safety Assessment (GDSA) and Performance Assessment (PA). Section 14 provides a summary of the progress and future plans.

This page is intentionally left blank.

2. STATUS OF TOUGH-FLAC SIMULATOR

The TOUGH-FLAC simulator (Rutqvist et al., 2002; Rutqvist, 2011), used within the SFWST Argillite R&D work package, has been adapted for modeling coupled THM processes associated with bentonite backfilled repositories in argillite host rocks. For rigorous modeling of the THM behavior of bentonite-based (swelling) buffer and back-fill materials, the BBM (Barcelona Basic Model) and BExM (Barcelona Expansive Model) have been incorporated into TOUGH-FLAC (Rutqvist et al., 2011; 2014b; Vilarrasa et al., 2016). Constitutive models to describe anisotropic THM behavior of shale rock have also been adapted. This model development has been accompanied by extensive testing, verification and validation, including participation within international collaborative projects, such as DECOVALEX. In FY20, development work has continued on improving the calculation speeds using the newest version of TOUGH (TOUGH3) and newest version of FLAC3D (V6 and V7), with linking through Python Scripts that were first presented in Rinaldi et al., (2018). Migrating to FLAC3D V7 also requires re-implementation and testing of BBM and BExM. In the following subsections, we present more details on the status of the TOUGH-FLAC, including the status of the numerical framework for coupled THM modeling and geomechanical constitutive models, followed by a list of completed verification and validation examples, as well as new verifications against analytical solutions.

2.1 TOUGH-FLAC Framework

As mentioned in the introduction, the TOUGH-FLAC simulator (Rutqvist 2011; 2017) is based on linking the TOUGH2 multiphase flow and heat transport simulator (Pruess et al., 2012) with the FLAC3D geomechanical simulator (Itasca, 2011). In this approach, TOUGH2 (Pruess et al., 2012) is used for solving multiphase flow and heat transport equations, whereas FLAC3D (Itasca, 2011) is used for solving geomechanical stress-strain equations.

For analysis of coupled THM problems, TOUGH2 and FLAC3D are executed on compatible numerical grids and linked through a coupled THM model (Figure 2-1) with coupling functions to pass relevant information between the field equations, which are solved in the respective codes. In the coupling scheme between TOUGH2 and FLAC3D, the TOUGH2 multiphase pressures, saturation, and temperature are provided to update temperature and pore pressure to FLAC3D (Figure 2-1). After data transfer, FLAC3D internally calculates thermal expansion, swelling, and an effective stress. Conversely, an element stress or deformation from FLAC3D is supplied to TOUGH2 to correct element porosity, permeability, and capillary pressure for the fluid-flow simulation in TOUGH2. The corrections of hydraulic properties are based on material-specific functions.

In a TOUGH-FLAC simulation, the calculation is stepped forward in time with the transient multiphase fluid flow analysis in TOUGH2, and at each time step or at the TOUGH2 Newton iteration level, a quasi-static mechanical analysis is conducted with FLAC3D to calculate stress-induced changes in porosity and intrinsic permeability (Figure 2-2). In this scheme, the fluid-flow sequence is solved first under fixed stress with a porosity correction $\Delta\Phi_c$ derived from the constitutive equations of solid:

$$\mathrm{d}\Phi = \left(\frac{b^2}{K} + \frac{b-\phi}{K_s}\right)\mathrm{d}p + \phi\alpha_s \mathrm{d}T - \Delta\Phi_c \tag{2.1}$$

$$\Delta\Phi_c = -\frac{b}{K}\mathrm{d}\sigma_v = -\frac{b}{K}(K\mathrm{d}\epsilon_v - b\mathrm{d}p - K\alpha\mathrm{d}T) \tag{2.2}$$

where K is the bulk modulus of porous medium, K_s is the bulk modulus of solid skeleton, b is the Biot's coefficient, p is the pore pressure, ϕ is the porosity, α_s is the volumetric thermal expansion coefficient of solid grains, T is the absolute temperature, σ_v is the mean stress, and ϵ_v is the volumetric strain. The resulting pressure and temperature are prescribed in the mechanical sequence. This corresponds to so-called stress-fixed iterations in the sequential scheme, in which the solution becomes unconditionally stable. The resulting THM analysis may be explicit sequential, meaning that the porosity and permeability are evaluated only at the beginning of each time step, or the analysis may be implicit sequential, with permeability and porosity updated on the Newton iteration level toward the end of the time step using an iterative process.

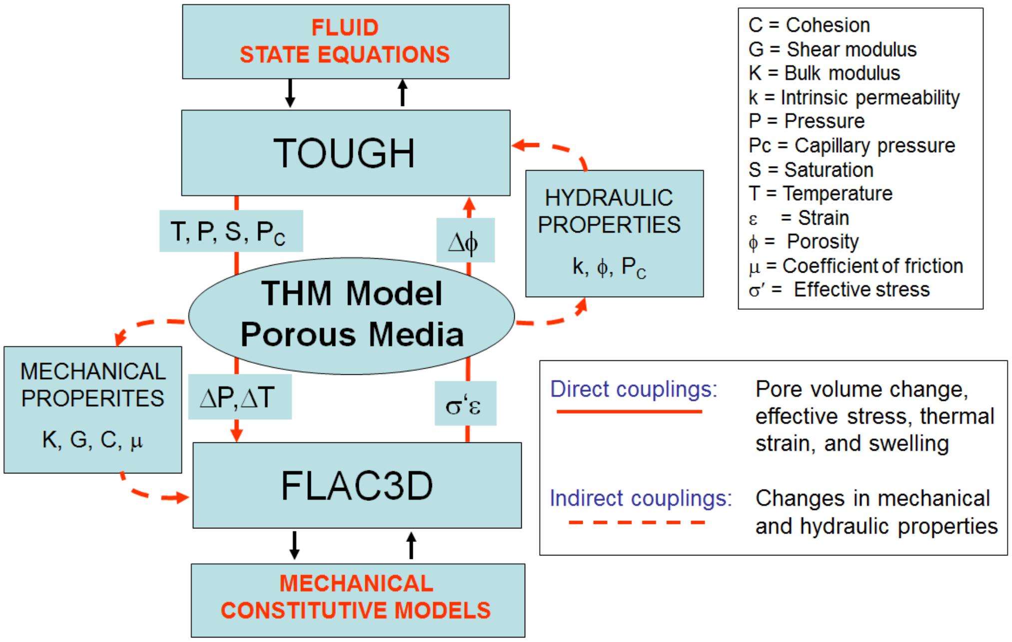

Figure 2-1. Schematic of linking of TOUGH2 and FLAC3D in a coupled TOUGH-FLAC simulation.

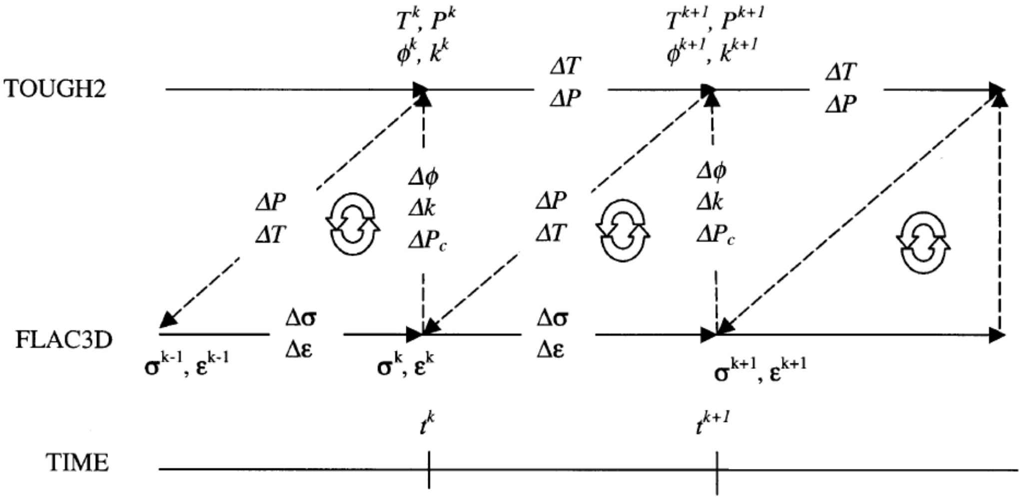

Figure 2-2. Schematic of a numerical procedure of linked TOUGH2 and FLAC3D simulations, with subscript *k* signifying time step.

2.1 Bentonite Constitutive THM Models in TOUGH-FLAC

Since 2010, the TOUGH-FLAC simulator has been adapted and applied to modeling issues related to nuclear waste disposal with bentonite backfilled tunnels (Rutqvist et al., 2011; 2014b). This includes implementation of the BBM (Alonso et al., 1990) for the mechanical behavior of unsaturated soils, which has been applied for modeling of a bentonite backfill behavior (Rutqvist et al., 2011). The model can be used to describe many typical features of unsaturated soil mechanical behavior, including wetting-induced swelling or collapse strains, depending on the magnitude of applied stress, as well as the increase in shear strength and apparent preconsolidation stress with suction (Gens et al., 2006). Figure 2-3 presents the yield surface of the BBM model in *q-p-s* space. The shaded surface corresponds to the elastic region at fully water-saturated conditions. The figure also shows how the yield surface expands at unsaturated and dryer conditions when suction increases. There is an increase in both the apparent pre-consolidation pressure along the load collapse (LC) yield surface and by the increasing tensile strength, which in turn leads to an increased cohesion and shear strength.

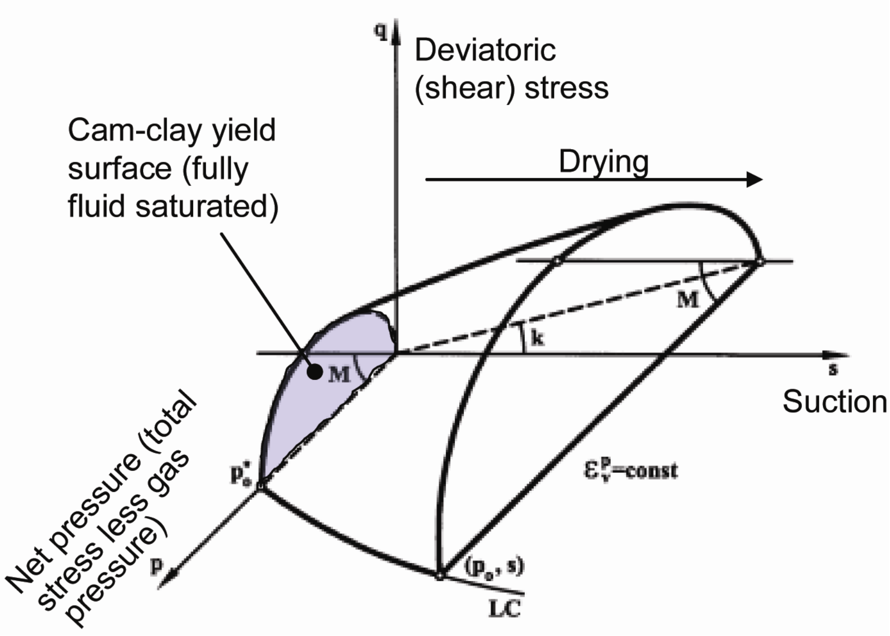

Figure 2-3. BBM constitutive model showing the yield surface in q-p-s space.

The BBM has been used for modeling bentonite-buffer behavior in various national nuclear waste programs in Europe and Japan. For example, the BBM was successfully applied to model the coupled THM behavior of unsaturated bentonite clay associated with the full-scale engineered barrier experiment (FEBEX) *in situ* heater test at the Grimsel Test Site, Switzerland (Gens et al., 2009). The BBM has also been applied to other types of bentonite-sand mixtures based on MX-80, considered as an option for an isolating buffer in the Swedish KBS-3 repository concept (Kristensson and Åkesson, 2008). As part of the Used Fuel Disposition (UFD) program, Rutqvist et al. (2014b) used the BBM for modeling of coupled THM processes around a generic repository in a clay host formation. In the last few years, as part of the UFD and current SFWST program, the BBM has been extended to a dual-structure model, corresponding to the Barcelona Expansive Model (BExM). In a dual-structure model, the material consists of two structural levels: a microstructure, in which the interactions occur at the particle level, and a macrostructure that accounts for the overall fabric arrangement of the material comprising aggregates and macropores (Figure 2-4) (Gens et al., 2006, Sánchez et al., 2005, Gens and Alonso 1992). A dual-structure model has important features for modeling the mechanical behavior of a bentonite buffer, such as irreversible strain during suction cycles. Moreover, a dual-structure model provides the necessary link between chemistry and mechanics, enabling us to develop a coupled THMC model for the analysis of long-term EBS behavior. This approach enables mechanistic modeling of processes important for long-term buffer stability, including effects of pore-water salinity on swelling (loss of swelling), conversion of smectite to nonexpansive mineral forms (loss of swelling), and swelling pressure versus exchangeable cations. Details of the development, testing and applications of the dual-structure model, were first presented in the report by Rutqvist et al. (2014a), and have also been published in a journal paper (Vilarrasa et al., 2016).

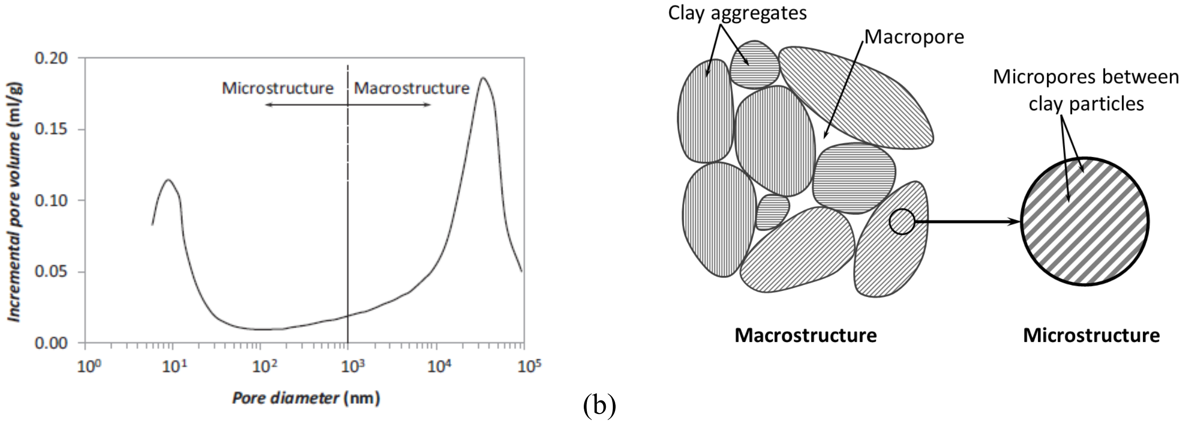

(a) (b)

Figure 2-4. (a) Pore size distribution, and (b) schematic representation of the two structural levels considered in the dual structure model. Clay particles are represented by the gray lines (Vilarrasa et al., 2016).

The further results of BExM model implementation, testing and validation were presented in the report by Zheng et al. (2016), including the results of modeling of (1) one swelling pressure test on Boom clay pellets, (2) two cyclic wetting-drying tests on one type of expansive clay, and (3) two tests with a combination of loading paths on compacted bentonite samples. Based on the simulation results, the model is capable to reproduce the observed behavior of expansive clays during experiments associated with suction changes. The computation results, which we obtained with BExM, agreed well with the experimental data, and also followed the same trend as the results presented by BExM developers (Zheng et al., 2006). However, considerable uncertainties still exist in the use of the BExM model, because of complexities in the underlying processes and a large number of parameters needed to define the constitutive dual-structure behavior of clays.

In FY20, work has been conducted to improve the implementation of the BExM model in TOUGH-FLAC, including implementation in newest versions of FLAC3D with testing against published data. This work is quite comprehensive and is, therefore, presented in Section 4 of this report.

2.2 Shale Constitutive THM Models in TOUGH-FLAC

Constitutive models of coupled THM processes in Argillite have been developed based on the results of modeling of a number of *in situ* experiments at Mont Terri and Bure underground research laboratories (URL's), considering anisotropic properties of clay and shale elasticity, strength, thermal conductivity, permeability, and thermal expansion.

The FLAC3D ubiquitous joint model can handle anisotropic strength properties of shale, and this model has been commonly used for geomechanical modeling of Opalinus Clay at Mont Terri (Corkum and Martin, 2007). The theory and implementation of this model in FLAC3D is described in the FLAC3D manual

(Itasca, 2011). The model accounts for an orientation of weakness (weak plane) in a Mohr-Coulomb constitutive model. The criterion for failure on the plane of a given orientation is based on the escalation of a composite Mohr-Coulomb envelope with the tension cutoff. The rock-strength input parameters include the friction angle and the tension cutoff with weaker properties for the weak (joint) planes compared to that of the intermediate intact rock. Figure 2-5 shows the results of a simulation involving a horizontal emplacement tunnel in Opalinus Clay with the horizontal bedding (Rutqvist et al., 2014b). On top and bottom of the emplacement tunnel we can see a shear failure that occurred along bedding planes, whereas the volumetric strain in the isotropic matrix rock is uniformly distributed around the tunnel.

The results of modeling of heater experiments at Mont Terri and Bure showed the need to take into account anisotropic thermal conductivity to match temperature measurements observed at the experiments (Garitte et al., 2017). Anisotropic thermal conductivity is not standard in TOUGH2 and TOUGH-FLAC and was implemented into the TOUGH2 source code. Anisotropic permeability can be considered in the standard TOUGH2 code for rectilinear grid.

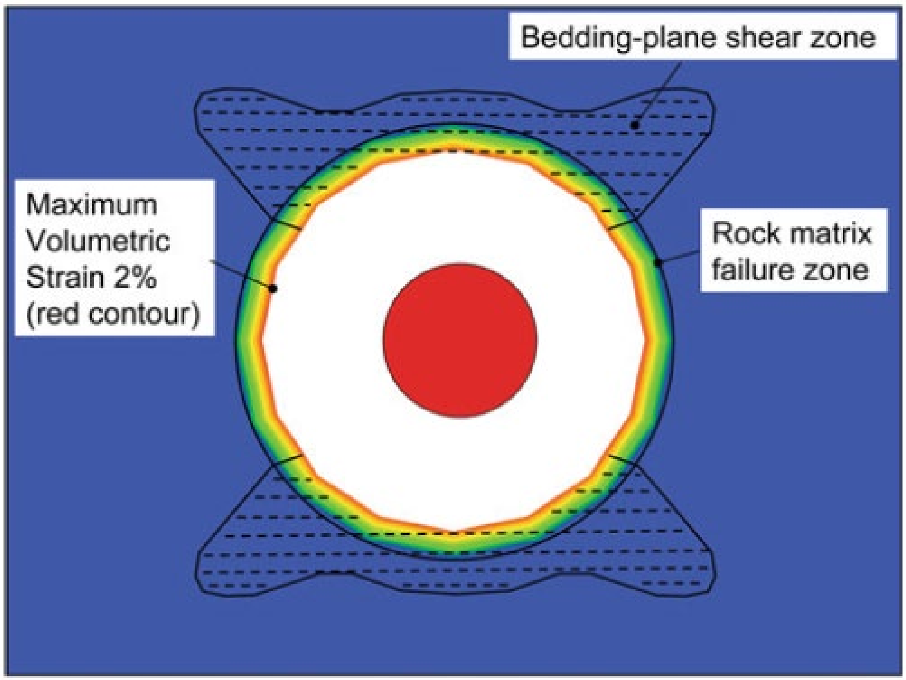

Figure 2-5. Volumetric strain contour and extent of failure zones related to horizontal bedding planes and rock matrix (Rutqvist et al., 2014b).

2.3 EDZ Models in TOUGH-FLAC

The EDZ is one of the most important features taken into account in the performance assessment of repositories in argillite, and was assigned the highest research priority ranking in the 2011 UFD Road Map (Nutt, 2012). Models of different sophistications have been developed and applied to model the EDZ using TOUGH-FLAC, including

1) Empirical stress-permeability model;

2) Non-linear elastic and brittle failure model; and

3) Anisotropic continuum damage model.

The three models are summarized in the following subsections.

2.3.1 Empirical stress-permeability model

An empirical stress-permeability model calibrated against in situ EDZ data is described in Rutqvist (2015). The empirical EDZ model was applied in a previous phase of the DECOVALEX project related to nuclear waste disposal in crystalline rock (Rutqvist et al., 2009). The empirical EDZ model was calibrated against EDZ data from the Tunnel Sealing Experiment (TSX) experiment conducted at the underground research laboratory in Manitoba, Canada (Martino et al., 2004).

The permeability around the tunnel was simulated using the empirical stress-permeability relationship in which permeability is a function of the effective mean stress, σ'_m, and deviatoric stress, σ_d, according to (Rutqvist et al., 2009):

$$k = [k_r + \Delta k_{\max} \exp(\beta_1 \sigma'_m \;)] \cdot \exp(\gamma \Delta \sigma_d) \tag{2.3}$$

where k_r is residual (or irreducible) permeability at high compressive mean stress, Δk_{max}, β_1 and γ are fitting constants, and $\Delta\sigma_d$ is the change in the deviatoric stress relative to a critical deviatoric stress for onset of shear-induced permeability.

Figure 2-6 compares simulated and measured permeability changes for $\beta_1 = 4\times10^{-7}$ Pa^{-1}, $k_r = 2\times10^{-21}$ m^2, $\Delta k_{max} = 8\times10^{-17}$ m^2, $\gamma = 3\times10^{-7}$ Pa^{-1}, and with the critical deviatoric stress for onset of shear-induced permeability set to 55 MPa.

The 55 MPa critical deviatoric stress roughly coincides with the extent of a cluster of microseismic events at the top of the tunnel and is also about a factor of 0.3 of the instantaneous uniaxial compressive stress of small-scale core samples, which is consistent with the stress level at which crack initiation was observed in studies of Lac du Bonnet granitic samples (Martin and Chandler, 1994). Thus, it is an example taken from a crystalline rock site, whereas such calibration could also be made using in situ data from an Argillite rock site, such as Mont Terri.

A model prediction for the longer term EDZ evolution of a nuclear waste emplacement tunnel was conducted based on the relationship calibrated against field measurements of EDZ during excavation (Ngyuen et al., 2009). Figure 2-7 presents the EDZ permeability distribution after excavation and at 1000 years after emplacement when the thermal-mechanical stress might be the highest. Figure 2-7 shows that there is some increase in EDZ permeability at 1000 years compared to that after excavation, though the changes are small.

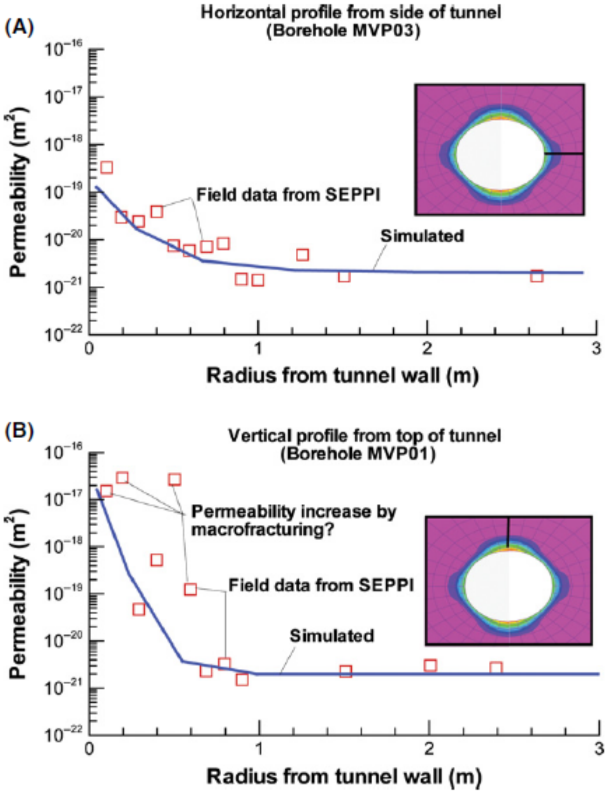

Figure 2-6. Simulated and measured permeability changes around the TSX tunnel (Rutqvist et al. 2009). Permeability versus radius: (A) along a horizontal profile from the side of the tunnel, and (B) a vertical profile from the top of the tunnel.

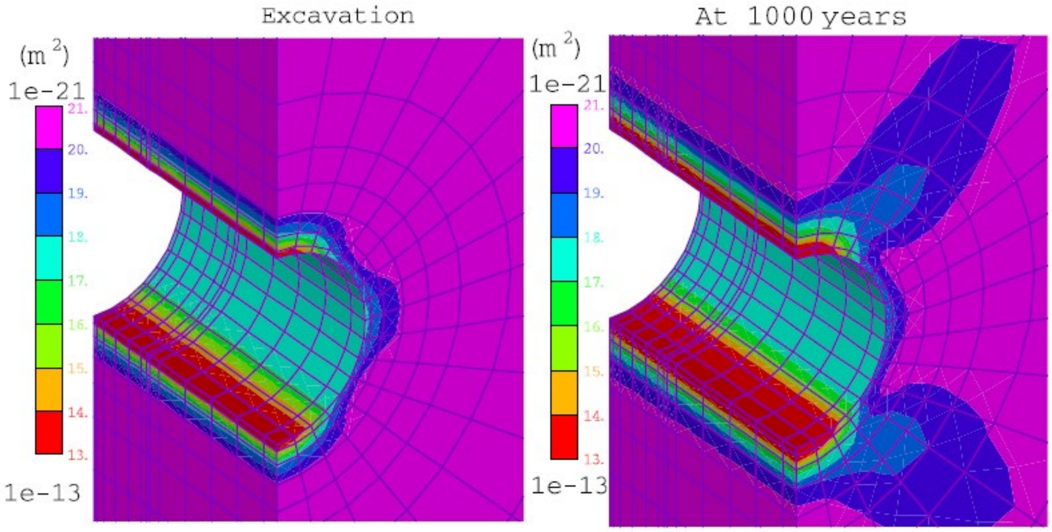

Figure 2-7. Calculated permeability distribution for the generic repository emplacement tunnel in crystalline rocks using the empirical stress-permeability relation (Nguyen et al., 2009).

2.3.2 Non-linear elastic and brittle failure model

A non-linear elastic and brittle failure model was implemented in TOUGH-FLAC (Liu et al., 2012). The non-linear elastic model, denoted the two-part Hooke's model (TPHM), provided a new constitutive relationship and associated formulations regarding rock hydraulic/mechanical properties. The usefulness and validity of the TPHM were demonstrated by the consistency between simulation results and field observations at the Mont Terri URL. The brittle failure model was applied using a fine-grid numerical approach, based on the explicit incorporation of small-scale heterogeneity of mechanical properties. Using the combination of the TPHM and the fine-grid numerical approach of the results of investigations were compared with field results at Mont Terri.

Figure 2-8 shows an example of calculated brittle failure and permeability changes around a tunnel in a host rock representing Opalinus Clay. The model simulation captured both the observed displacements and the size of the damage zone. Moreover, the fine-grid numerical approach, together with an explicit incorporation of the small-scale heterogeneity of mechanical properties, was able to capture the overall behavior of the EDZ, as demonstrated by the consistency between the simulated and the observed EDZ size, which was about 1 m on the side of the tunnel. The calculated permeability values are especially high in the EDZ within the tunnel sidewalls, varying between 2.39×10^{-14} m^2 and 7.45×10^{-13} m^2, which are consistent with measured data from pneumatic borehole injection tests at the Mont Terri Laboratory (Bossart et al., 2002; Bossart et al., 2004). Such a model validated against field data could also be used to calculate the EDZ evolution over the longer term. However, while the current model addresses permeability changes induced during excavation, it does not address sealing and healing processes that might be important over the long-term.

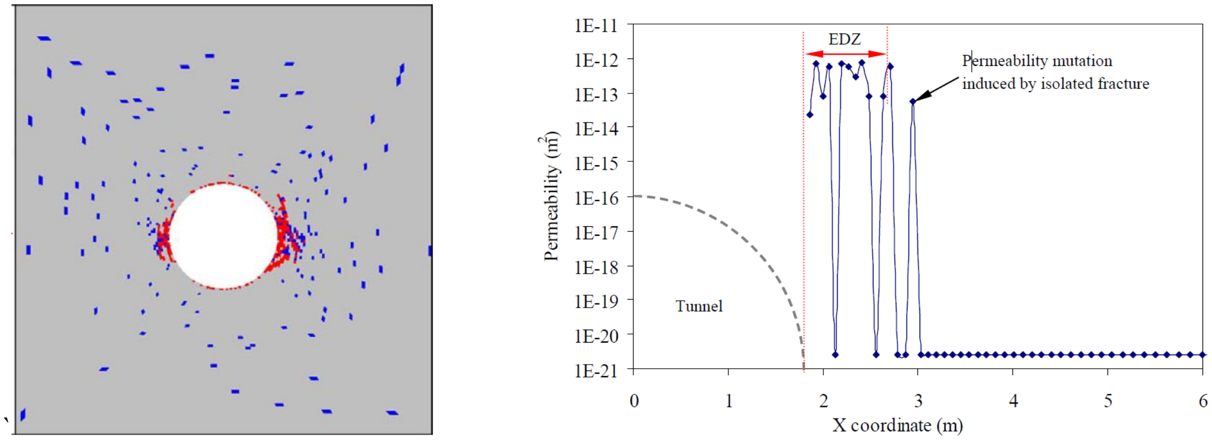

(a) (b)

Figure 2-8. (a) Calculated brittle failure (tension failure marked by RED color and shear failure marked by BLUE color), and (b) permeability changes around an excavation in argillite (Liu et al., 2012).

2.3.3 Anisotropic continuum damage model

In FY17, an anisotropic damage model named Deviatoric Stress Induced Damage (DSID) was implemented into the simulator to account for crack propagation due to microstructure changes (Zheng et al., 2017). This new damage model is hyper-elastic, i.e., the stress-strain relationship was derived from the expression of a thermodynamic potential, and was derived based on Continuum Damage Mechanics (CDM), which cannot be used to model cracks at the micro-scale, as opposed to micro-mechanics. The model implementation has been validated by comparison with modeling several laboratory experiments on granite and by comparing computation results with different codes. The agreement between simulation and experimental results proved that the damage model was implemented correctly in our simulator and was capable to reproduce the same non-linear mechanical behavior due to damage propagation. For instance, the damage model was utilized to predict the evolution of the disturbed rock zone (DRZ) around emplacement tunnels, where the model enabled to capture the micro-crack propagation induced by the excavation (Figure 2-9). In Figure 2-9, Ω_m is the dimensionless damage variable that could vary between 0 to 1.

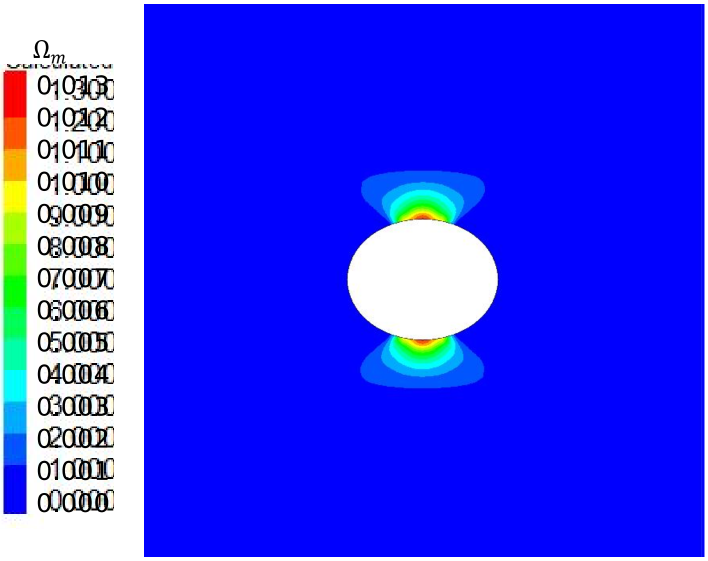

Figure 2-9. The simulation result of damage distribution at TSX experiment.

2.4 Development of TOUGH3-FLAC3D V6 and V7

The recent development of the TOUGH3 code allows for a faster and more reliable fluid flow simulator. At the same time, new versions of FLAC3D are released periodically, allowing for new features and faster execution. In the framework of the current activities, we have coupled for the first time the newly developed TOUGH3 (Jung et al., 2017) with the version 6.0 of FLAC3D (Itasca, 2018). After verifying the correctness of the solution compared to the previous version, we evaluated the performance of the newly developed approach, which allowed for running on a multi-processors machine. We maintained the sequential coupling between the two codes as described above, and accounted for the main modification:

(1) Using TOUGH3 for parallel processing of fluid flow,
(2) Accounting for Python flexibility (as embedded in FLAC3D) and using a binary file exchange, to speed up read/write operation,
(3) No need to restart FLAC3D each time step, avoiding restore/save of state file that can be quite large for large models.

In Message Passing Interface (MPI) codes, and in particular for TOUGH3, a processor is designed as “IOProcessors,” and takes care of all the input/output functionality of the code. The coupling approach for TOUGH3 and FLAC3D is illustrated in Figure 2-10. FLAC3D is started at the beginning of the simulation. Then, for each time step, before starting the iterations for solving the fluid flow problem, TOUGH3 invokes a subroutine to gather the information from all the processors. Such information (pressure, temperature, saturation and capillary pressure) are written to the binary file TOU_FLA by the IOProcessor, and write a flag file, read by FLAC3D. All this stage is basically done in serial by the IOProcessor, while all other *n* processors are idle. Given the right flag, FLAC3D (i) reads the TOU_FLA file (with Python), (ii) solves for the mechanical equilibrium (in parallel), (iii) writes the FLA_TOU file to transfer information to TOUGH3 (with Python), and finally (iv) modify the flag file for TOUGH. At this stage, the subroutine invoked previously by TOUGH3 is waiting for the right flag, then the IOProcessor serially reads the FLA_TOU file and distributes the variables/properties (bulk modulus, Biot’s coefficient, strain, and stress) to all *n* processors. Finally, the parallel computing can restart with the calculation of mechanically-induced changes of flow properties and with continuation of the iterations to finish the current time step.

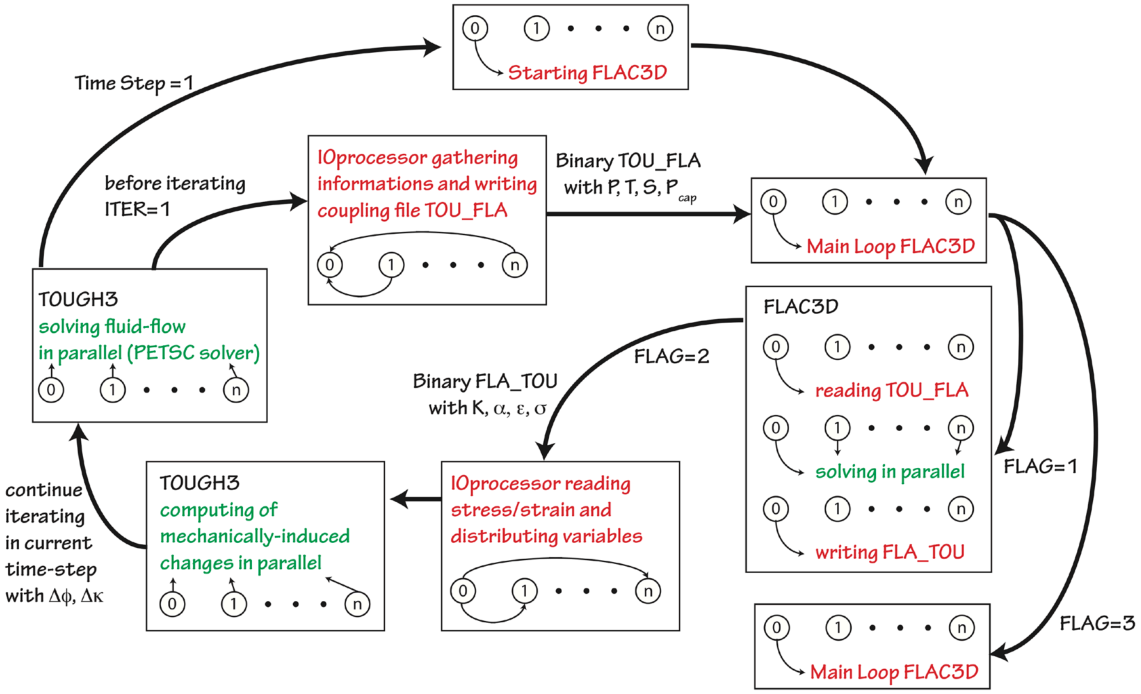

Figure 2-10. Illustration of a coupling between TOUGH3 and FLAC3D for each time step. Green parts are executed in parallel, while red parts are executed in serial. P, T, S, P_{cap} are pore pressure, temperature, saturation, and capillary pressure, respectively. K, α, ε, σ are bulk modulus, Biot’s coefficient, strain, and stress, and Δϕ and Δκ stand for porosity and permeability changes.

One of the limitations of FLAC3D is that it runs only on Windows-based machines. Then, to make use of the MPI parallelization provided in TOUGH3, we compiled the code in the Cygwin environment, which also allows for calling Windows-based programs (i.e., FLAC3D batch).

All simulations presented here were run on a large workstation with two 6-core CPUs Intel Xeon E5-2643 at 3.40 GHz and equipped with 64 GB RAM. This hardware configuration allows for using up to 12 processors, and it provides a relatively good scaling for TOUGH3-only models with a simulation being up to 6X faster, when run in parallel compared to serial for a mesh with about 850,000 elements.

Figure 2-11 shows the performance of TOUGH3-FLAC compared to TOUGH2-FLAC5. Similarly to the previous version, the code reaches peak performance by using only few threads in FLAC3D (3/4 core, 6/8 threads) for a mesh with 50’000 elements (Figure 2-11a). The total execution time decreased from about 1300 s with the old model to about 400 seconds, when accounting for the maximum number of threads (Figure 2-11b). By varying the number of elements, we observed a similar scaling/improvement in performance, up to 3.5 when using 10 cores/20 threads (Figure 2-11c). Worth to note that the current hardware is not optimal for FLAC3D, which works better on single, multi-threaded processor: indeed, we observe a rupture in performance scaling when the second processor is used. To highlight the role of TOUGH3, it is useful to compare the scaling with the number of cores but fixing the threads in FLAC3D (Fig, 2-11d). With respect to TOUGH2-FLAC5, most of the improvement is achieved by optimizing the coupling between the two codes. The use of TOUGH3 is quantified in about 8% and 5% speed increase when using 50’000 and 200’000 elements, respectively. TOUGH3-FLAC3D V6 is about 4 times faster than TOUGH2-FLAC5 for a mesh as large as 200’000 elements. In FY20, we have now changed from FLAC3D V6 to V7, which is the latest version of FLAC3D.

The developed approach is currently being used in the framework of BenVaSim code benchmarking, with excellent matching to analytical solutions. In the next phase, we will focus on (1) testing performances for larger meshes, and (2) applying a newly developed approach to conditions relevant to nuclear waste disposal.

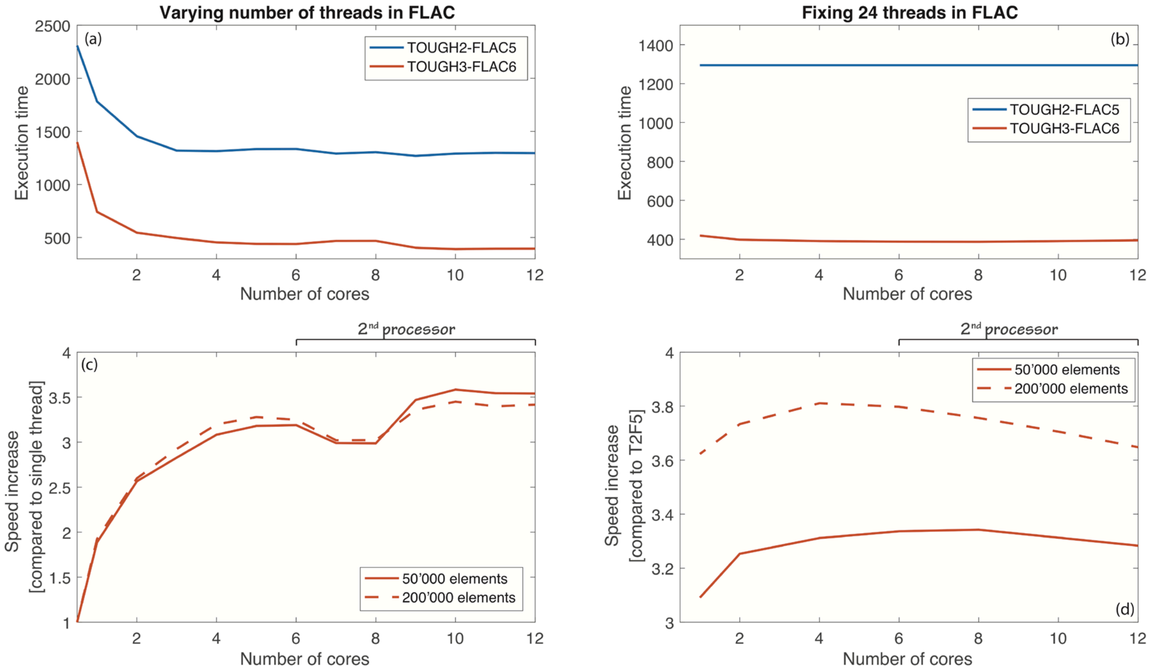

Figure 2-11. (a) Comparison of execution time as a function of the number of cores/threads for TOUGH3-FLAC6 (red) and TOUGH2-FLAC5 (blue). (b) Comparison between T3F6 and T2F5 as function of number of cores while fixing the number of threads to 24 in FLAC3D. (c) Execution speed improvement for 50’000 (solid) and 200’000 (dashed) elements as function of the number of cores/threads. (d) Execution speed improvement with respect to old version as a function of number of cores while fixing 24 threads in FLAC for 50’000 (solid) and 200’000 (dashed) elements.

This page is intentionally left blank.

3. STATUS OF TOUGH-RBSN SIMULATOR

The TOUGH-RBSN simulator (Asahina et al., 2014; Kim et al., 2017) has been used for modeling coupled THM processes related to fracture/damage behavior. The individual physical processes related to fracture propagation are represented by separate program modules: the TOUGH2 code for multiphase flow and mass transport based on the finite volume approach; and the rigid-body-spring network (RBSN) model for mechanical and fracture-damage behavior, which are sequentially coupled with each other. The discrete fracture network (DFN) approach is adopted in the coupling procedure, where fractures have enhanced flow properties as well as degraded mechanical properties in a discrete manner. This section presents more details on the TOUGH-RBSN simulator, including the status of the numerical framework for THM coupling procedure, modeling of discrete fractures for enhanced flow in the TOUGH2 code, and fracture determination in the RBSN approach. In FY19, anisotropic mechanical elasticity and strength was implemented and applied for modeling EDZ fracturing in Argillite (Kim et al., 2020). In this section, the current status of TOUGH-RBSN in presented in terms of coupling procedure and fracture modeling.

3.1 TOUGH-RBSN Coupling Procedure

Figure 3-1 shows a schematic flow diagram of the coupling procedure between the TOUGH2 and RBSN codes. Coupling modules are implemented in each side of the modelling codes, by which material properties and mechanical boundary conditions are updated with the outputs of primary variables of physical quantities. Pore pressure and degree of saturation are primary variables of the TOUGH2 analysis, which are involved in the RBSN simulation to determine the effective stress and swelling/shrinkage strain. In return, the primary variables of the RBSN model, stress/strain states, damage index, and fracture aperture, are used to evaluate hydrological properties and conditions for the TOUGH2 simulation.

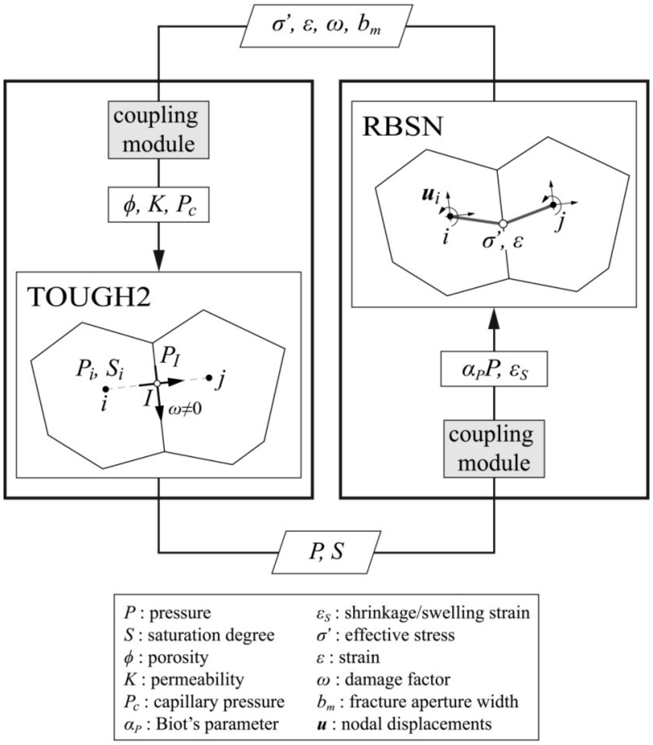

Figure 3-1. Coupling procedure of the TOUGH-RBSN simulator (adapted from Kim et al., 2017).

First, the TOUGH2 to RBSN link supplies pressure and degree of saturation to update the mechanical quantities. Based on the linear poro-elasticity theory, the effective (grain-to-grain) stress ${\sigma_n}'$ is calculated from the pore pressure P (Biot and Willis, 1957):

$${\sigma_n}' = \sigma_n + \alpha_p P \tag{3.1}$$

where σ_n is the total normal stress obtained from overall loading, including external loads; α_p is Biot's effective stress parameter. Note that tensile stress is taken to be positive for the sign convention. Also, the shrinkage/swelling effect due to the local changes of liquid saturations ΔS can be taken into account:

$$\Delta\varepsilon_s = \alpha_s \Delta S \tag{3.2}$$

where ε_s is shrinkage/swelling strain; and α_s is the moisture swelling coefficient. If a poro-elastic geomaterial is subjected to confinement conditions, the stress due to swelling/shrinkage can be calculated as

$$\Delta\sigma' = \Delta\varepsilon_s E \tag{3.3}$$

where *E* is the Young's modulus.

The fracture process of a local rigid-body-spring element is realized by degrading the springs. A fracture event entails a reduction of spring stiffnesses and a release of the associated elemental forces. For the degraded spring set, the modified stiffness matrix $\mathbf{D}'$ is given by

$$\mathbf{D}' = (1 - \omega)\mathbf{D} \tag{3.4}$$

where *ω* is a scalar damage index with a range from zero (undamaged) to 1 (completely damaged). For brittle fracturing, which is applied to the cases presented in this report, *ω* is directly switched from 0 to 1 once a fracture event occurs (i.e., the stress state of an element violates the failure criteria).

Next, the RBSN to TOUGH2 link supplies the effective stress and the strain calculated in the lattice element to update the hydrological properties of the corresponding TOUGH2 grid blocks i and j on the left side of Figure 3-1. Porosity, permeability, and capillary pressure are generally related with the effective stress and strain values (Rutqvist and Tsang, 2002).

If fracturing occurs at element *ij* (i.e., $\omega \neq 0$), the associated fracture node *I* and additional connections are activated in the TOUGH2 model. The permeability of an individual fracture depends on the hydraulic aperture b_h (Witherspoon et al., 1980). According to a parallel-plate model, the fracture permeability is defined as $b^2/12$. The hydraulic aperture is coupled to the mechanical aperture b_m (Rutqvist et al., 1998, 2000):

$$b_h = f(b_r + \langle b_m - b_r \rangle) \tag{3.5}$$

where $\langle x \rangle = 1/2(x + |x|)$ represents Macaulay brackets, b_r is the residual hydraulic aperture, and a dimensionless factor $f \leq 1.0$ accounts for the slowdown of flow in a natural rough fracture in comparison to the ideal case of parallel smooth fracture surfaces.

In the TOUGH-RBSN sequential coupling, TOUGH2 is a main driver of analysis, which controls the time stepping during the coupling procedure, while the RBSN approach solves the mechanical response as a quasi-static process at each time step. The selection of small time steps is important to find stable solutions of the mechanical response, so the TOUGH2 input defines the upper limit for time step size with a small value to avoid any abrupt change of hydrological conditions over time steps.

3.2 Model Discretization and Discrete Fracture Representation

The computational domain for both the TOUGH2 and RBSN calculations is tessellated using a Voronoi diagram (Okabe et al., 2000). The discretization process is carried out basically in three steps: 1) nodal point insertion, 2) Delaunay tessellation, and 3) Voronoi discretization. Within the domain, nodal points are positioned in regular or irregular formation. Introducing a parameter for minimum allowable distance can define the desired nodal density of the unstructured grid. The Delaunay tessellation is conducted based on the nodal positions, where each Delaunay edge defines the nodal connection of the corresponding lattice element. Through the dual Voronoi tessellation, the spatial domain is collectively filled with discrete polyhedral cells that render the elemental volumes. More detailed procedure of the domain partitioning is presented elsewhere (Yip et al., 2005; Asahina and Bolander, 2011).

For the discrete fracture network (DFN) approach, fractures and other discontinuities are explicitly modeled within the Voronoi grid. Voronoi cells generally represent the matrix component in a geomaterial constitution, and pre-existing or newly generated fractures are placed on the Voronoi cell boundaries. The geometry of fracture networks (e.g., orientation, length, curvature) can be obtained by observational mapping data, computer-generated statistical reproductions, or mechanical simulation results. An example of the discretization procedure in 2D modeling involving a straight fracture is as follows:

1. Generate a Voronoi unstructured grid for the spatial domain,
2. Overlay the reference fracture trajectory onto the grid,
3. Test all connections of natural neighboring nodes to check if they cross the fracture. For example, compare connections *ij* and *jk* in Figure 3-2, and
4. Collect the Voronoi cell boundaries corresponding to the nodal connections that cross the reference fracture (such as *ij*) and form discretized fractures.

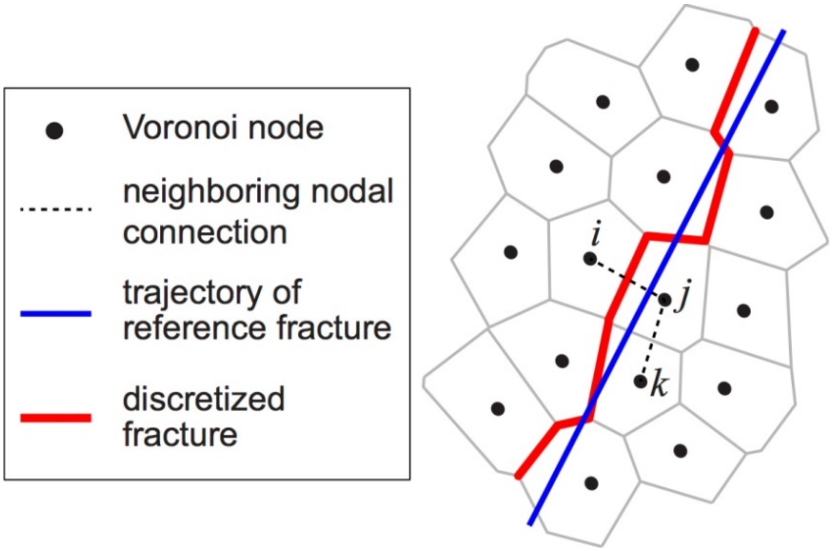

Figure 3-2. Fracture mapping and discretization within an unstructured Voronoi grid (adapted from Asahina et al., 2014).

By repeating the above process for multiple fractures, a network of discrete fractures can be generated. This fracture discretization process is completely automated and can be easily extended to more complicated geometries in 3D modeling. However, the grid size should be carefully chosen to obtain a sufficiently precise representation of the reference fracture. A finer grid can accommodate the discretized fractures that conform more closely to the reference fracture.

In the simulations using a grid structure of the ordinary Voronoi discretization, flow and mass transfer are enacted only through the connections of the neighboring Voronoi nodes (called cell-cell connections in Figure 3-3a. However, if fracturing occurs within the matrix, substantially enhanced flow may arise through the fracture path. In order to demonstrate the accelerate flow in the DFN approach, the grid structure is modified, for which additional interface nodes and the associated connections are introduced. As shown in Figure 3-3b, an interface node with increased permeability is inserted where the cell-cell connection intersects the Voronoi cell boundary. The original cell-cell connection is divided into two cell-interface (and vice versa) connections by the interface node. In addition, the connections between the interface nodes are established to activate flow channels in discrete fractures.

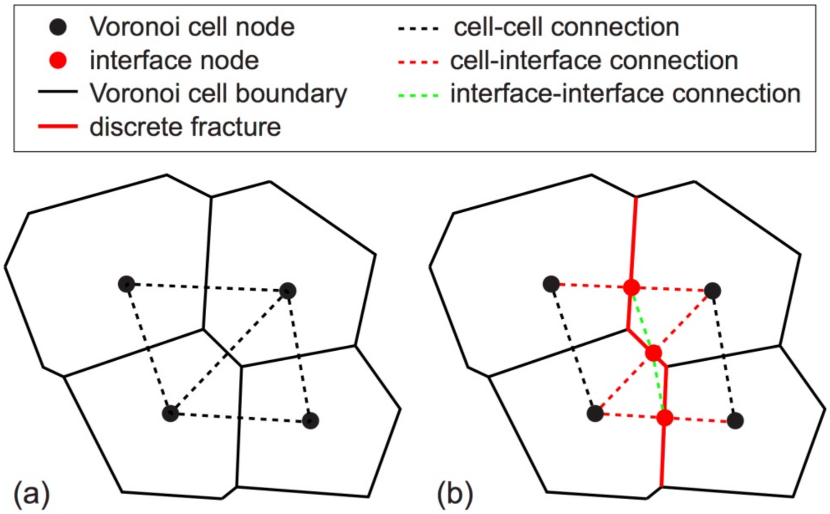

Figure 3-3. Transformation of the grid structure for enhanced flow through discrete fractures: (a) original Voronoi cell nodes and connections; and (b) insertion of interface nodes and connections.

3.3 Status of TOUGH-RBSN Verification and Validation

Coupled THM processes, including fracture propagation within argillaceous rocks and clay rich geomaterials have been simulated using the TOUGH-RBSN code with adequate constitutive models, which are verified and validated against laboratory tests and analytical solutions. In the following, completed verifications and validations of TOUGH-RBSN are listed with the references in which those activities are documented.

- Simulations of swelling stress development and desiccation cracking in geomaterials validated against independent laboratory test data (Asahina et al., 2014)
- Hydraulic fracture propagation in rock-analogue samples made of soda-lime glass with a designed fracture geometry (Kim et al., 2017)
- Excavation damage and fracture development influenced by the deformation and strength anisotropy of clay rocks (Kim et al., 2020)

In addition, LBNL was involved in DECOVALEX-2019, an international collaborative activity for validating various modeling approaches against laboratory and field collected datasets. TOUGH-RBSN has been used to model two-phase liquid and gas flow in a saturated bentonite sample with dilatant flow path and fracture generation. Intermediate results for 1D gas flow have been presented in Tamayo-Mas et al. (2018), including an extensive comparison of simulation results using 11 different modeling approaches with laboratory test data. The TOUGH-RBSN models, based on relevant conceptual models, exhibit key responses such as pressure/stress evolution in a plausible match with the experimental data. In FY20, we have focused on completing 3D modeling of spherical gas flow in bentonite samples, and the conceptual models and the updated results are presented in Section 6.

This page intentionally left blank.

4. BExM MODELING OF BENTONITE

Bentonite is an effective buffer material in the nuclear waste repository because of the following properties. First, the permeability of bentonite in a saturated state is small enough to ensure that the potential leakage of nuclear waste contaminants occurs only by diffusion, which is an extremely slow process. Second, bentonite undergoes swelling upon imbibition of water, which provides a self-sealing mechanism to tighten the gaps between the bentonite and the host rock.

These properties of bentonite are attributed to the characteristic behavior of a highly expansive clay. However, in a typical nuclear waste repository, buffers are subjected to drastic changes in thermal, hydraulic, and mechanical conditions due to heating of nuclear waste canisters, which could last tens of thousands of years. To predict the sealing capability of the buffer, a better understanding of how the buffer behaves in response to the heating of canisters in a nuclear waste repository is needed. In this study, numerical simulations of the buffer behavior under thermo-hydromechanically coupled conditions are performed with the Barcelona Expansive Model (BExM) implemented in FLAC3D. Verification tests of the constitutive model under several complex loading paths have been performed and comparisons have been made with the experimental and numerical results available in the literature to increase the confidence in applying the BExM for the THM simulation of the long-term behavior of nuclear waste repositories.

4.1 Introduction of the Barcelona Expansive Model

Barcelona Expansive Model is chosen here to model the bentonite buffer behavior. In the model, two structure levels are distinguished: the microstructural level, at which swelling of active minerals takes place, and the macrostructural level responsible for the rearrangement of granular-like skeleton formed by the aggregates. Evolution of the two structure levels and the interaction between them are considered explicitly under complex conditions, which provide an approach to reproduce the characteristic behavior of unsaturated expansive clay with clear physical interpretation of soil clay structures.

4.2 Physical interpretation of the micro- and macro-structures in BExM

Bentonite buffer material such as the MX-80 granular bentonite and Wyoming granular bentonite belongs to clay-like materials. Figure 4-1 (Collins & McGown 1974) is the schematic representation of the fabric features in clay from micro-scale to macro-scale. The fabric/structure refers to the arrangement of particles, groups and pore spaces.

Figure 4-1. Schematic representation of elementary particle arrangements: (a) individual clay lamella or platelet, (b) clay platelet group interaction, and (c) clothed silt or sand particle interaction (Collins and McGown, 1974).

Figure 4-2 from Seiphoori (2015) clearly shows the two main structure levels of the poured and compacted Wyoming granular bentonite indicated by the two peaks in the pore size distribution. Both structure levels have been considered explicitly in the BExM. The microstructure corresponds to the intra-grain pores indicated by the first peak shown around 10^{-2} μm and the macrostructure corresponds to the inter-grain pores indicated by the second peak around $10^{0.1}$ and $10^{1.1}$ μm.

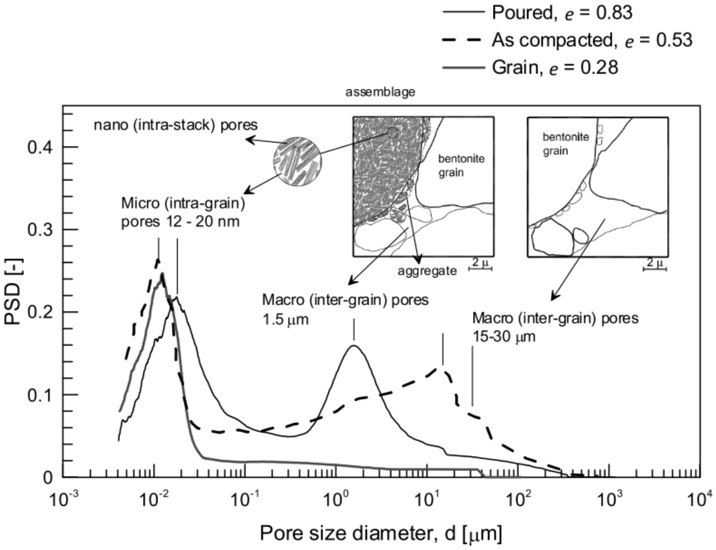

Figure 4-2. Two distinct structural levels in poured and compacted Wyoming granular bentonite (Seiphoori, 2015)

4.3 Microstructure of the bentonite

Volumetric deformation of active minerals, such as smectite and montmorillonite, takes place on the level of microstructures. The drastic change in soil fabric especially under suction loading distinguishes the active clay from a non-active clay. The distinctive behavior of expansive clay shows attributes largely to the structure of active clay minerals, and the induced interaction between clay minerals and pore water.

Active clay minerals including smectite or montmorillonite are the essential components of bentonite. They are crystalline minerals composed of two basic units of silicon tetrahedrons and aluminum octahedrons shown in Figure 4-3 (Seiphoori, 2015). The mineral groups are characterized by stacking arrangements of the basic units in Figure 4-4 (Seiphoori, 2015).

In Figure 4-4, the weak bonding between successive layers in smectite clay results in larger distance between two consecutive layers. The occupancy in between is filled by the combination of the molecule of H_2O and the ion Na^+. However, in non-active clay like illite, the layers are strongly held together by the presence of potassium ions. For active clay, the distance between the occupancy will be greatly influenced by the water content of the surrounding environment, which results in the volumetric change of microstructure. Change in the microstructure attributes to the large swelling strains bentonite experience in suction loading.

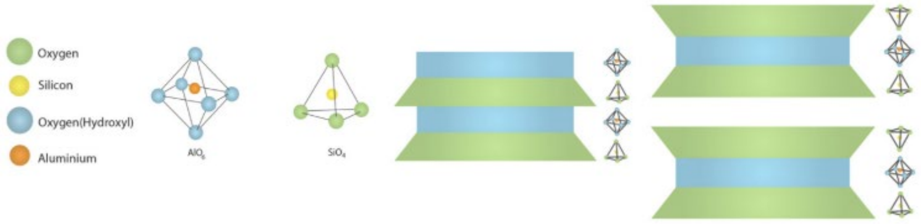

(a) basic crystals in clay mineral
(b) 1:1 structure in kaolinite
(c) 2:1 structure in illite and smectite

Figure 4-3. Crystal constitution of clay minerals: (a) aluminum octahedral and silicon tetrahedron units, (b) basic unit layers for kaolinite, and (c) smectite or illite (Seiphoori, 2015).

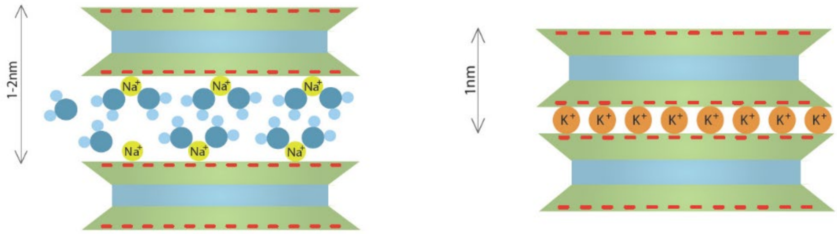

(a)
(b)

Figure 4-4. Crystal constitution of 2:1 structure clay: (a) weak bonding between successive layers in smectite clay minerals, (b) collapse (Seiphoori, 2015).

4.4 Behavior of the microstructural level in BExM

Evolution of the microstructural level referring to the variation in the distance between successive layer will have a predominant influence in swelling behavior of expansive clay like bentonite. Volume change of the microstructure largely depends on the water content of the surrounding environment, which is seen as recoverable deformation. In BExM, it is assumed that microstructural deformations are elastic and independent of the macrostructure so that a reasonable physical interpretation and the simplicity of the approach could be achieved. Microscopic stress $\hat{p}$ is defined as the summation between the net stress p and suction s. Hence, the neutral loading line could be defined in Figure 4-5 (Lloret et al., 2003) with no microstructural strain on the line. The microstructural volumetric elastic strain could be calculated as the equations in below and the choices between two alternative constitutive laws will depend on the type of expansion to the model.

$$\hat{p} = p + S_r s \tag{4.1}$$

$$d\varepsilon_{vm}^{e} = \frac{d\hat{p}}{K_m}, K_m = \frac{e^{-\alpha_m \hat{p}}}{\beta_m} \; or \; K_m = \frac{(1+e_m)\hat{p}}{K_m} \tag{4.2}$$

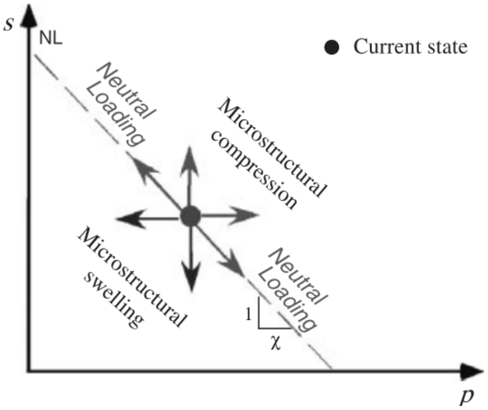

Figure 4-5. Microstructural swelling and contraction area divided by the Neutral Loading Line (Lloret et al., 2003).

4.5 Macrostructure of the bentonite and the behavior at macrostructural level in BExM

Macrostructure of the bentonite refers to the inter-grain pores between the neighboring bentonite grains indicating the structural arrangement of grains shown in Figure 4-2, which is similar to non-expansive clay at the macrostructural level. Based on the similarity of macrostructures, we assume a possibility of using the Barcelona Basic Model (BBM) (Alsonso et al., 1990) in the BExM model. The BBM is a widely used model for unsaturated non-active clay, and BExM inherits from BBM and includes it in its macrostructure. Figure 4-6 shows the yield surface defined in the BBM, which is characterized by two yield curves: LC--loading-collapse, and SI--suction-increase. The hardening laws for the two plastic mechanisms are controlled by the total plastic volumetric deformation and the maximum suction experienced in the history individually. The macrostructural volumetric elastic strain is expressed as a function of mean net stress and suction:

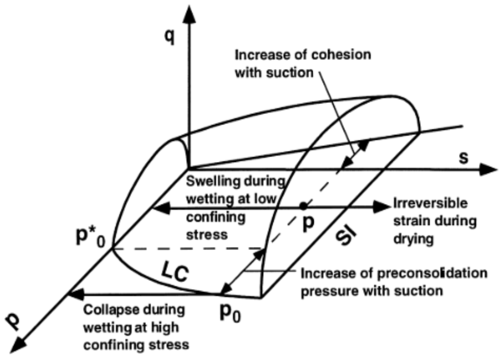

Figure 4-6. Yield surface in (p,q,s) space defined in BBM (Alonso et al., 1990).

4.6 Coupling between the two structural levels in BExM

Interaction between the two structural levels is an important component in BExM. Evolution of the microstructure, which largely depends on the water content of the soil, is considered independent of the macrostructure. However, the reverse is not true. Expansion or shrinkage in the microstructure will inevitably induce the change in grain arrangement, which will be reflected in the macrostructure. In BExM, the interaction mechanism is described as an interaction function between the volumetric strain in microstructure and the induced plastic volumetric strain in macrostructure shown. Figure 4-7 (Lloret et al., 2003) shows the generic interaction functions indicating the physical phenomenon underlying them. In Figure 4-7, f_D and f_I correspond to the swelling and shrinkage of the microstructure, respectively. The shape of f_D implies that when stress state is far from LC (p/p_0 is much less than 1), the interaction during wetting is strong. The small ratio between p/p_0 indicates that the macrostructure is in a dense state. Therefore, the expansion of the microstructure will cause large and irrecoverable strain in macrostructure and the macrostructure tends to transit to a more open structure. Therefore, the LC curve will move towards left and the specimen will become less dense with the strength of the interaction function decreasing accordingly.

So, the induced macrostructural plastic strain shows a dependency not only on the microstructural strain, but also on the stress state. Therefore, the coupling mechanism is quantitively defined in BExM by the interaction function between $d\varepsilon_{vM}^{p}/d\varepsilon_{vm}^{e}$ and p/p_0.Selection of f_D and f_I depends on the state of microstructure (f_D--for microstructural contraction and f_I -- for microstructural swelling).

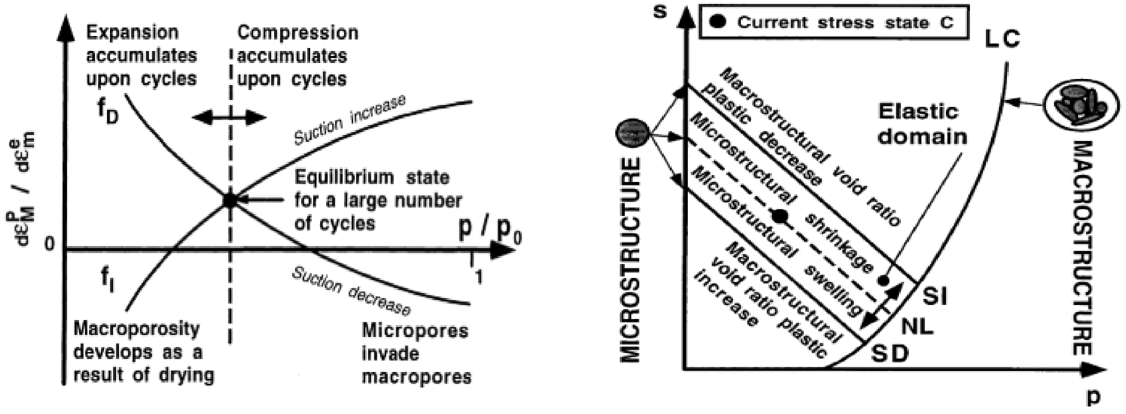

Figure 4-7. Micro-macro pore interaction mechanisms (Lloret et al., 2003).

4.7 Highly expansive clay behavior capture in BExM

BExM could capture the collapse of the soil structure indicated by the turning point in swelling pressure (Lloret et al., 2003, Sanchez et al., 2005) shown in Figure 4-8. Besides, it could reproduce the accumulation of suction induced strain, its dependency in stress state and the tendency to reach an equilibrium state under cyclic suction loading shown in Figure 4-8. For the combined suction and mechanical loading, it could reproduce the loading path dependencies in a void ratio shown in Figure 4-9 (Lloret et al., 2003).

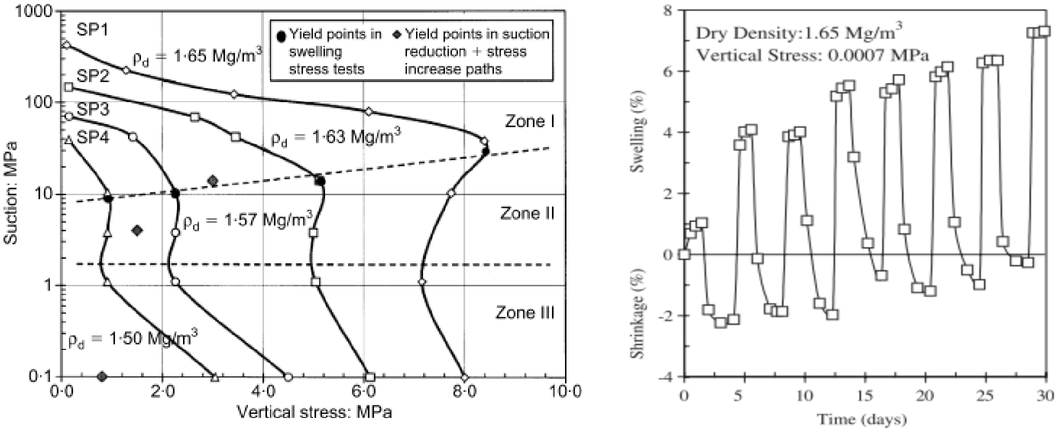

Figure 4-8. (a) Swelling pressure test, (b) Evolution of shrinkage and swelling in a cyclic suction loading test (Lloret et al., 2003).

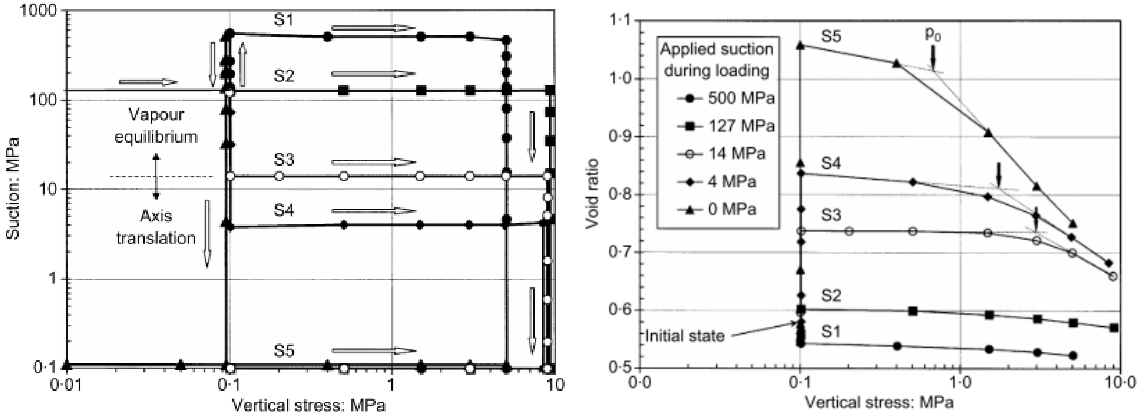

Figure 4-9. Loading path and evolution in void ratio in combined suction-mechanical loading test (Lloret et al., 2003).

4.8 Verification tests

The aim of the verification tests is to ensure that implementation of the BExM model can indeed capture the key features of bentonite. Verification tests include three parts. First is the swelling pressure test under the constant volume. Second is the oedometer test under two different vertical stress. They verify the swelling potential of the bentonite under suction loading from swelling pressure and volumetric strain individually. In the first two tests, only suction loading is on. Third is the combined mechanical and suction loading. Comparison have been made with experimental results and numerical results shown in related articles.

4.8.1 Swelling pressure test

Numerical simulations using the BExM have been carried out and the results compared with the numerical results given in the paper by Sanchez et al. (2005), using the same model parameters. Initial conditions correspond to the initial suction as 80MPa and a low stress state. A wetting path is then followed with a reduction of to 0.01 MPa. Finally, the sample is subjected to drying, up to the suction of 0.4MPa. The whole test is under constant volume. The results are compared in terms of suction versus vertical stress in Figure 4-10 and pre-consolidation pressure versus suction in Figure 4-11. The vertical stress versus suction (Figure 4-11) can also be obtained from laboratory tests, whereas the evolution of the pre-consolidation pressure is a model calculation.

It can be observed in Figure 4-10 that the model could reproduce the main trends in Sanchez's results closely related to vertical stress versus suction. The evolution of calculated pre-consolidation pressure appears to deviate more between these models. However, the deviation occurs at very small suctions of 0.01 MPa and also the evolution of the pre-consolidation pressure has very small impact on the swelling stress, which is very close between the models.

At the first stage, when going from 80 MPa to 10 MPa suction, the stress state of macro part remains within the LC yield surface. The stress change during this stage mainly comes from the stress compensation due the swelling induced by the reduction in suction. The swelling mechanism in the microstructure is active, which will induce macrostructural plastic strain for expansion. As a result, the preconsolidation pressure will become smaller and the LC curve will move to the left. So, the stress state has the tendency to get closer to the boundary of the yield surface. Finally, when the stress state reaches the LC curve, the yield mechanism in the BBM for the macro part will be activated with the subsequent collapse in the macrostructure. It corresponds to the turning point at about 10 MPa suction and 0.2 MPa vertical stress (Figure 4-10). The turning point is consistent between the models, but then the increase in preconsolidation pressure is somewhat different (Figure 4-11).

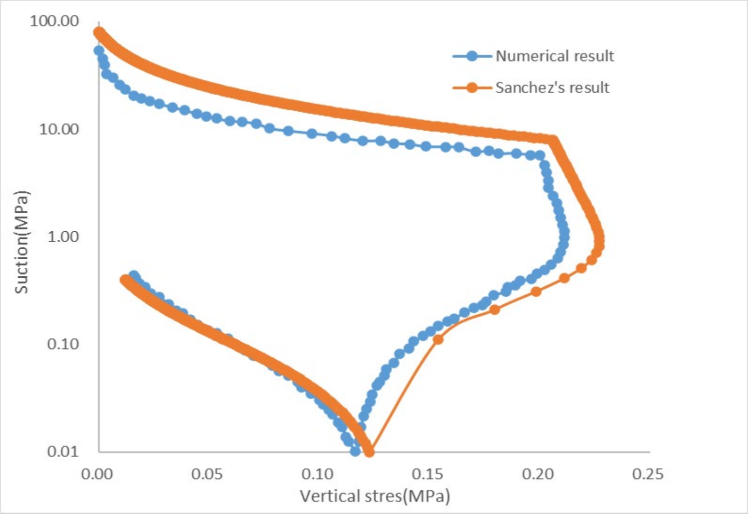

Figure 4-10. Comparison between the BExM and Sanchez et al. (2005) numerical results for the swelling pressure test.

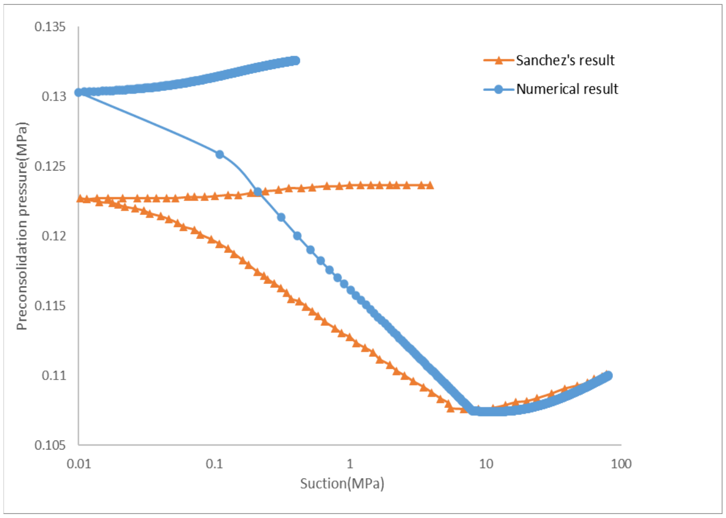

Figure 4-11. Comparison of the BExM and Sanchez et al. (2005) numerical results of the evolution of the pre-consolidation pressure.

4.8.2 Evolution of the specific volume under cyclic suction loading test

Response of bentonite under cyclic drying and wetting tests is important in the nuclear waste repository as buffer may experience cyclic suction loading because of the water flow to and from the host rock. As mentioned in Section 4.7, features of expansive clay behavior under cyclic suction loading are complex including the stress state dependency and strain fatigue.

We have compared the results of BExM numerical simulations with those given in Sanchez’s article (Sanchez et al., 2005). We examined the response of an expansive clay subjected to cyclic suction loadings under oedometric conditions at two different vertical stress levels. For the BExM numerical results shown in Figures 4-12 and 4-13, the volumetric strain in micro part is totally elastic, which fits the assumption in BExM. Besides, the numerical result could reproduce the tendency of reduction in the swelling capacity of the material when the vertical stress increases. Figures 4-12 and 4-13 show that the total volumetric strain will experience a larger increase under the pressure of 0.01MPa than that under the pressure of 0.1MPa. The strain fatigue feature shows a gradually smaller increase in the volumetric strain, which finally reaches the equilibrium state with a nearly zero change in volumetric strain in the cyclic suction loading.

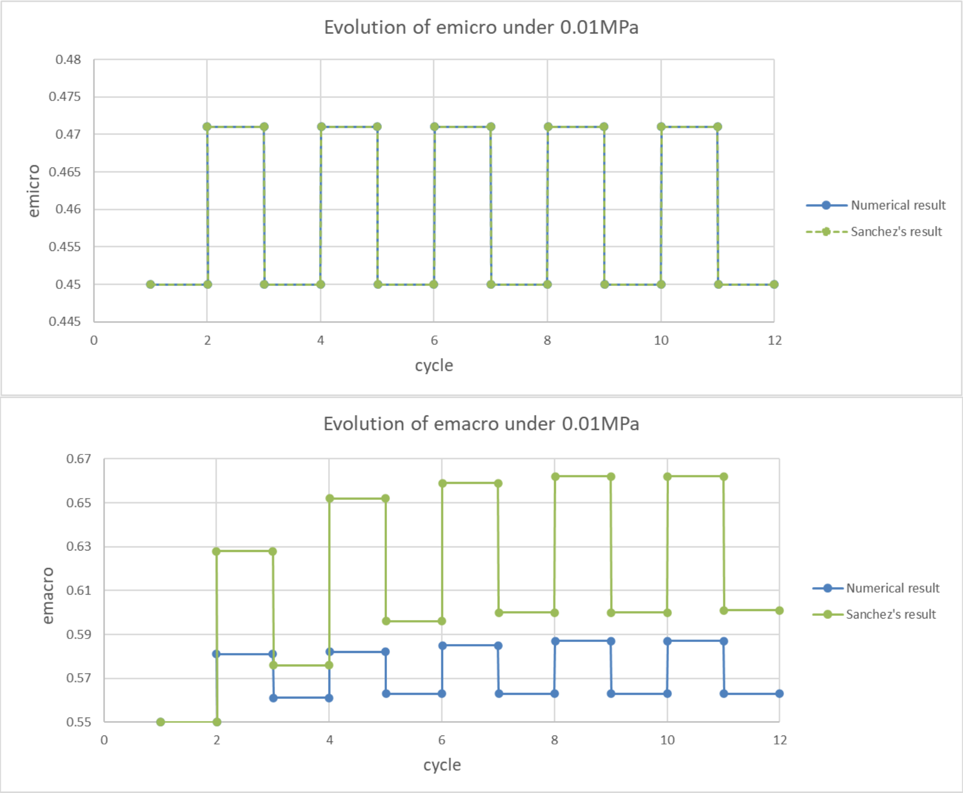

Figure 4-12. Comparison between BExM and Sanzhez’s numerical results for a swelling pressure test

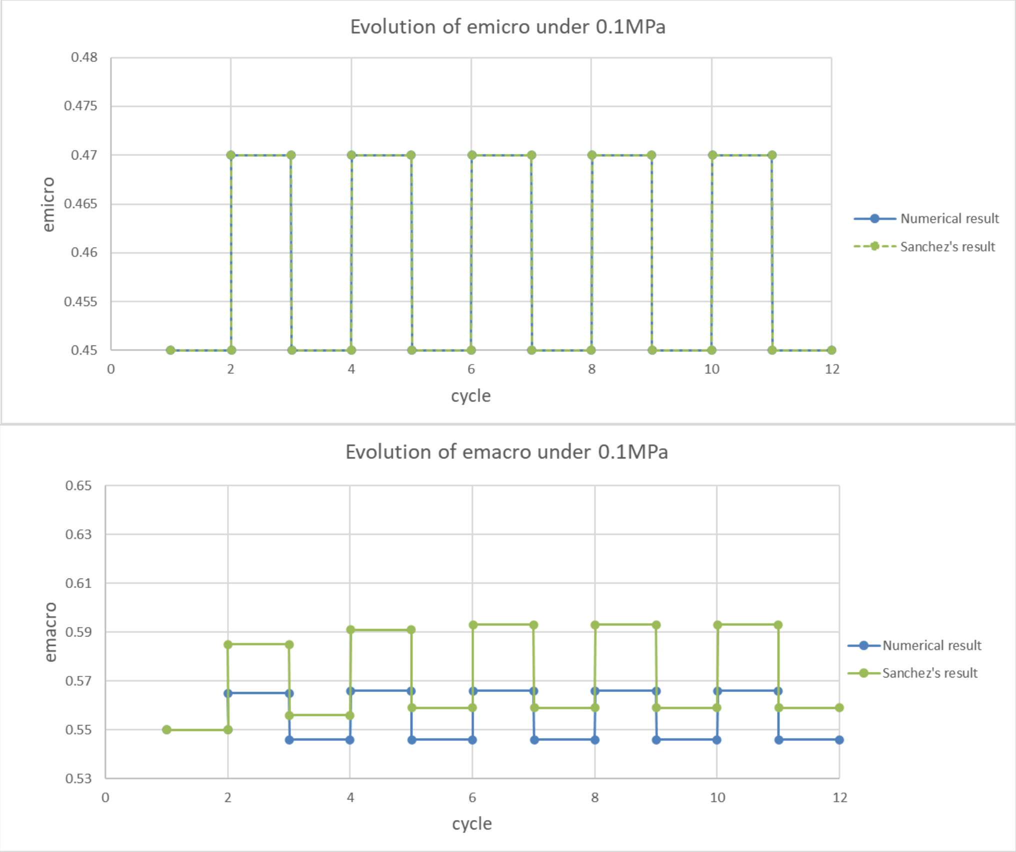

Figure 4-13. Comparison between the BExM and Sanchez's numerical results for a cyclic suction loading under a vertical stress of 0.1MPa.

4.8.3 Evolution in specific volume under combined mechanical suction loading

Combined loading paths S_1 and S_5 are shown in Figure 4-14 (Lloret et al., 2003). They share the same initial and final values of suction as well as a vertical stress, but their trajectories are different. In test S_1, the specimen is loaded under a high (550 MPa) suction up to a 5.1MPa. Then, a vertical load is added to 5.1MPa. Then, the specimen is wetted, reducing the suction to zero. In contrast, test S_5 is first wetted at a low applied vertical stress value of 0.1MPa, and then the sample, already saturated, is loaded to a vertical stress of 5.0MPa.

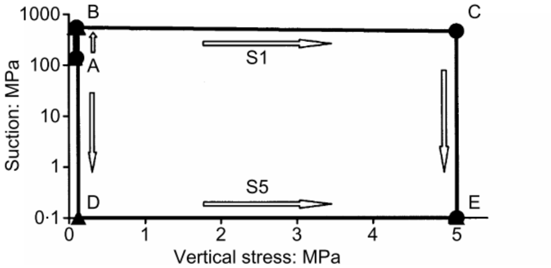

Figure 4-14. Loading paths S_1 and S_5

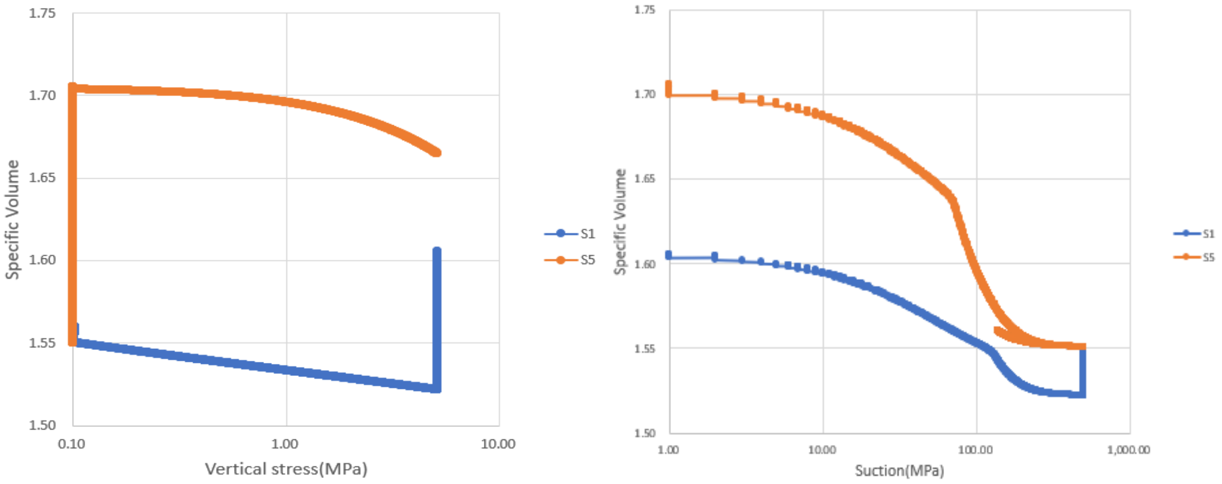

Figure 4-15. Evolution of a specific volume with vertical stress and suction in tests S_1 and S_5

Figure 4-15 shows the modeled evolution of a specific volume with vertical stress and suction for S_1 and S_5 in BExM. Major features of behavior under combined mechanical suction loading are reproduced correctly, including the following: (1) there are large swelling strains, when the material is wetted at a low stress shown in S_5, (2) the slope of the compression line changes during loading shown in S_5, indicating the yield, (3) the final specific volume is different in two samples, and the loading path dependence can be reflected at least in the relation to the volumetric strain.

This page is intentionally left blank.

5. FE EXPERIMENT AT THE MONT TERRI SITE (MONT TERRI PROJECT)

In this section, we present the current status of the FE Experiment at Mont Terri and updated results of TOUGH-FLAC modeling of the experiment. In particular, in FY20 we have extended the modeling for comparison with over five years of field data from the experiment. In the following, we first provide a description and status of the FE Experiment and then present the results of current THM modeling.

5.1 Description and Status of the Mont Terri FE experiment

The Mont Terri FE experiment has been conducted by NAGRA, Switzerland, as an ultimate test for the performance assessment of geologic disposal in Opalinus Clay, with focus on both the EBS components and the host-rock behavior. It is one of the largest and longest-duration heater tests worldwide, with focus on both the EBS components and the host-rock behavior. The FE experiment is being conducted in the side tunnel at Mont Terri, excavated along the claystone bedding planes, extending 50 m in length and about 2.8 m in diameter (Figure 5-1). Heating from emplaced waste is simulated by three heat-producing canisters of 1500 W maximum power each. Temperature is expected to exceed 100°C, with a target temperature of 125 to 135°C at the inner part of the buffer. A sophisticated monitoring program has been implemented, including dense instrumentation of the bentonite buffer and host rock, and extensive geophysical monitoring.

The experiment provides data useful for the validation of THM coupling effects regarding the processes in the host rock, while correctly accounting for (and examining) the emplacement tunnel temperature, saturation, and swelling pressure. Because it is a real field scale experiment, it is possible to achieve realistic temperature, saturation, and stress gradients. It will also be possible to test backfilling technology with granular bentonite, as well as lining technology with shotcrete, anchors, and steel ribs. Processes examined in the test cover many aspects of a repository evolution, such as criteria of desaturation of the EDZ during tunnel excavation and operation (including ventilation for about one year), as well as reconsolidation of the EDZ, resaturation, thermal stresses, and thermal pore-pressure increase after backfilling and heating (heating and monitoring period > 10 years).

In 2011, a niche in front of the FE tunnel was constructed, followed by a first phase of instrumentation of the rock mass surrounding the tunnel, using boreholes drilled from the niche. The FE tunnel was excavated by a road-header in 2012, following by another phase of instrumentation. The tunnel was open for a one-year ventilation period. This was followed by emplacing the heaters, bentonite buffer, and a concrete plug, after which the heating was gradually turned on during the fall of 2014 and early 2015, with applying the full heat power of 1350 W at all three heaters (H1, H2, H3) from February 18, 2015 (Figure 5-2). The heating is expected to go on for at least 15 years, with continuous monitoring of THM processes in both the bentonite buffer and a surrounding rock. After over 4 years of heating, the temperature at the heaters is approaching 130°C, and a relative humidity near the heaters in granular bentonite buffer stays low at around 10 to 20%. Some wetting is also taking place of other parts of the buffer, at some point reaching full saturation. No substantial swelling stress has been developed in the granular bentonite, with stresses increasing at some locations up to 0.4 MPa.

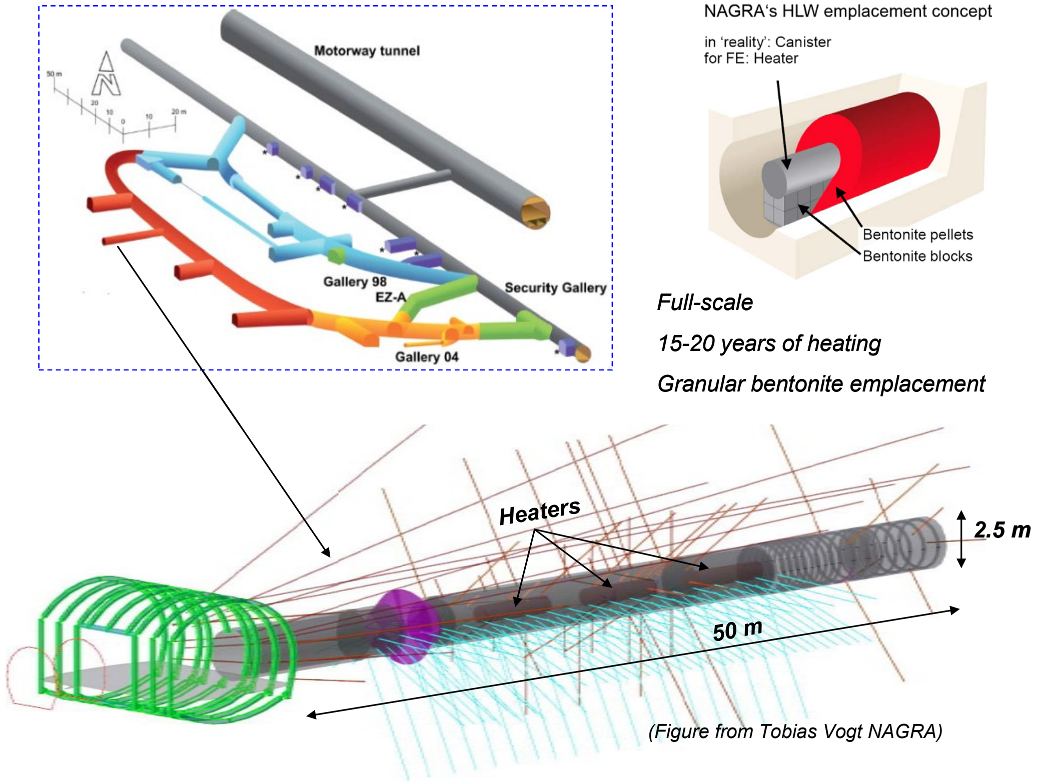

Figure 5-1. Plan view of FE experiment setup and borehole layout.

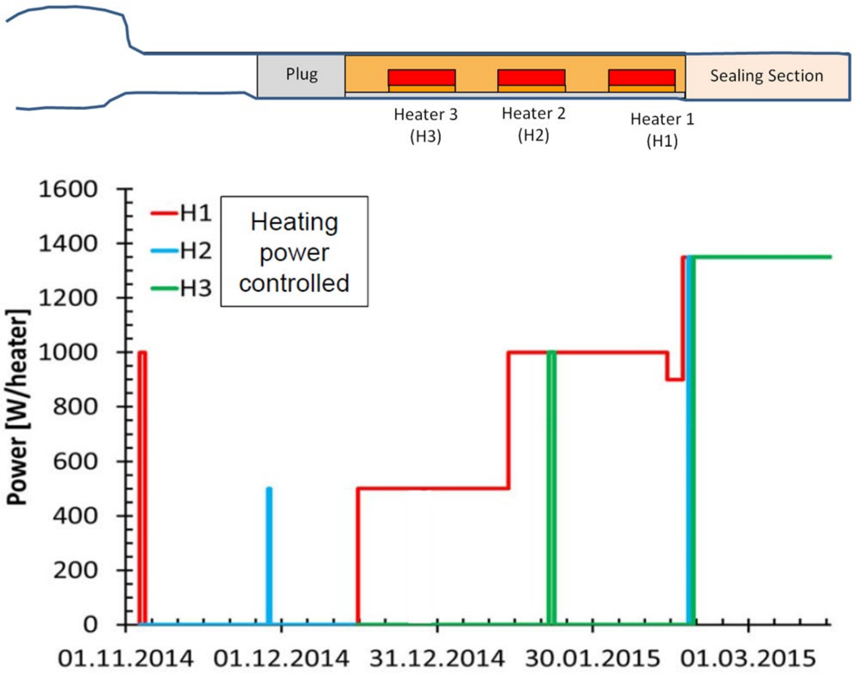

Figure 5-2. Heat power applied to H1, H2 and H3 during heater start-up at the Mont Terri FE experiment.

5.2 TOUGH-FLAC Model of the Mont Terri FE Experiment

For the FE experiment modeling, we have developed a conceptual model and modeling approach based on the previous milestone reports (Houseworth et al., 2013; Zheng et al., 2014, 2015, 2016; 2017). In FY18 and FY19, Rutqvist et al. (2018; 2019) continued to update the model based a comparison with longer term field data. Here we present the model and provide a brief update of the simulation results extended to about 5 years from the start of the heating.

The host rock is modeled using TOUGH-FLAC with anisotropic properties considering bedding planes of the Opalinus Clay. To accurately model anisotropic thermal and hydrological behavior, we created a TOUGH2 inclined mesh. Anisotropic mechanical material behavior is simulated using the FLAC3D ubiquitous joint model, with initial material properties derived from the analysis of the excavation design of the experimental tunnels. In the ubiquitous joint model, weak planes are assumed along the bedding planes of the Opalinus Clay, in which the shear strength properties are different along and across the bedding (Houseworth et al. 2013). For the bentonite, we started with the BBM model as applied by the Centro De Investigaciones Energéticas, Medio Ambientales Y Tecnológicas (CIEMAT) and Universitat Politècnica de Catalunya (UPC) (Garitte and Gens, 2012), and derived specific input material parameters for the MX-80 bentonite pellets, which are used as the emplaced buffer around the heaters. With this modeling approach, we were able to simulate THM processes in both the bentonite and host rocks, as well as their interactions.

Figure 5-3 presents the 3D TOUGH-FLAC numerical grid of the FE experiment. This model grid includes all material components used for modeling of the FE experiment, including the layered Opalinus Clay host rock, excavation disturbed zone, tunnel, three heaters, bentonite buffer, concrete liner, and a concrete plug. The following initial conditions for the model simulations were selected: 2 MPa pore-fluid pressure, and 15°C temperature for the host rock. Because the 2 MPa pore pressure does not represent hydrostatic conditions, the process is affected by the existing tunnel system. In our simulations, we first ran a simulation with an open tunnel at the atmospheric pressure for one year, creating a pressure drop and hydraulic gradient around the tunnel. Thereafter, we assumed instantaneous emplacement of the heater and the buffer to start the heating simulation.

The thermal and hydraulic material properties for modeling the FE experiment are given in Table 5-1. These properties are based on the modeling studies of several other smaller scale heater experiments at the Mont Terri laboratory, including the HE-D and HE-E experiments described in previous reports (Zheng et al., 2015; 2016). The intrinsic permeability of gas flow in the bentonite is about six orders of magnitude higher than the intrinsic permeability for liquid flow, and this is simulated in TOUGH2 using a high value of the Klinkenberg parameter. The initial saturations in granular bentonite and bentonite block are different than those in the previous HE-E experiment, and are for the FE experiment set to 16.5% for granular bentonite and to 75% for bentonite blocks.

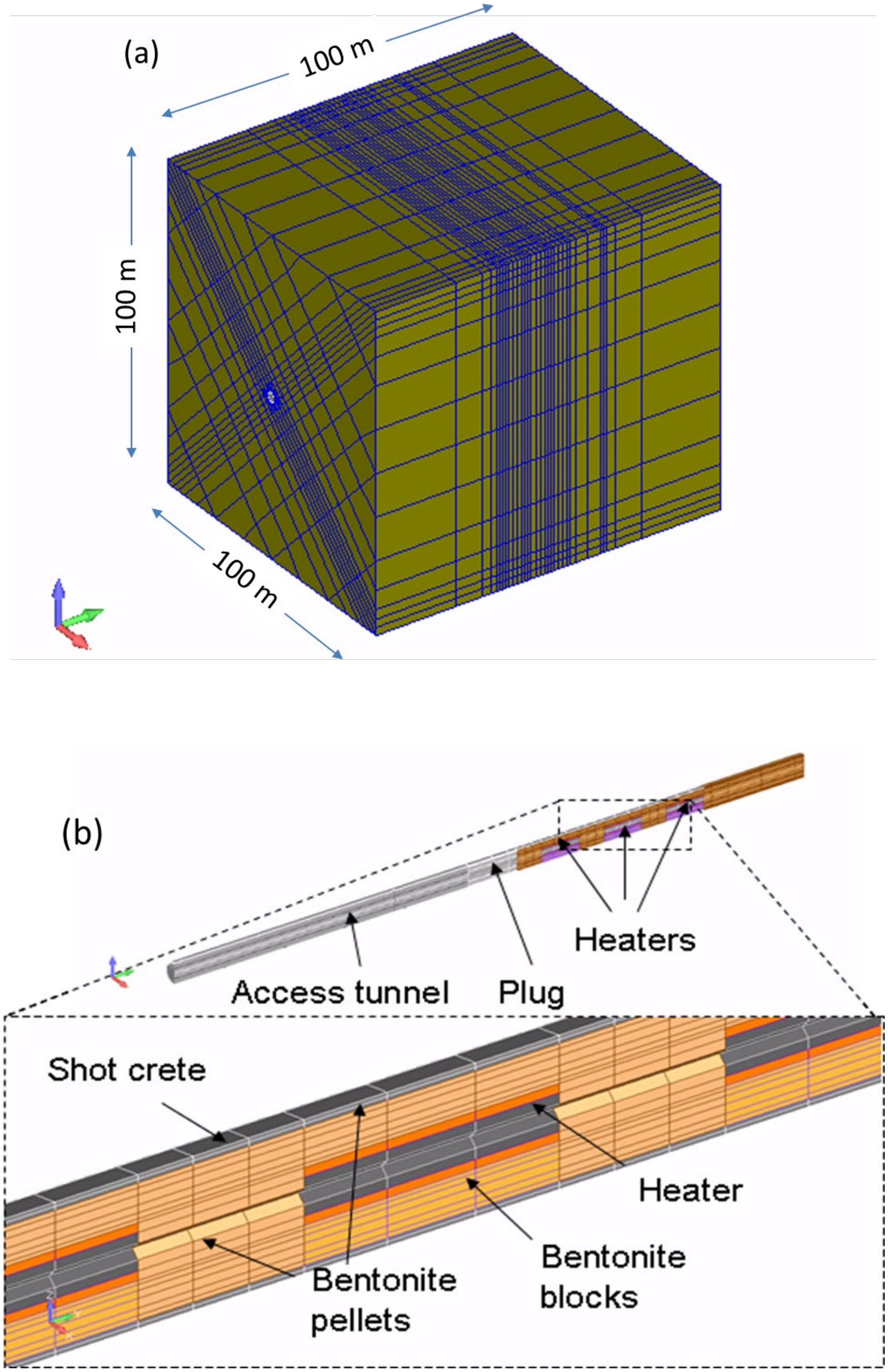

Figure 5-3. TOUGH-FLAC 3D numerical grid of the FE experiment: (a) Entire model, and (b) Materials and gridding of the EBS.

Table 5-1. Parameters used in modeling of the Mont Terri FE experiment.

Parameters	Symbol	Opalinus Clay	Granular Bentonite	Bentonite blocks	Concrete (shotcrete and plugs)	Unit
Grain density	ρ_g	2.7×10^3	2.7×10^3	2.7×10^3	2.7×10^3	kg/m^3
Porosity	$Ø$	0.15	0.46	0.389	0.15	-
Intrinsic permeability	k	5.0×10^{-20}	5.0×10^{-21}	2.0×10^{-21}	3.5×10^{-21}	m^2
Liquid relative permeability (Corey, 1954) $k_{lr}(S_l) = \left(\frac{S_l - S_{lr}}{S_{ls} - S_{lr}}\right)^A$	A	-	5	3	-	-
Liquid relative permeability (van Genuchten, 1980) $k_{lr}(S_l) = \left(\frac{S_l - S_{lr}}{S_{ls} - S_{lr}}\right)^{1/2} \left[1 - \left\{1 - \left(\frac{S_l - S_{lr}}{S_{sl} - S_{lr}}\right)^{1/m}\right\}^m\right]^2$	m	0.52	-	-	0.52	-
Capillary curve (van Genuchten, 1980) $\psi(S_l) = Po\left\{\left(\frac{S_l - S_{lr}}{S_{ls} - S_{lr}}\right)^{-1/m} - 1\right\}^{1-m}$	P_0	1.09×10^7	1.0×10^7	3.0×10^7	1.09×10^7	Pa
	M	0.29	0.4	0.32	0.29	-
	S_{ls}	1.0	1.0	1.0	1.0	-
	S_{lr}	0.01	0.0	0.0	0.01	-
Thermal conductivity (wet)	λ_{sat}	1.7	1.3	1.0	1.7	W/m°K
Thermal conductivity (dry)	λ_{dry}	1.06	0.3	0.5	1.06	W/m°K
Grain specific heat	C	800	950	950	800	J/kg°K

5.3 Simulation Results with Comparison to Monitored Data

In the FY16 milestone report, Zheng et al. (2016) demonstrated a good comparison of one-year simulation results and observations of the relative humidity in the buffer obtained using a tortuosity parameter as low as $\tau = 0.14$. In the FY17 milestone report, Zheng et al. (2017) confirmed the value of tortuosity of $\tau = 0.14$ based on the results of simulations and observations for a period of two years of heating for monitoring points at all three heaters. The simulation results have been updated using the results of onsite measurements (Rutqvist et al., 2018; 2019).

Figure 5.4 shows an example of the evolution of temperature and relative humidity at Heater 3 (H3). This data set is chosen because of good field data quality obtained with the sensor working properly for 4.5 years. The time zero in these figures is 12/28/2014, which is just after the start of heating at Heater 1 (H1). The results shown in Figure 5-4 confirm previous results of an excellent agreement in buffer temperature evolution, while some discrepancies are observed regarding the evolution of relative humidity.

The discrepancy between simulated and measured relative humidity is explained by the fact that the real distance between the sensor location and the rock wall in the field is not exactly the same in the model. In modeling, the tunnel is simulated as a perfect circle and the shotcrete thickness around the tunnel is constant while in the field the shape of the tunnel is not perfectly circular and the shotcrete thickness is not constant (Figure 5-5). In general, the inflow rate saturating the buffer is relatively slow due to the low permeability of the host rock.

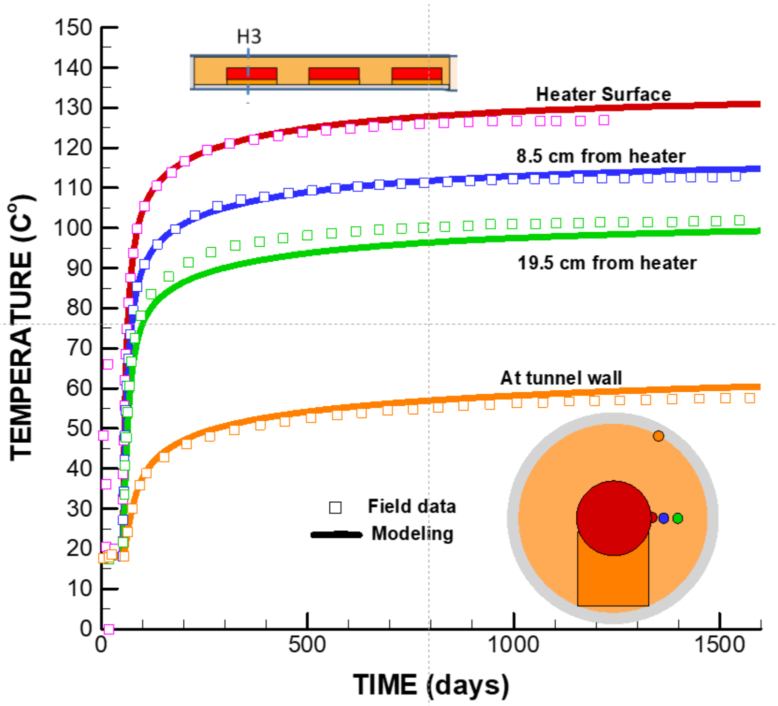

(a)

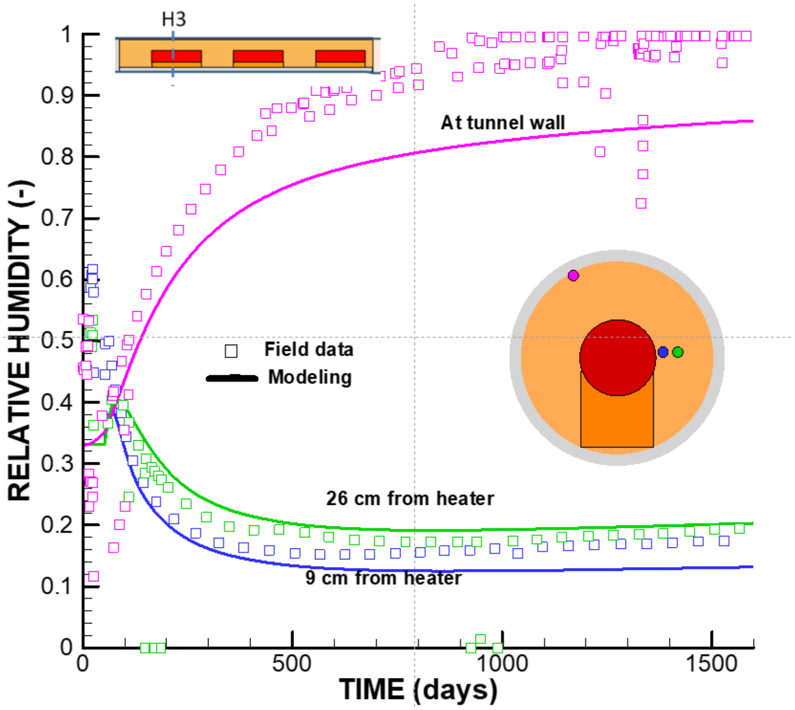

(b)

Figure 5-4. Comparison of modeled (lines) and measured (symbols) evolutions of (a) temperature and (b) relative humidity at the monitoring point located in granular bentonite at H3.

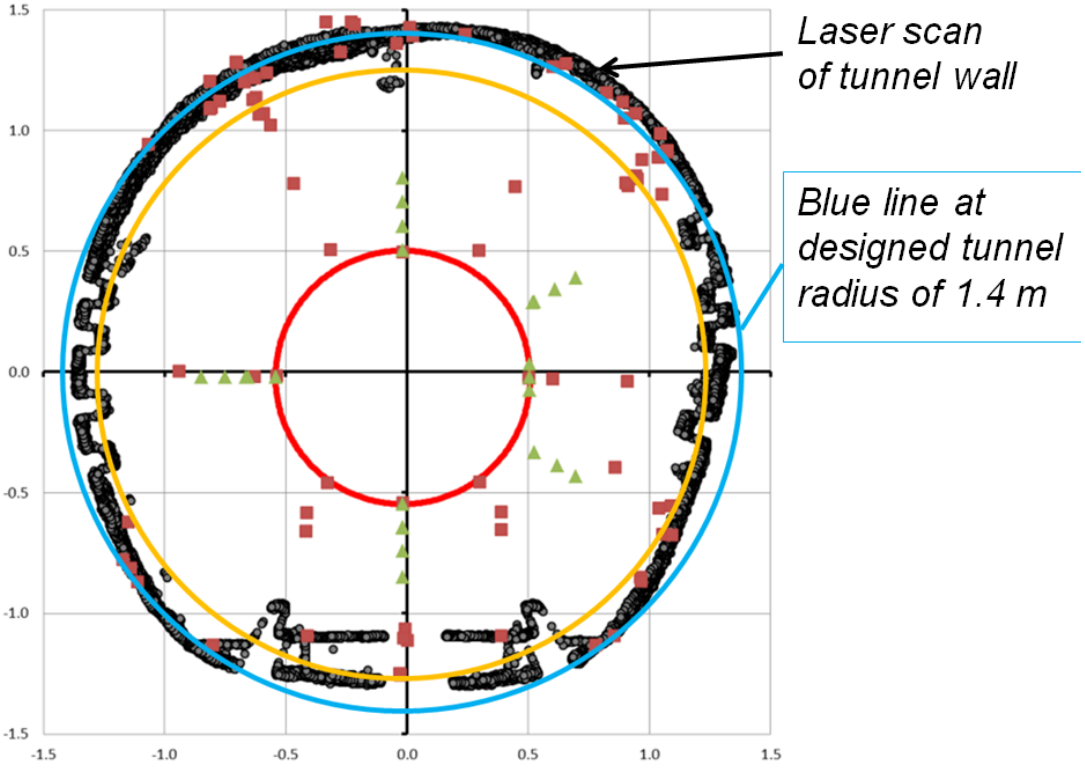

Figure 5-5. Comparison of the actual zigzag-shape cross-section of the tunnel from the laser scan with the circular shape of tunnel used in numerical modeling. The red circle in the middle is the heater. Squares and triangles indicate locations of some of monitoring sensors. Axis units are in meters.

5.4 Summary and Status the FE Experiment Modeling

We have conducted various types of modeling over the past few years, including benchmarking, heating design modeling, model predictions and interpretative modeling. Currently, we have interpreted data for up to 4.5 years of heating, including data on temperature and relatively humidity in the bentonite buffer and up to 2.5 years of pressure in the host rock. Some finding and lessons learned of the work to date are as follows:

- A good agreement between modeled and measured evolutions in buffer temperature and relative humidity was achieved for the FE experiment based on a model prediction using properties of bentonite and Opalinus Clay determined from the previous Mont Terri HE-E experiment.
- A value of the effective vapor diffusion coefficient and the tortuosity factor were calibrated against measured relative humidity evolution in the granular bentonite, but the value was much lower than that used for previous modeling of the HE-E experiment. This difference and the potential role of enhanced thermal diffusion of the early-time TH response in the buffer are open questions that warrant further studies.
- The values of the effective vapor diffusivity coefficient and the tortuosity factor for the bentonite block were determined based on the calibration of model parameters, and these values are much higher than those for the granular bentonite (0.33 for blocks vs 0.14 for granular bentonite).

Still after 4.5 years of heating and infiltration from the surrounding rock, no significant swelling stress has been developed in the bentonite buffer. Measurements show that the total pressure in the buffer is less than 0.4 MPa. We will continue modeling of the FE experiment using newly collected monitoring data, focusing on the mechanical evolution of the buffer and host rock. Moreover, the FE heater test will be part of DECOVALEX-2023, which will focus more on the large-scale pressure responses in the host rock.

6. HEATER EXPERIMENTS AT BURE IN COx CLAY STONE (DECOVALEX-2019)

In this section, we present recent TOUGH-FLAC modeling results related to the *in situ* heater experiment, conducted in Callovo-Oxfordian claystone (COx) at the Meuse/Haute-Marne Underground Research Laboratory (MHM URL) in Bure, France. Modeling of heater tests is one of the Tasks of the DECOVALEX-2019 project. In the following, we first provide a description of the DECOVALEX-2019 Task E and international modeling teams associated with this task; then provide a description of updated TOUGH-FLAC simulation results and the comparison to the *in situ* experiments associated in each step.

6.1 DECOVALEX-2019 Task E and International Modeling Teams

DECOVALEX-2019 Task E is a study addressing important issues related to the repository design and safety calculation, as well as a problem of upscaling from a sample scale to a repository scale. This study is also focused on the evaluation of the thermally induced pore pressure build-up and stress changes around a repository. Task E is coordinated by ANDRA (the French National Radioactive Waste Management Agency), and involves modeling of two *in situ* tests performed at the URL in Bure:

- The TED experiment, a small-scale heating experiment focused on the claystone THM behavior of the undisturbed rock mass in the far field; and
- The ALC experiment, a one-to-one scale heating experiment especially focused on the interaction between the surrounding rock and the support (steel casing in this case) in the near field.

Based on the results of modeling of two *in situ* tests, the impact of the heating experiments at the repository scale with several parallel cells will be evaluated. These results will be used to address some key technical challenges, such as the variability of the THM parameters, the determination of appropriate boundary conditions, and the potential thermally induced hydraulic fracturing between canisters. Modeling is used to represent a series of parallel cells.

DECOVALEX-2019 Task E is conducted by a step-by-step approach, from small-scale to full-scale studies (Figure 6-1). It is structured into four main steps:

- Step 1: Simple 3D THM modeling benchmark;
- Step 2: Interpretative modeling of the TED experiment (back analysis);
- Step 3: Modeling of the ALC experiment
    - Step 3a: Predictive modeling of the ALC experiment using the reference values for the rock mass parameters determined in Step 2;
    - Step 3b: Interpretative modeling of the ALC experiment;
- Step 4: Prediction at the repository scale of an area with several high-level waste cells.

The participating groups in the DECOVALEX-2019, Task E are:

- Canada: NWMO;
- France: ANDRA, University of Lille;
- Germany: BGR and UFZ;
- UK: RWM, Quintessa Ltd;
- USA: DOE, LBNL.

Currently, Step 1 (3D THM modeling benchmark), Step 2 (interpretative modeling of the TED experiment at Bure), Step 3 (blind prediction and interpretative modeling of the ALC experiment), and Step 4 (prediction of the temperature, pore pressure and stresses at the repository scale) have been completed. Several papers related to this task are submitted to a peer review journal.

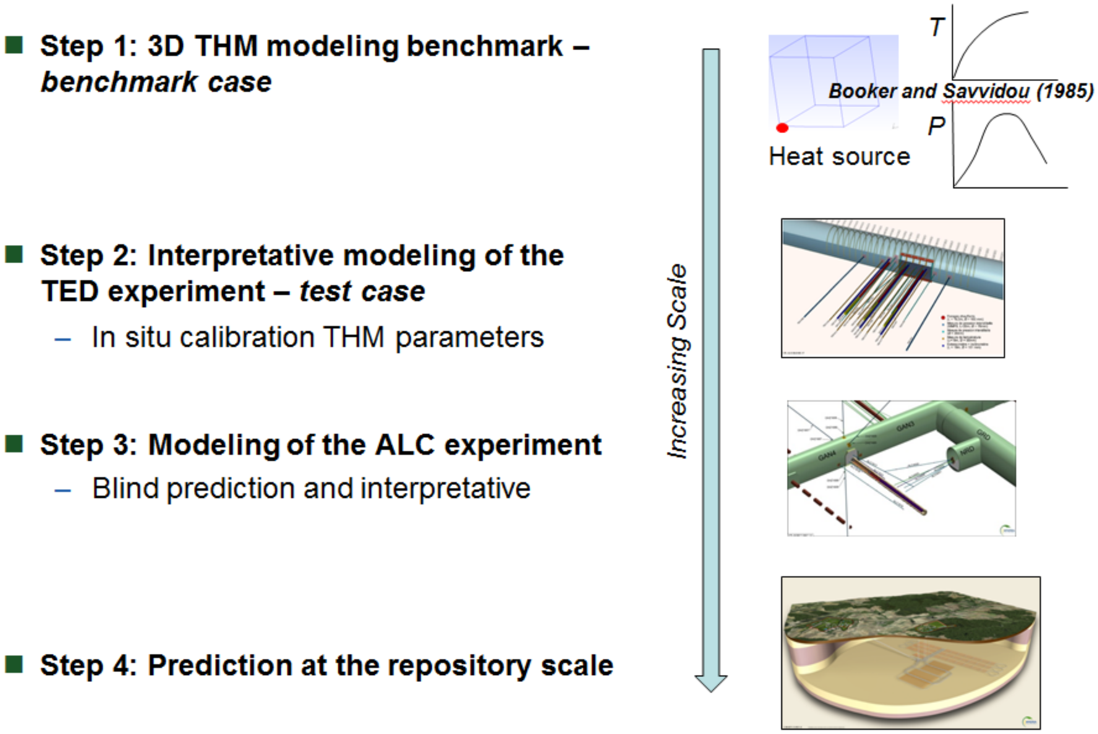

Figure 6-1. Overview of DECOVALEX-2019 Task E, illustrating the increasing scale of investigations.

6.2 Theoretical Background

The theoretical background of investigations of thermo-poroelasticity of porous continua is based on extending the theory of thermo-elasticity as applied to thermoelastic skeleton. The general form of the Helmholtz free energy ψ_s for a linear saturated thermo-poroelastic material is defined as (van Duijn et al., 2019; Coussy, 2004)

$$\psi_s = \psi_{so} + \frac{1}{2}\boldsymbol{\epsilon}:\mathbb{C}:\boldsymbol{\epsilon} - \frac{1}{2}\frac{\rho C_p}{T_0}(T-T_0)^2 - \frac{1}{2}\frac{1}{N}(p-p_0)^2 \tag{6.1}$$

$$-\mathbf{b}:\boldsymbol{\epsilon}(p-p_0) - \boldsymbol{\alpha}:\mathbb{C}:\boldsymbol{\epsilon}(T-T_0) + 3\alpha_\phi(p-p_0)(T-T_0),$$

where ψ_{so} is the free energy at the reference state with free strain; $\boldsymbol{\epsilon}$ is the strain tensor; $\mathbb{C}$ is the tensor of skeleton tangent elastic stiffness modulus; ρ is the density of the porous medium; C_p is the specific heat capacity; T_0 and T are the absolute temperature at the reference state and current state; N is the Biot's tangent modulus linking the pressure variation and the porosity variation; p is the current pore pressure; p_0 is the pore pressure at the reference state; $\mathbf{b}$ is the Biot's tangent tensor; $\boldsymbol{\alpha}$ is the tensor of skeleton tangent thermal dilation coefficients; and $3\alpha_\phi$ is the volumetric thermal dilation coefficient related to the porosity.

Within the framework of thermodynamics, constitutive equations of porous media can be derived from the Helmholtz free energy. The stress $\boldsymbol{\sigma}$ in solid skeleton is obtained as

$$\boldsymbol{d\sigma} = \boldsymbol{d}\left(\frac{\partial\psi_s}{\partial\epsilon}\right) = \mathbb{C}:\boldsymbol{d\epsilon} - \boldsymbol{bdp} - \boldsymbol{\alpha}:\mathbb{C}\boldsymbol{dT}. \tag{6.2}$$

The porosity of porous medium $\boldsymbol{\phi}$ is conjugated to the pore pressure in thermodynamics:

$$\boldsymbol{d\phi} = \boldsymbol{d}\left(-\frac{\boldsymbol{\partial\psi_s}}{\boldsymbol{\partial p}}\right) = \boldsymbol{b}\colon \boldsymbol{d\epsilon} + \frac{\mathbf{1}}{\boldsymbol{N}}\boldsymbol{dp} - \mathbf{3}\boldsymbol{\alpha_\phi dT}. \tag{6.3}$$

The porosity can also be linked to the fluid part:

$$\boldsymbol{d\phi} = \frac{\boldsymbol{dm_f}}{\boldsymbol{\rho_f}} - \boldsymbol{\phi}\frac{\boldsymbol{dp}}{\boldsymbol{K_f}} + \mathbf{3}\boldsymbol{\phi\alpha_f dT}. \tag{6.4}$$

Combining equations (6.3) and (6.4), the fluid continuity equation is

$$\frac{\boldsymbol{dm_f}}{\boldsymbol{\rho_f}} = \boldsymbol{b}\colon \boldsymbol{d\epsilon} + \frac{\mathbf{1}}{\boldsymbol{M}}\boldsymbol{dp} - \mathbf{3}\boldsymbol{\alpha_m dT}, \tag{6.5}$$

where m_f is the fluid mass content; ρ_f is the fluid density; $\frac{1}{M} = \frac{1}{N} + \frac{\phi}{K_f}$; K_f is the fluid tangent bulk modulus; and $\alpha_m = \alpha_\phi + \phi\alpha_f$, where $3\alpha_\phi$ is the volumetric thermal dilation coefficient related to the porosity and $3\alpha_f$ is the fluid tangent coefficient of volumetric thermal dilation (Coussy, 2004; Xu and Prevost, 2017).

The fluid flux is calculated by Darcy's law:

$$\mathbf{F}_f = -\frac{\mathbf{k}}{\mu_f} \cdot \left(\nabla p - \rho_f \mathbf{g}\right) \tag{6.6}$$

where $\mathbf{F}_{\boldsymbol{f}}$ is the fluid flux vector, $\mathbf{k}$ is the intrinsic permeability, $\boldsymbol{\mu_f}$ is viscosity of the fluid, and $\mathbf{g}$ is the gravitational acceleration.

The flow of heat in the soil is assumed to be governed by Fourier's law:

$$\mathbf{F}^h = -\lambda_t \nabla T. \tag{6.7}$$

Here $\mathbf{F}^h$ is the heat flux vector, and λ_t is the thermal conductivity.

In the solid skeleton, the momentum balance equation is solved according to:

$$\boldsymbol{\nabla} \cdot \boldsymbol{\sigma} + \rho \boldsymbol{g} = \rho \frac{d\boldsymbol{v}_s}{dt}, \tag{6.8}$$

where $\boldsymbol{\nabla} \cdot$ is the divergence operator, $\boldsymbol{v}_s$ is the velocity of the solid skeleton, and *t* is the time.

If the material is assumed isotropic, the second order tensor **b**, **k**, and $\boldsymbol{\alpha}$ are reduced to scalars, *b*, *k*, and α. Moreover, the bulk modulus *K* can be used to calculate the mean stress.

6.3 TOUGH-FLAC Simulation Results of Task E

6.3.1 Step 1: 3D THM modeling benchmark

Step 1 of Task E is a basic benchmark test conducted to assess the consolidation of an infinite homogeneous saturated porous media around a point continuous heat input. Modeling results were compared with the analytical solution of Booker and Savvidou (1985) developed based on the hypothesis that the pore water and the solid grains are incompressible. The 3D model is generated with FLAC3D, and the simulation is launched with the module EOS1 (Equation of State 1) in TOUGH2. In FY20, we have improved the simulation with a larger domain, and derived updated equations, which can capture the effect of Biot's coefficient, based on the work by Smith and Booker (1993). The detailed model setup can be found in the paper (Xu et al., 2020). Here, we only present new results of comparison between modeling results and the analytical solution in terms of temperature, pore pressure, displacements and stresses evolution up to 100,000 hours (about 11 years) for several points of the modeling domain listed in Table 6-1.

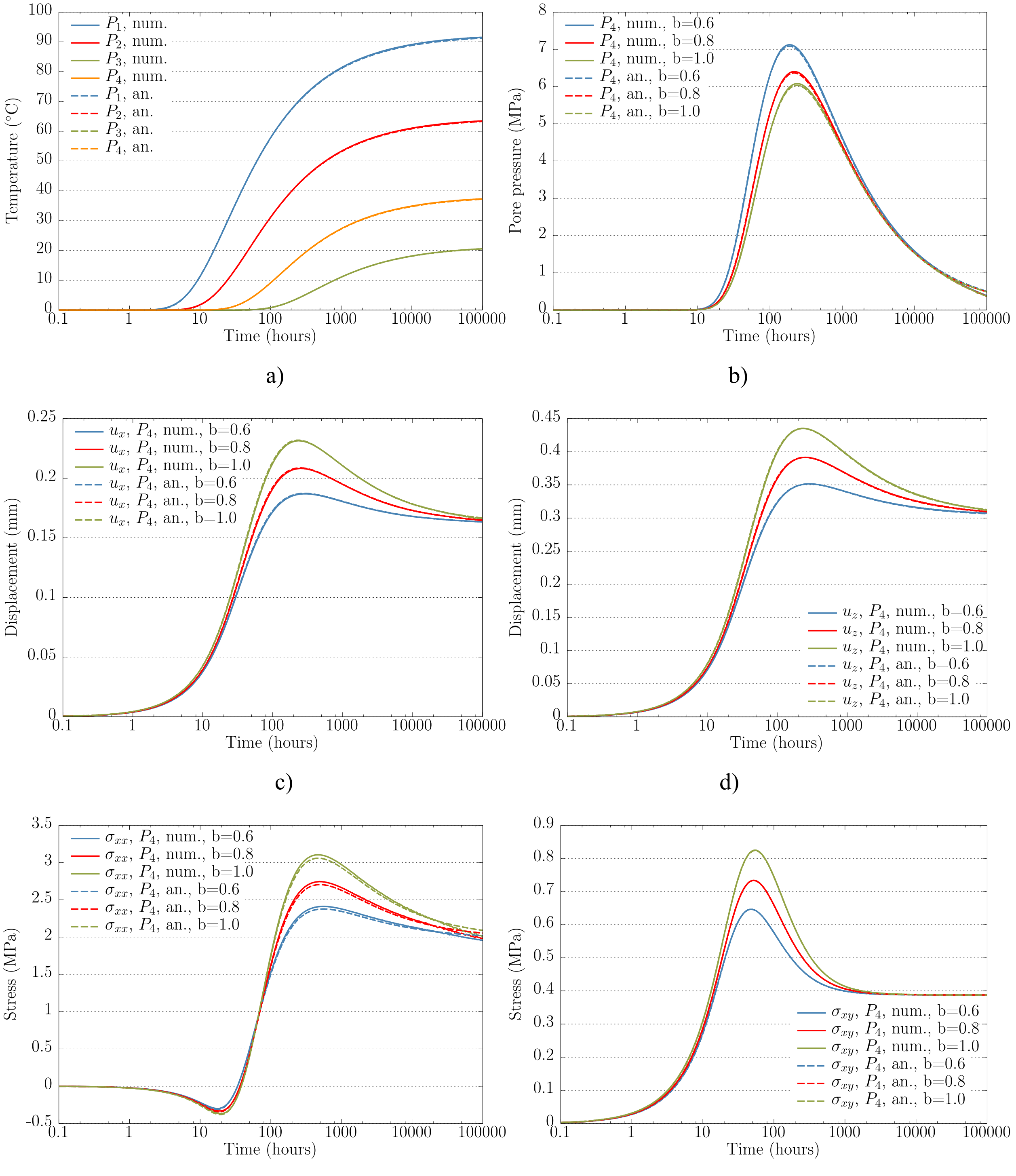

a) b)

c) d)

e) f)

Figure 6-2. Simulation results of 3D THM modeling (num) with comparison to analytical solution (an) for different Biot's coefficient, b=0.6, 0.8 and 1.0. a) Temperature evolution at P1, P2, P3 and P4; b) Pore pressure evolution at P4; c) Displacement, u_x, evolution at P4; d) Displacement, u_z, evolution at P4; e) Stress, σ_{xx}, evolution at P4; f) Stress, σ_{xy}, evolution at P4.

Table 6-1. Points of the modeling domain for which numerical results were obtained in Step 1 of the THM verification case.

Points	(x, y, z) in meters	Quantity
P1	(0.35, 0.01, 0.01)	Temperature
P2	(0.51, 0.02, 0.01)	Temperature
P3	(1.51, 0.07, 0.01)	Temperature
P4	(0.32, 0.51, 0.61)	Temperature, pressure, displacements, stresses

Compared to the previous work of Rutqvist et al. (2019), all results computed with different Biot’s coefficients are improved and match the analytical solutions accurately. With a reduction in Biot’s coefficient, the magnitude of deformation and stress in the porous medium decreases. This benchmark case verifies that the current model can capture the effect of Biot's coefficient in coupled THM processes.

6.3.2 Step 2: TED experiment

The TED experiment lasted three years from 2010 to 2013. It involved three heaters at a depth of 490 m, installed in three parallel boreholes separated about 2.7 m (Figure 6-3). The heaters were 4 m long and were installed at the end of 160 mm diameter and 16 m long boreholes, drilled from a main drift and parallel to the maximum horizontal stress. This arrangement represented a similar configuration to high-level nuclear waste cells with parallel micro-tunnels, but at a smaller scale. The TED experiment was heavily instrumented with 108 temperature sensors in the rock mass, 69 temperature sensors in the three heater boreholes, 18 piezometers, two extensometers and inclinometers, and 10 temperature sensors at the level of the main drift. The temperature measurements during the TED experiment showed that the rock has an anisotropic thermal conductivity, because at the same distance from the heater, the temperature increase was higher in the bedding plane than that in the perpendicular direction. Observations of pore pressure also showed that its evolution depended on the location with respect to the bedding plane; following a power law increase, the pore pressure increased faster in the direction parallel to bedding than that in perpendicular direction.

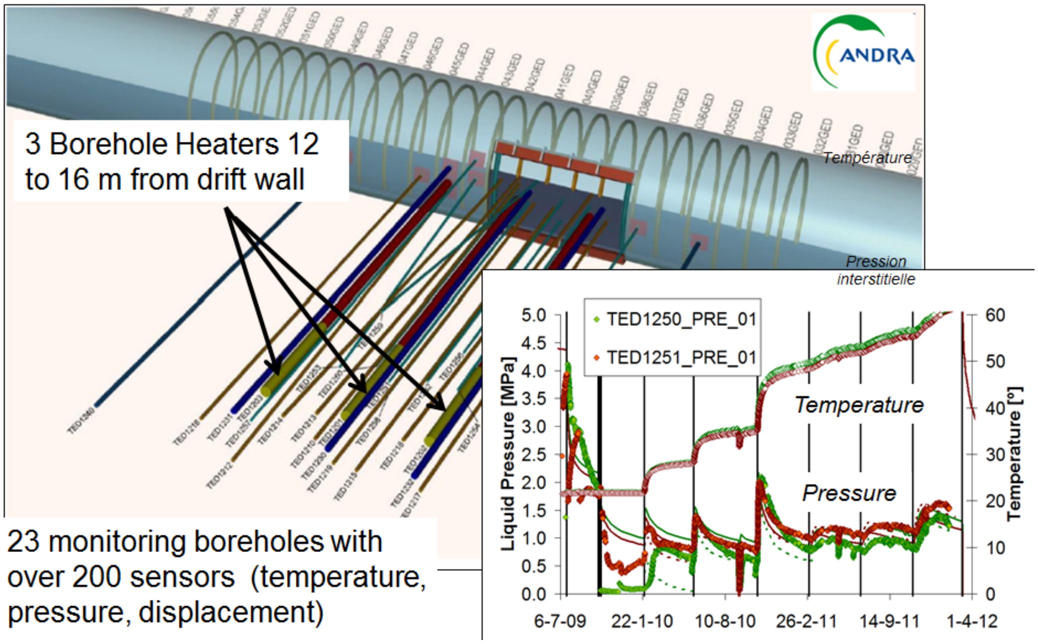

Figure 6-3. The schematic of the TED experiment at Bure. The insert on the figure is the graphs of pressure and temperature evolution, which were used by modeling teams in DECOVALEX-2019 Task E for interpretative modeling.

The purpose of Step 2 is to model the THM response of COx claystone in the TED experiment and to calibrate the numerical models against experimental data. This modeling of the TED experiment will also help improve understanding of physical phenomena observed.

The domain geometry is a cube with a side length of 50 m. The model represents only a half of the GED drift (Figure 6-4). Three heaters are embedded at the center of the domain with surrounded refined grids. For modeling purposes, it is assumed that the whole domain remains saturated during the experiment. In the previous work, the model started with an instant excavation of the GED tunnel, followed by drilling of other boreholes. Then, at 506 days after excavation, the heating phase started and was running for 1251 days. Heater 1 was turned on first, and it took three steps to reach the planned heat power of 600 W. After Heater 1 operating for 400 days, Heaters 2 and 3 were turned on, following three heat power steps to reach the power of 600 W. A cylindrical EDZ of 1m thickness was simulated around the GED tunnel. The effect of the variability of permeability due to excavation was simulated (Figure 6-4a). The THM simulations were conducted using the simulator TOUGH-FLAC, with water properties calculated from the steam table equations (IFC-1967). We have recalibrated thermal conductivity, mechanical properties and permeability of COx rock, because we applied other conditions, such as some drainage boundaries.

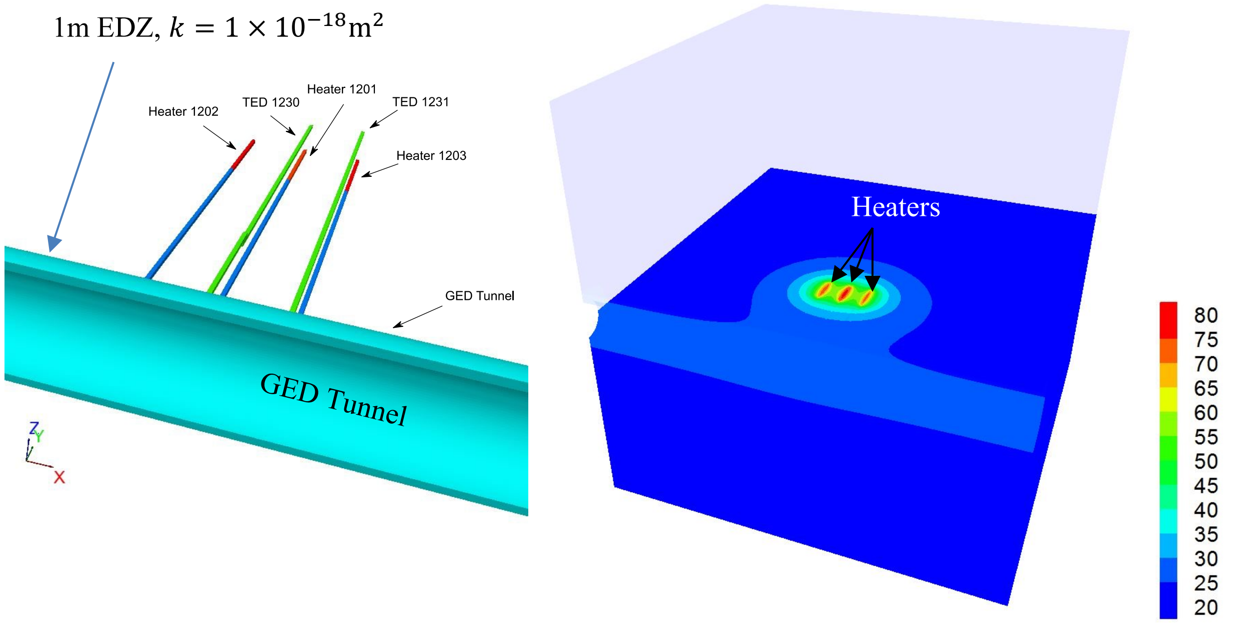

a) b)

Figure 6-4. a) The model setup the position of heater boreholes (Heaters 1201, 1202, and 1203), extensometer boreholes (TED 1230 and TED 1231), and GED tunnel surrounded by 1m EDZ and b) Temperature distribution at 1509 days.

In TED experiment, six sensors were placed at different boreholes near heaters to measure the temperature evolution during the heating stage. The collected data were used as a basis for calibration of thermal properties. Figure 6-5 displays the calculated temperature results based on the results of simulations with calibrated parameters. As the figure shows, a good agreement was achieved between the model prediction and experimental data at Boreholes 1210, 1219, 1250, and 1251. The calibration of the thermal properties is generally acceptable, although the model overestimated the temperature by about 3 ºC to 5 ºC at the two points (sensors in Boreholes 1253 and 1258) farthest from the heater, but the experiment team reported that these two sensors were unreliable.

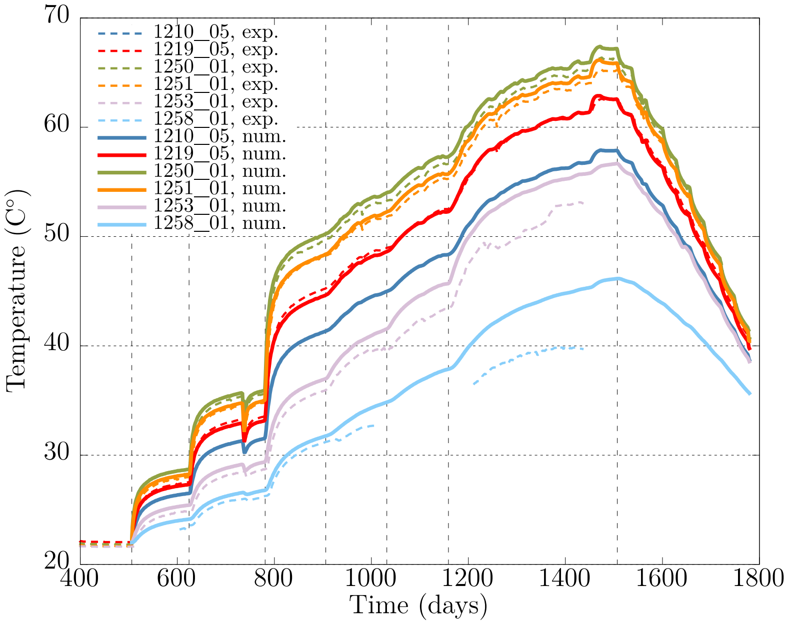

Figure 6-5. Comparison of temperature evolution at measuring points simulated with calibrated thermal conductivity (solid lines) and measured at different monitoring points (dashed lines).

Figure 6-6a presents the simulation results and experimental observations of pore pressure at the sensor positions in Boreholes 1253 and 1258. The figure demonstrates that the simulated pore pressure in Borehole 1253 is in a good agreement with experimental data recorded by the sensor. Although some disagreements of pore pressure at Borehole 1258 are noted, especially the pore pressure at the beginning of the heating phase, but after 800 days the predicted pore pressure agrees well with experimental data. Figure 6-6b displays the simulated and observed pore pressure at five sensor positions in Borehole 1240. Compared with experimental data, the trend of pore pressure change has been captured while the magnitudes of pore pressures at peak are underestimated. The model simulations with recalibrated parameters provide a generally good comparison of predictions on temperature and pore pressure, although discrepancies exists especially before 400 days and after 1200 days. However, no measured data on stresses are available.

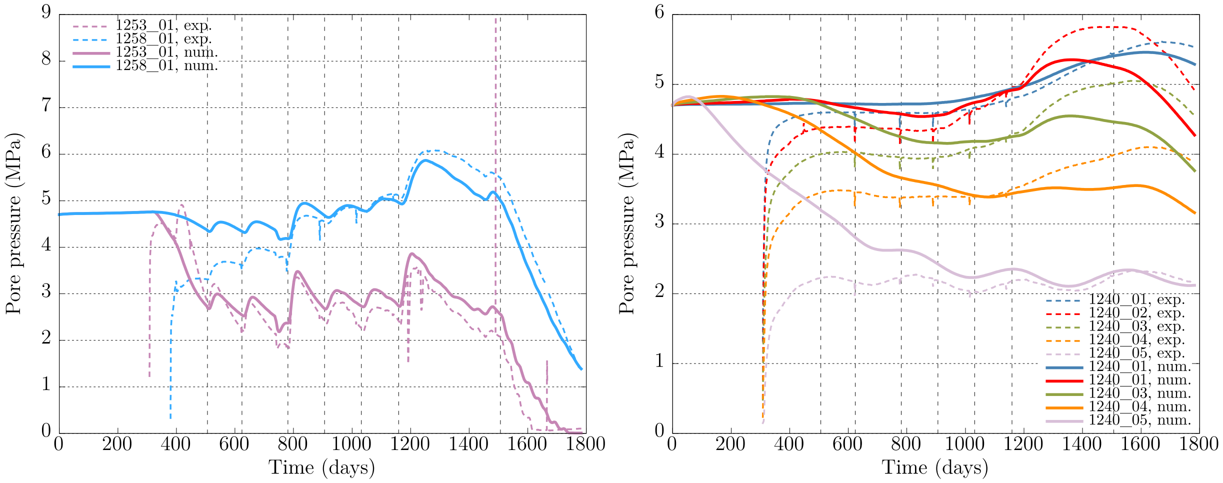

a) b)

Figure 6-6. a) Pore pressure evolution at Boreholes 1253 and 1258. b) Pore pressure evolution at Boreholes 1240.

6.3.3 Step 3: ALC experiment

The heating phase of the ALC experiment in the MHM URL started in 2013, and it is an ongoing *in situ* heating test. The experiment is a full-scale representation of a single high-level waste cell in COx claystone. The ALC1604 micro-tunnel was drilled from the GAN drift, and has a total length of 25 m. The heated part in the ALC experiment is located in the body part of ALC1604 between 10 and 25 m along the length (Figure 6-7), and is made up of five heating elements. Each element is 3 meters long and has a diameter of 508 mm. The ALC experiment was heavily instrumented with temperature and relative humidity sensors, piezometers, strain gauges, and displacement sensors. The temperature measurements made during the ALC experiment showed the same phenomenon of an anisotropic thermal conductivity as in the TED experiment. A conclusion about the anisotropy was drawn because of the different temperature at the same distance from the heater. In particular, the temperature increase is higher in the bedding plane than that in the perpendicular direction. Observations of pore pressure showed that its evolution is dependent on the location with respect to the bedding, and strong hydro-mechanical (HM) coupling induces the opposite pore pressure change near ALC1604 after its excavation. In the vertical direction, the volumetric strain is positive (volumetric expansion), indicating the pore pressure decrease, while in the horizontal direction, the volumetric strain is negative (the volume decreases), causing the pore pressure increase.

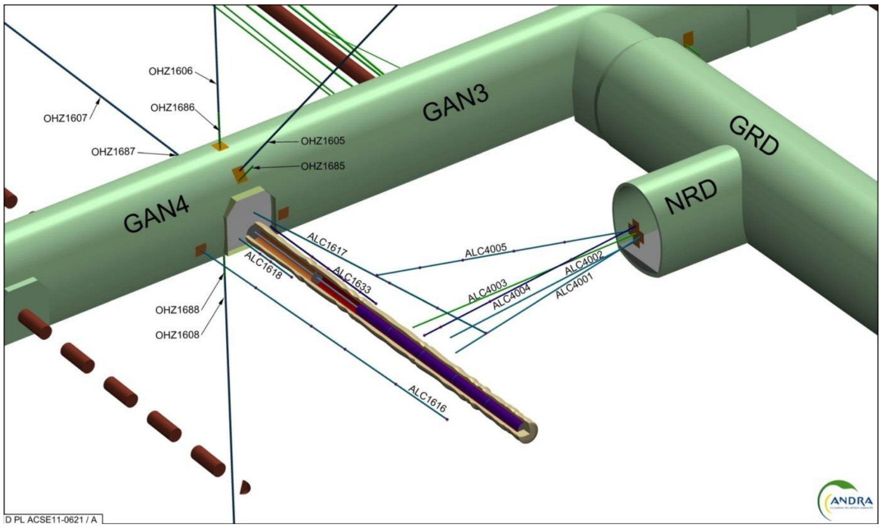

Figure 6-7. The ALC experiment at Bure with various monitor boreholes and micro tunnel ALC1604, which are being used in DEOVALEX-2019, Task E, for interpretative modeling.

The purpose of Step 3 is to predict the THM response of COx claystone in the ALC experiment with calibrated material parameters from the TED experiment. Modeling of ALC experiment will help investigate the behavior of the cell and the casing under thermal loading, and understand the THM behavior of the COx and of the interface between rock mass and casing.

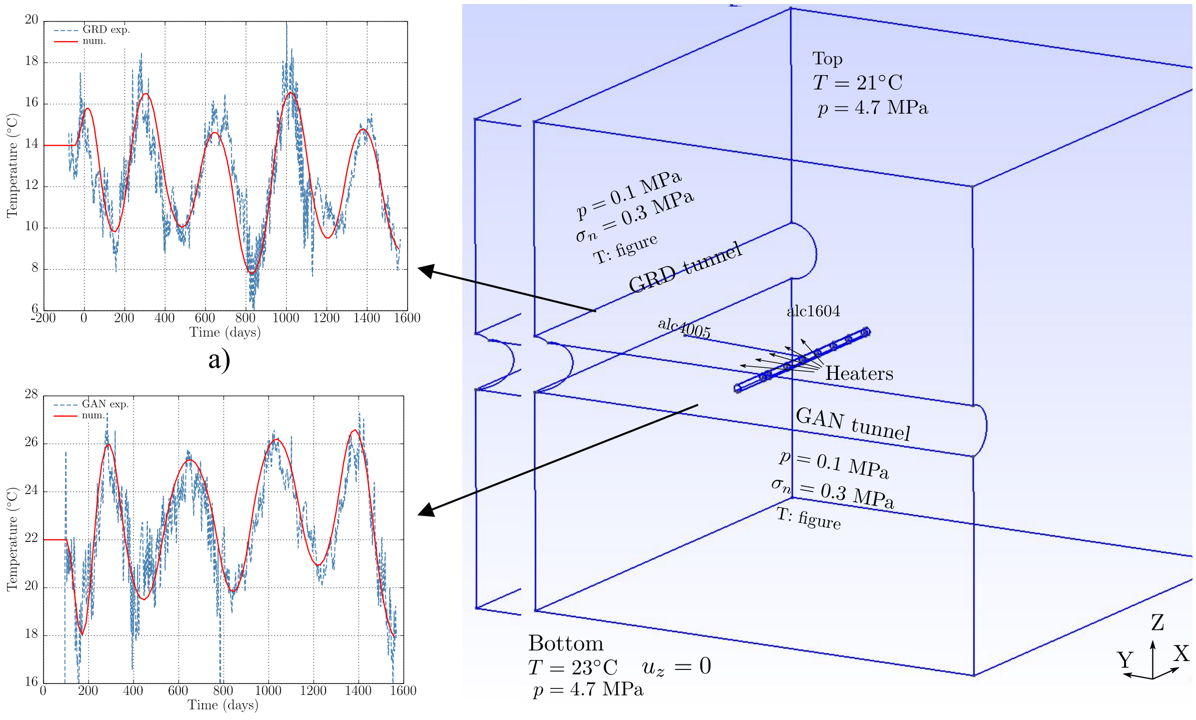

a)

b)

c)

Figure 6-8. Geometry of the model with boundary conditions: a) Observed and simulated temperature evolution at GRD tunnel; b) Observed and simulated temperature evolution at GAN tunnel; and c) Geometry of the simulation domain and boundary conditions on each surface.

The geometry model domain is a cube with a side length of 50 m centered in height at z = 0, with a half of the GAN tunnel excavated along the y-direction, and a half of the GRD tunnel excavated along the x-direction (Figure 6-8c). Five heating elements are located in ALC1604 between 10 and 25 m along x-direction. The heaters are discretized with refined elements. Casing and gap inside the borehole are both explicitly discretized (Figure 6-9). For modeling purposes, it is assumed that the whole domain remains saturated during the experiment. An additional draining borehole, ALC4005, is explicitly modeled with excavation and drainage shown in Figure 6-8.

In the simulation, the model started with instant excavations of GAN and GRD tunnels, followed by drilling of other boreholes. Then, at 458 days after the excavation, the heating phase started and was running for about 1500 days. The time zero, corresponding to the excavation of tunnels, is at 11/01/2011. A heating test at a very low power (33 W/m, 495 W in total) was conducted between January 31 and February 15, 2013. The main heating phase started on April 18, 2013, at a constant nominal power of 220 W/m (3300 W in total) for the 15 m parts occupied by the heater elements (i.e., 660 W per element). The initial pore water pressure (when excavation started) is set constant at 4.7 MPa over the entire domain. The initial stress field in the model domain is estimated from field investigations: the major horizontal stress σ_H is set to 16.1 MPa in y-direction, and the horizontal minor stress σ_h and the lithostatic stress σ_v are set, respectively, to 12.4 MPa in x-direction and 12.7 MPa in z-direction.

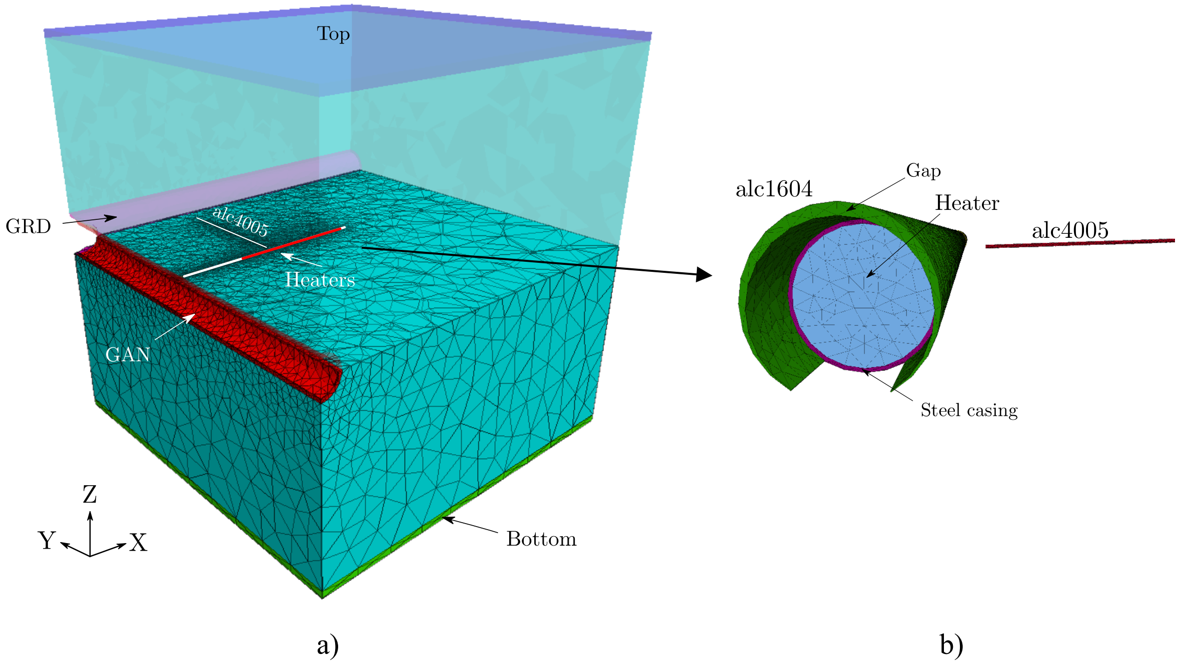

a) b)

Figure 6-9. Mesh generation within the simulated domain: a) Mesh in the entire domain. b) Mesh generation for heater, casing and the gap between them.

The THM computation of the ALC experiment is conducted with the parameters calibrated from the TED test. In the field, six sensors were placed in different boreholes near heaters as displayed in Figure 6-10 to measure the temperature and pore pressure evolution during the whole process. Figure 6-11 displays a comparison of the simulated temperature with experimental data recorded by sensors. The figure shows a good agreement between the model prediction and experimental data. However, at sensors 1617-1 and 1617-2, the model predicted a higher temperature than observed data, while at sensors 1616-5 and 4005-4, the model underestimated the temperature. A possible explanation is that the simulation is based on an assumption of homogeneous host rock, while the *in situ* COx claystone is heterogeneous.

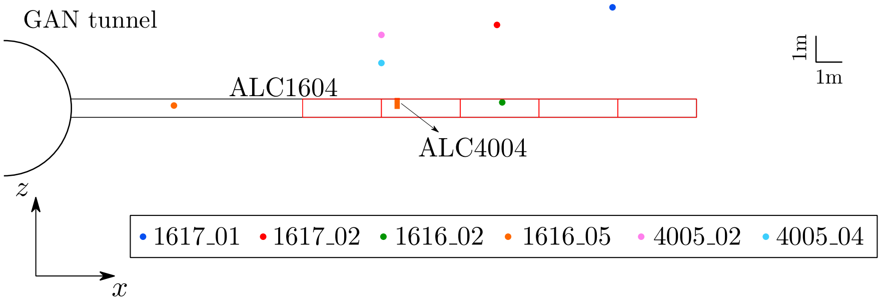

a) A plane view from the right y-plane.

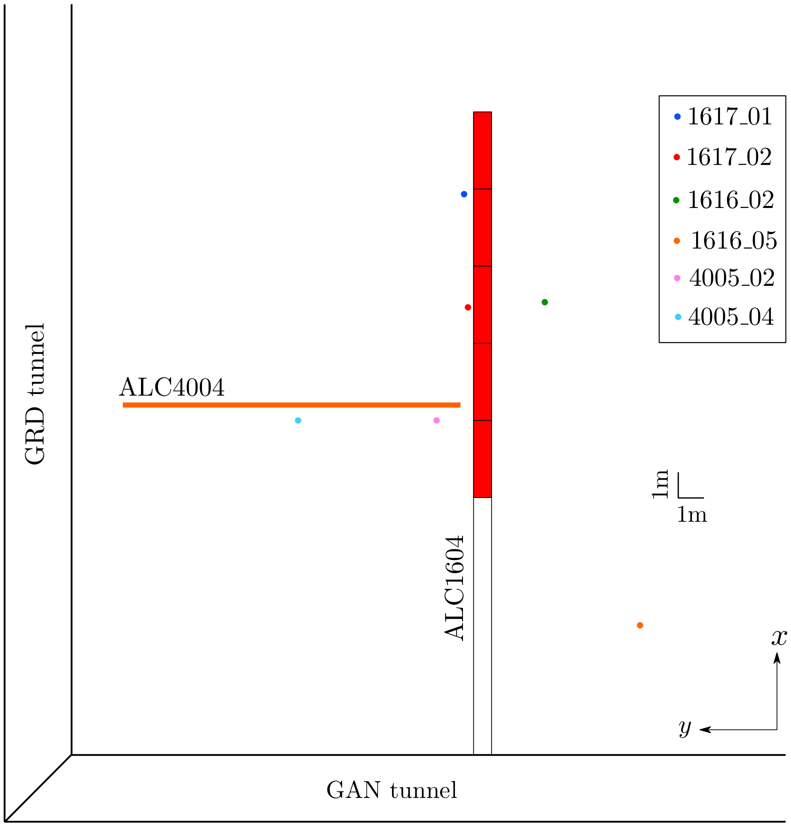

b) A plane view from the top.

Figure 6-10. Monitoring points in the domain.

In the previous work as reported in Rutqvist et al. (2019), we have compared numerical results of pore pressure and experimental field observations. Figure 6-12 presents this comparison about pore pressure at the sensor positions in the boreholes. From the figure, the pore pressure decreases after the initial excavation of the GAN and GRD tunnels, which is due to the drainage conditions applied on tunnel surfaces. Later, with the emplacement of the heater cell, the pore pressure grows, and then slowly dissipates over a few years.

Figure 6-13 presents a plane view of the pore pressure evolution below the plane z = 0 at different times during the heating phase. At 258 days, which is 81 days after the main heating phase started, the water pressure starts to increase due to the thermally-induced pressurization. Tracking the results in Figure 6-13, from 258 to 1402 days, it can be observed that the pore pressure near the heated ALC1604 micro-tunnel grows and propagates farther into the host rock. The magnitude of pore pressure rises sharply during the early heating phase, then starts to dissipate back towards the hydrostatic state.

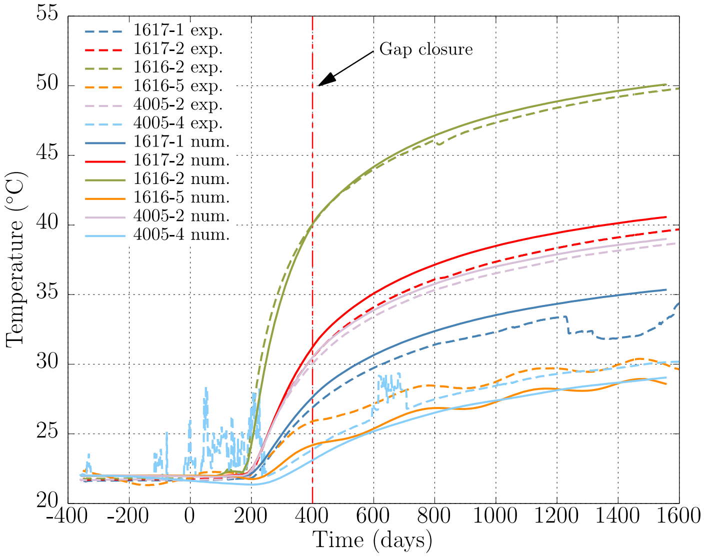

Figure 6-11. Simulated (solid lines) and observed (dashed lines) temperature evolution at measuring points.

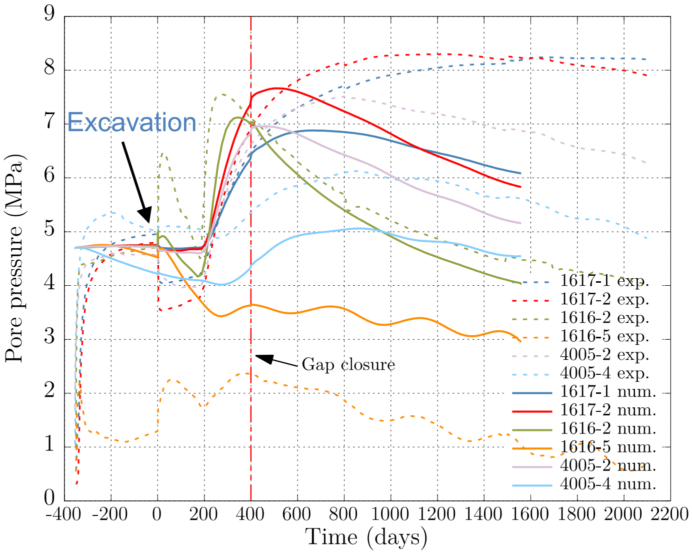

Figure 6-12. Simulated (solid lines) and observed (dashed lines) pore pressure evolution at sensor points.

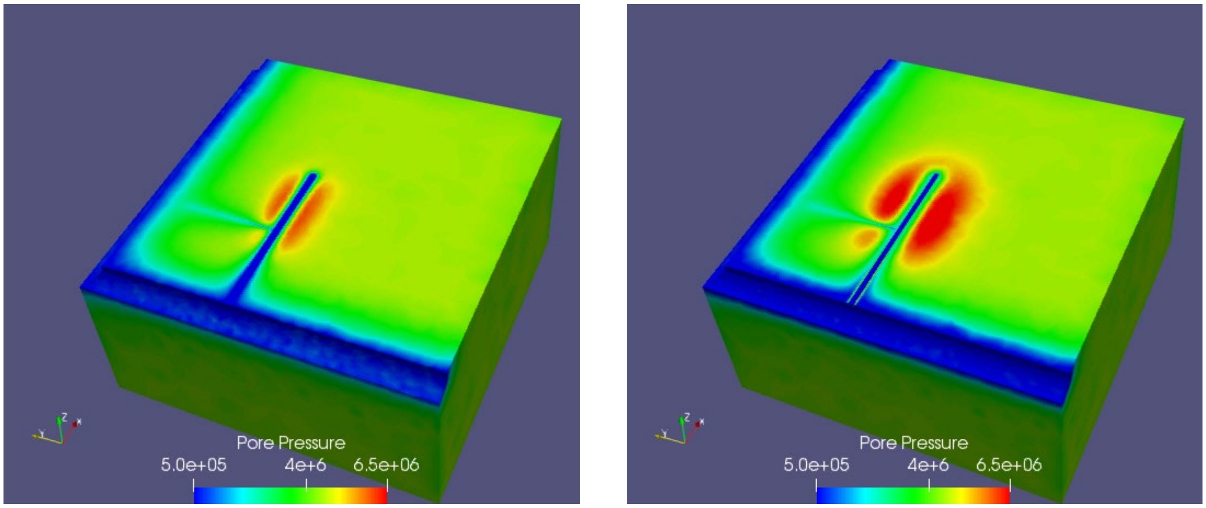

a) 258 days b) 401 days

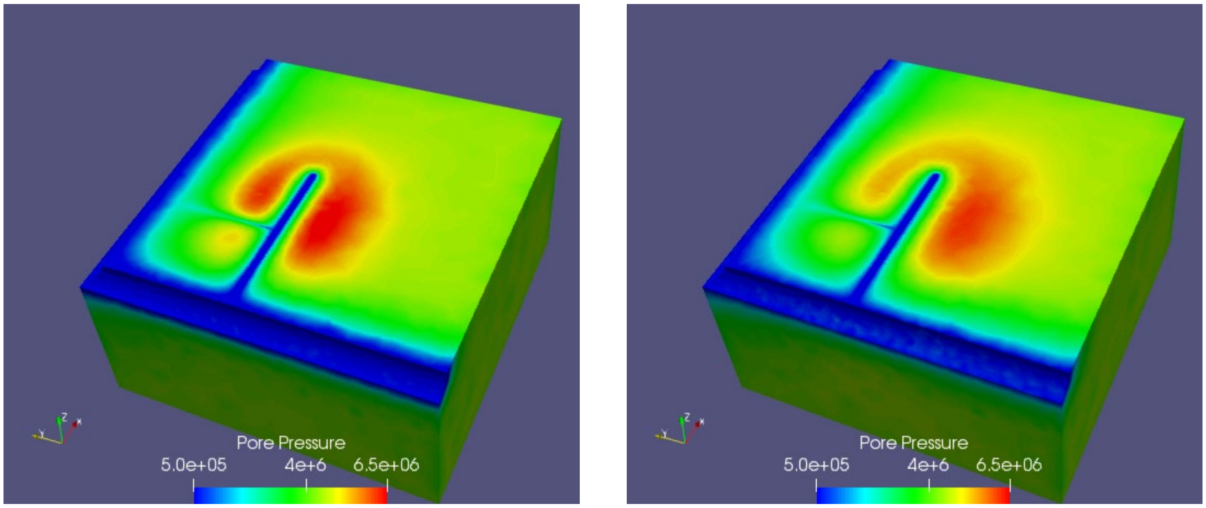

c) 795 days d) 1402 days

Figure 6-13. Simulation results of pore pressure evolution in the ALC experiment at different times.

Based on the comparison, a good agreement at sensor 1616-2 during the heating phase is achieved between model prediction and measured data, while the other results do not match the observations well enough. Therefore, to improve the numerical computation and to better capture the behavior of the pore pressure evolution, we launched a parametric study of different rock properties (Rutqvist et al., 2019). However, it is impossible to achieve a good agreement at all monitoring locations considering homogenous and elastic porous media in the coupled THM model. This may indicate some irreversible or time-dependent processes that are not included in the current linear thermo-poroelastic model.

6.3.4 Step 4: Model at the repository scale

Step 4 is conducted to predict the THM behavior of COx claystone with multiple cells at the repository scale. Following the French concept, the HLW packages will be placed in a set of parallel micro-tunnels of 0.80 m diameter and 150 m length (Figure 6-14). The HLW zone covers an area of around 8 km². The 3D geological model of the COx has been developed gradually since 2000s as the field investigations have progressed, based on the results of investigations performed in deep boreholes and at the underground laboratory. The main objective of Step 4 is to investigate how to develop a reliable numerical model for THM simulations at the repository scale (i.e., representative of several parallel cells distributed within several hundreds of meter). This study is focused on modeling to assess differences and impacts from different modeling approaches among the different research teams in this DECOVALEX Task.

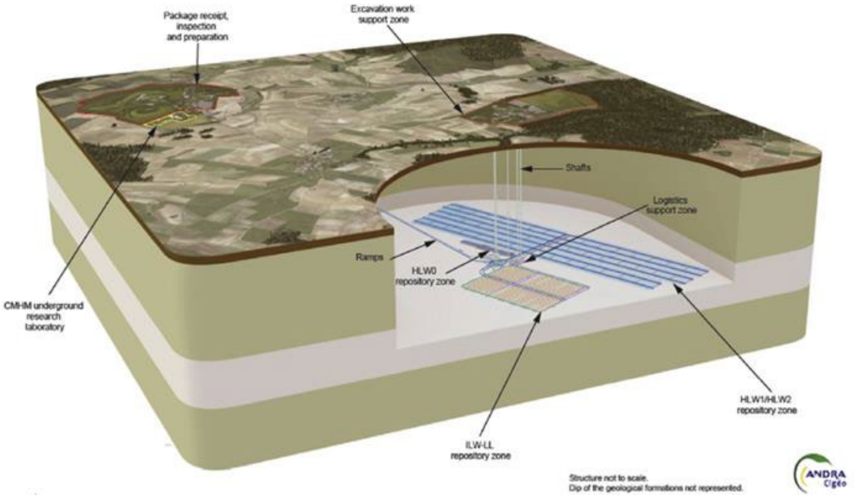

Figure 6-14. Diagram of the facilities of the Cigeo project (Plua et al., 2020).

6.3.4.1 3D THM Model

This section presents the development and results of the repository scale 3D THM modeling. We first explain the model setup, followed by simulation results on the evolution and distribution of temperature, pressure and stress. Finally, an investigation of the modeling approach with the same geometry for the access-drift backfill is presented.

Model setup

The repository modeling domain is represented by a quarter symmetry of a full-scale repository with the dimensions 2000 m×1500 m×1000 m as Figure 6-15 shows. In the modeling domain, eight geological layers are considered with the properties listed in Table 6-4 in terms of a mineralogical composition (Plua et al., 2020). Three main unit layers of the COx formation are taken into account: the Clay unit (UA), the Transition unit (UT), and the Silty Carbonate-Rich unit (USC). The cells for disposal of nuclear waste canisters are designed to be at a depth of 560 m underground in the UA2-UA3 formation. The access and connection tunnels are explicitly modeled with 3D geometries. 28 cells are placed on one side of the access tunnel with the cell spacing of 52.3 m between each other. The points we used to plot the results are displayed in Figure 6-15, and the detailed location information is summarized in Table 6-2. One of the critical outputs is the vertical effective stress as this indicates the potential for inducing hydro-fracturing as a result of thermal pressurization.

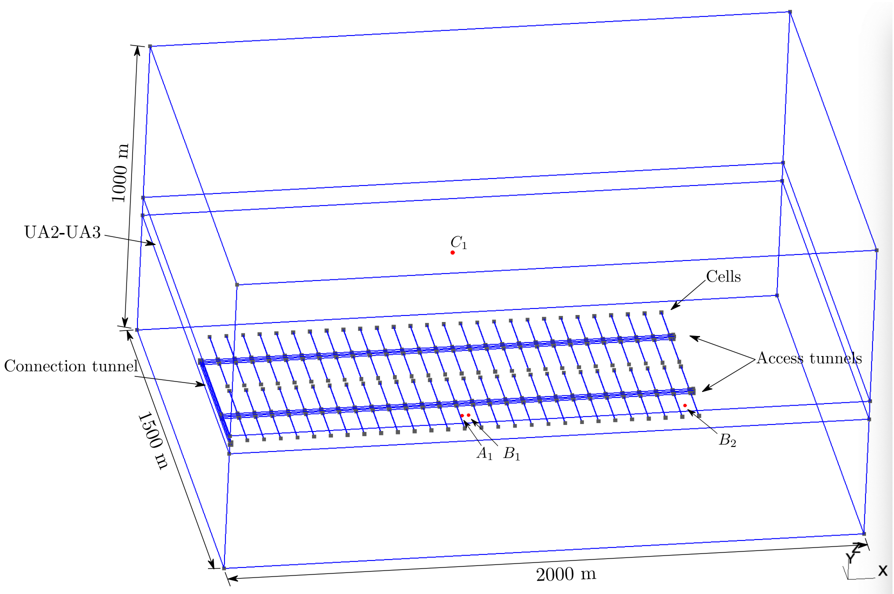

Figure 6-15. Simulation domain of step 4 for THM 3D simulation.

Table 6-2. Points for output numerical results of step 4.

Points	Positions	(x, y, z) in meters	Output Quantity
A_1	2.5ϕcell from the cell center.	(734.2, 86.1, -560.)	Temperature, pore pressure, Total/Effective stress.
B_1	In the middle between 14th and 15th cell.	(758.35, 86.1, -560.)	Temperature, pore pressure, Total/Effective stress.
C_1	Above B on the top surface.	(738.35, 86.1, 0.)	Displacement.
B_2	In the middle between 27th and 28th cell.	(1438.25, 86.1, -560.)	Temperature, pore pressure, Total/Effective stress.

Based on the site description provided by ANDRA, the initial temperature is linearly distributed with depth, with 7.7 ºC at the top and 37.7 ºC at 1000 m depth at the model domain bottom. The pore pressure is distributed with the gradient of 0.01 MPa/m with depth, considering hydro-static conditions. Based on ANDRA's best estimation of the stress field with depth, the initial stress distribution with depth is applied with a gradient of 0.024 MPa/m for vertical stress and minor horizontal stress, and with the gradient of 0.032 MPa/m for the major horizontal stress.

The simulation starts at the instance of excavation of access and connection tunnels followed by 10 years of drainage into these open tunnels. Thereafter the drilling of 112 (28×4) cells (horizontal micro-tunnels) is simulated to take place instantly, followed by another 2 years of drainage. The reference date at 0 year corresponds to beginning of excavations. The heat power from waste canisters emplaced in the cells starts at 146 W/m, then decays following the curve as Figure 6-16 shows.

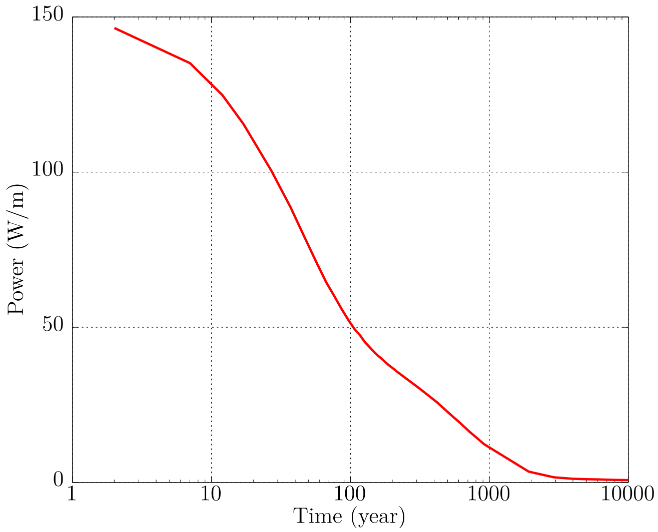

Figure 6-16. Decay heat power per meter along each cell applied in the model.

In the whole repository, the top surface at ground is free of stress, while the bottom surface is constraint to zero vertical displacement. The vertical symmetric boundaries are fixed to zero normal displacements, while the far-field vertical boundaries are applied linearly varying stress with depth according the aforementioned initial stress gradients. Boundary conditions of the cells and the access tunnels during three stages are listed in Table 6-3 (Plua et al., 2020). The atmospheric pressure imposed in the access tunnel for 10,000 years, as defined in Table 6-3, implies that these tunnels remain open and not water filled for 10,000 years. In our modeling, we investigate this option by simulating a case of a backfilled tunnel that is being resaturated due to inflow from the surrounding rock.

Table 6-3. Boundary conditions on the cell and tunnel walls in step 4 (Plua et al., 2020).

		Cells	Access tunnel
-10 – 0 years	T	24.5 ºC	24.5 ºC
	H	Hydro-static pore pressure.	Atmospheric pressure.
	M	Considered As UA2-UA3 with lithostatic stress.	Free surface.
0 – 2 years	T	Initial temperature.	Initial temperature.
	H	Atmospheric pressure.	Atmospheric pressure.
	M	Free surface.	Free surface.
2 – 10,000 years	T	Heat power	Initial temperature but can change.
	H	No flux.	Atmospheric pressure.
	M	Free surface.	Free surface.

Material parameters for COx claystone and other formations were provided by ANDRA as described in Plúa et al. (2020). The mean values of THM parameters of each unit are listed in Table 6-4. Water properties in the TOUGH-FLAC simulation are calculated from the steam table equations (IFC-1967).

Table 6-4. THM parameters of different rock formations used in the repository scale modeling (Plua et al., 2020).

Rocks	E_v	E_h	ν	b	n	K_v	K_h	ρ	λ_v	λ_h	α_s	C_p	Depth
	GPa	GPa		-	-	m^2	m^2	kg/m^3	W/m/K	W/m/K	1/C	J/kg/K	M
Barrois Limestone	3.6	3.6	0.3	0.6	0.13	1.00E-19	1.00E-19	2450	1.1	1.54	2.20E-05	1024	0~103.4
Kimmeridgian	3.6	3.6	0.3	0.6	0.13	1.00E-19	1.00E-19	2450	1.1	1.54	2.20E-05	1024	103.4~211.4
Carbonated Oxfordian	30.	30	0.3	0.6	0.13	1.00E-16	1.00E-16	2470	2.3	2.3	4.50E-06	925	211.4~488
USC	12.8	19.2	0.3	0.6	0.15	1.87E-20	5.61E-20	2480	1.79	1.79	1.75E-05	978	488~517.4
UT	8.5	12.75	0.3	0.6	0.173	1.87E-20	5.61E-20	2450	1.47	2.205	1.75E-05	978	517.4~532.6
UA2-UA3	7.	10.5	0.3	0.6	0.193	1.87E-20	5.61E-20	2430	1.31	1.965	1.75E-05	978	532.6~595.8
UA1	12.5	18.75	0.3	0.6	0.164	1.87E-20	5.61E-20	2460	1.63	2.445	1.75E-05	978	595.8~635
Dogger	30.	30	0.3	0.6	0.1	1.00E-18	1.00E-18	2470	2.3	2.3	4.50E-06	925	635~1000

Results

Figure 6-17 presents the calculated results in terms of temperature, pore pressure, displacement, and stress. The temperature is 24.5 ºC at time = 0, which corresponds to the occurring of the instantaneous excavation of cells. The temperature at point A_1 near the cell peaks at about 57 ºC after 25 years, whereas the peak temperature at point B_1 in the middle between cells is about 42 ºC (Figure 6-17a) after 500 years. Figure 4-18a displays the temperature distribution at 50 years. As the figure shows, the temperature increases between the cells with the range from 40 to 50 ºC. At about 2,000 years, the temperature evolutions at points A_1 and B_1 merge, indicating a uniform temperature in the repository layer, follow the same evolution and decrease towards ambient temperature till the end of the simulation.

The pore pressure changes at points A_1 and B_1 are different as Figure 6-17b shows. At point A_1, the early time drainage into the cell results in a reduction of pore pressure. After the waste is emplaced, due to the thermal pressurization in the low permeability COx claystone, the pore pressure is expected to increase rapidly, and peaks at 10.2 MPa, which is 4.6 MPa higher than the initial hydrostatic pressure. The pore pressure at point B_1 increases to a peak of 10.5 MPa at 35 years. After 35 years, the fluid pressure at both locations begin to dissipate, and almost follow the same path for up to 2,000 years when hydrostatic equilibrium is re-established. Figure 6-18b presents the pore pressure distribution at 50 years. As this figure shows, the pore pressure surrounding the cells increases to about 9 MPa at 50 years, and propagates horizontally between cells, resulting in an evenly distributed high pore pressure between cells.

Figures 6-17c shows the vertical displacement change at point C_1 on the top surface. The heat induced thermal expansion in the UA2-UA3 clay formation leads to a ground surface heave of 88 mm. The peak surface uplift occurs at around 1,700 year, which is delayed compared to repository peak temperature as surface uplift is due to the cumulative thermal expansion of host rock and overburden, which takes longer to propagate to the surface ground. Later, with contraction and energy dissipation during the cooling period, the surface heave reduces to 20 mm at 100,000 year.

Figure 6-17d displays the evolution of vertical Terzaghi effective stresses at points A_1 and B_1 in the UA2-UA3 layer. The vertical Terzaghi effective stress is calculated from the vertical total stress and the pore pressure, $\sigma'_{zz} = \sigma_{zz} + p$. Negative stress indicates compressive stress. The evolution of stress in Figure 6-17d results from pore pressure changes and thermal stress based on thermo-poroelasticity. The vertical effective stress at both points follow the pore pressure evolution path. A substantial effective stress increase (indicating a less compressive stress) at point B_1 happens and peaks about 40 years, with the magnitude of -3.2 MPa, which increases the potential for tensile failure (e.g. $\sigma'_{zz} = 0$). The increase in the effective stress close to zero is mainly due to the thermal induced pressurization in fluid. For point A_1, it is relatively safer, since the peak of the effective stress is -7.2 MPa. Figure 6-18c displays the vertical effective stress distribution across the repository at 50 years. Different from the pore pressure, the vertical effective stress increases more significantly between cells, and propagates horizontally towards the cells.

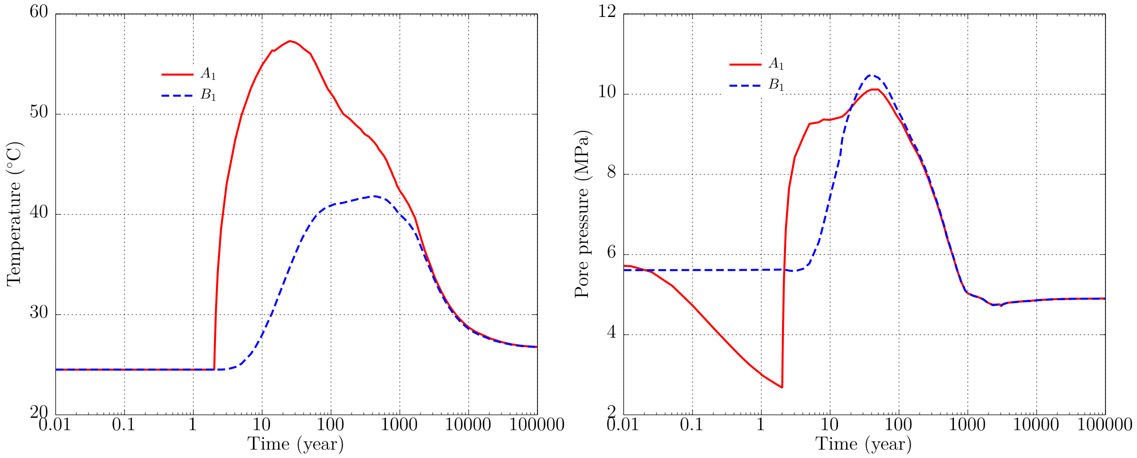

(a) Temperature evolution at A_1 and B_1. (b) Pore pressure evolution at A_1 and B_1.

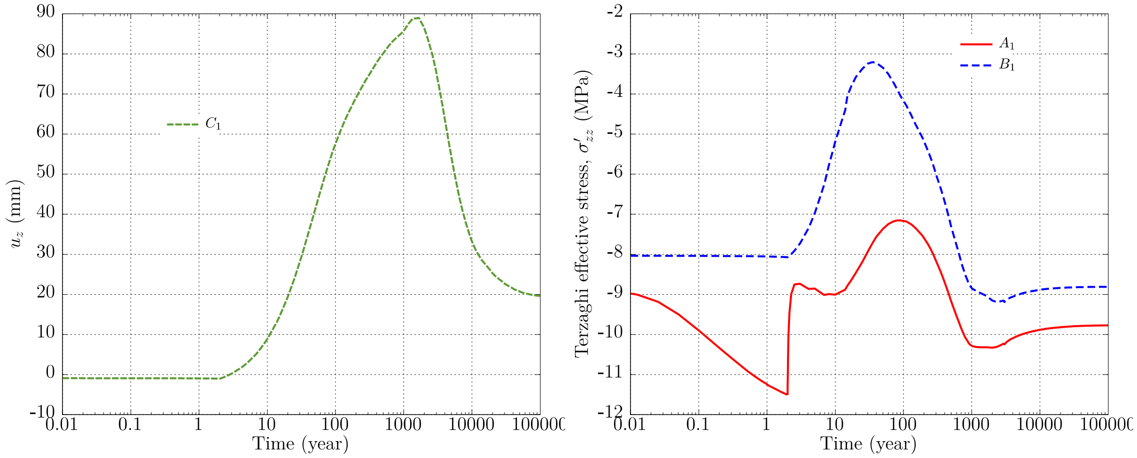

(c) Displacement changes at C_1. (d) Vertical Terzaghi effective stress changes at A_1 and B_1.

Figure 6-17. 3D THM simulation results of Step 4.

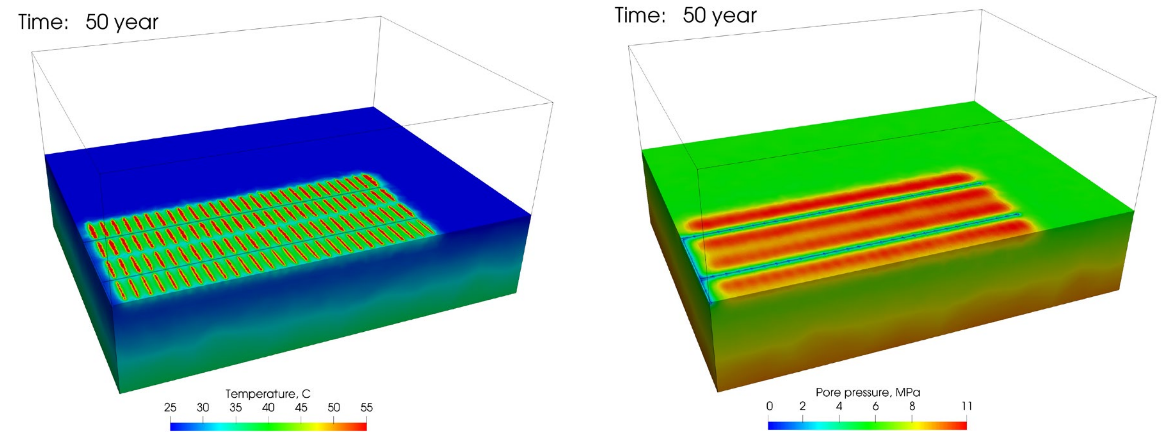

(a) Temperature distribution at 50 years. (b) Pore pressure distribution at 50 years.

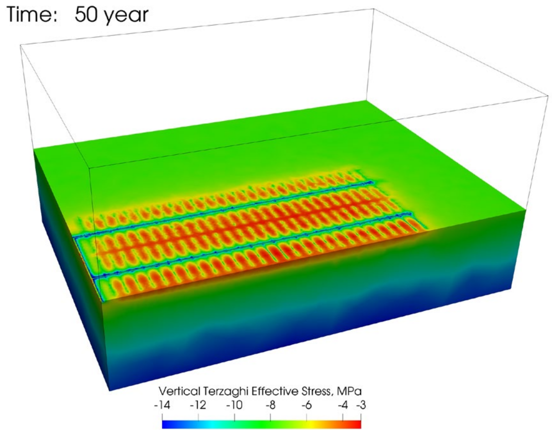

(c) Vertical Terzaghi effective stress distribution at 50 years.

Figure 6-18. Temperature, pore pressure and Terzaghi effective stress distribution at 50 years.

Figure 6-19 presents the simulated results at point B_2 with comparison to B_1, to show the edge effects. Point B_2 is a middle point between the 27th and 28th cells near the right edge of the emplacement zone. But point B_2 is subjected to different surrounding THM conditions from B_1, since it is close to unheated zone. As Figure 6-19 illustrates, the evolutions of temperature and vertical effective stress at B_2 follow similar paths as B_1 before 10 years. Due to the different position, the thermal energy and fluid at B_2 can transport to the right open space, resulting in a temperature decrease after 50 years, and an earlier pore pressure dissipation. As Figure 6-19b shows, a lower vertical effective stress at B_2 is obtained, indicating that B_2 has a lower potential of tensile fracturing than B_1.

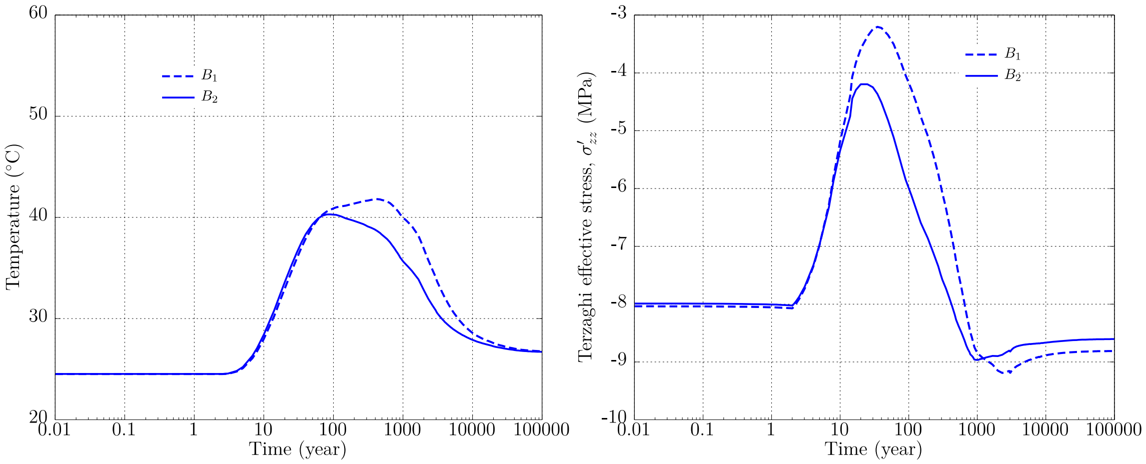

(a) Temperature evolution at B_1 and B_2. (b) Vertical Terzaghi effective stress changes.

Figure 6-19. The comparison of THM simulation results between B1 and B2.

Backfilled tunnels with bentonite

Here we investigate the case of all tunnels being backfilled and calculate the resaturation of the backfill. This situation is assumed that all tunnels are backfilled with a bentonite-crushed rock mixture. The Young's modulus of backfill is assumed to be 17 MPa, initial saturation is 65%, and the permeability is assumed one order magnitude higher than the UA2-UA3 layer. The alternative case is marked as "3D, backfilled" in the results presented in Figure 6-20.

The temperature evolution is almost the same for both cases. For the simplicity, we didn't present the temperature comparison here. As Figure 6-20 displays, the pore pressures for both cases follow the same path before 200 years. After that time, the access tunnels are almost fully saturated with water in the backfilled case, resulting in a slower drainage from host rock to access tunnels, which is captured in Figure 6-20a. The displacement evolution paths at C_1 in both cases also diverge after 200 years when the bentonite inside access tunnels are fully saturated. The increase of vertical displacement in the backfilled case is due to the expansion of the backfilled material inside tunnels. The model also predicts a higher peak value of vertical effective stress at Point A_1, while the peak at B_1 is the same as the original case.

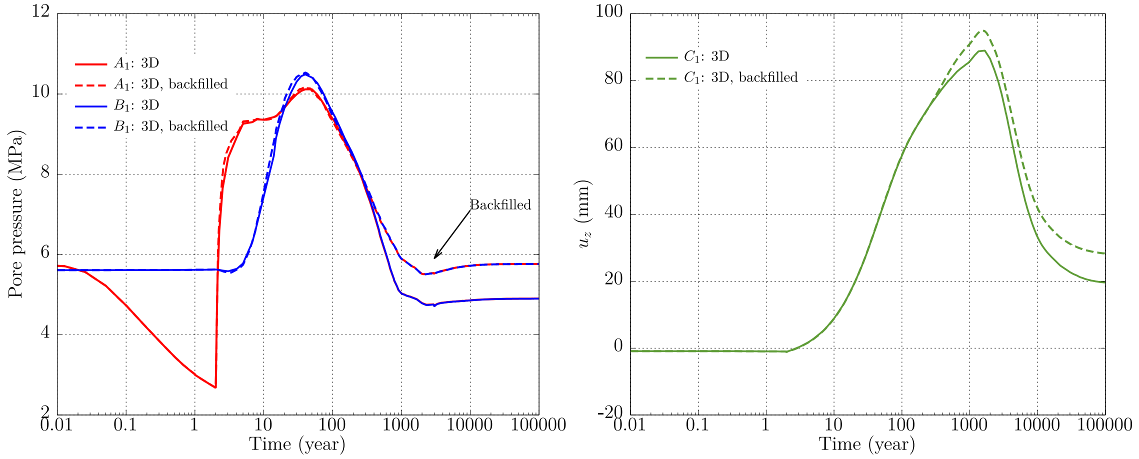

(a) Pore pressure evolution at points A_1 and B_1.

(b) Displacement changes at point C_1.

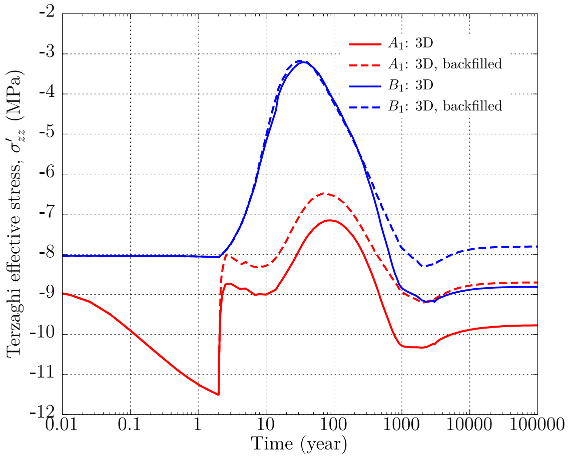

(c) Vertical Terzaghi effective stress changes at points A_1 and B_1.

Figure 6-20. The comparison of THM simulation results of step 4 between two 3D cases.

6.4 Summary and Status of the Bure Heater Experiment Modeling

In FY20, along with Task E of the DECOVALEX-2019 project, we have updated the model to predict THM processes at the repository scale. The current progress on this task is:

For Step 1, we have improved the model to achieve a good agreement of temperature, pore pressure, stresses, and asess the difference between our model simulations and theoretical solutions.

For Step 2, we have determined THM parameters of claystone from the TED experiment, including calibration of the thermal conductivity to match the temperature evolution during the heating phase, and back analysis of the simulation results to determine permeability. The heating phase of the TED experiment has been simulated with TOUGH-FLAC with good match to experimental data.

For Step 3, we predicted the THM behavior of COx claystone during the ALC experiment by utilizing parameters of claystone from those calibrated from modeling of the TED experiment. The heating phase of the ALC experiment has been simulated with TOUGH-FLAC and compared the simulation results with experimental temperature and pore pressure data.

For Step 4, we have conducted new 3D THM simulations of the parallel cells at the repository scale. Two alternative modeling approaches are conducted to investigate the effect of backfilled materials in tunnels.

Future work will be dedicated to modeling of hydro-fracturing induced by a temperature shock and thermal pressurization in COx claystone at the MTM laboratory. The work will be part of the a new DECOVALEX-2023 project.

This page intentionally left blank.

7. MODELING OF GAS MIGRATION IN CLAY USING TOUGH-FLAC AND TOUGH-RBSN (DECOVALEX-2019)

In this section, we present the results of LBNL's activities aimed at modeling gas migration in clay related to Task A of the DECOVALEX-2019 project. This is an international collaborative activity, in which LBNL scientists gain access to the results of unique laboratory experiments of gas migration. These results are now used for numerical modeling to better understand the processes, to improve numerical models, and which will ultimately be applied in the performance assessment of nuclear waste disposal in host clay rocks and bentonite backfill. The Task A of DECOVALEX-2019 is coordinated by the BGS. The BGS is also sharing their extensive data sets on coupled THM processes during gas migration in bentonite and claystone. In FY20, LBNL conducted new simulations of spherical gas flow through bentonite and compared the simulation results with experimental data, which are described in the following sections.

7.1 Gas Migration in Clay

Gas migration in clay-based buffer materials has been the subject of a number of international research programmes in the field of nuclear waste disposal, including both laboratory scale and *in situ* experiment (e.g., Horseman et al., 2004; Harrington et al., 2012; Cuss et al., 2014). Substantial insight has been gained in the phenomenology of gas transport processes in bentonite and claystone under different THM conditions. A number of model approaches have been proposed for the interpretation of the experimental results and for the analysis of gas release scenarios from geological repositories in the context of long-term safety assessment. The predictive capability of the gas transport models is yet limited, indicating that basic mechanisms of gas transport in bentonite are not understood in sufficient detail to provide the ground for robust conceptual and quantitative models.

The processes governing the movement of repository gases through bentonite and argillaceous host rocks can be split into two components: (1) molecular diffusion (assumed to be governed by Fick's law), and (2) bulk advection (Harrington, 2016). In repository concepts such as the Swedish KBS-3, corrosion of metallic materials under anoxic conditions will lead to the formation of hydrogen. Radioactive decay of the waste and the radiolysis of water are additional source terms. If the rate of gas production exceeds the rate of gas diffusion within the pores of the barrier or host rock, a discrete gas phase will form. Under these conditions, gas will continue to accumulate until its pressure becomes sufficiently large, and it may enter the surrounding formation.

Four primary phenomenological models describing gas flow, shown in Figure 7-1, can be defined as following: (1) gas movement by diffusion and/or solution within interstitial fluids along prevailing hydraulic gradients; (2) gas flow in the original porosity of the fabric, commonly referred to as viscocapillary (or two-phase) flow; (3) gas flow along localized dilatant pathways, which may or may not interact with the continuum stress field; and (4) gas fracturing of the rock similar to that performed during hydrocarbon stimulation exercises (Harrington, 2016).

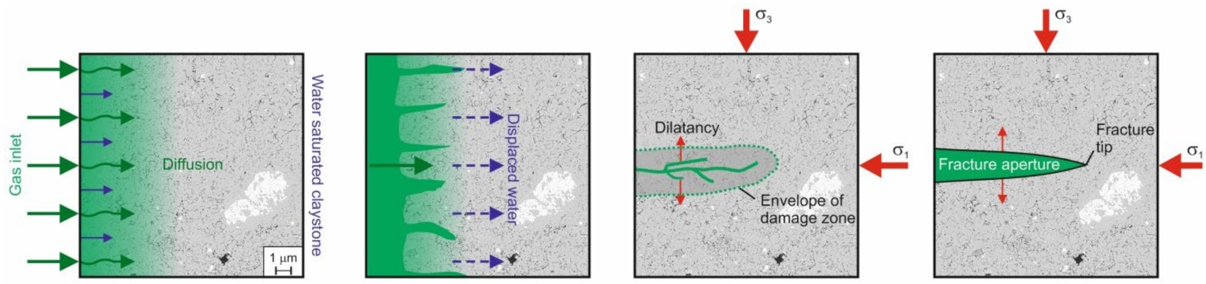

Advection and diffusion of dissolved gas

Visco-capillary flow of gas and water phase ("two-phase flow")

Dilatancy controlled gas flow ("pathway dilation")

Gas transport in tensile fractures ("hydro-/gasfrac")

Figure 7-1. Conceptual models of gas flow (Harrington, 2016)

Studies on gas migration in clays (Horseman et al., 1999; 2004; Harrington and Horseman, 1999) indicate that classic concepts of porous medium two-phase flow are inappropriate and continuum approaches to modeling gas flow may be questionable, depending on the scale of the processes and resolution of the numerical model. However, the detail of the dilatant mechanisms controlling gas entry, flow and pathway sealing are unclear. As such, development of new and novel numerical representations for the quantitative treatment of gas in clay-based repository systems is therefore required (Harrington, 2016).

7.2 LBNL Model Approaches for Gas Migration

LBNL is exploring two complementary approaches for modeling gas migration associated with DECOVALEX-2019 Task A (Figure 7-2):

1) Continuum modeling approach using TOUGH-FLAC simulator (Rutqvist et al., 2011), and

2) Discrete fracture modeling approach using TOUGH-RBSN simulator (Kim et al., 2017)

The continuum approach is based on current developments and applications of TOUGH-FLAC for the modeling of long-term THM performance of nuclear waste repositories in clay host rocks. The TOUGH2 code and other continuum models have been used in the past to model gas migration in clay considering heterogeneous clay properties with pressure dependent permeability, but without considering geomechanical coupling (e.g., Senger and Marschall, 2008; Senger et al., 2014). In this study, a continuum approach will be extended to include full geomechanics coupling within the framework of TOUGH-FLAC. The discrete fracture modeling approach is based on current development of the TOUGH-RBSN simulator, in which the opening of grain boundaries for dilatant gas migration is modeled explicitly using a fracture mechanics approach. The TOUGH-RBSN has previously been applied for modeling fluid driven hydraulic fracturing and complex fracturing in clay host rocks (Kim et al., 2017). The TOUGH-RBSN should be suitable for modeling of complex flow paths associated with dilatant gas migration in clays.

In FY20, this task has been completed as part of DECOVALEX-2019. Here we present the final results of the spherical flow simulations with TOUHG-RBSN.

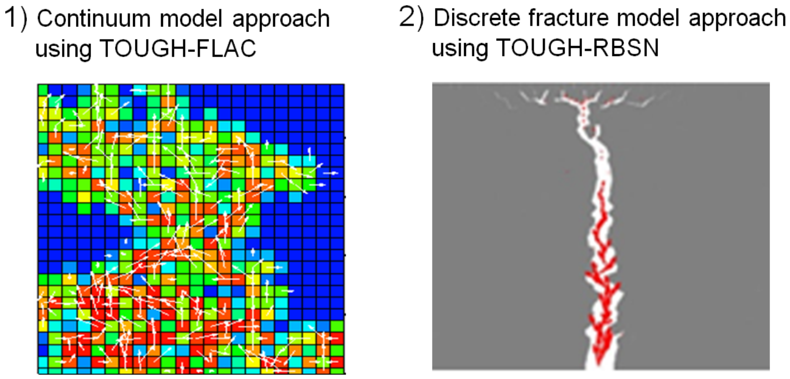

Figure 7-2. Schematic of modeling approaches employed by LBNL for modeling gas migration through clay associated with DECOVALEX-2019 Task A. To the left, the continuum approach using TOUGH-FLAC is illustrated involving heterogeneous properties with the possibility of the formation of dilatant flow paths through pressure or strain dependent permeability in individual cells. The actual color figure to the left is from TOUGH2 modeling (Senger and Marschall, 2008), in which the white arrows show gas flow velocity and colors are gas saturation. To the right, the discrete fracture modeling approach using TOUGH-RBSN, involving complex fracturing to simulate the formation of dilatant flow paths. The red shows the fluid flow pathways through the fracture shown in white color.

7.3 Laboratory Experiments of Spherical Gas Migration in Bentonite

Stage 2 experimental data have been collected to describe 3D spherical gas flow through a saturated sample of MX-80 bentonite. The experiment was conducted by BGS, who has also tested the 1D gas flow through bentonite to obtain the Stage 1 experimental data. The experiment is conducted on a cylindrical bentonite sample, 120 mm in height and 60 mm in diameter. The sample is placed in a pressure vessel that allows for monitoring of the evolution of pressure and stress at different locations along the sample, as well as inflow and outflow rates through filters (Figure 7-3).

The gas injection port is located at the center of the sample, and staged hydration and gas injection processes have been carefully controlled over 700 days to minimize the perturbation of the system/sample and better reflect realistic conditions of a deep geological disposal facility. The DECOVALEX teams performed numerical simulations of coupled gas pressure and stress responses for the period from 735 to 835 days, when the gas breakthrough occurred.

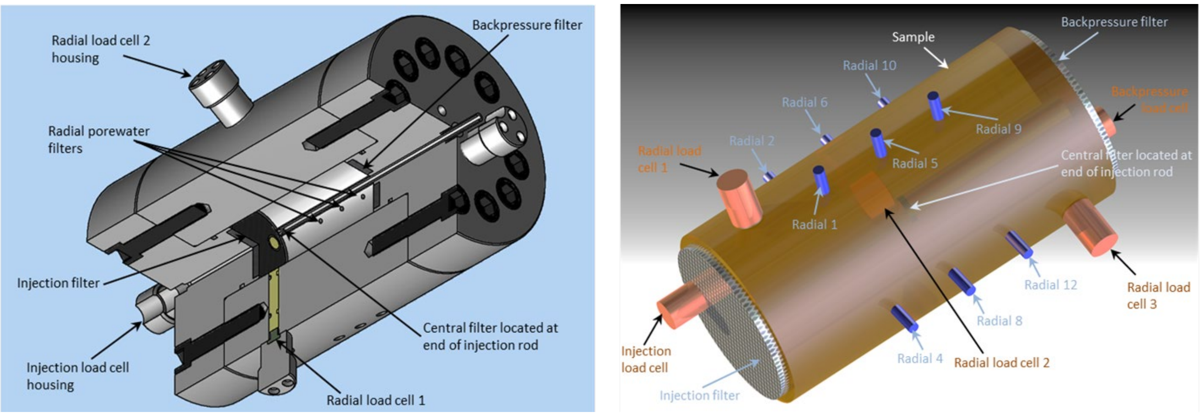

Figure 7-3. Left: Cut-away diagram of the pressure vessel showing the apparatus components and instrumentation. Right: image of the sample showing the relative positions of the load cells and pore pressure filters (Harrington, 2016).

Figure 7-4 shows experimental results of pressure/stress evolutions and inflow/outflow rates between 735 days and 835 days of gas injection. Standard temperature and pressure (STP) are defined as 273.15 K, 101.325 kPa respectively. The peak in gas pressure (around day 767.6) is followed by a protracted negative pressure transient leading to a quasi-steady state by around day 825 (Figure 7-4a). During this period, the change in injection pressure is crudely mirrored by stress which exhibits none of the apparent chaotic patterns observed at earlier breakthrough events. The reduction in the variability of stress from day 768 onwards is accompanied by the development of stable outflow conditions, with flux localized to one drainage array (Figure 7-4b).

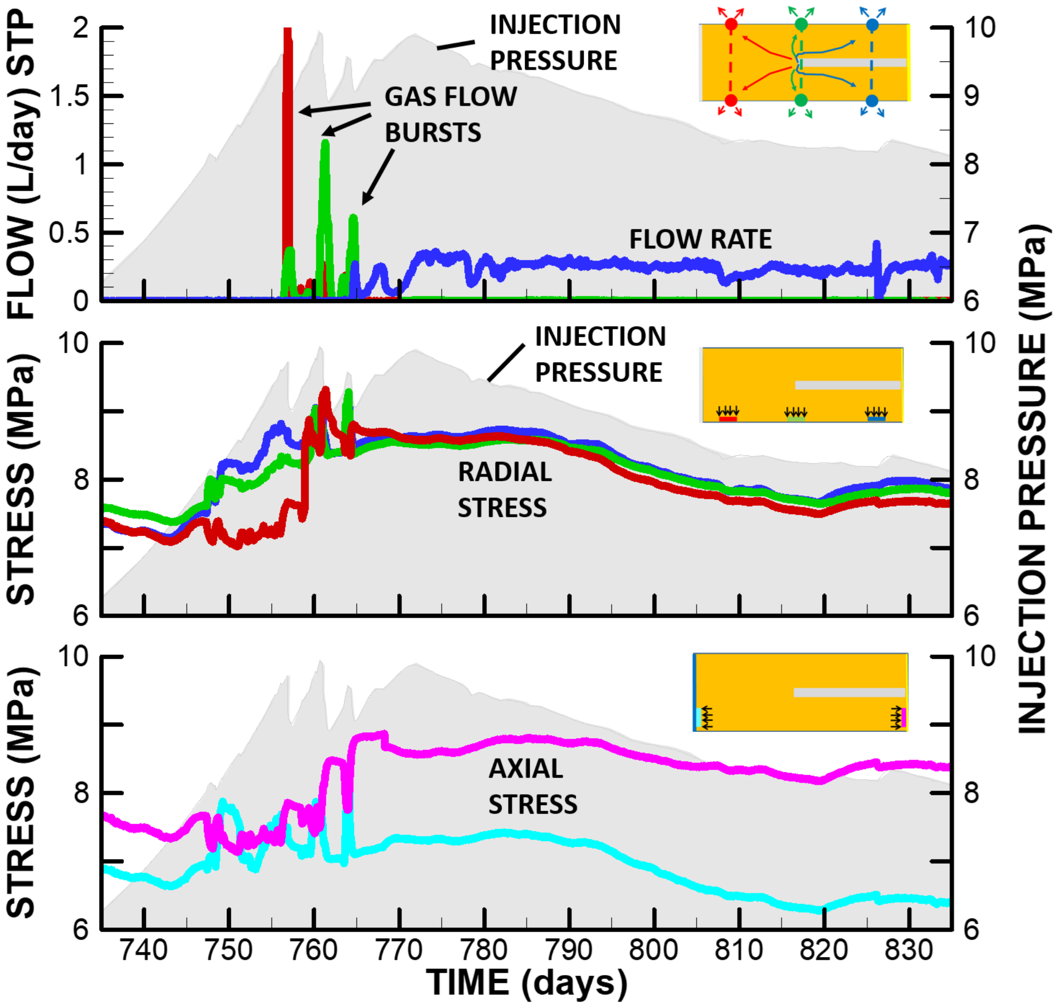

Figure 7-4. Observed 3D spherical gas flow test results: (upper) outflow (middle) radial stress and (lower) axial stress with shaded area being injection pressure (Data from Harrington et al., 2017).

7.4 TOUGH-RBSN Modeling of Gas Migration Experiments

The TOUGH2 model configuration comprises two types of elements. The first element type is cell elements, whose geometry is associated to the Voronoi cells. The cell elements represent the matrix/grain bulk, for which the porosity-dependent permeability is defined as (Gens et al., 2009)

$$k = k_0 \frac{\phi^3}{(1-\phi)^2} \frac{(1-\phi_0)^2}{{\phi_0}^3} \tag{7.1}$$

where k_0 is the intrinsic permeability, and ϕ_0 is the initial porosity.

The other element type is interface elements, which represent potential fractures or pre-existing fractures embedded in a portion of the matrix volume. It is assumed that the interface element is positioned at the common boundary of two adjacent cell elements, and one fracture plane cut the element into two parallel plates. The permeability is calculated as the sum of two components:

$$k = k_{\mathrm{matrix}} + k_{\mathrm{fracture}} \tag{7.2}$$

where each component is conditionally calculated based on the fracture activation. If an interface element is yet to be fractured, k_{matrix} is calculated as in Equation (7.1) and $k_{fracture}$ is simply assumed to be zero. On the other hand, if the interface element is fractured, $k_{fracture}$ will be predominant to enhance the total permeability, and k_{matrix} is assumed to revert to the initial intrinsic permeability k_0. This conditional expression of the permeability is written as

$$\mathrm{k} = \begin{cases} \mathrm{k}_0 \frac{\phi^3}{(1-\phi)^2} \frac{(1-\phi_0)^2}{{\phi_0}^3}, & \text{if unfractured} \\ \mathrm{k}_0 + \frac{\mathrm{b}^3}{12\mathrm{a}}, & \text{if fractured} \end{cases} \tag{7.3}$$

where a is the element width, and b is the fracture aperture.

For two-phase flow simulations in TOUGH2, we employed a van Genuchten capillary pressure model (van Genuchten, 1980) and a Corey relative permeability model (Corey, 1954), which are both functions of degree of saturation of local elements. Pressure and flow responses observed from the gas injection experiment interpret that gas only flows into the fully saturated specimen at a certain level of gas pressure or above. This conditional gas penetration is implemented by introducing a gas entry pressure with the corresponding residual gas saturation in the capillary pressure function. The van Genuchten capillary pressure model is used to define the water retention curve as

$$\mathrm{P_c(S)} = \mathrm{P'_0}\left([\mathrm{S}^*]^{-1/\lambda} - 1\right)^{1-\lambda} \tag{7.4}$$

with $S^* = (S - S_{lr})/(1 - S_{lr})$. The relevant capillary pressure parameters are adopted for MX80 bentonite (Senger and Marschall, 2008). For fractured elements, the apparent gas entry pressure P'_0 of the element will be scaled by the function of permeability as

$$\mathrm{P'_0} = \mathrm{P_0}\left(\frac{\mathrm{k_0}}{\mathrm{k}}\right)^{1/3} \tag{7.5}$$

The relative permeability-saturation relationships of liquid (k_{rl}) and gaseous (k_{gl}) phases are parameterized using the Corey model as

$$\begin{gathered} \mathrm{k_{rl}(S)} = \hat{\mathrm{S}}^4 \\ \mathrm{k_{rg}(S)} = \mathrm{m_g}\left(1 - \hat{\mathrm{S}}\right)^2\left(1 - \hat{\mathrm{S}}^2\right) \end{gathered} \tag{7.6}$$

where $\hat{S} = (S - S_{lr})/\left(1 - S_{lr} - S_{gr}\right)$ and m_g is a multiplying factor for the enhanced gas permeability. The residual saturations S_{lr} and S_{gr} are provided to limit the mobility of the respective phases, i.e., for both liquid and gaseous phases, their mobilities only in the range of $S = \left[S_{lr}, 1 - S_{gr}\right]$. To avoid unphysical situation with $P_c = \infty$, larger S_{lr} for the relative permeability is usually chosen as compared to S_{lr} for the capillary pressure (Pruess et al., 2012). S_{gr} can be used to define the air entry pressure in the capillary pressure function.

In the mechanical simulations, effective (grain-to-grain) stress $\sigma_n{}'$ is calculated from the pore pressure P based on the linear poro-elasticity theory (Biot and Willis, 1957):

$$\sigma_n{}' = \sigma_n - \alpha P \tag{7.7}$$

where σ_n is the total normal stress obtained from overall loading, including external loads; $P = \max(P_g, P_l)$ is taken as the highest pressure between gas and liquid phases; and α is Biot's effective stress parameter. Note that tensile stress is taken to be positive for the sign convention. Also, the shrinkage/swelling effect due to the local changes of liquid saturations ΔS can be taken into account:

$$\Delta\varepsilon_s = \alpha_s \Delta S \tag{7.8}$$

where ε_s is shrinkage/swelling strain; and α_s is the hydraulic shrinkage coefficient. If a poro-elastic geomaterial is subjected to confinement conditions, the stress due to swelling/shrinkage can be calculated as

$$\Delta\sigma' = \Delta\varepsilon_s \mathrm{E} \tag{7.9}$$

where E is the Young's modulus.

However, the results of the Stage 2 preliminary simulations, conducted in FY18, revealed a substantial discrepancy of simulated and experimental stress-time series data. Instead of using Equation (7.7), we have introduced Bishop's effective stress calculation, where the pore pressure consists of partial contributions of gas and liquid phases:

$$\sigma_n{}' = \sigma_n - P_g + \chi(P_g - P_l) \tag{7.10}$$

where χ is Bishop's coefficient that is dependent on the degree of saturation of a two-phase system. Here, the expression proposed by Khalili and Khabbaz (1998), is used:

$$\chi = \begin{cases} 1 & \text{for } P_g - P_l < P_{ae} \\ \left(\frac{P_g - P_l}{P_{ae}}\right)^{-0.55} & \text{for } P_g - P_l \geq P_{ae} \end{cases} \tag{7.11}$$

where P_{ae} is a gas entry pressure.

The fracture process of a local rigid-body-spring element is simulated by degrading the springs. A fracture event entails a reduction of spring stiffness and a release of the associated elemental forces. For the degraded spring set, the modified stiffness matrix $\mathbf{D'}$ is

$$\mathrm{D}' = (1 - \omega)\mathrm{D} \tag{7.12}$$

where ω is a scalar damage index with a range from 0 (undamaged) to 1 (completely damaged). For brittle fracturing, which is applied to the cases presented in this report, ω is switched from 0 to 1 once a fracture event occurs (i.e., the stress state of an element violates the failure criteria). The stress criticality of a lattice element is calculated as

$$R_f = \sigma_e / \hat{\sigma} \tag{7.13}$$

where σ_e is the element stress state, and $\hat{\sigma}$ is the critical stress defined by failure criterium. In this study, we used the Mohr-Coulomb criterium to determine the failure of lattice elements.

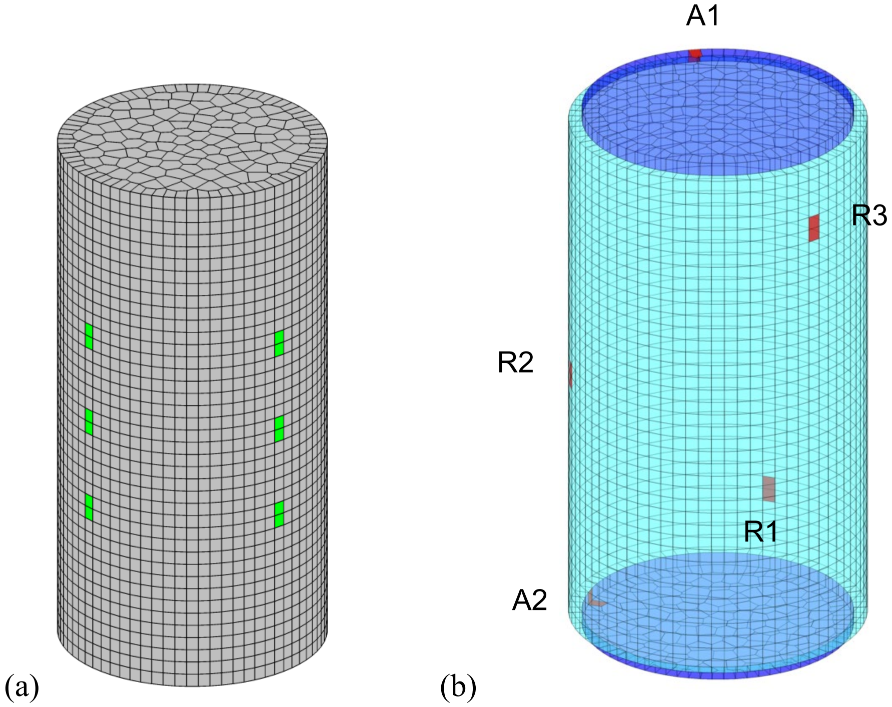

Figure 7-5. 3D Voronoi mesh generation: (a) Mesh discretization of bentonite domain. Six green marks (and six hidden on the other side) indicate the locations of porewater sensors for outflow measurements; and (b) Outer elements are padded for zero-displacement constraints. Red marks indicate the location of load cells, where the local stress values are measured.

For modeling of spherical gas flow in bentonite, we generated a 3D Voronoi mesh of a cylinder with dimensions of 120 mm height and 60 mm diameter, which is composed of 7,856 Voronoi cells and 33,316 element connections (Figure 7-5). Additional padding elements are placed on the axial ends and the circumferential surface to provide a constant volume boundary condition (zero-displacement constraints). Initial mechanical confinement is assumed with the axial stress of 7.25 MPa, the radial stress of 7.75 MP in the sample, and the initial pore pressure of 1 MPa is given for a fully water-saturated state. While the padding elements surrounding the sample domain are hydrologically constrained, a fully gas-saturated element with 168 ml of volume represents the injection system, which is directly connected to the center of the sample domain. A constant injection rate of 2.75×10^{-9} m^3/s at STP is maintained throughout the simulation. Elements at 12 locations on the circumferential surface of the sample, indicated by green marks in Figure 7-5a, are connected to the backpressure boundary element with a constant 1 MPa pressure. Outflow values are measured at the connections between those circumferential elements and the backpressure boundary element. Reactions are measured at the constrained padding elements to derive stress values, which are coloured in red in Figure 7-5b.

Model parameters are listed in Table 7-1. The current TOUGH-RBSN model includes all the baseline parameters conforming to the values suggested from the DECOVALEX Task A coordinator from BGS. Pre-calibration processes have been performed to match the experimental data, and the calibrated parameters are given in the notes of Table 7-1.

Table 7-1 Material parameters for TOUGH-RBSN 1D modeling of gas flow through MX-80 bentonite samples.

	Meaning	Symbol [units]	Value
Basic reference values	Young's modulus	E [MPa]	307
	Poisson's ratio	ν [-]	0.4
	Porosity	ϕ_0 [-]	0.44
	Intrinsic permeability	k_0 [m^2]	3.4×10^{-21}
HM coupling parameters	Pore compressibility[1]	c_p [Pa^{-1}]	4.44×10^{-9}
	Biot's coefficient	α_p [-]	1
	Swelling coefficient	α_s [-]	0.0
Mohr-Coulomb failure criterion[2]	Tensile strength	f_t [MPa]	0.001
	Cohesive strength	c [MPa]	0.04
	Internal friction angle	β [deg.]	4.5
van Genuchten capillary pressure model[3]	Apparent gas entry pressure	P_0 [MPa]	18
	Residual liquid saturation	S_{lr} [-]	0.01
	Shape factor	λ [-]	0.45
Corey relative permeability	Residual liquid saturation	S_{lr} [-]	0.8
	Residual gas saturation[4]	S_{gr} [-]	0.0709
	Enhancement factor for k_{rg}	m_g [-]	1

Note:

[1] The pore compressibility is analytically derived from the bulk modulus K: $c_p = \frac{1}{K\phi} = \frac{3(1-2\nu)}{E\phi}$.

[2] The strength parameters are set to match the timing of fracture initiation and gas breakthrough.

[3] The parameters are adopted from Senger and Marchall (2008).

[4] S_{gr}= 0.0709 corresponds to the air-entry pressure P_{ae}= 7 MPa, which is the pressure difference between injection and backpressure points at the breakthrough.

Figure 7-6 presents the injection pressure evolution compared to the experimental result. With a constant injection rate, the pressure of the injection boundary element develops with a decent agreement with the experimental curve up to the peak, and the timing and the level of the peak pressure are comparable to the experimental results. Though the simulation does not demonstrate the multiple pressure drops around the peak in the experiment, the simulated pressure in the post-peak region has similar trend of decrease, and the final pressure is comparable to the pressure evolution in the experiment.

Figure 7-7 shows inflow and outflow rates through the sample. Inflow rate was gradually increasing starting from about 745 days, when the initial gas entry occurred, and then around 761 days jumped to match the level of the injection rate, which implies the gas breakthrough. About one day after the inflow rate jumped, the gas breakthrough affected the flow response through radial pore water arrays. In the experiment, only one radial array took a dominant outflow in concordance with the inflow rate, whereas the simulation exhibits lower outflow rates for all three radial arrays. Multiple lower outflow rates with no dominant flow direction indicate that the inflow diverges to multiple outflows connected through the fractures. For that reason, we plotted the total outflow rate combining the three outflow rates at the radial arrays. Figure 7-8 presents the total gas volume within the sample, which is derived by cumulative integration of flow rates over time. Gas volume suddenly increases and soon levels off at the breakthrough, and then levels up to the end of simulation.

Figure 7-9 shows the stress evolutions measured at the locations of load cells. The stress measurements are well fitted with the experimental data prior to the gas breakthrough, but the increase of stresses looks steep after the breakthrough. Moreover, the simulated stress evolutions plateau out after the gas breakthrough while the experiment exhibits a gradual attenuation of stress measurements to the end. The results can interpret that a new approach with Bishop's equation for the effective stress calculation works well before discrete fractures occur, but it needs to be improved to model the two-phase pressure in the fractured elements.

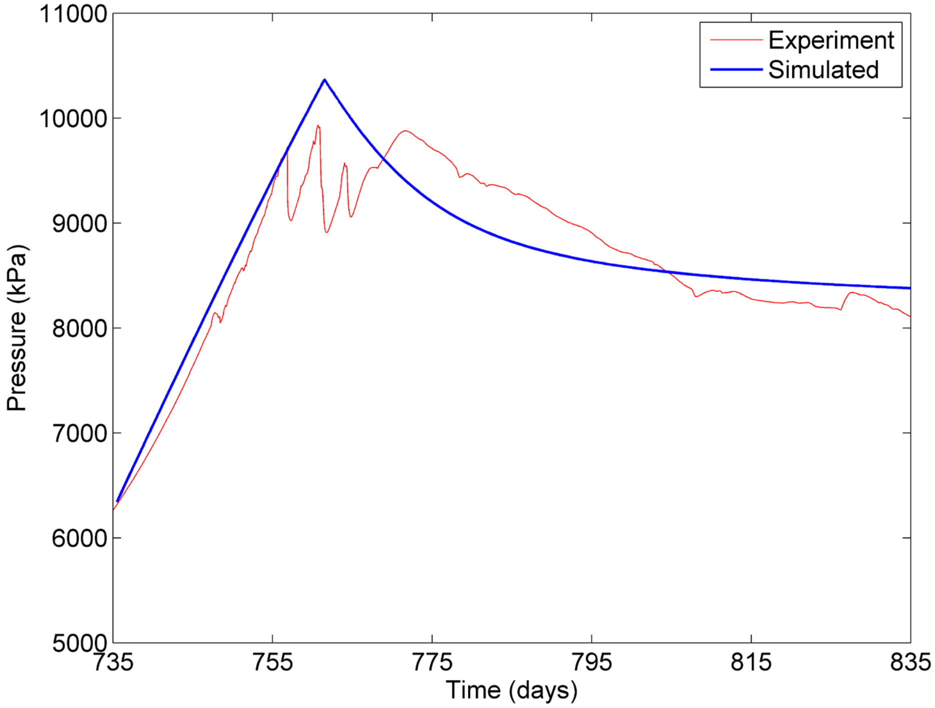

Figure 7-6. Comparison of simulated and experimental injection pressure trends.

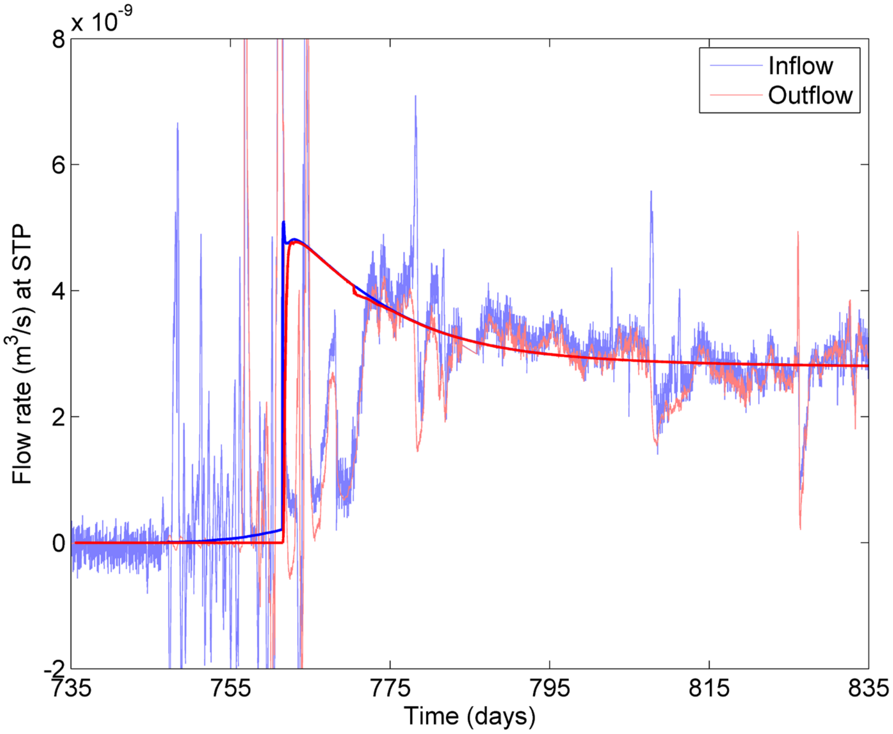

Figure 7-7. Comparison of simulated and experimental flow rate evolutions.

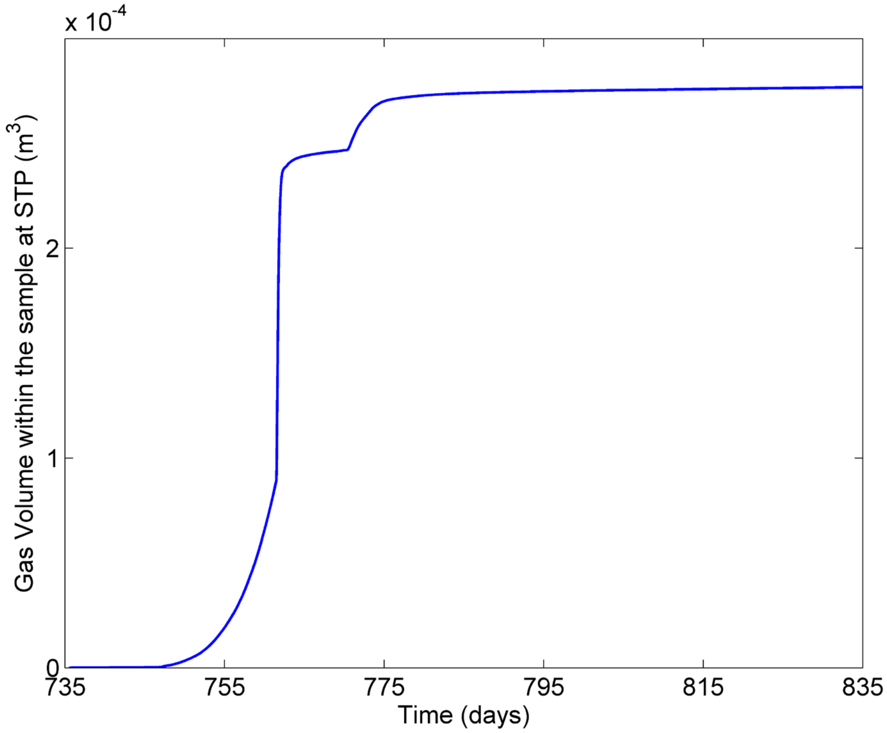

Figure 7-8. Cumulative total gas volume within the sample in the simulation.

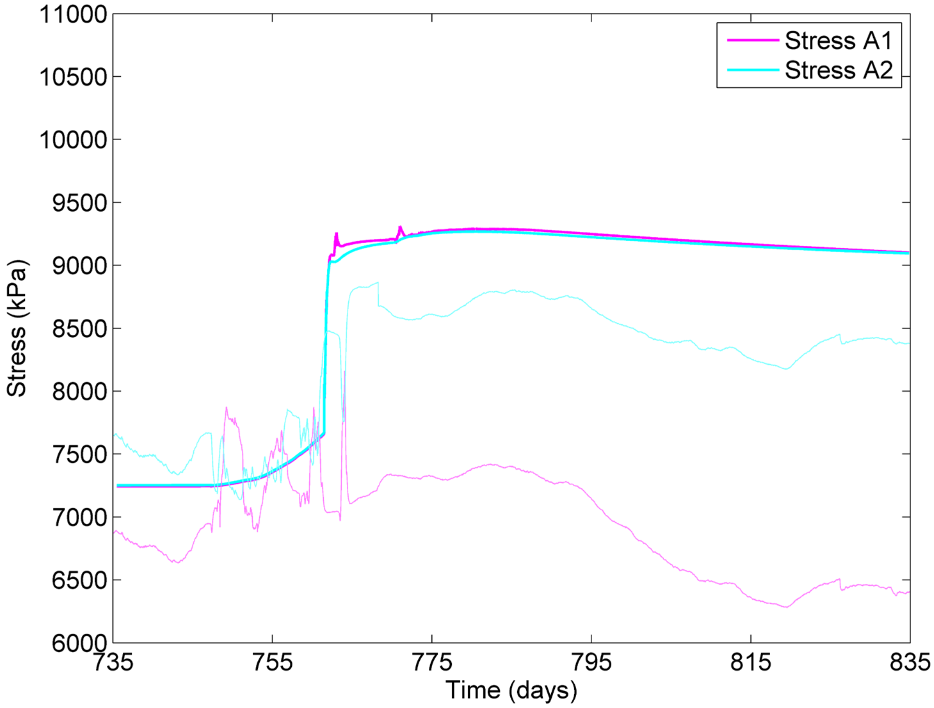

(a)

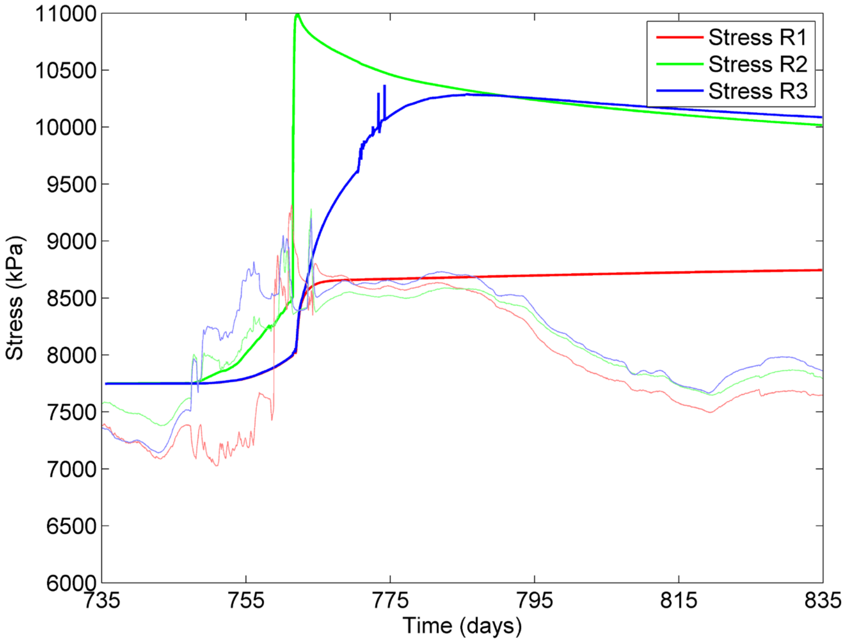

(b)

Figure 7-9. Comparison of trends of simulations and experimental data: of (a) axial stress, and (b) radial stress trends in the experiment and the simulation.

Figure 7-10 shows snapshots of fracture development during gas injection. Fractures are initiated at the center of the sample, where the gas injection occurs. Then, the main fracture cluster grows into a spherical shape toward the lateral surface of the sample. After the fracture cluster reaches the lateral surface, near-surface fractures propagate in the longitudinal direction. These non-uniform fracture patterns form a heterogeneous enhanced permeability domain within the sample, where preferential flow paths would be generated.

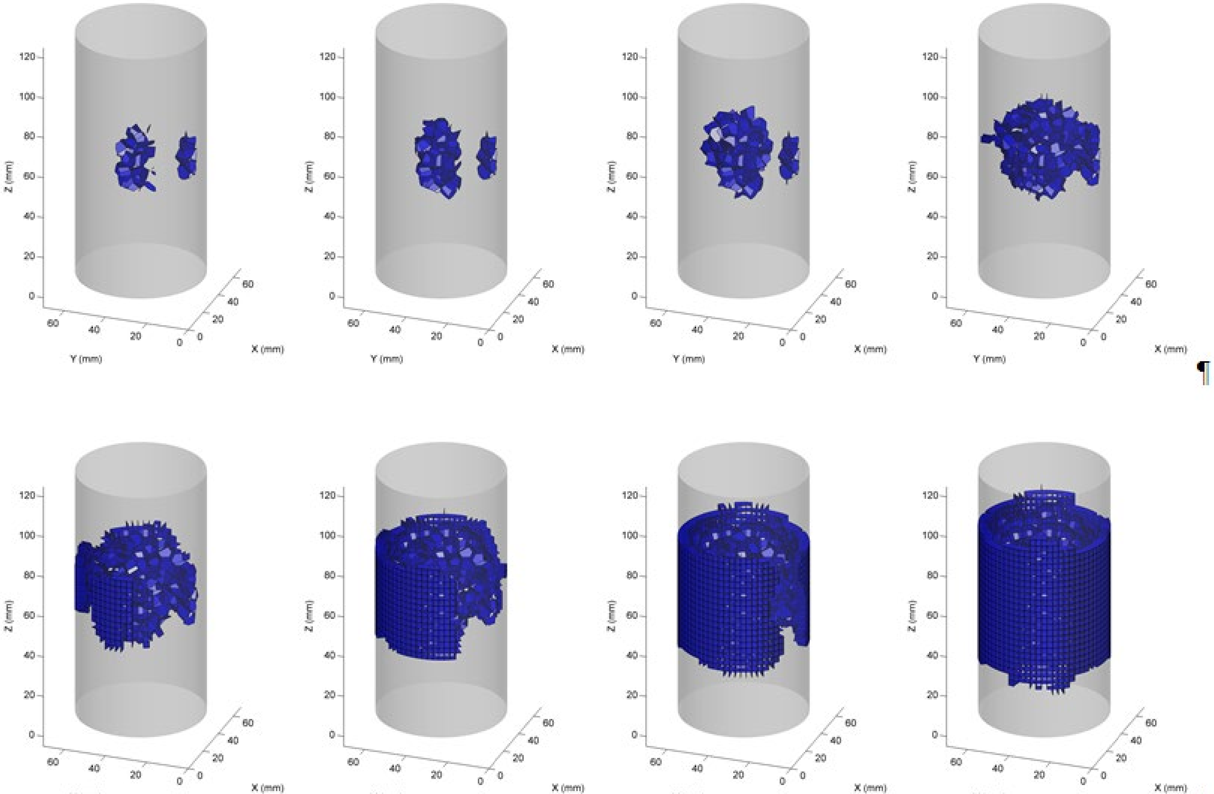

Figure 7-10. Non-uniform fracture development in the 3D (spherical) gas breakthrough.

This DECOVALEX-2019 Task A is now completed with continuation in DECOVALEX-2023 that will involve modelling of the Large-Scale Gas Injection Test (Lasgit) conducted at the Äspö Hard Rock Laboratory in Sweden.

8. PORE-SCALE MODELING OF TWO-PHASE FLOW IN ROUGH FRACTURES

8.1 Introduction

Investigating two-phase flow in fractured porous media is of importance to various subsurface practices. In nuclear waste disposal systems, transport of gases that can be produced by metal corrosion (Xu et al., 2008), radiolysis (Christensen and Sunder, 2000) and microbial activities (Pedersen, 1999) may have large impacts on their long-term performances (Birkholzer et al., 2012; Claret et al., 2018; Tsang et al., 2015). Migration of the gas-water interfaces is also an important mechanism for the transport of radionuclides due to their preferential sorption on the interfaces (Wan and Wilson, 1994). In addition, local pressure build-up due to gas production and accumulation can trigger mechanical responses including fracturing (Kim et al., 2011), along with processes such as desiccation (Fauchille et al., 2016).

In reservoir scale modeling, two-phase flow in fractures are typically treated using the continuum approach, in which effective parameters such as relative permeabilities are used (Xu et al., 2008). However, this approach may miss important dynamics that arise from the interplay between surface tension, viscous, inertial and buoyancy forces at the micro-scale (Cihan and Corapcioglu, 2008; Berg et al., 2013; Raeini et al., 2014; Armstrong et al., 2015), which is dependent on the fracture morphology.

Direct numerical simulations of microscopic processes that govern two-phase flow in realistic geometries are needed to improve our conceptualization and representation of two-phase flow dynamics in continuum scale simulations. For instance, a new relationship describing pore-throat conductivity for pore network models was developed based on pore-scale simulations (Raeini et al., 2014). Crandall et al (2009a) simulated two-phase flow in porous media, showing results in good agreement with experimental measurements while being able to extend the observations to systems beyond the experimental capability. Using direct numerical simulations, Crandall et al (2009b) investigated two-phase flow in a natural rock fracture, confirming complex dependence of the flow dynamics on fluid properties, flow rate, and fracture geometry. The simulation results were also used to derive a new set of relative permeability curves.

The overall objectives of this study are to investigate the impacts of rough fracture geometries on different two-phase flow scenarios, to relate the microscopic processes and macroscopic properties, and to provide implications for the dynamic evolution of fractures. This chapter reports the results of preliminary investigations using realistic geometries from two fractures and two-fluid systems with different density and viscosity characteristics.

8.2 Methods

8.2.1 Model description

In this study, the traditional mesh-based Computational Fluid Dynamics (CFD) approach is used. The simulations were performed in the open source software package, OpenFOAM (Open Field Operation and Manipulation) (Jasak, 2009) and related open source libraries. For two-phase systems, OpenFOAM implements the volume of fluid (VOF) method, which treats the two phases as an effective single phase when solving the continuity and momentum equations:

$$\nabla \cdot \boldsymbol{U} = 0 \tag{8.1}$$

$$\frac{\partial(\rho\mathbf{U})}{\partial t} + \nabla \cdot (\rho\mathbf{U}\mathbf{U}) = -\nabla p + \mu[\nabla\mathbf{U} + (\nabla\mathbf{U})^{\mathrm{T}}] + \mathbf{F} \tag{8.2}$$

where $\mathbf{F}$ is the body force, e.g., surface tension force, and $\boldsymbol{U}$, ρ and μ are weighted average between the two phases based on the volume fraction of the two phases.

$$\boldsymbol{U} = \alpha \boldsymbol{U_w} + (1-\alpha)\boldsymbol{U_{nw}} \tag{8.3a}$$

$$\rho = \alpha \rho_w + (1-\alpha)\rho_{nw} \tag{8.3b}$$

$$\mu = \alpha \mu_w + (1-\alpha)\mu_{nw} \tag{8.3c}$$

where α is the volume fraction of the wetting phase, and the subscripts *w* and *nw* denote the wetting and non-wetting phase, respectively.

The solver used here is InterGCFoam (https://bitbucket.org/HWUCarbonates/geochemfoam-4.0). It builds upon the OpenFOAM solver interFoam, and implements a modified version of the algorithm developed by Raeini et al. (2012) to sharpen the volume fraction field in the calculation of the surface tension force (Maes, 2018). This algorithm is referred to as the algebraic VOF, because the interface is not explicitly reconstructed from the volume fraction field. The transport of volume fraction field is solved from the advection equation given by

$$\frac{\partial \alpha}{\partial t} + \nabla \cdot (\alpha \mathbf{U}) = 0 \tag{8.4}$$

In interfoam, the multidimensional universal limiter with explicit solution (MULES) scheme was used to compress the interface. The transport equation is given as

$$\frac{\partial \alpha}{\partial t} + \nabla \cdot (\alpha \mathbf{U}) + \nabla \cdot (\alpha(1-\alpha)\mathbf{U_r}) = 0 \tag{8.5}$$

where $\mathbf{U_r}$ is the compression velocity defined as the velocity difference between the wetting phase and non-wetting phase, and the additional term in Equation (8.5) ensures a sharper interface.

To further reduce spurious velocity that arises from local force imbalance, a series of filtering processes were added into interGCFoam. First, the volume fraction field is smoothed by recursively interpolating it between cell centers and face centers:

$$\alpha_{s,i+1} = C_{SK}\langle\langle\alpha_{s,i}\rangle_{c\to f}\rangle_{f\to c} + (1-C_{SK})\alpha_{s,i},\ \alpha_{s,0} = \alpha \tag{8.6}$$

where the subscript i is the number of iterations, and $\mathrm{C_{SK}}$ is a coefficient between 0 and 1.

Normal vector ($\boldsymbol{n_I}$) of the interface is then calculated based on the smoothed volume fraction field α_s and is given by

$$\boldsymbol{n_I} = \frac{\nabla\alpha_s}{|\nabla\alpha_s|} \tag{8.7}$$

The curvature (κ) and the surface tension force at the face centers ($f_{c,f}$) are given by

$$\kappa = \nabla \cdot (\boldsymbol{n_I}) + \boldsymbol{n_I}\nabla(\langle\boldsymbol{n_I}\rangle_{c\to f})\boldsymbol{n_I} \tag{8.8}$$

$$f_{c,f} = \sigma\langle\kappa\rangle_{c\to f}\delta_{pc} \tag{8.9}$$

where σ is the surface tension, and the delta function (δ_{pc}) is formulated based on a modified volume fraction field that is curtailed and rescaled using the coefficient C_{PC}, which is between 0 and 1:

$$\delta_{pc} = \nabla\alpha_{pc} = \nabla\left\{\frac{1}{1-C_{PC}}\left[\min\left(\max\left(\alpha, \frac{C_{PC}}{2}\right), 1-\frac{C_{PC}}{2}\right) - \frac{C_{PC}}{2}\right]\right\} \tag{8.10}$$

To eliminate non-physical velocities parallel to the fluid interface, the components of the surface tension force that are parallel to the fluid interface are filtered:

$$f_{c,f,filtered} = f_{c,f} - f_{c,f,filt\parallel} \tag{8.11}$$

$$\nabla \cdot \nabla P_c = \nabla \cdot f_{c,f,filtered} \tag{8.12}$$

$$f_{c,f,filt\parallel} = \frac{\delta_{pc}}{\delta_{pc}+\epsilon}\left(C_{filt,relax}f_{c,f,filt\parallel}^{old} + C_{filt}\langle\nabla P_c - (\nabla P_c \cdot \boldsymbol{n_I})\boldsymbol{n_I}\rangle_{c\to f}\boldsymbol{n_I}\right) \tag{8.13}$$

where ϵ is a constant on the order of 10^{-4}, $C_{filt,relax}$ and C_{filt} are coefficients between 0 and 1, and P_c is the capillary pressure. The value of $f_{c,f,filt\parallel}$ starts with zero, and the filtering process stops when the components of dynamic capillary force parallel to the fluid interface converges to zero.

The capillary flux (ϕ_c) is further filtered to remove non-physical fluxes:

$$\phi_c = |\boldsymbol{S}|(f_{c,f} - \nabla P_c) \tag{8.14}$$

$$\phi_{c,filtered} = \phi_c - \min(\max(\phi_c, \phi_{c,thresh}), \phi_{c,thresh}) \tag{8.15}$$

$$\phi_{c,thresh} = C_{\phi,filt}|f_{c,f}|_{avg}|\boldsymbol{S}| \tag{8.16}$$

where $C_{\phi,filt}$ is a user specified coefficient, and $\boldsymbol{S}$ is the vector area of a face.

In capillary dominated regime, additional filtering based on the capillary pressure gradient is performed as follows.

$$\phi_{c,thresh} = 1.5 \iint \langle\langle \nabla P_c \rangle_{c\to f}\rangle_{f\to c} \cdot \langle \boldsymbol{n_I} \rangle_{c\to f} \tag{8.17}$$

$$\phi_{c,gPc_{corr}} = \min(\max(\phi_{c,filtered}, \phi_{c,thresh}), \phi_{c,thresh}) \tag{8.18}$$

8.2.2 Fracture geometries and meshing

The fracture geometries used in the simulations are from two previous experimental studies using fracture core samples from the Amherstburg formation (Ellis et al., 2011) and the Duperow formation (Ajo-Franklin et al., 2017), respectively. It should be noted although these two formations are not argillite and rich in carbonates, the investigation of the impacts of realistic fracture roughness on two-phase flow phenomena should be broadly applicable to different systems. Two 4.6 mm long and 2.7 mm wide subsections were selected from the Amherstburg fracture (Figure 8-1 (a)&(b)), which was imaged with a resolution of 27 µm. Another subsection (Figure 8-1 (c)) with a length of 1.7 mm and a width of 0.8 mm was selected from the Duperow fracture. The Duperow fracture has large aperture contrast and the original resolution of xCT images is 6.75 µm.

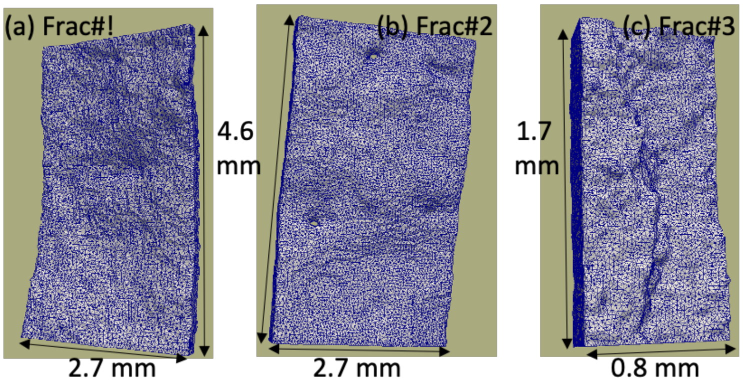

Figure 8-1. Unstructured tetrahedral meshes of the three fracture geometries used in the two-phase simulation. (a) and (b) are from the Amherstburg fracture (Ellis et al., 2011), and (c) is from the Duperow fracture (Ajo-Franklin et al., 2017).

Unistructural tetrahedral meshes were generated for the three fracture geometries using an open source 3D volumetric mesh generator iso2mesh (Fang et al., 2009). To preserve the fracture morphology, minimal smoothing and simplifications were applied in generating the surface meshes. Parameters used to generate the volume meshes were optimized to ensure good mesh quality, as quantified by the *checkmesh* utility in OpenFOAM, and numerical performance.

8.2.3 Simulation setup

Two-fluid systems were simulated, to capture variations in density and viscosity that can be expected in natural and engineered systems. The fluid properties and interfacial properties of the air-water system and the $scCO_2$-brine system are summarized in Table 8-1. A flow velocity of 0.01 m/s is used in all simulations.

Table 8-1. Parameters used in the simulations of two-fluid systems (Wang et al., 2016).

Property	**air-water system**	**$scCO_2$-brine system**
Density, wetting phase	998 kg/m^3	1034 kg/m^3
Kinematic viscosity, wetting phase	9.4e-7 m^2/s	6.4e-7 m^2/s
Density, non-wetting phase	1.2 kg/m^3	658 kg/m^3
Kinematic viscosity, non-wetting phase	1.5e-5 m^2/s	7.75e-8 m^2/s
Surface tension	0.072 N/m	0.03 N/m
Contact angle (on carbonate)	30°	70°

The boundary conditions are summarized in Table 8-2.

Table 8-2. Boundary conditions used for the simulations.

Boundary Condition	**Velocity [m/s]**	**Pressure [Pa]**	**Volume fraction of water**
Inlet	Uniform fixed value	zeroGradient	Uniform fixed value
Outlet	zeroGradient	Uniform fixed value	zeroGradient
fractureWalls	noSlip	zeroGradient	Constant contact angle

For the simulations, the numerical scheme *cellMDLimited leastSquares 1.0* is used for the gradient terms, *Gauss linear limited 0.5* is used for the Laplacian terms, *Gauss vanLeer* is used for the divergence terms of the volume fraction, and *Gauss linearUpwind grad(U)* is used for the divergence terms of velocity. The numerical scheme for the surface gradient is set to *limited 0.5* because of the complex geometry. The solver and coefficient information are summarized in Tables 8-3 and 8-4, respectively.

Table 8-3. Solver setup for interGCFoam.

	Pcorr	**P**	**U (laminar)**
Solver	GAMG	GAMG	BiCGStab
preconditioner	GaussSeidel	GaussSeidel	DILU
Tolerance	1e-8	1e-7	1e-6
relTol	1e-5	1e-3	1e-3

Table 8-4. Filtering coefficients.

coefficients	**values**
C_{SK}	0.1
Number of smoothing	1
C_{PC}	0.1
C_{filt}	0.1
$C_{filt,relax}$	0.999
$C_{\phi,filt}$	0.01

8.3 Results

Overall, without large aperture contrast, the displacement front, i.e. the non-wetting and wetting phase interface, is relatively blunt (Figure 8-2 (b)&(c) and Figure 8-3(b)). The wetting phase (water and brine) is displaced with a small amount remain in the fracture. For the air-water system, in which the contact angle is smaller and thus is more wetting, the residual water content is slightly higher with more water trapped in local rough spots and at the two sides of the fractures (Figure 8-2(c)). In these cases, there is no clear correlation between the aperture map (Figure 8-2(a), Figure 8-3(a)) and the spatial distribution of the wetting and non-wetting phases (Figure 8-2(b) & (c), Figure 8-3(b)).

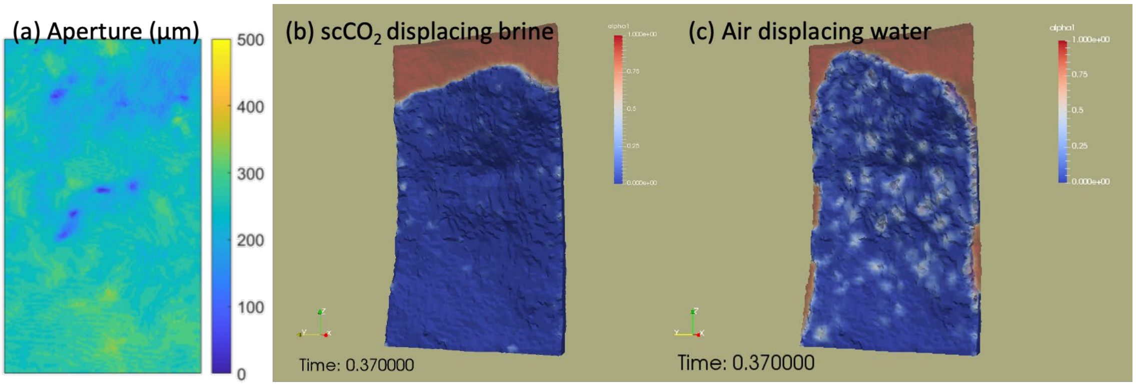

Figure 8-2. (a) 2D projection of the fracture aperture on the fracture plane for Frac#1, (b) and (c) are the spatial distribution of the volume fraction of the wetting phase (α, e.g. eqn(3)) after 0.37 seconds in the scCO$_2$-brine and air-water system, respectively. The invading non-wetting phase is shown in blue with $\alpha = 0$ and the wetting phase being displaced is shown in red with $\alpha = 1$. α values between 0 and 1 indicate the interface or local trapped residuals.

On the contrary, when the fracture aperture has large contrast and strong spatial correlation, i.e. well-connected patterns such as a channel (Figure 8-3(c)), the invading non-wetting phase flows through the fracture preferentially through the channel, whereas the wetting phase remain in the small aperture region. As a result, the residual water content is higher. However, mineral reactions that may occur in the region occupied by the aqueous phase is not expected to alter the fracture significantly even though the amount of aqueous phase is considerable if the aqueous phase remain disconnected as shown in the figure.

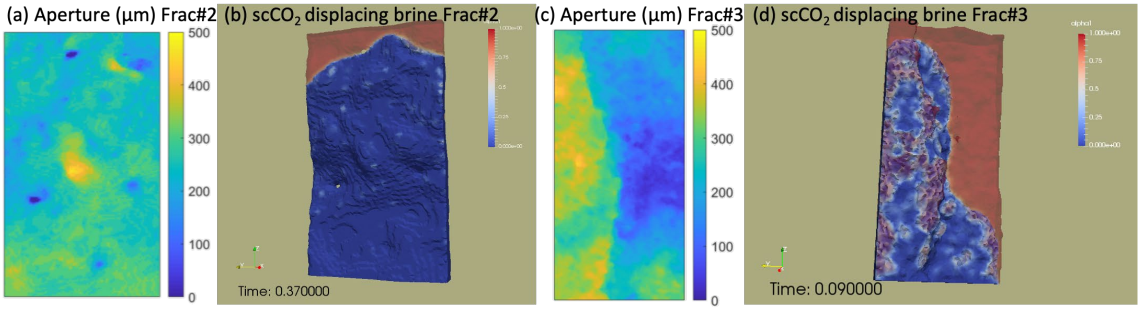

Figure 8-3. (a) and (b) 2D aperture map and spatial distribution of two phases in Frac#2 after 0.37 seconds, and (c) and (d) 2D aperture map and spatial distribution of two phases after 0.09 seconds of injection in Frac#3.

Under the scenario when a mixture of the two-fluid phases (50% each) is injected, the two immiscible fluids occupy different parts of the fracture as the mixture goes through. Without large aperture contrast, the aqueous phase flows through the fracture and is contact with the fracture surface almost equally (Figure 8-4(a)). As such, any reactions between the aqueous phase and the mineral phases and resulting fracture opening are likely to be uniform. With the large aperture contrast, the non-wetting phase again preferentially flows through the large aperture channel (Figure 8-4b). As shown in Equations (8-2) and (8-5), the two-phase flow dynamics are dependent on the macroscopic flow conditions (i.e., pressure gradient or bulk velocity), fluid properties (e.g., viscosity), and the interfacial tension force that is dependent on the surface tension and local geometry or roughness. These factors are explicitly accounted for, and the preferential flow of non-wetting phase in the large aperture channel is primarily a result of locally stronger capillary force in the small aperture regions. In this case, the aqueous phase may interact with the mineral phases and lead to continuous enlargement of the small aperture region. This is consistent with previous experimental observations that in presence of two-phase flow, self-organization phenomena such as worm holing in porous media that is observed in single phase system is suppressed (Ott et al., 2015).

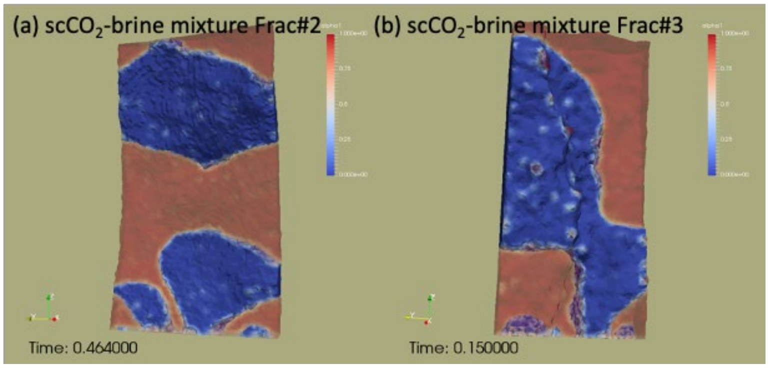

Figure 8-4. Spatial distribution of the two-fluid phases in the Frac#2 (a) and Frac#3 (b), when a mixture is injected.

8.4 Summary and future work

In this report, pore-scale two-phase flow simulations were performed in three real realistic fracture geometries in two-fluid systems. The simulation results showed uniform displacement of the wetting phase when the fracture aperture variations are relatively small and have no strong spatial correlation. In contrast, with large aperture contrast and spatial correlation, the non-wetting fluid phase flows preferentially through the connected large aperture channel. In reactive systems, these spatial patterns will impact the reactions and the dynamic evolution of the fracture. For instance, in the mixture injection scenario, positive feedback between flow and reaction that typically results in wormholing or channelization will be suppressed in the two-phase system. Further simulations will be performed to quantify the interface velocity and macroscopic properties such as saturation, relative permeability, etc. These results will be compared with those from other reservoir scale continuum simulations to improve representation of two-phase flow in fractures.

9. SHORT- TO LONG-TERM HYDROMECHANICAL RESPONSE OF FAULTS AND EDZ IN ARGILLITE HOST ROCK

9.1 Introduction

Repository-induced effects such as creation of an Excavation Damage Zone (EDZ), gas generation and thermally-induced pore pressure perturbations may result in the reactivation of pre-existing features (fractures, faults or bedding planes) within the host rock and consequent permeability increase. Understanding such reactivation due to pressure and stress changes, the possible formation of permeable pathways, and their potential long-term sealing is critical in assessing the performance of radioactive waste repositories in shale formations. In 2015, a fault activation experiment was conducted by injecting high-pressure synthetic pore water in a fault zone intersecting the Opalinus Clay formation at 300 m depth in the Mont Terri URL (Switzerland). In 2018, a new experiment started with the permanent installation of a new sensor to monitor long term coupled fault pore pressure and three-dimensional displacements. Key concluding points from these experiments are:

- Complex opening and slip was measured on the fault,
- High transmissivity flow paths developed at least temporarily and "local" (~meters) to the injection under high pressure injection,
- When injection pressures dropped, the feature apparently closed, but, since 2015, the pressure in the ruptured patch did not recover, remaining ~0.45 MPa below its initial value.

In 2019, significant pore pressure changes coupled to fault displacements were triggered by ongoing excavation work for a new Mont Terri gallery ~40 to 50 m away from the fault, at distances significantly further than a few tunnel diameters.

In this chapter we firstly present a bibliographic review of fault activation and potential for self-sealing in argillite host rock. Secondly, we show the results of integration of different types of continuous observations to analyze remote fault activation induced by the excavation of a new Mont Terri gallery in 2018. It is also the opportunity to demonstrate the capabilities of the permanent SIMFIP probe set across the fault. The SIMFIP has been used to monitor continuously the fault movements since October 2018. The concept of this new monitoring instrument has been developed and deployed in the field within the frame of this project with the idea to capture high resolution signals that can provide the information on the fault hydromechanical evolution in host rocks. Thirdly, we present the results of 3D fully coupled numerical modeling in 3DEC of experiments at Mont Terri. Different mechanisms of fault hydraulic transmissivity evolution are tested to analyze the field measurements related to a fault over-pressurization. We propose a conceptual model typical to analyze the evolution of low permeability faulted host rocks. Finally, we discuss the short- to long-term response of the Mont Terri fault to various loadings that occurred during the 2015 - 2020 period, including artificial fluid injections in the fault and gallery excavations remote from the fault. We show that shear is a necessary mechanism for fluids to circulate in the fault, and, with this 5-year continuous observations of fault pore pressures, we discuss whether or not self-sealing may have occurred following the activation periods.

Review of previous research on fault activation and sealing

9.1.1 Activation mechanisms and their effects on fault hydraulic conductivity

Faults zones affecting host rocks or cap rocks contain “scaly” fabric that is an anastomosing network of polished surfaces where clay rich rock split into progressively smaller flakes (Vannucchi, 2020). Scaly fabric is organized into lenses and preferentially observed in phyllosilicate-rich rocks. It may influence multiple modes of slip, from creep to tremor to seismic slip. It is a macroscopic, multi-scale structure that has, to date, been impossible to create under laboratory conditions. Hydromechanical tests conducted in mesoscale experiments showed significant differences in the hydromechanical response of scaly fabric lenses compared to individual fault shear planes (Guglielmi et al., 2016). Pressurization of scaly clay lenses produces complex slip on multiple planes but no significant leakage even at high pressure levels close to the fracturing pressure. Macroscopic natural planes such as principal or secondary shear planes in fault zones all display about the same hydromechanical behavior, which is characterized by a sudden increase in leakage from zero to several liters per minute when the injection pressure reaches the fault normal stress (i.e., the clamping stress). Thus, although permeability of inactive fault zones in clay is close to the intact rock’s one, these faults may display a highly heterogeneous dynamic hydromechanical response to pore pressure variations. Scaly clay lenses inside clay fault cores may inhibit leakage, significantly reduce the fault zone’s Young modulus by a factor of ~10 compared to the intact rock, and to reduce the transverse anisotropy often related to bedding planes in the host rock (Jeanne et al., 2017). In Mont Terri shales, fault permeability sudden increases by a factor of 10-to-100 were observed during periods of pressure increase above the Fault Opening Pressure (Guglielmi et al., 2016). We also found that these large hydraulic pathways apparently almost fully close when fault is depressurized.

In the FS-Experiment (Guglielmi et al., 2016) significant permeability enhancement is associated with a significant normal opening of the fault features in the injection interval although some shear movement is also measured. Observations in the EDZ commonly show that extensile fracturing triggers permeable features at both the Bure URL (Armand et al., 2014) and Mont Terri (Lanyon et al. 2014). Thermal pressurisation may also result in tensile fracturing and an eventual permeability increase (Li & Wong, 2016), although this was not observed in heating experiments at Bure (Armand et al. 2017). Away from EDZ, elevated pore pressures due to repository-induced gas or temperature effects and consequent reduction of effective normal stresses on faults may also cause dilation. This might dissipate over long time scales by pressure diffusion inducing the long-term recovery in effective stress and reloading of the fracture). Normal stress reloading as a sealing mechanism was observed at laboratory scale (Cuss et al. 2011, Zhang 2013, 2017) and in URL tests (Meier et al. 2002, de la Vaissiere 2014, 2015). Zhang (2013) has suggested a general exponential closure law for permeability reduction on reloading. In addition to the effects of increased normal stress, other sealing mechanisms such as swelling and disaggregation mechanisms may reduce the fault permeability. To our knowledge, there is no clear information on the sealing potential of a thick fault zone that experienced a dilatant activation associated with an over-pressure event.

In the laboratory, shear deformation of clay fractures at sufficiently high normal stress, may initially increase permeability but finally results in sealing (Cuss et al., 2011; 2013; 2014). Fang et al. (2017) proposed a conceptual model where in clay-rich material with weak/ductile fracture walls, when shearing, the soft minerals readily deform and comminute into smaller particles and fill the trough and water infiltration causes clay swelling leading to a thin layer of clay-rich foliage that seals the fracture. At larger scale at the Bure URL, Armand et al. (2014) provided complex observations on shear fractures hydraulic conductivity at about 2 radii from the tunnel axis. Some shear fractures could not be impregnated with resin despite relatively large overpressure. These fractures showed hydraulic conductivity values similar to undisturbed or slightly disturbed rock mass conditions. Nevertheless, they also observed more open shear fractures (i.e. resin-impregnated) as splays to the extension fractures and at the boundary of the zone of extension fractures. They concluded that significant permeability was only associated with zones including extension fractures. The information is of importance when considering that a fault is a zone which reactivates in a complex mixed mode, thus involving the creation of a combination of shear and tensile fractures (Guglielmi et al., 2020a).

9.1.2 Reactivated fault long-term evolution and self-sealing.

In a review of fault sealing behaviour in siliciclastic rocks, Pei et al (2015) identified different processes of fault sealing: clay/phyllosilicate smearing, cementation, cataclasis, diffusive mass transfer by pressure solution or quartz cementation and porosity reduction by disaggregation and mixing. These different processes may occur individually during deformation or may be combined. Clay/phyllosilicate smearing is the most relevant process to self-sealing. The Shale Gouge Ratio (SGR) (Yielding et al., 1997) is defined to estimate the clay content and used as a proxy to estimate the self-sealing potential of faults affecting siliciclastic rocks. Overall, there is good supporting evidence for the use of index such as the SGR as a predictor of fault seal, but field testing and detailed studies of the fault structure in shale-rich host rocks are still lacking to build confidence in any application in the absence of strong “hydrogeological“ evidence (such as pressure or fluid contrasts). Detecting a fault hydraulic conductivity variation in a shaly host rock is a challenge that requires also the development of new types of monitoring instrumentation.

Where a fault has been reactivated by repository-induced effects, the key parameters controlling self-sealing will be the local clay content, and effective stress. It may be highly difficult to use the SGR given the intrinsically high content of shales in the fault materials, and the poor contrast with the clay content in the intact rock. The thresholds might be very difficult to define compared to faults in siliciclastic rocks. In addition, any fractures in a thick fault zone might not seal. It is observed in Mont Terri Main fault that the fault zone contains lenses of scaly clay intercalated with intact rock and fractured damage zones. Fault zones are highly heterogeneous at the macroscale, and the continuity of the scaly clay lenses is not proven, resulting in an eventual increase in fault permeability. A further concern is the potential for stress heterogeneity around faults caused by mechanical property contrasts, slip on discontinuities or injection and production activities. Such effects are likely to be of most significance in brittle formations, but may increase uncertainty on the effective stress acting on the fault. Indeed, slight 10-20°rotations and variations of principal stresses ranging from 0.5 MPa to1 MPa were estimated depending on the tested intervals in and around the Mont Terri Main Fault during the FS tests (Guglielmi et al., 2016; 2020b). It was observed that these stress differences could partly explain the measured fault leakage pressures.

9.2 Continuous monitoring of the Mt Terri fault hydromechanical response to a remote gallery excavation

In 2018, a SIMFIP probe has been designed for long term monitoring of fault hydromechanical variations with an application to the detection of the potential leakage through a low permeability faulted caprock or hostrock. This probe prototype was installed into a vertical borehole drilled across the Main Fault at the Mont Terri URL. Key objective is to image the evolution of leakage in the fault during fault activation, and how fault can eventually seal long after activation. Here we report on the SIMFIP monitoring from its installation in October 2018 until April 2020. We discuss the effects of a stress variation induced by the excavation of a new gallery in the Mt Terri laboratory 30-to-50m away from the SIMFIP. We compare the SIMFIP three-dimensional displacement measurements with uniaxial displacements distributed in a nearby borehole. This allows us to *in situ* “calibrate” the SIMFIP instrument and to characterize the effects of a remote stress variation on a fault activation in a host rock analogue. Results are of importance since the fault activation is clearly identified while the excavation front is located several gallery diameters away from the fault.

9.2.1 SIMFIP installation at Mont Terri

The SIMFIP probe has been installed in a vertical borehole at a depth of 22 m below the galleries. It is straddling the entire fault thickness (Figure 9-1a-d). In details (Figure 9-1b,c), the fault contains complex geological structures characterized by (i) a high density of fractures with orientations mainly ranging from N30 to N70, dipping 20 to 60° SE, and by (ii) thick lenses of 'scaly' fabric where the rock splits progressively into smaller fish-like flakes. The fault zone is bounded by two major fault planes, respectively at 21.15 and 26.15 m (Figure 9-1c).

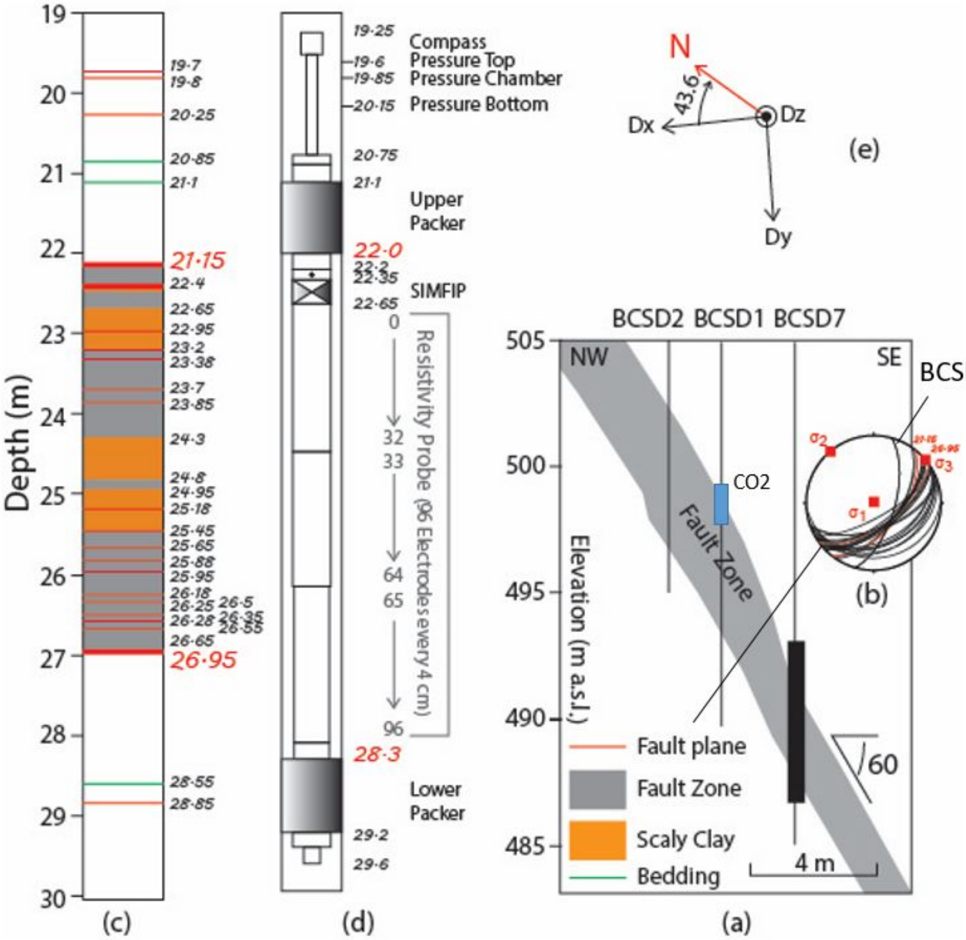

Figure 9-1. (a) SIMFIP probe installation across the Mt-Terri Main Fault (black rectangle in borehole BCSD7). Blue rectangle in borehole BCSD1 is the zone where the gaseous CO_2 dissolved in water is injected. Borehole BCSD5, which is projected on this cross section, is hosting a distributed extensometer that monitors displacements across the fault zone and in the intact rock. (b) Stereographic projection of the Main Fault fractures (the commonly used Mt-Terri state of stress is plotted in red). (c) Detailed log of the borehole Main Fault structures. (d) Plan of the SIMFIP probe. (e) Orientation of the relative displacements (D_x, D_y, D_z) of the upper packer (the lower packer is fixed).

In order to monitor the hydromechanical behavior of the entire fault zone, a 6.3m long SIMFIP interval was designed, sealed by two 0.9 m long inflatable packers (Figure 9-1d). In this configuration, the SIMFIP sensor is measuring the relative displacement of the upper packer, the lower packer considered fixed. Thus, the packers play two roles, sealing the interval to isolate fault zone pore pressure variations and anchoring the SIMFIP to measure the displacement of the fault hanging wall relative to the foot wall. A compass set above the upper packer allows orienting the displacement measurements. Borehole pressures are monitored below the lower packer (Pressure bottom), between the packers (Pressure chamber) and above the upper packer (Pressure Top). Finally, water resistivity electrodes were distributed every 4 cm along the entire length of the SIMFIP chamber in order to localize where eventual leaks could occur from the fault zone into the borehole. We assume that, for example, dissolved CO_2 leak would change the formation water resistivity enough to be detected by the resistivity probe.

9.2.2 Overview of the October 2018 to April 2020 monitoring results

The SIMFIP probe was installed in the borehole immediately after drilling. Figure 9-2 shows the results of the 17 months monitoring period starting during the installation on October 10th, followed by a period of tuning the packers pressure until December 19th, and finally a period of baseline monitoring, which is still ongoing. Chamber pressure first increased to a peak of 5.83 bars on December 1st, 2018, followed by a decrease to ~3 bars in March 2019. Displacements display a large initial variation associated to the peak pressure. Displacements then remain at a plateau while pressure is decreasing, highlighting an initial irreversible response of the borehole following the deployment of the SIMFIP and lasting about 5 months. During that initial period from October 2018 to March 2019, there is no water resistivity variation. In April 2019, all SIMFIP signals are at steady state, and the SIMFIP probe is at equilibrium with the formation.

After April 2019, two events occurred:

- The excavation break-through of a new Mont Terri gallery occurred on May 27th, 2019 (Point 1 in Figure 9-2).
- The injection of dissolved gaseous CO_2 in water in borehole BCSD1 started on June 11th, 2019, and is still running (Point 2 in figure 9-2). The key idea of this long term, low pressure-low flowrate injection is to test the fault potential injectivity to dissolved gas while the fault is not activated. Indeed, the fault opening pressure to water injections was determined around 4.8 MPa. The initial fault permeability (when fault is not activated) was estimated to be $\sim 10^{-18}$ to 10^{-20} m^2. It is slightly higher than the intact rock's permeability, and it is in agreement with lab-scale estimations. Injection pressure is thus maintained relatively constant at ~4.5 MPa. The total injected volume was 17.95 liters, corresponding to an injectivity in the fault core of ~0.08 ml/min.

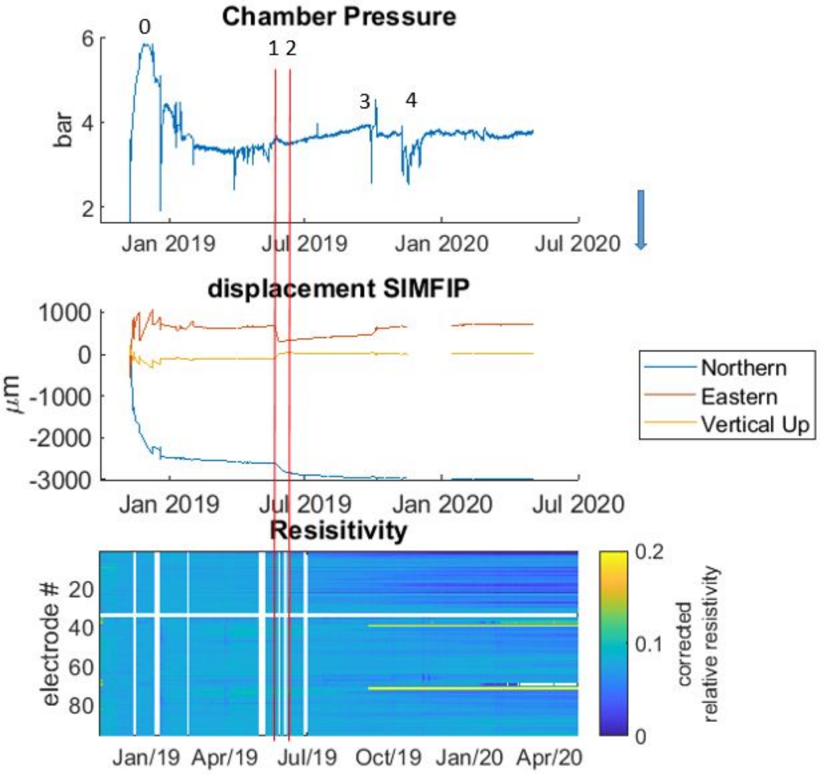

Figure 9-2. Long term fault zone pore pressure, displacement and water resistivity monitoring with the SIMFIP probe set in Borehole BCSD7 (Figure 9-1): Upper graph - chamber pressure, Middle graph - (Northern, Eastern, Vertical) displacement of the upper packer of the SIMFIP probe (Fault hanging wall). Lower graph – chamber water resistivity monitoring using 94 electrodes distributed every 4 cm along the entire length of the chamber.

The excavation break-through corresponds to the date when the new gallery was connecting with the existing Mt Terri galleries. It happened at about 30 meters from the SIMFIP probe. There is a pore pressure peak and an irreversible step in the displacements at the break-through (Point 1 and red line in Figure 9-2). No clear water resistivity variation is observed. Following the start of the dissolved gas injection on June 11th (Point 2 and red line in Figure 9-2), there was a slow pressure and displacement increase, but this trend might also have been initiated earlier. The clearest signal is a decrease of the water relative resistivity observed on electrodes 1 to ~30, which are monitoring the upper part of the fault zone. Such signal could highlight some potential connection with the injection intherval although the mixing of the gas with the formation water should theoretically increase the water resistivity. It might be possible that some complex geochemical interactions with the fault minerals modifies the signal. Changes in pH and in the CO_2 isotopic content of these waters that support the application of traces in the injection brine mixed with the formation water. As expected, there is no clear displacement signal since the fault is supposed to remain inactive during this injection.

Finally, Points 3 and 4 in Figure 9-2 highlight periods of borehole manipulations (some re-testing of the packers at point 3, and water sampling at the injection zone in borehole BCSD1 at point 4).

9.2.3 Borehole nearfield fault evolution following the installation period from October 2018 to March 2019: Conclusions and Perspectives.

Prior to February 2019, the chamber pressure was affected by negative spikes corresponding to periods of packers testing (Figure 9-2, upper graph). The control of the packer response is crucial because this probe is equipped with sliding-end packers in order to ensure an optimal sealing of the isolated interval that permanently matches with borehole dimension evolution related to interval pressure variation and to borehole clay walls deformations. Thus, because the packers slide while their pressure is varying, it affects the chamber pressure and the displacement measurements (since the SIMFIP is anchored with the packers -- see Figure 9-2, upper and middle graphs). The packers pressure increase was inducing a chamber pressure decrease, a SIMFIP vertical extension (positive D_z variation), and an equal radial displacement. Interestingly, this response matches laboratory calibrations, and, thus, any deviation from it observed in the field might highlight a true hydromechanical evolution of the formation. To minimize the effect of packers on the long term SIMFIP displacements, an automatic control of packer's pressure was installed in December 2019. This control maintained a constant packer pressure at with minimal variations of ±0.025 bar.

The chamber pressure increased to 5.83 bar during November-December 1st, 2018, period (maximum was at Point 0, shown in Figure 9-2, upper graph). Then, from December 1st, pressure decreased to reach a quasi-steady state at about 3.31 bar in March 2019. These long-term pressure variations are related to borehole pressure equilibration with formation pressure, which occurred in about 5 months, given very low formation permeability. Displacement variations followed these long-term pressure variations. Displacement amplitudes were from 0.3 to 2.3 mm, depending on the displacement component (more than 70% of the displacement occurred after about 1.5 months). These values are in reasonable accordance with strain relaxation effects associated to borehole or gallery excavation observed in other Mt-Terri experiments.

In Figure 9-3a, we picked the displacements at four points during the rising pressure period--November 11th, 21st and 26th, and during the quasi-constant period--March 27th. The corresponding displacement vectors are plotted in a stereographic lower hemisphere projection (Figure 9-3b), and compared to the orientation of the fault zone fracture and the state of stress (Figure 9-3c). During the pressure rising period, the displacements were oriented N165 to N150 dipping 15 to 45° SE. This is in a good agreement with a normal faulting regime characterized by slip along the existing fault zone fractures. After the maximum pressure was reached, there was a drastic rotation of the displacements to N330 - 25º NW, which corresponds to a normal closing of the fault zone fractures. These observations show that shearing of pre-existing fault zone fractures may have guided stress relaxation following the borehole excavation. Slip along fractures may have triggered convergence of the chamber walls, also causing the initial chamber pressure increase. Slip might also have produced dilation and a slight permeability increase around the borehole, which explains the following chamber pressure decrease until its eventual equilibrium with the formation pressure. The Mohr-Coulomb plot (Figure 9-3c) shows that some of the fault zone fractures could potentially be reactivated in shear if we consider the commonly admitted stress tensor and a 0.12 coefficient of friction for fractures. Thus, these long-term observations may show how stress relaxation around a borehole in shales is eventually followed by dilation and drainage.

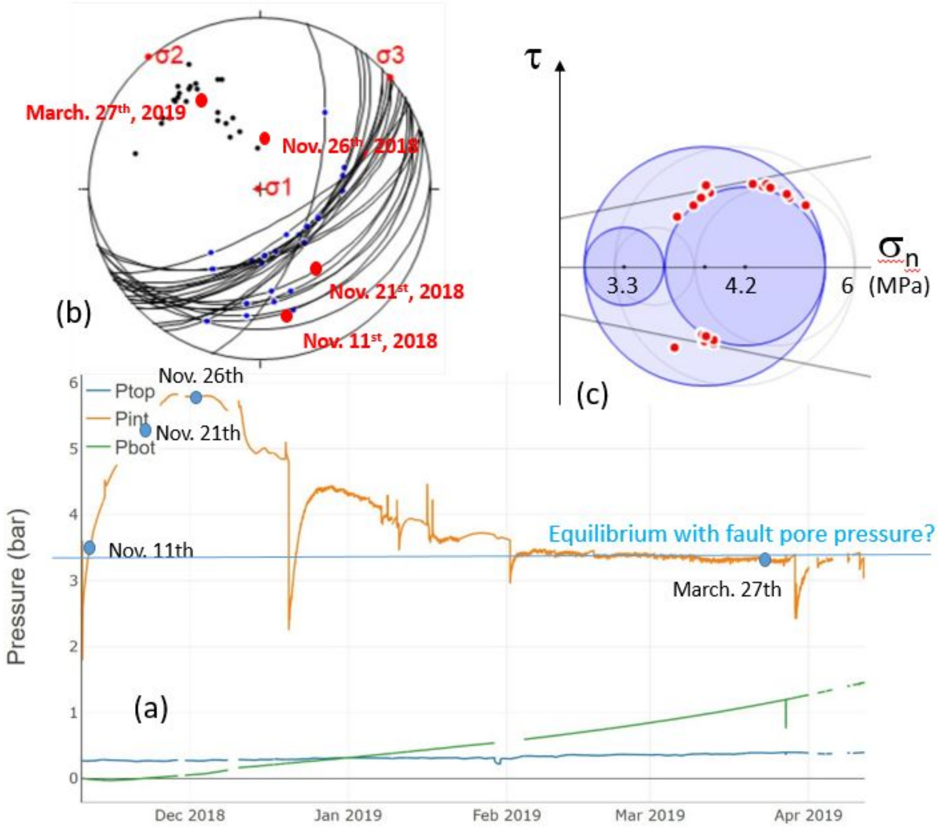

Figure 9-3. (a) Blue points show where the SIMFIP displacements have been picked during the Chamber pressure variations. (b) Stereographic projection of the displacement vectors (red points), fault zone fractures (black lines, black points are the fractures poles) and principal stresses from the Martin and Lanyon tensor commonly used at Mt Terri (blue points on the fracture traces show the orientation of the calculated slip vectors given the considered tensor). (c) Mohr-Coulomb graph of shear and normal stresses calculated on each fracture planes (red points, the inclined lines show the elastic limit given a 0.12 friction coefficient of a no-cohesion fault).

9.2.4 Fault response to stress loading from the remote gallery excavation

Monitoring during the excavation of the new Mt Terri gallery was a unique opportunity to obtain data to characterize the effects of a far field stress/strain perturbation on the fault hydromechanical stability. It was also an opportunity to compare the SIMFIP signals with those from other types of sensors, thus to test the monitoring system deployed for the FS-B fault activation experiment. The excavation of the gallery started on March 20th, 2018, at Point 2, shown in Figure 9-4a, and ended on May 27th, 2019, when the new gallery was connected with the existing ones. This so-called break-through of the new Mont Terri gallery occurred at the FS and FS-B experimental zones (Figures 9-4a, b).

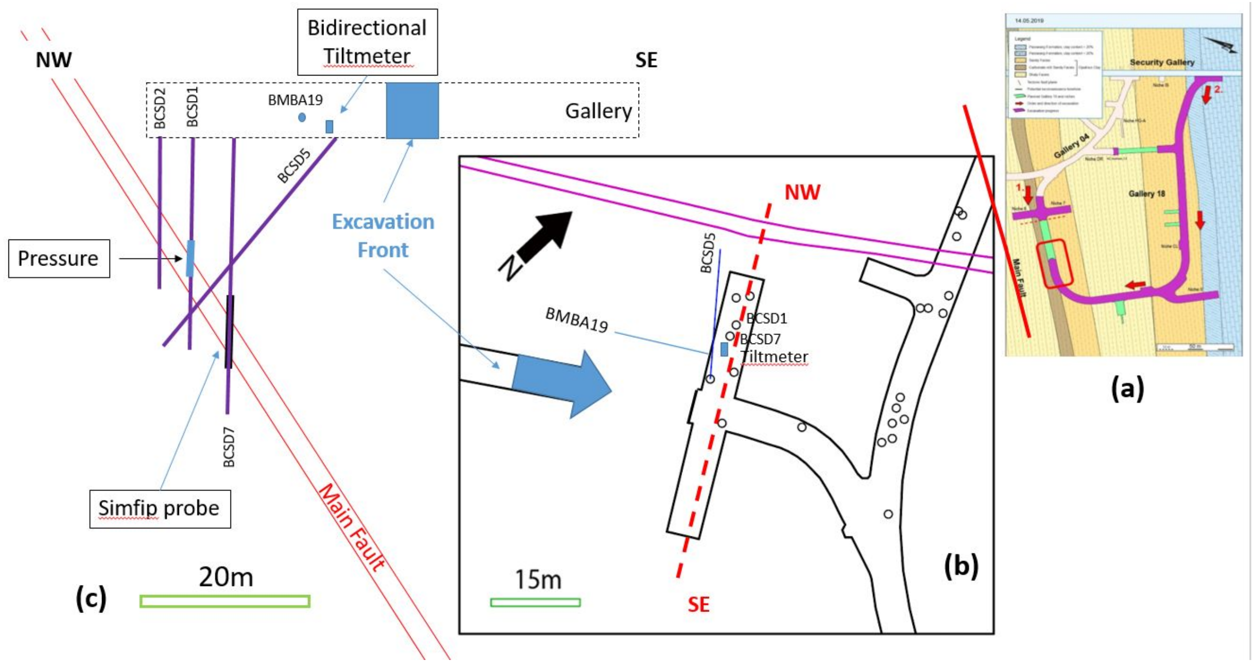

Figure 9-4. (a) Map of the new gallery (purple) excavated at Mt Terri in 2018-2019. The red rectangle shows the excavation front approaching the FS-B zone in April 2018. (b) Detailed map of the FS zone. The approaching excavation front is depicted as the blue arrow. (c) Vertical cross section showing the different monitoring boreholes with deployed instruments (the NW-SE cross section is shown in Figure 9-4b by a dashed line).

Here we compare the fault movements monitored by the following instruments:

- SIMFIP three-dimensional fault displacement and pore pressure in borehole BCSD-7
- Fault pore pressure monitored in borehole BCSD-1
- Distributed strains monitored in borehole BCSD-5 from surface across the fault zone. Two types of strain measurements were conducted in this borehole. Relative axial displacements between a series of anchors spaced every 0.5 m across the fault zone. A DSS optical fiber is cemented behind the borehole casing to monitor the axial strains with a resolution of 1m. Borehole BCSD-5 is drilled almost normal to the average fault surface.
- Bi-axial tiltmeter set at the gallery floor close to the head of borehole BCSD-7
- Distributed stress monitoring in borehole BMBA19. Each stress measurement is made with a Glozl© total pressure cell. Nine pressure cells are distributed every 25 cm to provide measurements in different directions in order to get an estimate of the stress tensor's variations. Borehole BMBA19 is almost parallel and located at the elevation of the gallery excavation.

Such a comparison between instruments is unique. It was made possible by the strong collaboration between the FS-B and the CS-D projects (ETH, Switzerland). In addition, the Mt Terri consortium provided the access to the data from the Mine-by-Test MB-A experiment (BGR, Germany).

We focus on the April-June 2019 period, when the excavation came close and parallel to the Main Fault (Figure 9-4 a, b). There was no excavation from April 4th to May 7th, 2019, then excavation was continuous at a rate of 6 days/week until breakthrough (Figire 9-5). All BMB-A19 sensors show the same succession of stress increase and decrease related to the excavation progress. Periods of stress increase correspond to periods of excavation. After the excavation breakthrough, all sensors showed stress increase. The amplitude of stress changes is of 0.3 to 0.7 MPa. The data analysis show that there was a period of stress decrease during a period of no excavation, when different sensors showed a stress relaxation at different times. The sensors at the borehole bottom, which are closer to the excavation front, decreased first (purple box) followed by the ones close to the borehole (red box in Figure 9-5).

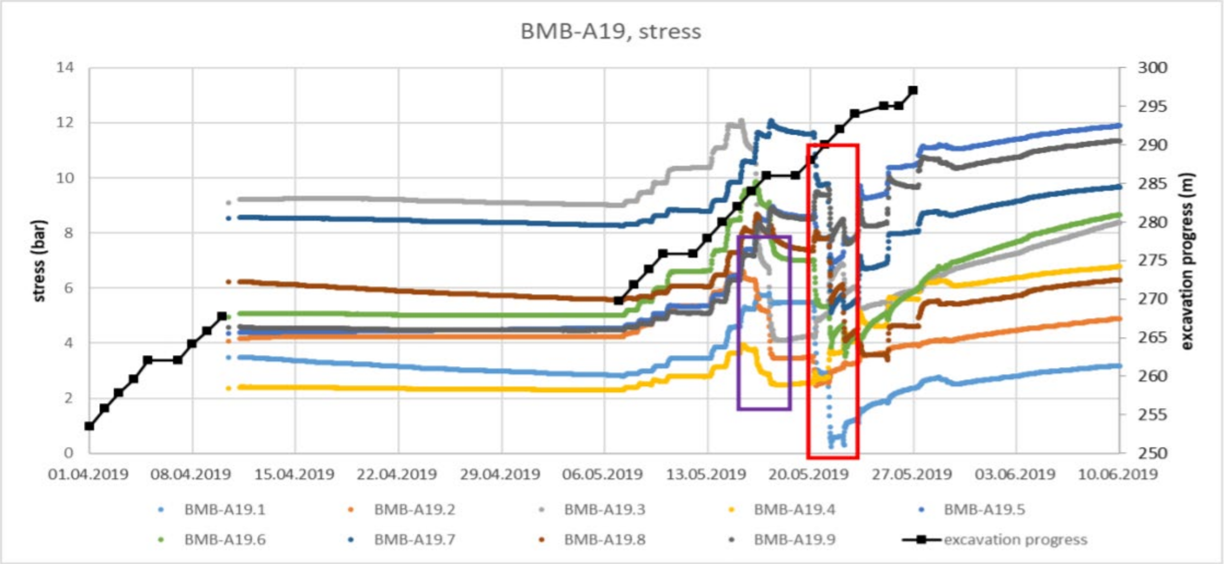

Figure 9-5. Stress variations with time compared to excavation progress at borehole BMB-A19. The sensors are numbered from the bottom to the top of the borehole -- A19.1 (the closest to the excavation front) to A19.9. The sensors are spaced every 0.24 m.

Figure 9-6 shows pore pressure variations in the fault zone during the excavation period (see Figure 9-4c for the sensors layout). There is a 0.03 to 0.11 MPa pressure increase respectively in boreholes BCSD1 and BCSD7 during the excavation period. After the excavation breakthrough (vertical dotted black line), pressure dropped at both points. The difference in pressure between the two points was mainly related to the different sizes of the two isolated zones, as the SIMFIP zone straddling the entire fault thickness, while the BCSD7's zone is a 1 m long zone straddling the top of the fault.

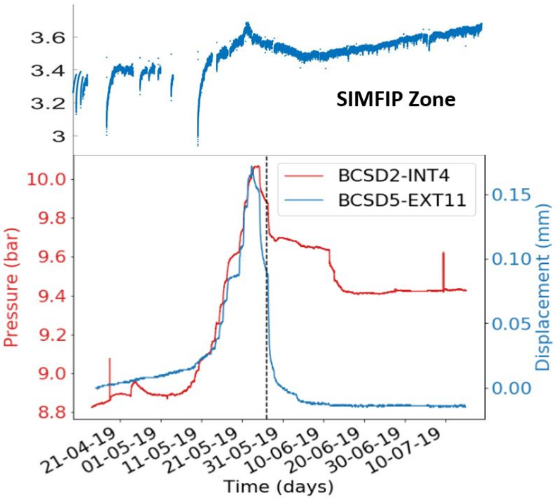

Figure 9-6. Fault pore pressure variations with time at two monitoring points in the fault (locations are in Figure 9-4). In BCSD2, the pore pressure is compared to the displacement between two anchors set in borehole BCSD5 at the nearest location to the BCSD2 pressure measurement.

The SIMFIP clearly captured a movement of the fault hanging wall relative to the foot wall that was caused by the excavation (Figure 9-7). First detected signals occurred on May 14th, while the excavation front was 32 m away from the SIMFIP (Figure 9-7a, b). During excavation periods, the displacement rate increased (Figure 9-7b). When the front approached the distance of about 23 m from the SIMFIP, there was a sharp increase in the displacement rate until the breakthrough occurred. The subsequent breakthrough displacement rate was smaller, and there was an offset showing that some irreversible displacements were caused by the excavation. Figure 9-7c demonstrates that the excavation period likely caused a slightly reverse shear along the fault plane, while the post excavation period was characterized by a dominant opening normal to the fault plane. The reverse shear is consistent with a transfer of the compressive strength increase observed during excavation at BMB-A19 (Figure 9-5). The normal opening is consistent with the pore pressure decrease observed in the fault (Figure 9-6).

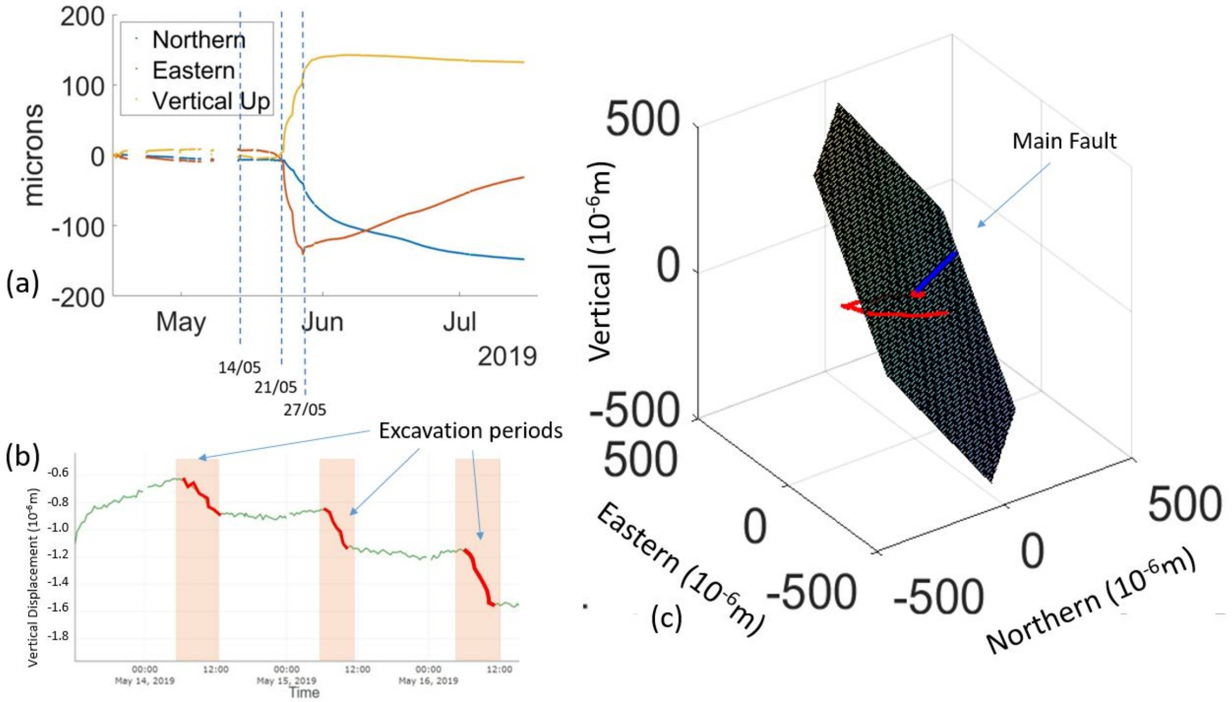

Figure 9-7. SIMFIP displacement variations related to the Mt Terri gallery excavation. (a) Fault hanging wall displacement versus time, (b) Details of the vertical displacement variation with the excavation periods, (c) Three-dimensional displacements (red curve) compared to the average fault plane orientation.

In Figure 9-8, we have projected the SIMFIP displacements on the axis of borehole BCSD5 in order to compare with DSS strains and with uniaxial displacements. Both amplitude and time variations of displacements are consistent (Figure 9-8a). The SIMFIP shows a slight negative variation before May 21st which is not seen on the potentiometer. After May 21st, there was the same positive displacement, which was of a smaller magnitude at the SIMFIP. This discrepancy is related to the 3D nature of the signal. The BCSD5 displacement can only be measured parallel to the borehole axis. It, thus, integrates both the initial borehole shearing and the late borehole stretching observed in 3D with the SIMFIP. This is why the BCSD5 displacement appears larger than measured at the SIMFIP. Displacements and deformations appear distributed at the top and the bottom of the fault zone (Figure 9-8 c, d), and are not localized on one single surface, but distributed along meter-thick zones within the fault.

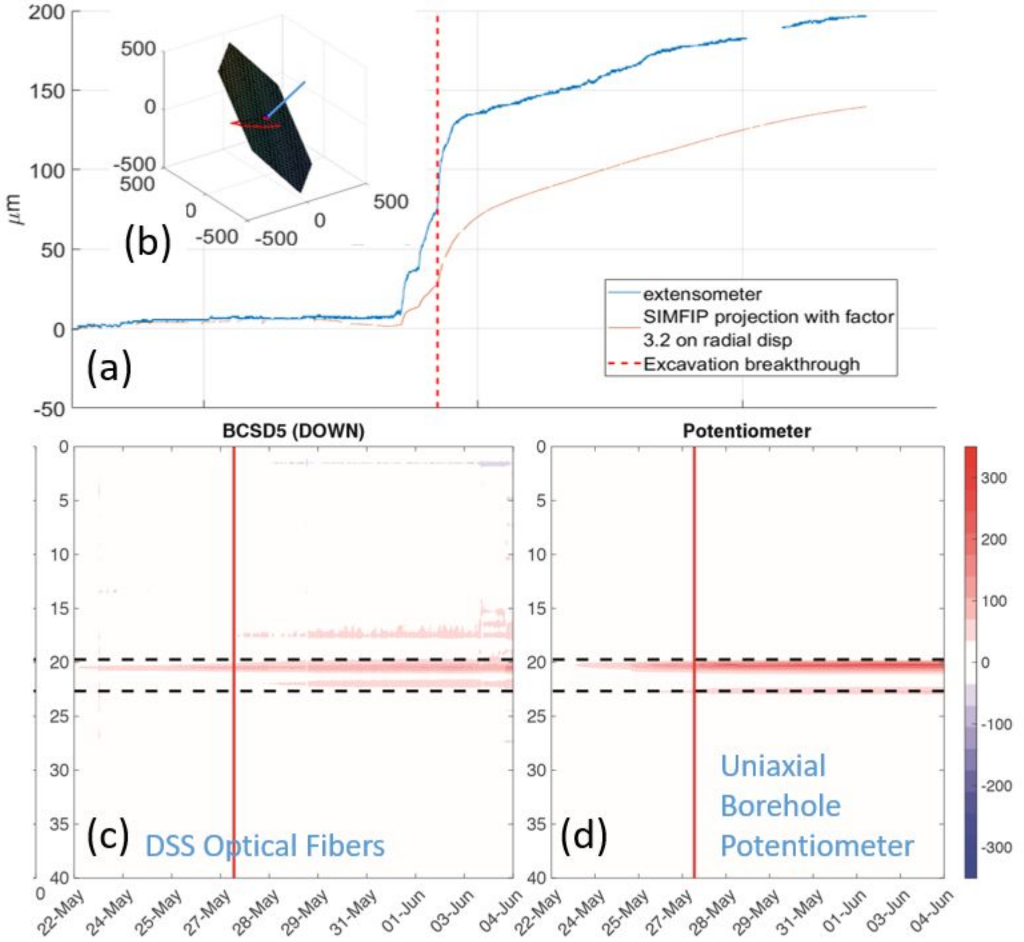

Figure 9-8. SIMFIP displacement compared to DSS optical fibers strains and to local displacements measured in borehole BCSD5. (a) SIMFIP displacement projection on the CSD5 axis (blue line perpendicular to the fault plane shows the orientation of BCSD5 in Figure b). (c) DSS strain measurements with borehole depth, in meters (black dotted lines show the location of the top and the bottom of the Main Fault zone intersected by BCSD5). (d) Borehole displacements versus borehole depth (displacements unit is micrometer).

9.2.5 Interpretation and Conclusions

Figure 9-9 is a synthesis of a preliminary analysis of the fault activation induced by the gallery excavation. The displacement vectors corresponding the slightly reverse shear during excavation (Point 2) and to the opening after the breakthrough (Point 3) are plotted on a stereogram with the different fault zone fractures (Figure 9-9a). We consider that the local state of stresses is in the range of what was estimated in borehole BFS2 (see Figure 9-9a for the borehole layout) by inverting the 3D displacements and fluid pressure during pressure step rate tests performed with another SIMFIP probe at 40.6 m and 37.2 m depths during the FS experiments in 2015 (Guglielmi et al., 2020b). This tensor is characterized (1) by one principal stress σ_1 or σ_2 almost perpendicular to the average fault strike, and (2) by very close magnitudes of σ_1 or σ_2 (Figure 9-9b). These results are in agreement with the average stress tensor in the Mt Terri URL. In that context, a

0.7MPa increase in the total stress associated to a 0.1 MPa pore pressure increase in the fault will make the Mohr circle larger and move it to the right. Then, considering a 0.12 fault friction coefficient (Aoki et al., 2017), it appears that some fractures of the fault zone can be brought to a Mohr-Coulomb failure (Figure 9-9c). Thus, the transfer of stress during the excavation could potentially trigger the observed reverse slip, thanks to the low range of the mean stress typical of the stress state at such relatively shallow depths. The post excavation fault opening and associated fault pressure drop might relate to a poroelastic effect induced by pore pressure relaxation around the newly excavated gallery (Figure 9-9d). Indeed, modeling studies of the BMB-A data (Jaeggi and Madaschi 2017) show that, just after excavation, there is a pore pressure drop oriented perpendicular to bedding (or to the Main fault since it has the same strike as the bedding), while it rotates to bedding parallel for later times.

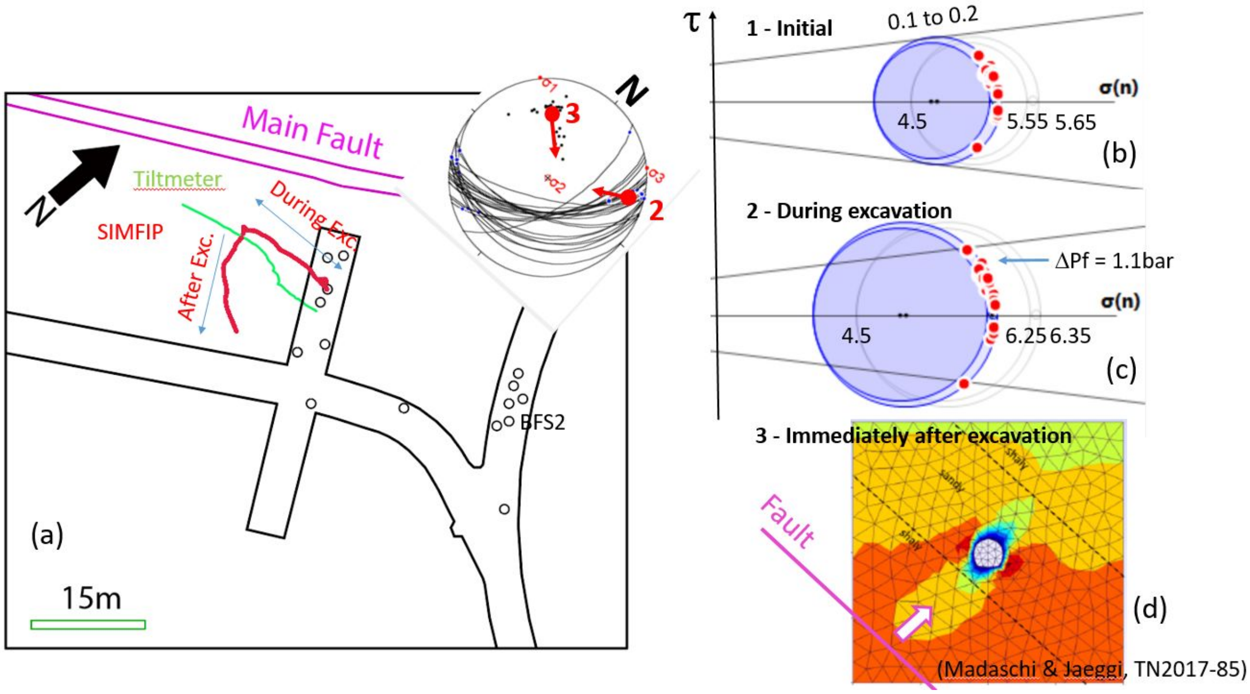

(Madaschi & Jaeggi, TN2017-85)

Figure 9-9. (a) Map view of SIMFIP displacements and stereographic projection (lower hemisphere) of the two main displacement vectors (2 – Reverse shear during excavation, and 3 – Normal opening after excavation breakthrough). (b) Initial state of stress after Guglielmi et al. (2020b). (c) Modified state of stress induced by excavation. (d) Pressure change modeled immediately after excavation (Jaeggi and Madaschi, 2017).

In summary, the effects of the gallery excavation were captured by all the FS-B zone instruments (and by other monitoring sensors not mentioned in this report). The SIMFIP showed a contrasted fault response between the excavation and the post-excavation periods. Range of magnitudes of the SIMFIP displacements as well as the main direction of displacements are very consistent with all the other sensors. One lesson learnt is that combining the localized SIMFIP three-dimensional measurement with behind casing cemented DSS fibers allows for a refined interpretation of the fault activation mechanisms. These are characterized by reverse shearing followed by normal opening of hundreds of microns coupled to slight pore pressure changes of ~0.1 MPa. For the first time to our knowledge, this dataset highlights that a fault can be activated in a host rock several gallery diameters away from the excavation (about 30 to 50 m away from the excavation gallery). It also shows that the excavation is inducing complex stress transfers in the host rock and a contrasted response of the fault zone caused by compression during excavation followed by extension during the post excavation hydromechanical relaxation around the newly created gallery.

After 1.5 year of continuous monitoring, the SIMFIP was able to capture borehole integrity evolution, fault response to remote pressure changes, and to eventually detect a dissolved gas slow leakage in a non-active fault. Moreover, the SIMFIP measurements were successfully compared to a wide variety of other measurements such as distributed optical fibers (DSS), distributed uniaxial borehole displacements, stress, tilt and pressure measurements. It shows that a permanent SIMFIP is sensitive to events occurring tens of meters around. Although being a local measurement, it provides a valuable information about the modes of activation of a fault zone, allowing for an *in situ* tuning of most of the other measurements thanks to its ability to detect microscale 3D displacements between two points that could be separated by several meters inside a borehole.

9.3 Mt Terri fault hydromechanical response to pore pressure increase

We used the *in-situ* data collected during the 2015 FS experiment (Guglielmi et al., 2020a) directly in the fault (i.e., called “Main Fault Zone” in the project) in order to understand the hydromechanical response of a low permeability fault zone to a local pore pressure increase induced by a water injection. This modeling phase is continuation of research described in the Rutqvist et al. (2019). The key objectives of the current study are to estimate the fluid flow process in a low permeability formation, and how the fluid pressure response in and outside the fault zone is sensitive to the fault hydromechanical properties and a stress state. We tested different fluid flow models, taking into account the friction and permeability constitutive laws incorporated in coupled hydromechanical 3D numerical models. First idea is to model measured hydraulic response of the fault zone during the stress perturbation induced by the fluid injection. To model fluid flow in the fault, we have used the cubic law and a crack flow model to activate the fluid flow in the ruptured parts (in shear failure) of the fault. One of the main objectives of the present study is to describe the potential links between the fluid leakage and the evolution of fault properties. We propose to estimate whether this fluid flow and fault displacement can provide information on rupture and pressurization induced in the fault by injections, or whether it provides information on stress perturbations far from the areas invaded by fluid leakages.

We present the experimental response of the fault and the numerical method of the 3D Distinct Element Code (3DEC) that was used to model the coupling between fluid flow, friction and permeability evolution in a single fault (Itasca, 2016). Second, we present the model conditions and the details of the parametric study conducted to estimate the hydromechanical response of the fault zone to different physical parameters and a stress state. Finally, we show the effects of this local fault dislocation on the surrounding intact host rock.

9.3.1 Observations of the complexity of Fault Rupture and Fluid Leakage in Argillite rock

We observed rupture growth caused by controlled fluid injections at 340 m depth within a fault zone in the low permeability Opalinus Clay in the Mont Terri URL (Guglielmi et al., 2020a). The rupture mechanisms were evaluated using measurements of the three-component borehole wall displacements and fluid pressure in two sections of the fault zone and located horizontally 3 m apart from each other (Figure 9-10). One section was set across a secondary segment of the fault and used for stepwise fluid injection intended to trigger rupture growth. The other section was set across the principal shear zone of the fault for monitoring.

After stepwise pressure increase up to 5.95 MPa at injection, rupture initiated as slip activation (see red vector in the stereographic plot in Figure 9-10), followed by an overall opening of the fault planes connected to the injection. After 19 seconds of continued injection, displacements occurred at the monitoring point on the principal shear zone. These displacements were about 2.4 times larger than that in the secondary fault segment. Overall, the displacements corresponded to a normal fault activation. About 9 seconds after the displacement front arrived, a strong pressure increase of 4.17 MPa was measured at the monitoring point, indicating a hydraulic connection had formed along the initially very low permeability fault planes between the injection and the monitoring points.

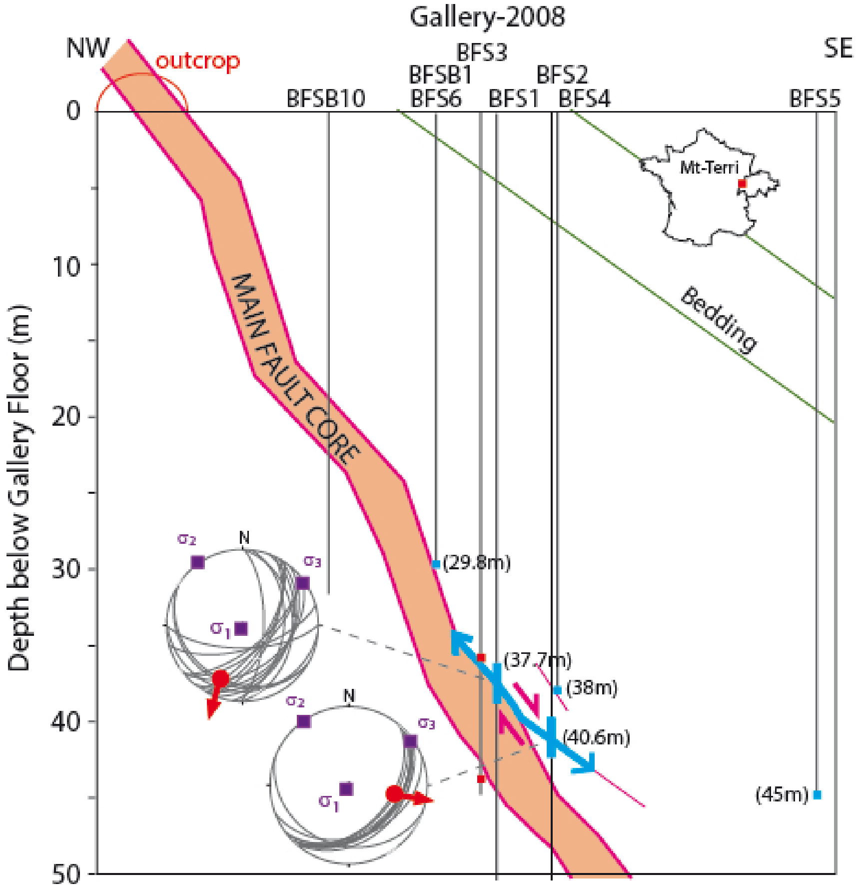

Figure 9-10. Vertical cross section of the FS fault activation experiment. Injection interval corresponds to the blue rectangle located at 40.6m below the gallery. Monitoring interval is the blue rectangle located at 37.7m below the gallery. Points located at 29.8m, 38m and 45m monitored the pore pressure respectively into the fault zone, in a secondary fault zone outside the main fault, and in the intact argillite rock. Stereograms show a lower hemisphere projection of the fault planes intersecting the injection and the monitoring intervals. The red arrows are the main directions of fault displacements during fault activation.

Figure 9-11 shows the pore pressure variations at different locations in and off the fault zone during the pressure test conducted at the 40.6m depth interval (see Figure 9-10 for locations of the measuring points). The main fault activation event occurs at 17:30 (dashed red line in Figure 9-11). Apart from the two hydraulically connected highly pressurized points at 40.6 m and 37.7 m, the other measurements displayed a very low magnitude variation. The other point located in the fault at 29.8 m depth showed a 10^{-4} MPa instantaneous drop and a residual $0.5\text{x}10^{-4}$ MPa drop. This proves that this point was not connected to the pressurized patch during the injection, but it recorded a slight irreversible pore pressure drop. The point located at a 38 m depth on a secondary fault and the point located at a 45 m depth in intact argillite both displayed a 10^{-4} to 1.5 10^{-4} MPa irreversible pressure increase. Since obviously these three points were not hydraulically connected to the injection, they all displayed an instantaneous and irreversible response to rupture. This pressure change might thus reflect the stress drop associated to the rupture, and we thus conducted numerical modeling to estimate the size and the mode of the rupture zone.

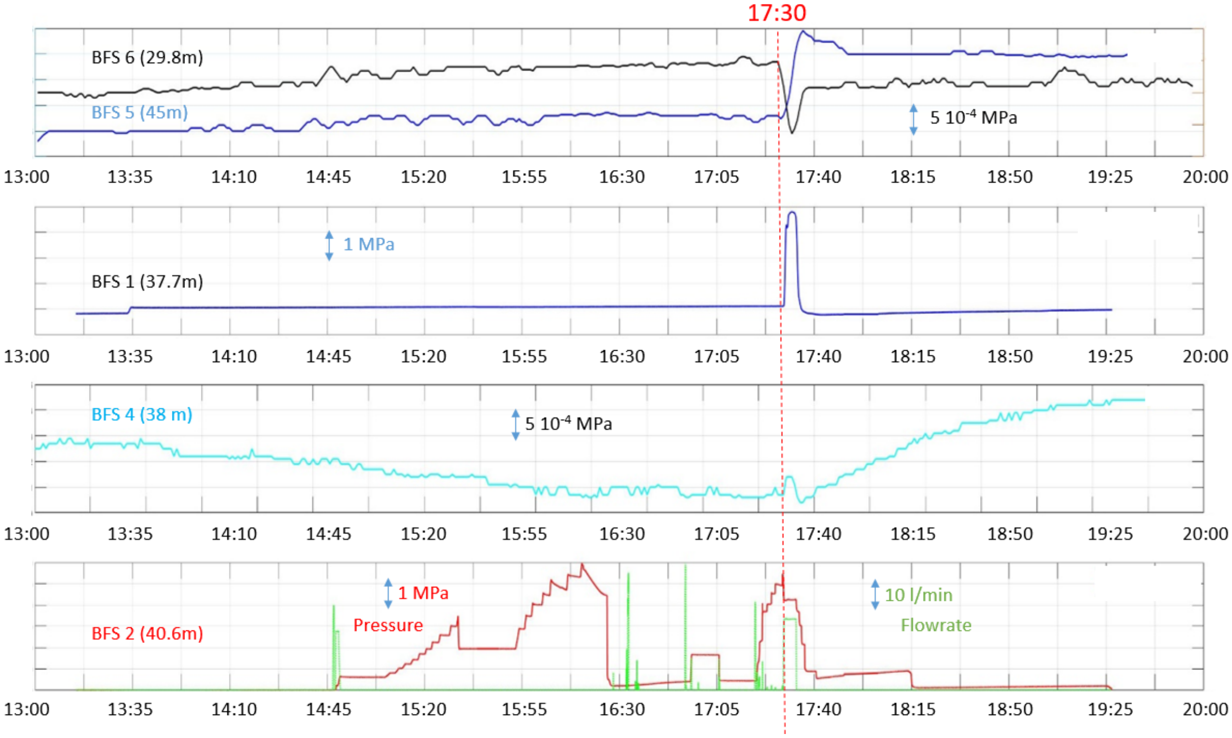

Figure 9-11. Pore pressure variations in and off the fault zone during the main fault rupture induced by the fluid injection. Rupture occurred at 17:30. Pressure observation points are shown in Figure 9-10.

9.3.2 Numerical Method, Model Setup and Modeling Procedure

The Distinct Element Method (DEM)（Cundall, 1988） used in the 3DEC code (Itasca, 2016) is a numerical technique for simulating discontinuous rock media. The code simulates the coupling between stress and fluid flow in discrete fractures or faults embedded in an impervious or a permeable rock matrix. The method is an explicit, time-marching procedure. During each time step of the simulation, the method uses force-displacement relations describing the interaction between blocks. The positions of blocks are updated through the differential equations of motion (Newton’s laws) and constitutive equations to determine block translation and rotation.

In this study, we use this approach to calculate the fluid pressure, the fracture displacement and stress. The method has been previously used to evaluate the hydromechanical behavior of fractured rocks and fault zones during fluid pressurization (Cappa et al., 2006; Guglielmi et al., 2008; Cappa et al., 2018), showing that the evolution of fault hydraulic diffusivity is a fully coupled problem depending on stress and fluid pressure (Guglielmi et al., 2015a and 2020a).

9.3.2.1 Force, displacement, friction and stability conditions in faults and fractures

In DEM, normal (ΔF_n) and shear (ΔF_s) elastic force increments are calculated as follows:

$$\Delta F_n = -k_n \cdot \Delta u_n \cdot A_c \tag{9-1}$$

$$\Delta F_s = -k_s \cdot \Delta u_s \cdot A_c \tag{9-2}$$

where k_n and k_s are the normal and shear stiffnesses (Pa/m), Δu_n and Δu_s are the normal and shear displacement increments (m), and A_c is the contact area (m^2). The calculated shear force (F_s) is compared to the shear strength (F_s^{μ}) and determines whether slip is initiated. If the magnitude of the shear force exceeds the shear strength, then:

$$F_s = F_s^{\mu} = \mu \cdot F_n \tag{9-3}$$

where μ is the coefficient of friction. Once the onset of failure is detected at a sub-contact of the fracture based on the Mohr-Coulomb failure criterion (Jaeger and Cook, 1979), unlike Coulomb friction with a constant coefficient of friction, fault slips and the coefficient of friction evolves as a function of the slip velocity (v) using the Dieterich type evolution equation (Dieterich, 1979):

$$\mu(v,\theta) = \mu_0 + a\, ln\left(\frac{v}{v_0}\right) + b\, ln\left(\frac{v_0\theta}{D_c}\right) \tag{9-4}$$

$$\frac{d\theta}{dt} = 1 - \frac{v\theta}{d_c} \tag{9-5}$$

where μ_o is the friction coefficient at a reference slip velocity (v_o). The parameter a quantifies the direct effect of a change in slip velocity. The parameter b describes the effect of the state variable, we use the "aging law" (Dieterich, 1979). The characteristic slip distance, d_c, governs the evolution of the state variable (θ). The magnitude of the characteristic slip distance depends on the surface roughness and fault gouge (Dieterich, 1979). The evolution of the state variable is assumed to be independent of changes in the effective normal stress ($\sigma_n' = \sigma_n - P$) that can affect the fault slip due to changes in fluid pressure. This law accounts for the decrease in friction (slip-weakening) as the slip increases, and the increase in friction (healing) as the time of contact or slip velocity increase. The two effects act together such that $(a\text{-}b) > 0$ leads to strengthening of the fault, stable sliding and creeping motion, and $(a\text{-}b) < 0$ leads to weakening of the fault, frictional instability, and accelerating slip. Fault slip is computed from the unbalanced forces of the two sides of the fault which is based on the frictional equilibrium.

In summary, for a hydromechanical modeling of pressurized fractures or faults, each cells of the interface can be in three different states: "separation", "slip", and "stick". This state may change at each time step. Thus, an element can be open or closed (i.e., state is separation) under the applied fluid pressure and stress, and "stick" or "slip" if the shear stress of an element exceeds or not the Mohr-Coulomb criterion. When an element is not surpassing the Mohr-Coulomb criterion, its state is "stick."

9.3.2.2 Fluid flow model

Injection of fluid leads to change of pressure and fluid flow in a fault or a fault network, and consequently, change of stress over the fault surface and change in aperture follow. The cubic law (Witherspoon et al., 1980) governs the fluid flow in the faults:

$$Q = -\frac{b_h^3 \cdot w}{12\mu} \Delta P \tag{9-6}$$

where Q is the flow rate (m^3/s), ΔP is the increment in fluid pressure (Pa), μ_f is the viscosity of fluid (Pa.s), w is the fault width (m), and b_h is the hydraulic aperture (m), which is defined as:

$$b_h = b_{ho} + \frac{\Delta\sigma_n'}{k_n} + \Delta u_s \cdot \tan\psi \tag{9-7}$$

where b_{ho} (m) is the initial aperture at zero normal stress, $\Delta\sigma_n{}'$ is the increment in effective normal stress, Δu_s (m) is the shear slip increment, and ψ is the dilation angle (°). Dilation occurs only as the fracture slips, and the relationship between permeability and the hydraulic aperture is given by

$$k = \frac{b_h^2}{12} \tag{9-8}$$

Experimental and numerical analyses have shown that the cubic law is adequate to simulate fluid flow and hydromechanical effects along smooth surfaces (Brown, 1989; Zhang et al., 2019).

The numerical solution for fluid flow is based on the fluid domain network structure (Itasca, 2016). Each domain has a uniform fluid pressure and can communicate with the neighboring domains. Thus, the fluid flow is governed by the difference in pressure between adjacent domains. At each time step, the fluid pressure (P in P_a) is updated considering the net fluid flow and the domain volume change (ΔV):

$$P = P_0 + K_w Q \frac{\Delta t}{V} - K_w \frac{\Delta V}{V_m} \tag{9}$$

where P_0 is the initial fluid pressure (P_a), K_w (P_a) is the fluid bulk modulus, and $V_m = (V^t + V^{t-1})/2$, with V^{t-1} and V^t, the previous and new domain volumes (m^3), respectively.

In this study, we also use the “crack flow model” implemented in 3DEC to simulate fluid flow in the activated parts in shear failure of the fault plane, and prevent flow from occurring in the remaining elastic parts. This assumption is justified in very low permeability fractured rocks like shales.

9.3.2.3 Model geometry and boundary conditions

We selected a three-dimensional model (40 m × 40 m × 40 m), which considered fluid injection into a single fault plane (dip direction of N177°, dip angle of 37°, and origin in the model at 0,0,0) in a homogeneous elastic and impervious medium. The fault zone geometry tested here is inferred from previous geological studies (Nussbaum et al., 2011; Nussbaum et al., 2017; Guglielmi et al., 2020b). The remote principal stress ($\sigma_1 = 5.5$ MPa, $\sigma_2 = 4.7$ MPa, $\sigma_3 = 3.8$ MPa) applied at the model boundaries and resolved on the fault plane are constant, which are based on previous studies (Martin and Lanyon, 2004; Guglielmi et al., 2020b). During injection, the fluid pressure in the fault is increased stepwise from 0.5 MPa to 5.4 MPa, as observed in the 2015 FS experiment (Figure 9-11, red curve in the bottom graph). This corresponds to a time-dependent loading history. Injection occurs in a point source that figures the injection chamber at 40.6m depth (Figure 9-11). The total time of injection was 650 seconds. The initial value of the ratio of the shear stress to the normal stress ($\tau_o/\sigma_o = 0.0919$) was calculated at the injection point in the fault representing the conditions of the *in-situ* experiment (Guglielmi et al., 2020b). Thus, the modeled injection represented an extreme fluid pressurization ($P_{max} = 5.4$ MPa) relative to the pre-stress conditions on the fault, because a total drop of effective normal stress and shear stress was expected before the end of the simulated time.

In our analysis, the observed fluid pressure at the observation well at 37.7 m (Figure 9-11) was matched to evaluate the temporal and spatial evolution of the fluid diffusion and rupture propagation. We also calculated the pressure variations at the three other monitoring points. We subsequently evaluated, in a sensitivity study, the influence of several key parameters on the fluid pressure and mechanical response, including fault hydromechanical properties and pre-stress conditions.

9.3.2.4 Hydromechanical and frictional properties of fault and rock

The fault hydromechanical and frictional properties and the rock elastic properties were taken from previous studies on the "Main Fault" zone (Table 9-1) (Jeanne et al., 2017; Jeanne et al., 2018; Guglielmi et al., 2020b). The values represent average values of the Opalinus clay at the Mont Terri Underground Research Laboratory (Bock, 2009).

Here, we modeled the fault slip with the rate-and-state friction law (Marone, 1998). We assumed a slightly rate-weakening behavior for the fault, and used the following frictional parameters: $\mu_o = 0.375$, (a-b) = -0.002, and $d_c = 10$ microns (Table 9-1). These values fall within the range of frictional parameters measured in laboratory tests at low stress conditions on the "Main Fault" samples collected in deep boreholes into the shale rock formation (Orellana et al., 2018a; Orellana et al., 2018b; Orellana et al., 2019). However, we have to note that most of laboratory tests on these samples reveal a general rate-strengthening behavior, which indicates that such faults when reactivated would slip seismically. This is not the case in the field where a swarm of ~60 seismic events were recorded during the rupture. This is the reason why we consider a slightly rate-weakening behavior for the fault.

Table 9-1. Model hydromechanical and frictional parameters for faults and rock

Parameter	Value	Units
Bulk modulus of rock *(K)*	5.9	GPa
Shear modulus of rock *(G)*	2.3	GPa
Rock density (ρ_r)	2500	kg/m^3
Fault elastic stiffness (k_n, k_s)	100, 50	GPa/m
Initial friction coefficient (μ_o)	0.375	(-)
Rate-and-state constant *(a)*	0.001	(-)
Rate-and-state constant *(b)*	0.003	(-)
Critical slip distance (d_c)	10	µm
Initial hydraulic aperture (a_{ho})	10	µm
Dilation angle (ψ)	2	Degree
Initial fluid pressure (P_o)	0.5	MPa
Fluid Bulk modulus (K_w)	2	GPa
Fluid density (ρ_f)	1000	kg/m^3
Fluid viscosity (μ_f)	0.001	Pa.s
Stress ratio (τ_o/σ_o)	0.0919	(-)

In simulations, the evolution of fluid pressure, fault opening, fault slip, stress, friction, and hydraulic aperture as a function of time and space were calculated. A series of 17 simulations were conducted to evaluate the sensitivity of the hydromechanical response of the fault zone to the following parameters during the fluid injection:

- The initial pre-stress conditions
- The initial friction coefficient of the fault
- The initial hydraulic aperture of the fault
- The dilation angle of the fault

For numerical accuracy, the mesh size is refined in a zone of 12 m × 12 m around the injection point (0.35 m) and gradually increased to 0.65 m towards model boundaries. An adaptive time stepping algorithm was used to adapt the time step as function of the unbalanced force. When the fault was close to seismic failure, the time step was reduced to small value on the order of a millisecond. When the mechanical state of the fault was far from the failure, the time step was increased to values of about a second.

9.3.3 Modeling results

9.3.3.1 Comparison of different fluid flow models

We compared three different fluid flow models to reproduce the fluid pressure observed at the observation:

(1) A constant permeability model (i.e., the cubic law and a constant value of hydraulic aperture);

(2) A variable permeability model (i.e., the cubic law and a value of hydraulic aperture that changes with the evolution of fault normal displacement);

(3) A variable permeability model activated at failure (i.e., crack flow model mentioned in section 2.2.)

Figure 9-12A presents the three model solutions. Results show that the observed fluid pressure is well reproduced with a variable permeability model activated at failure. The other models do not match the data. The fluid pressure is underestimated in time, shape and amplitude. The best match between experimental and calculated curves indicates that the phases of rapid increase of fluid pressure and maintenance of maximum pressure are well reproduced, while the beginning with the slow increasing phase of the fluid pressure is not reproduced. The model shows that the fluid pressure first started to slightly decrease in the initially unruptured parts of the fault plane, and then increased quickly at failure. After the increasing pressure stage, the pressure stabilized at a maximum value of about 4 MPa, consistently with field data. The initial decreasing stage is associated with very small fault opening (< 1 micron) due to the stress perturbation transferred from the surrounding ruptured parts of the fault that influenced the unruptured parts at a proximal distance.

This result demonstrates that fluid flow in such low permeability rock can only occur in the ruptured parts of the fault plane. At failure, the fault first slips slowly (Figure 9-12B) as observed in the experiment (Figure 9-12D). Then, the fault opens sharply, slip accelerates and the permeability increases. The instantaneous permeability enhancement allows fluid pressure to migrate from ruptured to unruptured parts of the fault. The pressure increase is fast and intense, and produces a pronounced weakening in the activated patch. Although the amplitude of fault displacements is under-estimated compared to the field data, the temporal sequences is well reproduced with fault slip at the first place without any changes in fluid pressure, and then intense fault opening and accelerating slip when pressure increases. Underestimation of displacement is explained by the complex reactivation of several fault planes in the field. This complexity has not been introduced in this model.

Figures 9-12C-F present the evolution of the fronts of fluid pressure and shear stress. We define the pressure front in the fault as the position of the limit of the pressurized zone where the fluid pressure is zero. The limit of the shear stress zone is defined as the position of the outer rim of the patch where the shear stress after the peak is zero. Results indicate that the fluid pressure front follows the migration of peak shear stress where rupture occurs, and that the limit of the shear stress region continuously develops ahead of the pressure front over the whole temporal sequence of injection. The pressure drop observed at point BFS 6 is explained by the very small fault opening (< 1 micron) due to the stress perturbation at the tip of the shear stress zone, ahead of the pressurized zone. Indeed, in the model this monitoring point remains outside the pressurized zone (Figure 9-12F). Thus, the model predicts that fluid pressure increases only when the fault fails in response to a progressive loading by slip. Although the initial distribution of permeability is uniform in the fault, the fluid flow is not homogeneous and occurs in channeling flow in the direction of permeability enhanced by shear slip. This is consistent with previous studies showing that permeability enhanced by shear slip may become dominant when fluid flow in the fault occurs in channeling flow (Watanabe et al., 2008) or in a low-permeability gouge (Samuelson et al., 2011).

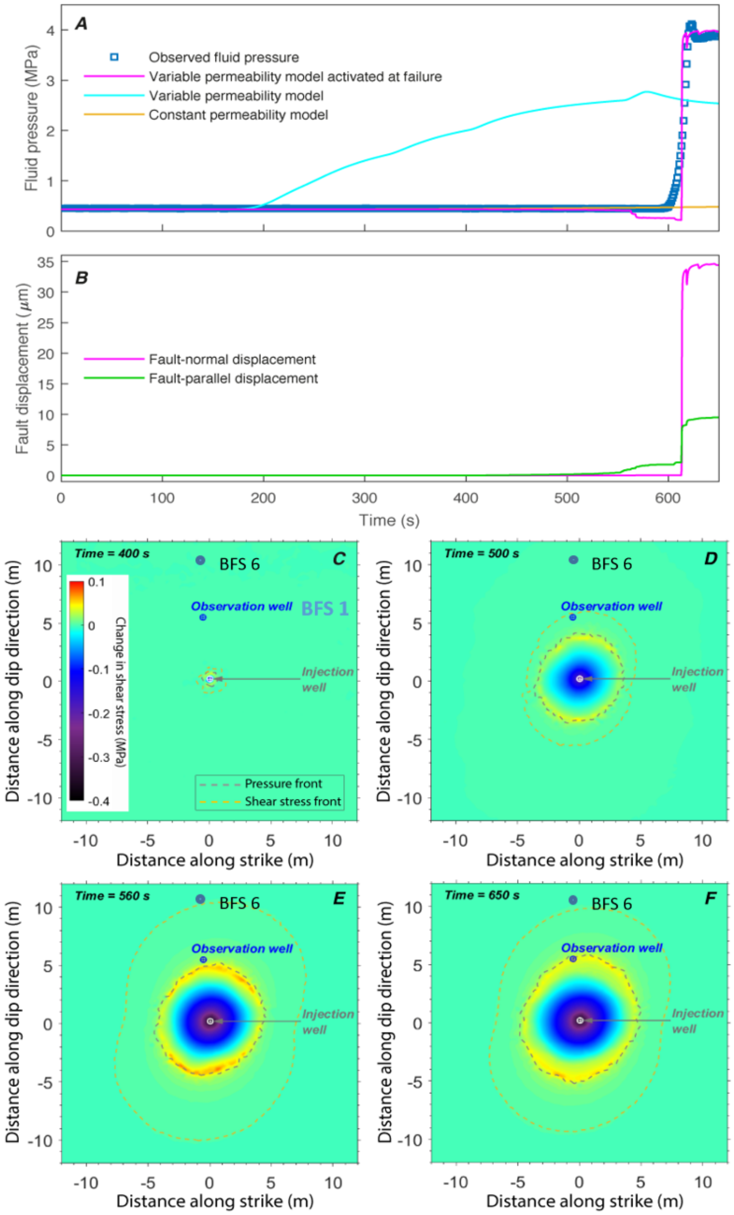

Figure 9-12. Coparison of modeling and measured fluid pressure at the observation well in response to the imposed pressure at the injection well. (A) Best-fit solution for fluid pressure calculated with a variable permeability model activated at failure. For comparison, the fluid pressure calculated along the fault with a variable permeability and a constant permeability is presented. (B) Fault displacement calculated for the best-fit solution obtained with the variable permeability model activated at failure. (C-F) Spatial distributions of the change in shear stress relative to the initial value at the indicated times for the best-fit solution. On each snapshot, the dashed contours represent the locations of the fluid pressure front and the dashed orange contours mark the locations of the shear stress front.

Figure 9-13 shows the displacement field during fault activation in a vertical cross section perpendicular to the fault strike. This model geometry is slightly different from the one described previously since we added a secondary fault where the injection point was located in order to better reproduce the field geometry (Figure 9-10). Model reproduces well the normal faulting displacements with the fault hanging wall slipping downwards to the left of the figure. The thick red arrow represents the pressurized zone which is of smaller extent than the displacement zone as described in Figure 9-12. This model also shows the location of the pore pressure monitoring points. It appears that BFS 4 and BFS 5 are located in the compression zone induced in the intact rock by the fault movement. Displacements at BFS4 and BFS5 are of the orders of 10 to 80 microns and pore pressure increases are the orders of 10^{-4}MPa. We calculate that it corresponds in these zones to a stress variation of ~10^{-4} MPa which is in good accordance with the observed pore pressure increase.

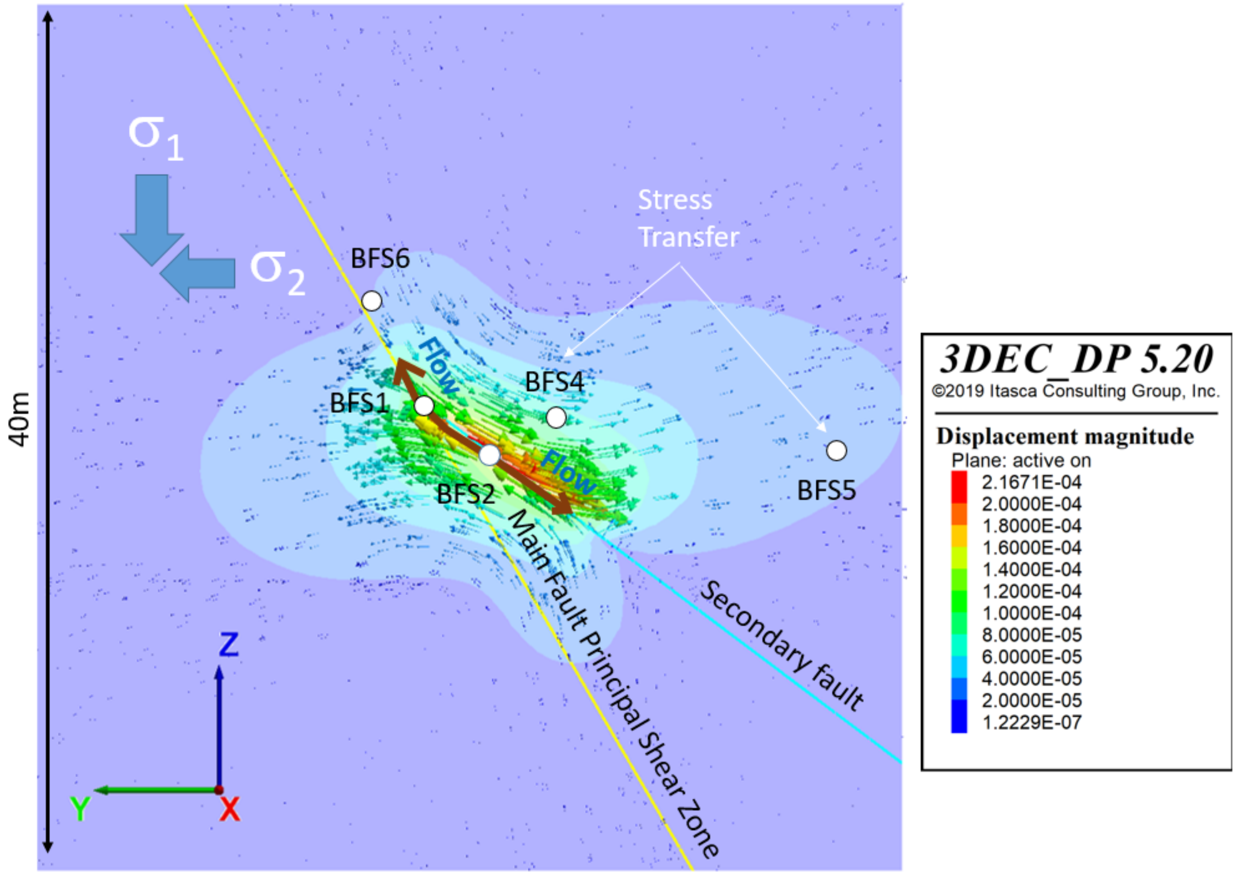

Figure 9-13. Displacement field calculated at rupture in a vertical plane perpendicular to fault strike.

9.3.3.2 Sensitivity analysis of the hydraulic response to the hydromechanical fault properties and stress state

9.3.3.2.1 Effect of the initial pre-stress conditions

Figure 9-14 shows the comparison of the hydromechanical response of the fault to different levels of initial stress conditions with the ratio of the shear stress to the effective normal stress (τ_o/σ_o). We have chosen the best-fit solution presented in the previous section as the reference case ($\tau_o/\sigma_o = 0.0919$) for comparison. Compared to this reference case, results indicate that the initial stress state influences the starting time of the fluid pressure increase and associated fault displacements. In addition, the amplitude of the fault slip is also sensitive to the stress state, although the maximum amplitude of the fault opening is less sensitive. Results show that the higher the stress ratio, the earlier is the fluid pressure increase and the starting of fault slip. Also, the higher the stress ratio, the stronger is the slip amplitude. The slip develops with sequences of slow and rapid accelerations. The major fault opening event always occur later than the fault slip. When the peak value of fault opening is reached, rapid sequences of closing and opening then occur due to the breaking of one of the three subcontacts (i.e., nodes) in a triangular zone of the grid mesh. When a subcontact breaks, the fault opens and pressure drops.

Thus, our model confirms that the pre-stress conditions and, therefore, the criticality (i.e., closeness to failure) of the fault is an important parameter to explain the temporal evolution and the amplitude of the fluid pressure and fault displacement response during fluid injection.

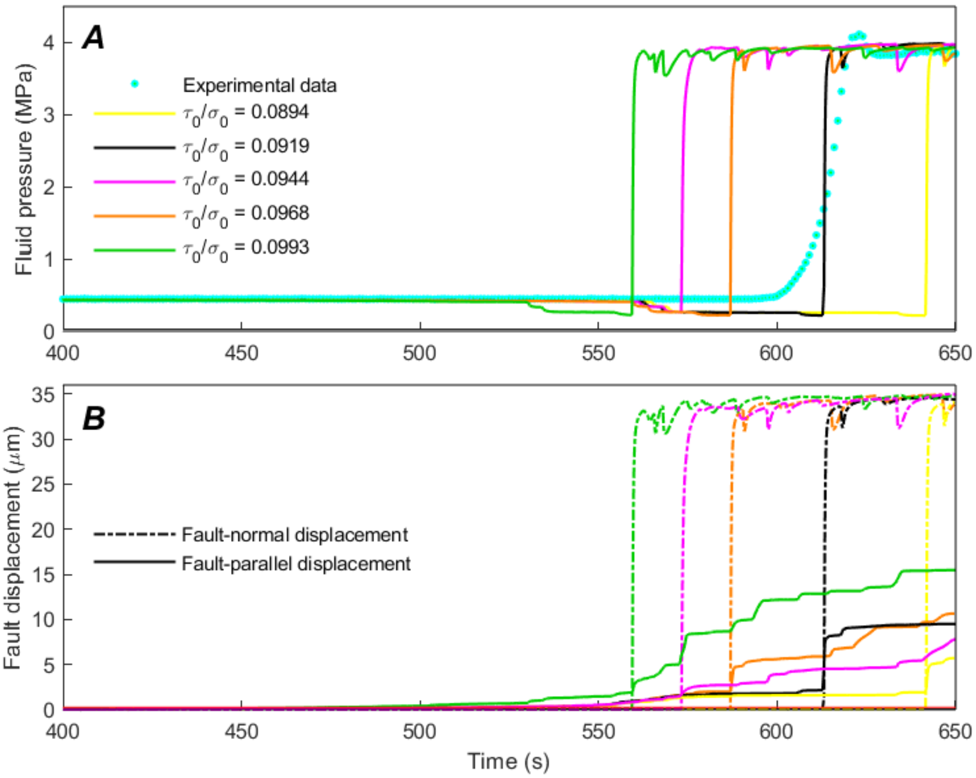

Figure 9-14. Effect of different pre-stress conditions (τ_o/σ_o) on the (A) fluid pressure and (B) fault displacements calculated at the observation point. τ_o is the initial shear stress and σo is the initial effective normal stress at the injection.

9.3.3.2.2 Effect of the static friction coefficient

Figure 9-15 indicates that the initial static friction coefficient has an influence both on the temporal evolution of fluid pressure and fault displacements. For a case with a small friction coefficient ($\mu_o = 0.365$), a slow failure starts (around 500 seconds) earlier compared to cases with a higher friction coefficient that delays the starting time of failure. Thus, the lower the friction coefficient of the fault, the earlier is the triggering of fault slip and the fluid pressure increase. The fault slip is reduced when the friction is higher. This is attributed to the fact that the fault has a greater resistance to failure. When the pressurization in a ruptured region of the fault, this promotes a longer sequence of slip.

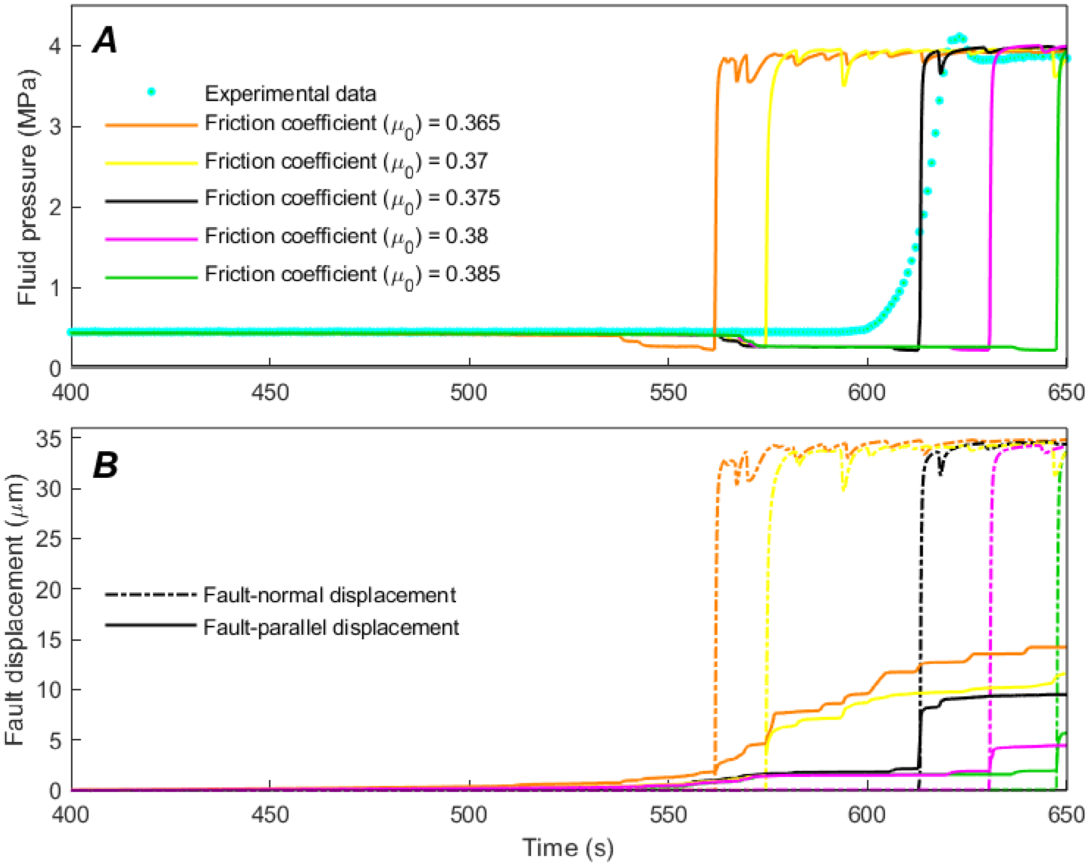

Figure 9-15. Effect of different fault friction coefficient (μ_o) on the (A) fluid pressure and (B) fault displacements calculated at the observation point.

9.3.3.2.3 Effect of the initial hydraulic aperture

Figure 9-16 shows the comparison of the hydromechanical response of the fault zone to different values of the initial fault hydraulic aperture. The smaller the initial hydraulic aperture, the later is the starting point of the fault opening and pressure increase. For a larger initial aperture, the change in aperture at failure occurs earlier. Thus, fluid pressure penetrates farther into the fault for a given injected pressure and time increment for a high initial aperture. The more widespread the pressure increase (with a larger radius of influence), the greater the force acting on the fault surface area, which, in turn, induces additional stress perturbation that helps propagate a slip.

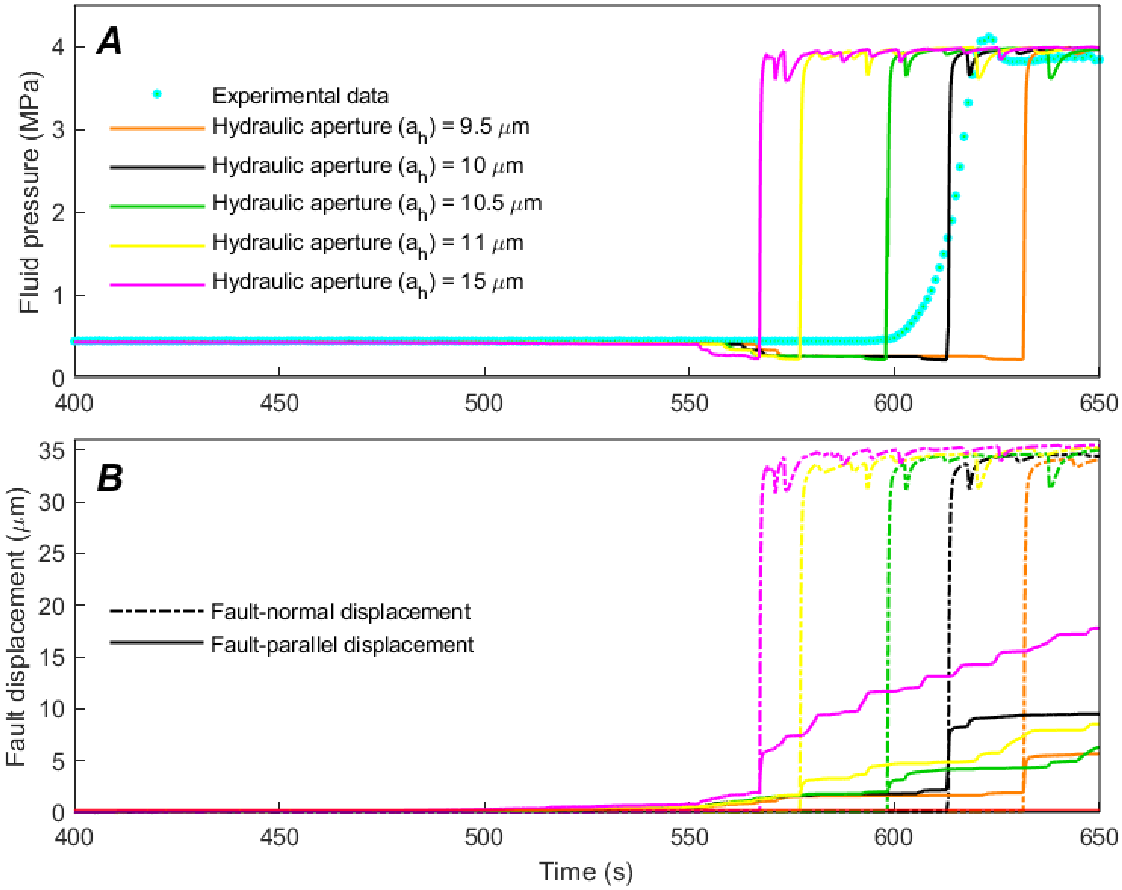

Figure 9-16. Effect of different fault hydraulic aperture on the (A) fluid pressure and (B) fault displacements calculated at the observation point.

9.3.3.2.4 Effect of the fault dilatancy

Figure 9-17 shows the comparison of the hydromechanical response of the fault zone to different values of the fault dilation angle. Similar to the effect of the initial hydraulic apertures, the smaller the fault dilation angle, the latter is the starting point of the fault opening and pressure increase. For a larger dilation angle, the change in aperture at failure occurs earlier. Thus, fluid pressure penetrates farther into the fault for a given injected pressure and time increment for a high dilation angle. The more widespread the pressure increase (with a larger radius of influence), the greater the force acting on the fault surface area, which, in turn, induces additional stress perturbation that helps propagate slip and open the fault for pressurization.

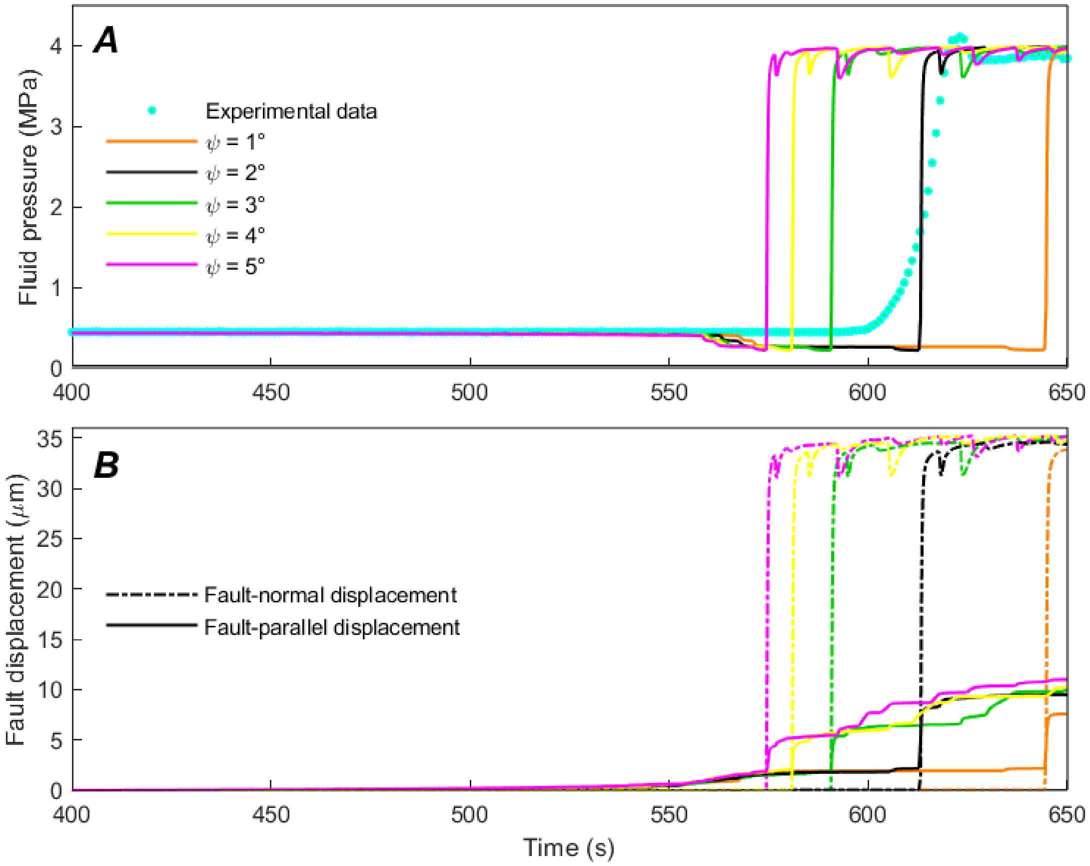

Figure 9-17. Effect of different fault dilation angle (ψ) on the (A) fluid pressure and (B) fault displacements calculated at the observation point.

9.3.4 Interpretation and Conclusions

We developed a 3D fully coupled hydromechanical numerical model to analyze the displacement, fluid pressure and injection flowrate data measured during an injection pressure-step-rate test conducted to activate a fault affecting the Mont Terri Opalinus Clay. We find that the fluid pressure measured at an observation point spaced of few meters from injection is relatively well reproduced with a crack flow model that simulates fluid flow and permeability evolution in the part of the fault activated in shear failure, and prevent flow from occurring in the remaining elastic parts. This assumption is justified in very low permeability fractured rock like shales. Conversely, a conventional fluid flow model based on the cubic law, with or without permeability changes, does not reproduce the shape, the amplitude and the time evolution of the observed fluid pressure. This result shows that fluid pressure diffusion in a low permeability host rock can be controlled at the first place by the stress perturbation and failure ahead of the pressurized zone. This is fundamentally different of continuous fluid flow model employed to explain pressure diffusion in permeable media.

Our models show two mechanisms of fault activation in an initially low permeable inactive shale fault (Figure 9-18). In the nearfield of the pressure source, fault is opening when the injection pressure induces a drop to almost zero of the normal stress on the fault. This is consistent with previous theoretical studies that demonstrated that a local fluid pressure must get close to the total fault normal stress before a fault slip being triggered (Viesca & Rice 2012). One reason may be that an elevated fluid pressure is required to activate the fault which is not favorably oriented towards stress as described in different previous theoretical works (Axen 1992; Rice 1992; Faulkner & Rutter 2001; Garagash & Germanovich 2012). In addition to that, it appeared that in such a shale fault, this effect is amplified by the initial very low initial permeability of the fault and by the low rigidity of the rock surrounding the fault. This is creating conditions for a mixed opening and shearing rupture mode of propagation. Indeed, fluid needs to force its way through ruptured patches within the fault. Result is an exceptionally high normal displacement measured at the injection point compared to the fault tangential displacement. Further away, in zones surrounding the fluid pressure front, slip is driven by increased shear stress and frictional weakening. Indeed, failure in the pressurized fault patch increases the shear stress beyond the pressure front where the shear strength reduces as a function of the slip velocity. The reduction in fault strength is more pronounced in the pressurized zone than in the immediate surrounding region. Models show that the larger the change in fault permeability in the pressurized zone the larger is the slipping a zone (Cappa et al., 2018). In addition to the stress criticality of the fault, the size of the slip zone is also influenced by the size of the fault surface area affected by overpressure. These models thus give complementary information about the mechanisms of permeability creation, highlighting that fault opening is more important than fault slip for creating flow paths in shale faults.

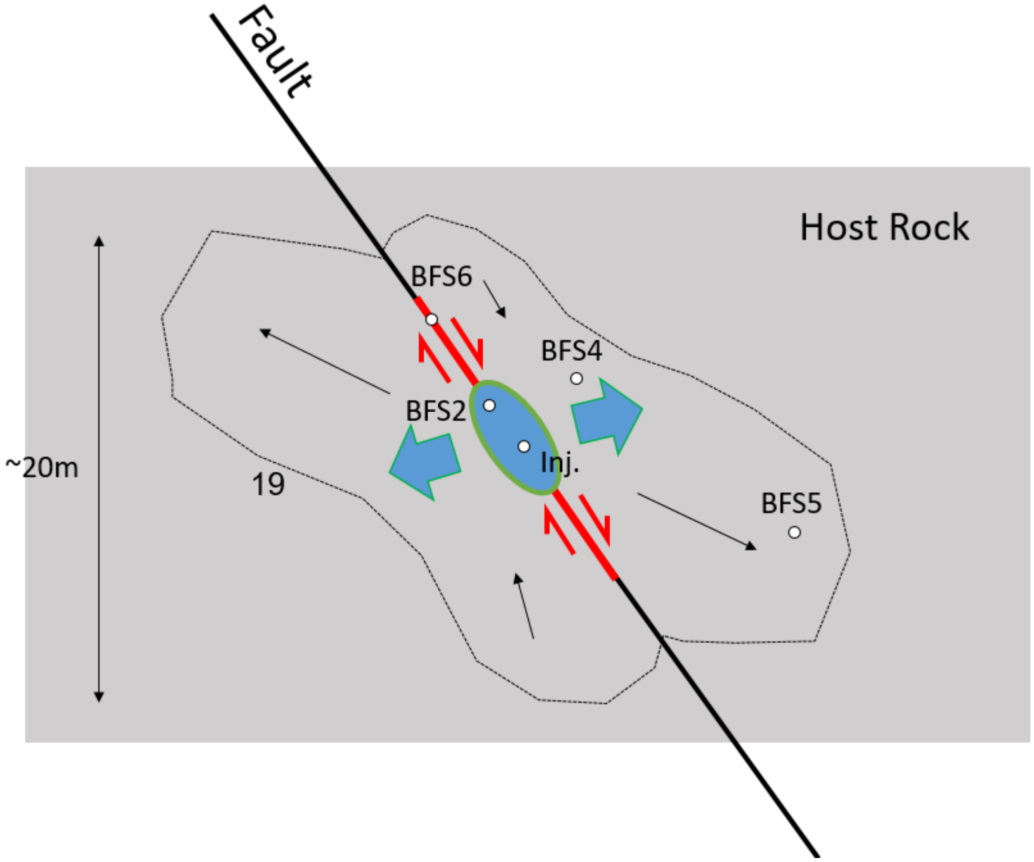

Figure 9-18. Conceptual model of fault activation induced by excess pore pressures in a very low permeable argillite rock. Blue indicates pressurized zone with mechanical expansion and red arrows showing shear activation along the fault. Black arrows indicated displacement and stress transfer.

9.4 Short- to long-term pore pressure signals related to fault activation in the Mt Terri argillite

Figure 9-19 shows the pore pressure evolution continuously monitored at BFS4, BFS5 and BFS6 point from January 2015 until April 2020. This time period includes the experiments of fault activation by fluid injections in November 2015 and the Mt Terri gallery excavation period from March 2018 to May 2019. The three monitoring points are located in Figure 9-19b (their location can also be found in Figure 9-10).

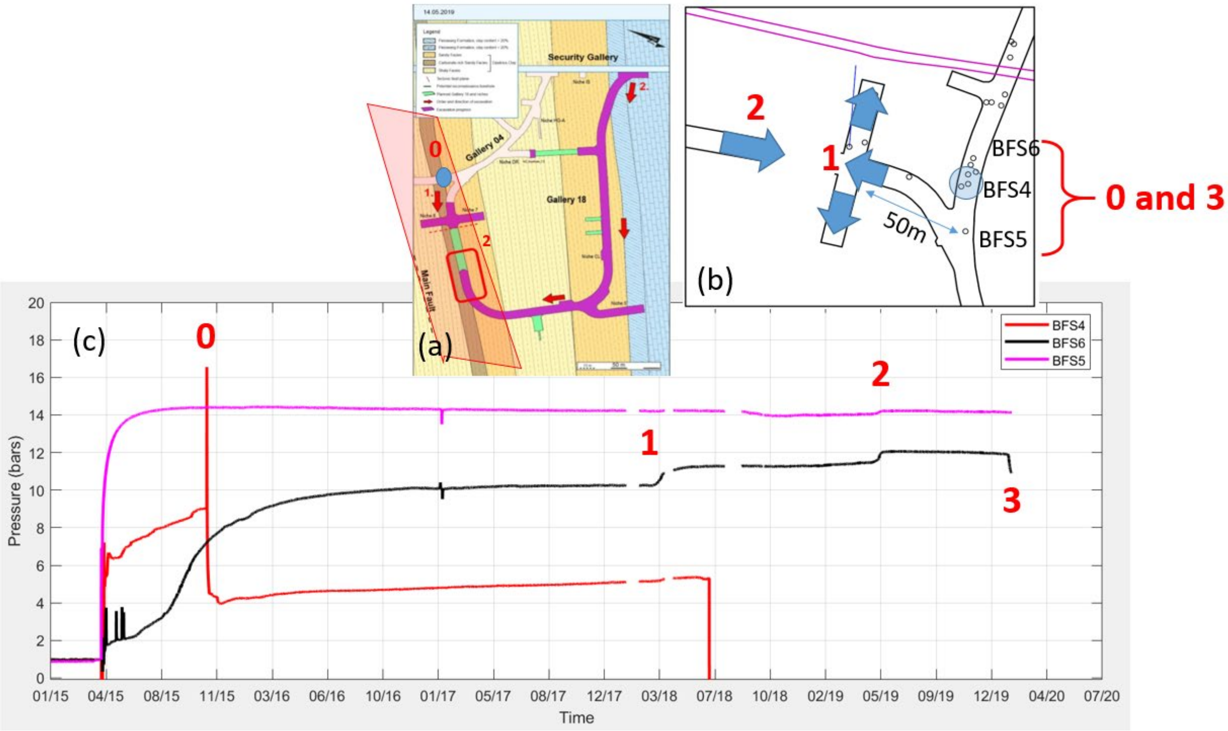

Figure 9-19. Pore pressure variations related to short- and long-term fault activation effects in the argillite rock of Mt Terri.

The pressure activation experiments are clearly seen at BFS4 (Point 0 in Figure 9-19c). Indeed, during one test conducted at 37.2 m depth (different from the one described in Section 9.4), the BFS4 was hydraulically connected to the injection borehole. This explains the sudden large pressure increase to about 16 bars. Interestingly, after the fault stimulation, pressure droped to a value of 4 bars slowly increasing with time until the sensor broke, but never recovered to its initial value. There are two possible explanations to that long-term hydraulic response: (1) Damage induced during fault activation created a large pore volume that cannot be filled over the observation time scale given the very low permeability of the host rock; and (2) The BFS4 point is still hydraulically connected to the injection borehole which is about 2 m away. This borehole was left open and unsaturated after the tests. If it is the case, this would show that the BFS4 fracture did not seal with time or did not fully close at the end of the injection test. As in the test modeled in Section 9.4, this point experienced a mixed mode failure involving shear and normal opening of preexisting secondary faults.

Points 1 and 2 in Figure 9-19 respectively correspond to the excavation initiation in zone 1 and to the excavation break-through in zone 2 (Figure 9-19a). BFS6, which is located in the Main fault displayed larger pore pressure increase than BFS5, which is in the intact rock. Both showed irreversible increases occurring 50 to 70 m away from the excavation. As described in Section 9.3, such increases may correspond to a compressive stress transfer during the excavation period. The pore pressure decrease related to the post excavation relaxation was not seen at these points, probably because of a local effect related to pressure perturbation around the newly created gallery. Here the points are away from this gallery and no pressure effect could be expected. If the pore pressure increase at BFS6 follows the same mechanism as observed in borehole BCSD-7 (Section 9.3), it could be related to a reverse shear activation of the fault at this point.

Finally, Point 3 showed a sharp pressure drop at BFS6, which was caused by drilling of a new borehole about 2 meters away. Damage induced by drilling may have connected BFS6 to the new borehole affected by the atmospheric pressure.

All these examples, thus, show no pore pressure recovery several months to years following either an overpressure or a stress transfer fault activation event in the Mt Terri main fault. It leaves open the question whether such complex thick fault zones in argillite may or may not self-seal after reactivation.

9.5 Conclusion

Understanding fault reactivation due to pressure and stress changes, the possible formation of permeable pathways, and their potential long-term sealing and healing are critical in assessing the performance of radioactive waste repositories in shale formations. Since 2015, three semi-controlled fault activation projects called FS, CS-D and FS-B have been conducted in a fault zone intersecting the Opalinus Clay formation at 300 m depth in the Mont Terri URL (Switzerland).

In 2015, the FS injections conducted in five borehole intervals set at different locations within the fault zone showed that injected fluids could only penetrate the fault when the injection pressure equals the clamping stress on the fault, in which case they trigger complex opening and slip behavior on different structures inside the three meter thick fault zone. One key finding is that the initially very low permeability of the fault increases strongly at rupture. The FS experiments gave valuable insights into the spatial extent of the hydraulic perturbation and its evolution after the initial activation event. During the fault activations in 2015, poroelastic stress transfer was observed in a large Opalinus Clay volume around the rupture patch, producing pore pressure drop of ~4 x 10^{-4} MPa in the host rock up to 20 m away from the ruptured fault patch. Since then, the pressure in the ruptured patch did not recover, remaining ~0.45 MPa below its initial value. This unexpected result suggests a long-term modification of the fault zone hydrogeological response clearly related to irreversible changes in the fault pore pressure caused by the activation.

In 2019, installation of the two new CS-D and FS-B experiments in the same fault started with an extensive characterization program of cored boreholes drilled parallel and across the Main Fault core. This characterization covered a large 100 m scale fault zone volume including the volume of the earlier 2015 experiments. New types of measurements were added to track the long-term leakage in the fault, including additional pore pressure monitoring, injected water geochemical tracing, distributed strain monitoring using DSS, DTS and DAS optical fibers cemented behind casing, and time-lapse three-dimensional cross-hole active seismic imaging across the fault zone. In May and June of 2019, prior to the actual fault activations planned in the CS-D and FS-B experiments, the exhaustive multi-parameter monitoring network captured significant pore pressure changes coupled to fault displacements triggered by ongoing excavation work for a new Mont Terri gallery. This unexpected hydromechanical response of a fault ~40 to 50 m away from an excavation, thus at distances significantly further than a few tunnel diameters, is of crucial importance in assessing the long-term loss of faulted host rock integrity.

Future work will include (i) probing the effects of new types of fault activations in argillite, such as thermal pressurization, and (ii) the re-testing of the features stimulated in the 2015 FS experiment to eventually detect some traces of activation induced damage and sealing. We will use the developed instrument and the theoretical concepts to define protocols to estimate in situ fault activation, induced seismicity and self-sealing potentials of faults affecting argillite rocks.

This page is intentionally left blank.

10. MODELING MONT TERRI FAULT SLIP EXPERIMENTS (DECOVALEX-2019)

LBNL is a task lead for the modeling efforts for the DECOVALEX-2019 fault slip experiment, and is also conducting model simulations as a research team. This section provides a brief summary and some example results, while a complete coverage is given in Graupner et al., (2020) and Rutqvist et al., (2020).

Figure 10.1 provides an overview of the experiments, which are denoted in the Mont Terri project as the 'FS Experiment.' The experiment explores the coupling between fault reactivation in a clay host rock and the potential enhanced fluid displacement through a low permeability formation.

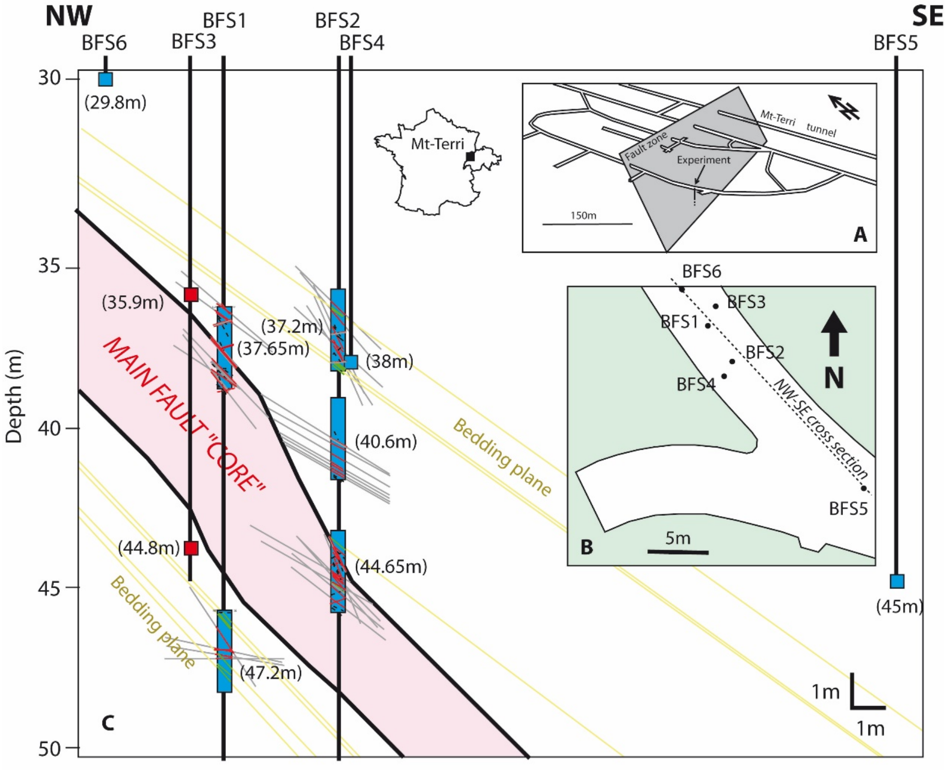

Figure 10-1. Mont Terri fault activation experiment setting. A – Mont Terri main fault with the location of the experiment (red squares-seismic sensors, blue squares-piezometers, blue rectangles-injection and monitoring intervals). B – Cross section of the Main Fault with the locations of the packed-off sections.

At Mont Terri, a total of five injection tests were conducted beneath, within and above the Main Fault during the two measurement campaigns of June and October-November 2015. Two tests related to injection at two difference sections of BFS2 were selected for modeling within Task B of DECOVALEX-2019. The tests were selected as they provided data for fault activation, both at the main fault and a minor fault in the fault damage zone.

10.1 DECOVALEX-2019 Task B Modeling Steps

Task B of DECOVALEX-2019 is conducted in the following three steps with progressively increasing complexity:

Step 1) Model inception: A benchmark calculation of activation of a single fault plane,

Step 2) Minor fault activation: Interpretative modeling of observed minor fault-activation, and

Step 3) Major fault activation: Interpretative modeling of observed activation in a major fault

Step 1 started with modeling of a single fault plane broadly representing the minor fault to be modeled in Step 2. The real step pressure injection scheme was applied during this initial benchmark modeling, and reasonable estimated properties for Opalinus Clay and the minor fault are taken from the site investigations at Mont Terri. Step 3 was focused on another injection experiment conducted from another section of the same injection borehole, which resulted in shear activation and permeability changes along the main fault.

10.2 STEP 2 MODELING OF FAULT ACTIVATION EXPERIMENT

In the following subsections, we first present the Step 2 field experiment and data with some general observations and interpretations, followed by the models and their parametrizations, and finally the model results with comparison between simulated and experimental data.

10.2.1 Field experimental data

The Step 2 fault activation experiment was conducted by fluid injection into a 2.4-m long isolated injection chamber of borehole BFS2 with monitoring of fluid pressure responses in borehole BFS4 located at a horizontal distance of 1.5 m (Figures 10-2). 12 discontinuity planes intersecting the injection chamber of BFS2 being pressurized during the experiment (Figure 10-2). Most of these discontinuities strike N030°-060°E and dip 50-70°SE and thus one or several of these discontinuities could be opened and activated during the borehole pressurization. The stress field estimated at the Mont Terri Laboratory (Corkum and Marin, 2007) is oriented such that the maximum stress is approximately vertical at a magnitude of 6 to 7 MPa, while the intermediate principal stress is approximately horizontal at 4 to 5 MPa and oriented approximately perpendicular to the average strike of the discontinuities observed in the BFS2 borehole section (Figure 10-2a).

Figure 10-3 presents the field data during this injection experiment. Injection flowrate, injection chamber pressure and borehole displacements were monitored at a 500Hz sampling frequency. The borehole deformations were measured between anchors, fixed to the borehole wall in a 0.5 m vertical section of the injection borehole. Thus, the deformation measurements are anchored within the central part of the injection chamber. The anchor displacements shown in Figure 10-3b are the displacements of the upper anchor relative to the lower anchor, in vertical up, northern and western directions. Moreover, the relative displacements shown in Figure 10-3b have been corrected to filter out elastic deformations of the equipment and injection chamber in order to deduce the displacement of the discontinuity itself.

The fluid flow data in Figure 10-3 show a sharp increase in injection flow rate at about 430 seconds, which is about 10 seconds after the injection pressure was increased to the peak pressure of just above 6 MPa. At this point in time, a sharp increase in fluid pressure can be observed at the monitoring point in borehole BSF4, located about 1.5 m horizontally from the injection point. Thereafter, as the injection pressure is reduced below about 4 MPa, an abrupt decrease in injection flow rate is noted at 453 seconds. The anchor displacements in Figure 10-3 indicate that fracture deformation occurs already during the first few injection pressure steps, with displacements correlated to injection pressure steps. This may be interpreted as opening of the small fracture around the injection borehole that had been previously created during the initial hand pump injection. The displacements shown in Figure 10-3 indicate opening of a steeply dipping discontinuity.

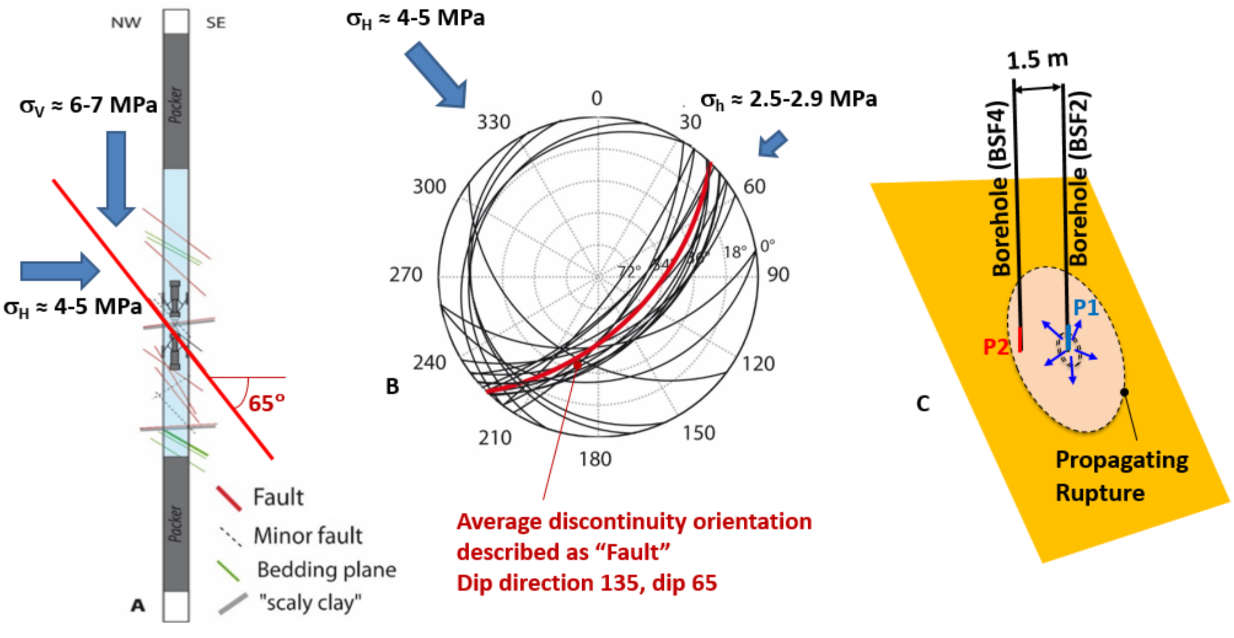

Figure 10-2. Mapped fractures within injection chamber of Step 2 fault activation experiment and synthesized Mont Terri stress estimates based on Corkum and Martin (2007). (A) vertical cross section of the injection chamber, (B) lower hemisphere stereographic projection with average discontinuity orientation marked in red, and (C) conceptual model of injection-induced rupture propagation along the weak plane to finally connect P1 with P2 (Rutqvist et al., 2020).

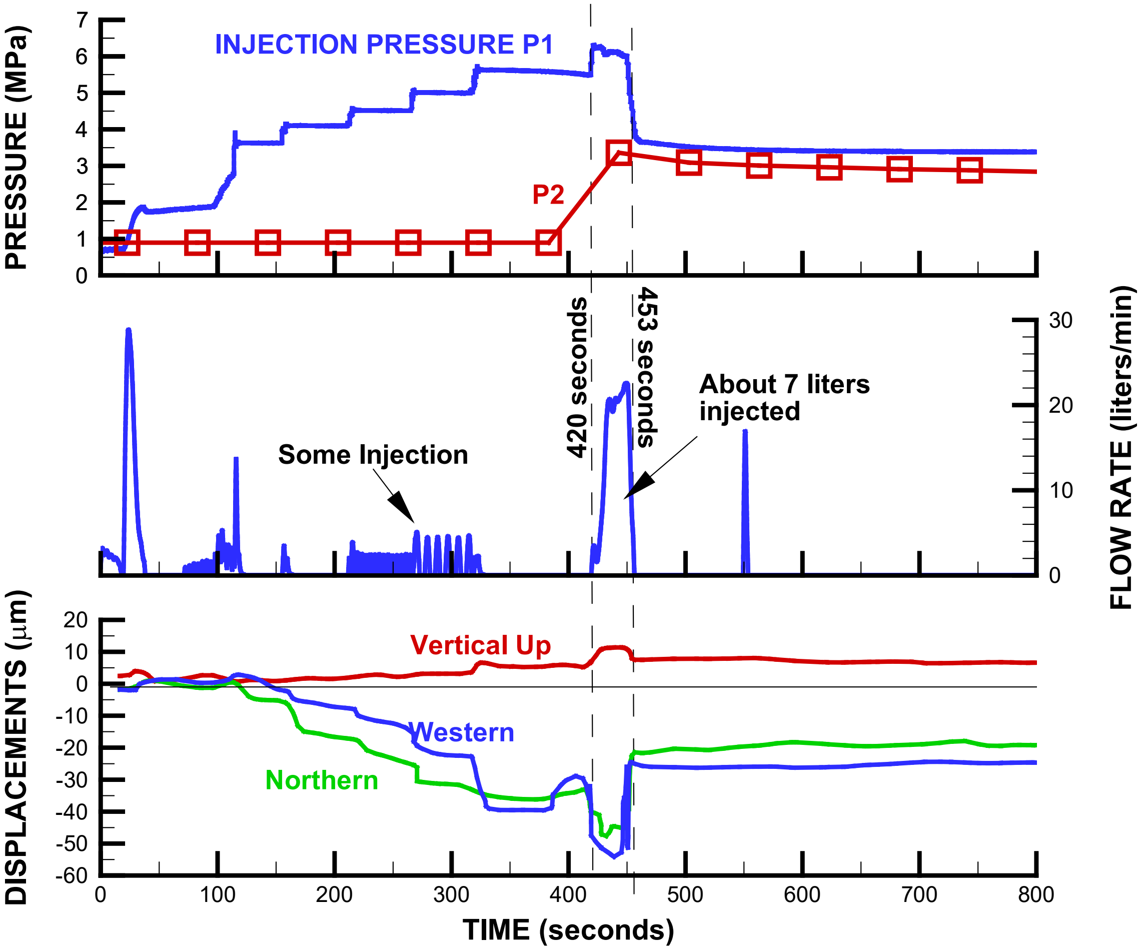

Figure 10-3. Field data related to the Step 2 fault activation experiment conducted within the damage zone of the Mont Terri Main Fault (Modified from Guglielmi et al. (2017). (Top) Controlled injection pressure P1 in BFS2 and resulting pressure response P2 at BFS4, (Middle) injection rate into BFS2 and (Bottom) anchor displacements at the injection borehole BFS2.

10.3 Models and parameters

The teams applied similar models to those that had been developed and verified in the previous benchmark tests. Also, most teams assumed a similar geometry, i.e., activation of a discontinuity dipping 65° and with the strike being approximately parallel to the minimum principal stress direction. As seen in Figure 10-2, this is consistent with the estimates of the in-situ stress field at Mont Terri (Corkum and Martin, 2007). This means that the potential for shear activation of the fault would depend on the shear stress as a result of the difference between the vertical and maximum horizontal stress magnitudes.

Figure 10-4 shows the mesh design for the six different models applied by various teams for the Step 2 modeling. CNSC's COMSOL and LBNL's TOUGH-FLAC models are half symmetric, which is possible considering the orientation of the fault relative to the stress field, with the minimum compressive stress oriented along the strike of the fault. Other models, including KIGAM's TOUGH-FLAC model, ENSI's OGS model, as well as LBNL's and INER's 3DEC models include the entire 20 m cube and can therefore be exposed to a stress field that is not exactly orthogonal to the strike of the fault (Rutqvist et al. 2020).

The key for predicting the timing of the rupture is to accurately calibrate the parameters to induce shear failure or tensile failure and rupture propagation at 420 seconds. All teams applied a friction angle of 22 degrees, which was a parameter given to the teams in the earlier benchmark calculation and this value is based on laboratory testing on Opalinus Clay within the Mont Terri project. A number of teams also followed the benchmark calculation by assuming a cohesionless fault, i.e., cohesion was set to 0. Note that this would also imply a tensile strength equal to 0. Considering such strength properties, teams then varied the stress magnitudes and orientations to calibrate for rupture initiation and thereby attempted to achieve the best possible match with observed data.

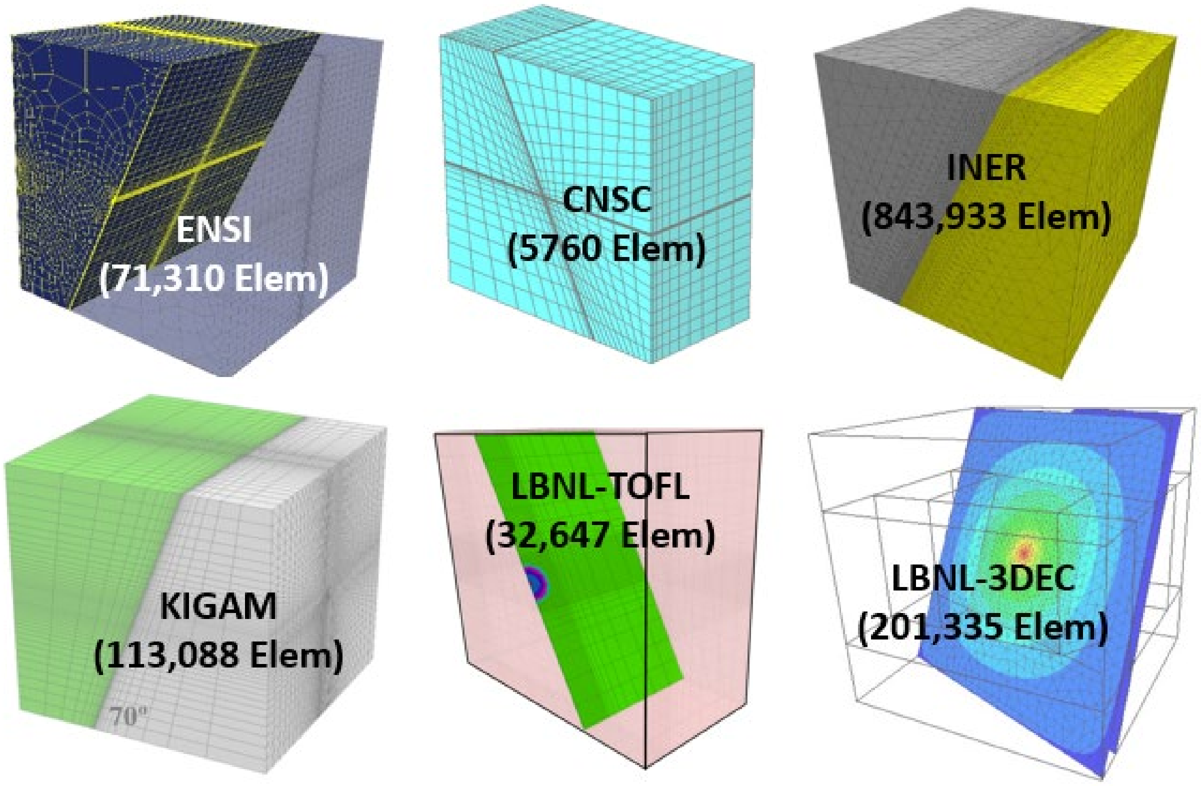

Figure 10-4. Mesh discretization applied by the different teams for modeling the Step 2 fault activation experiment (Rutqvist et al., 2020).

10.4 Modeling results with comparison to field data

Figure 10-5 presents comparison of the field data with the simulation results obtained with the six models that were applied to the Step 2 fault activation experiment. A good agreement with field data is obtained by all the modeling teams regarding the timing of the abrupt flow rate increase at 430 seconds and the subsequent flow rate decrease at 453 seconds (Figure 10-5a). A similarly good agreement is achieved for the timing of the pressure response at the monitoring well (Figure 10-5b), as well as the trends of the borehole anchor displacements (Figure 10-5c). The CNSC modeling shows a smoother pressure responses at the monitoring borehole with a final pressure at the end (800 seconds) that is closer to the field measurements.

The total injection flow volume and the evolution of the injection rate is captured very well by most teams (Figure 10-5a). Good agreement is achieved regarding the relative anchor displacements, especially for the north and west relative displacements (Figure 10-5c). The north and west displacements are each at an angle approximately +45° and -45° off the discontinuity dip direction, but are approximately equal in magnitude. The key parameters to match the measured anchor displacements are normal stiffness, shear stress, shear strength, and the dip of the discontinuity. The normal displacement determines the fracture opening that occurs at each pressure step during the initial 420 seconds of the injection. Thereafter, around 420 seconds, the rupture occurs, which induces some additional displacements and this is followed by a rebound when the injection pressure is reduced.

After reaching the peak injection pressure of 6 MPa, most teams calculated a shear failure with a relatively small shear displacement (Figure 10-5d). Several modeling teams found that a large shear slip upon shear failure needs to be prevented in order to match the observed anchor displacements. This was achieved by some of the teams by either keeping the shear stress on the fault relatively small (i.e., limiting the difference between σV and σH), or by considering an increased cohesion.

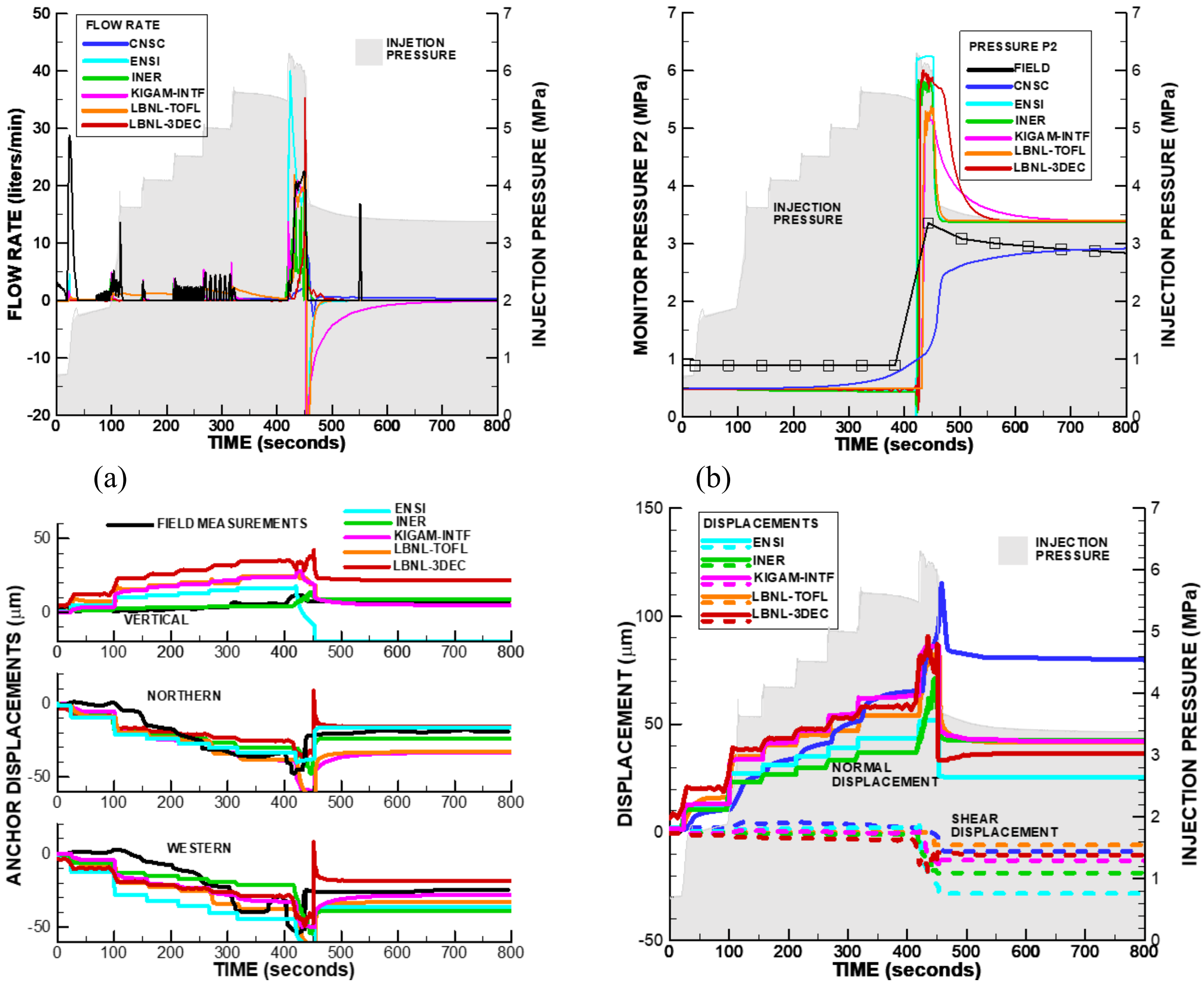

(a) (b)

(c) (d)

Figure 10-5. Comparison of modeling results with field data for the Step 2 fault activation experiment with the controlled injection pressure in gray shade and other field data in black. (a) Injection flow rate, (b) pressure at P2, (c) anchor displacements at P1, and (d) fracture normal and shear displacement at P1.

Overall, this DECOVALEX-2019 task has (1) resulted in important model developments and adaptations of numerical simulators to simulate fault activation, and (2) provided a better understanding of the hydromechanical behavior of minor faults and fractures in low-permeability shale formations. The key for accurately representing the two activation experiments is an application of a hydromechanical fault model that captures the abrupt activation behavior. The first characteristic of this activation behavior is a sudden increase in fracture permeability and flow rate along with a rupture propagation that is triggered at a certain injection pressure magnitude higher than the estimated stress normal to the discontinuity. The second characteristic is a sudden hydraulic closure of the discontinuity that occurs when the injection fluid pressure is reduced to about 1 to 2 MPa less than the stress normal to the fault. The fact that the activated discontinuity closes as soon as the pressure decreases provides an important and beneficial feature for nuclear waste disposal in argillaceous clays, i.e., demonstrating a self-sealing mechanism, which keeps the host rock barrier tight and limits the longevity of transport pathways (Rutqvist et al., 2020).

11. COUPLED MICROBIAL-ABIOTIC PROCESSES IN EBS AND HOST ROCK MATERIALS

Experiments on potential microbial activity present in materials collected from the FEBEX experiment continued with experiments on additional samples. Initial experiments focused on the materials in the high heat zone and control zone (Figure 11-1). Current tests expand the test materials to include intermediate temperature zones. Details of the samples can be found in previously published reports (Villar, 2020; Bárcena, 2015). To summarize, samples were collected at the FEBEX site in 2015. Before sampling, clays were cooled in the formation. After removal they were subsampled, removing external surfaces that had been in contact with extraction equipment. The final samples had an average volume of 18 cm^3 and were wrapped in plastic, vacuum sealed in aluminized Mylar bags, and stored at room temperature.

Current experiments are designed to determine if these materials possess microbial communities capable of metabolizing H_2, and how the FEBEX treatment impacted those capabilities. In FY19, two sets of materials were tested from a 'heater zone' (BD-48-6, high temperature) and from a 'cold zone' (BD-59-10) (Figure 11-1). In FY 20, two sample locations were added, one at BD-48-5 (mid high temperature) and the other at BD-48-4 (mid low temperature).

To prepare the sample of each clay type, the Mylar bags containing the subsamples were opened and a piece was broken away from the large block. This subsample was placed on an autoclaved piece of Al foil in the biosafety cabinet and scraped with a sterilized razor blade to remove the outer surfaces. Scrapings and foil were removed and the sample was placed on a new autoclaved piece of foil. A fresh sterile razor blade was then used to remove about 5 g of clay. This 'fresh' (newly exposed) layer of clay was mixed and distributed amongst 60 mL serum vials (6 for each clay type) containing 10 mL of sterile minimal salts media (Sigma M9 minimal salts, MSM), which contains small amounts of PO_4^{3-} and NH_4^+. MSM was purchased 5x concentrated (Sigma), so actual addition was 2 mL of medium and 8 mL of DI water (milliQ). The medium and water were added to 60 mL serum bottles through a 0.2 μm filter. 15 psi of gas mix was added to each serum bottle. This was done by starting with a full serum bottle of air, adding 7 mL of CO_2, and pressuring to 15 psi with a N_2/5% H_2 mix. All gas was filtered through a 0.2 um filter. This method provided a consistent gas mix for all bottles, with an average final composition of 5% CO_2, 2.8% H_2, 9% O_2, with a balance of N_2. Sterile control samples (autoclaved clay) and blanks (no clay, only media) were run for comparison purposes. Although numbers varied slightly for each experiment, 4-6 samples were prepared of each clay type, and additional 2-3 samples of autoclaved controls for each clay, and 3 blank controls for the experiment.

Samples were placed horizontally on a rocking table and incubated at 35°C. To monitor activity, gas composition of the serum bottle headspace was analyzed periodically. Gas analysis was performed on a Shimadzu GC-8AIT with Ar carrier gas, which allowed for simultaneous quantitative determination of H_2, O_2, N_2, and CO_2. GC conditions were as follows: Ar flow 0.4 kg/cm^2, detector and injection temperature 150°C, Column temperature 35°C, 80 mA current, CTRI packed column. Calibration of H_2, O_2, N_2, and CO_2 was completed prior to sampling bottles with known concentrations of gases. Samples were analyzed immediately after removing from the incubator and replaced after sampling. To sample, an alcohol saturated wipe was put on the serum stopper for 5 min to sterilize the surface of the stopper. A sterile 22-gauge needle connected to a gas tight syringe was then inserted into the stopper and 100 μL of headspace was removed and injected into the GC. A new needle was used for each bottle when sampled.

To date, four separate experimental starts have been executed, called simply Experiments 1, 2, 3 and 4. Experiment 1, started early FY19, did not produce usable data, but helped with the method development process. Experiment 2 included the high temperature clay, BD-48-6 and the control clay, BD-59-10 and has been ongoing, with some re-gassing steps, for over 400 days (Figures 11-2 and 11-3) Data from Experiment 2 continues to show consumption of H_2 in sample 59-10 sample, and no activity in the 48-6, blank, or control samples. At day 150 and 350 the 59-10 samples were re-gassed due to depletion of the H_2 in the headspace. CO_2 concentration remained relatively unchanged, some shifts were observed during the re-gassing. 59-10 also shows steady consumption of oxygen.

To further evaluate the activity in the samples, 3 samples of the 59-10 (reps 3,4 and 5) and 1 sample of the 48-6 (rep 1) were sacrificed at day 237 and submitted for DNA sequencing. Extraction of sufficient DNA from the clay for analysis was challenging but sufficient material was eventually recovered. Results from the sequencing (Table 11-1 and Figures 11-4 and 11-5) show clear enrichment of the active 59-10 sample and no enrichment in the 48-6 samples. Comparison with previous studies indicate that these bacteria types have been found in clays and have been shown to be able to utilize hydrogen. (Mayilraj and Stackebrandt 2014; Greening et al. 2015; Lopez-Fernandez et al. 2015).

Experiment 3 reproduced the samples in Experiment 2 and added samples 48-5 and 48-4. These two additional samples were located in cooler zones than 48-6 (48-5 higher temperature than 48-4) to investigate whether the intermediate temperature samples would show activity. This experiment also included a subset of 59-10 samples with a varied CO_2 concentration in the headspace. Experiment 3 did not show the same level of activity as experiment 2 in 59-10, and showed little activity in the other clay types (48-6, 48-5, 48-4) (Figure 11-6). It is suspected that the differences are likely due to a higher solid to liquid ratio. To mediate this at day 200, additional 10 mL media was added to the bottles to increase fluidity, and some more activity was seen in the 59-10 sample, but still showing slow response. In particular, although gas consumption is slower than previous observed, there appears to be activity with the highest activity seen in a bottle with an elevated CO_2 concentration of 6 % (average concentration in other bottles was 4.5%). Another possibility is that higher O_2 in Experiment 3, since the hydrogenase enzyme used to metabolize hydrogen is inhibited when O_2 is above 10%, and the start of the experiment many of the bottles were close to that level, and H_2 activity increased when O_2 levels were lowered. Due to uncertainty and needed adjustments in solids to liquid ratio, this experiment was restarted as Experiment 4, which is a repeat of the Experiment 3 setup. While this experiment has been ongoing for 3 months sampling has been limited by the COVID shutdown so no results are available at this time.

The preliminary results from Experiment 2 indicate that clay materials maintain microbial communities with the potential to metabolize H_2. However, it is interesting that the material from the hot zone did not show that potential. Whether that is due to the heating or the drying or both is unknown at this point. The higher liquid to solids ratio or O_2 levels in experiment 3 appears to have limited microbial activity further. Experiment 4 was planned to more closely replicate experiment 2 by adjusting solids and lowering O_2 to confirm previous experimental results. Planned work for the remaining of the fiscal year will focus on monitoring the new Experimental setup (experiment 4) and doing some chemical analysis on the previous experiments to see if there were additional chemical driver for the low activity in Experiment 3 (e.g., pH).

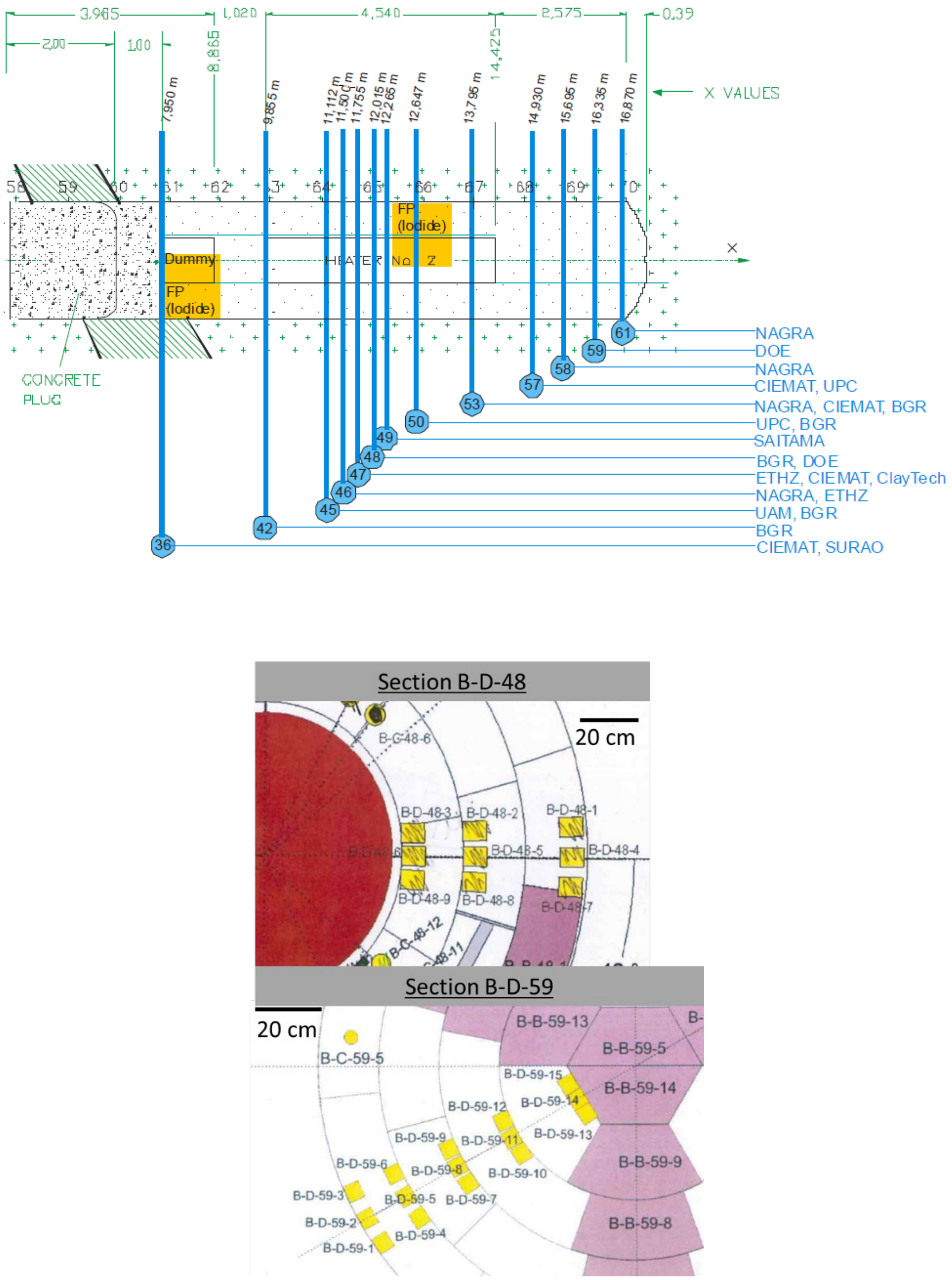

(a)

(b)

Figure 11-1. Locations of bentonite samples in original FEBEX experiment. (a) Longitudinal cross-section along FEBEX tunnel, and (b) cross-sections B-D-48 and B-D-69 (modified from Villar et al., 2017)

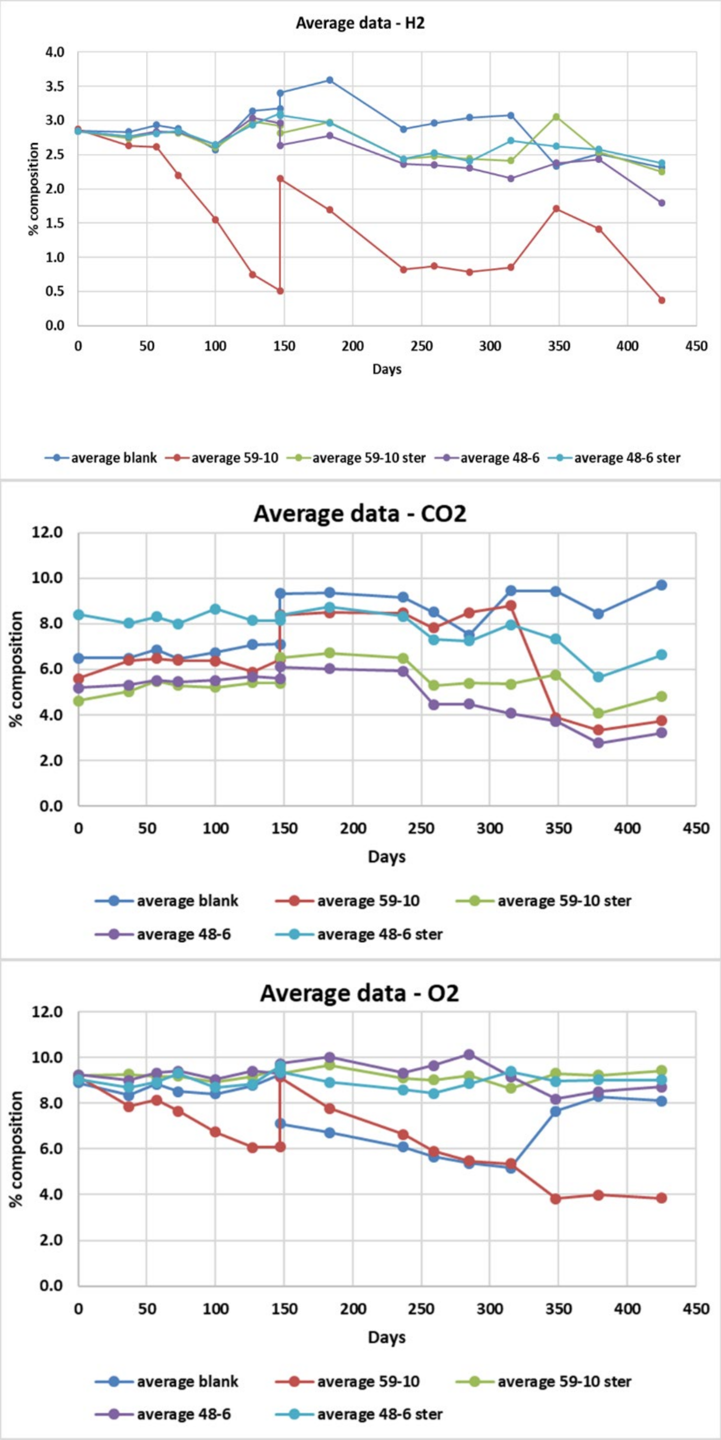

Figure 11-2. Averages of H_2, CO_2, and O_2 concentrations in each condition for Experiment 2. For the 59-10 and 48-6 samples there are 6 replicates, for the sterile control there are 3 replicates, and there are 2 blanks. Spikes of H2 concentration at day 150 and 350 are due to regassing of the headspace to replace depleted H_2.

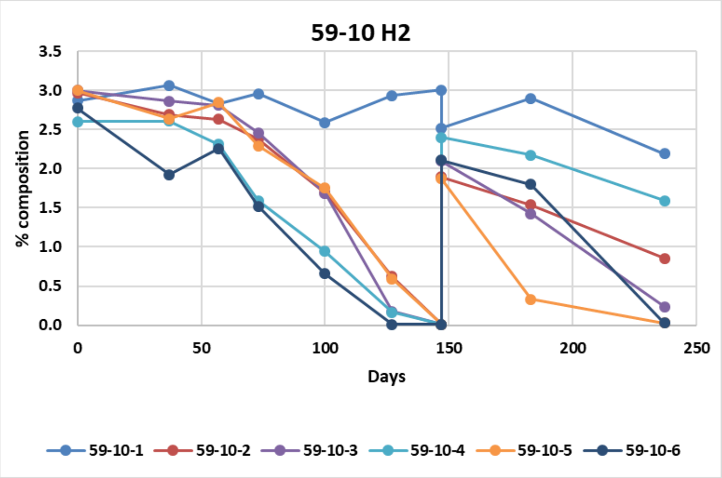

Figure 11-3. Above are individual plots of the six 59-10 bottles for the first 237 days. 59-10-1 is showing very little consumption of H_2, 59-10-2 and 59-10-4 are showing moderate activity and 59-10-3,5, and 6 are showing higher activity. Bottles 59-3, 4, and 5 were sacrificed for DNA sequencing

ID	Clay	H2 cons. level	Growth	Sample name
806rcbc144	48	low	No	48-6-1
806rcbc180	59	high	Yes	59-10-5
806rcbc168	59	medium	Yes	59-10-4
806rcbc156	59	high	Yes	59-10-3

Table 11-1. ID and sample names for DNA sequencing

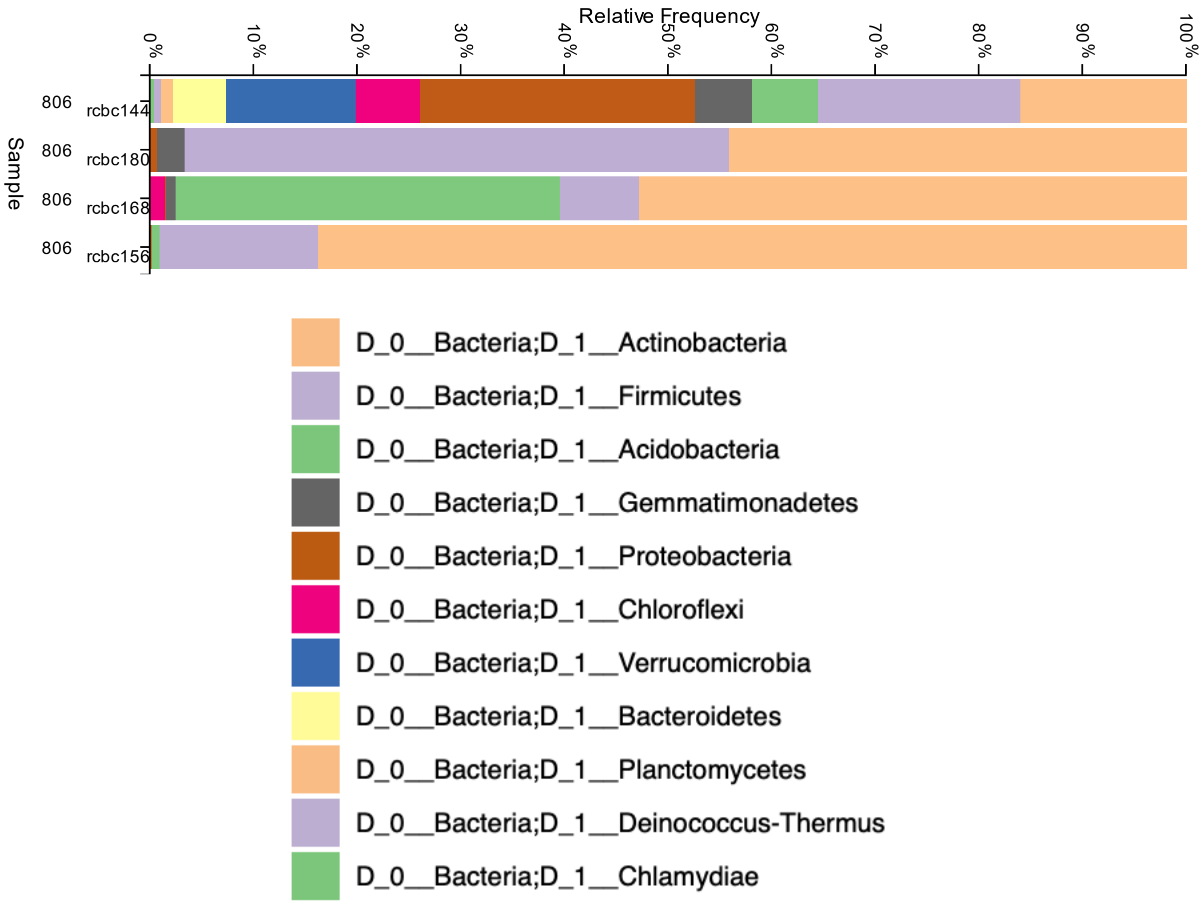

Figure 11-4. DNA sequencing results showing Taxonomy by Phylum.

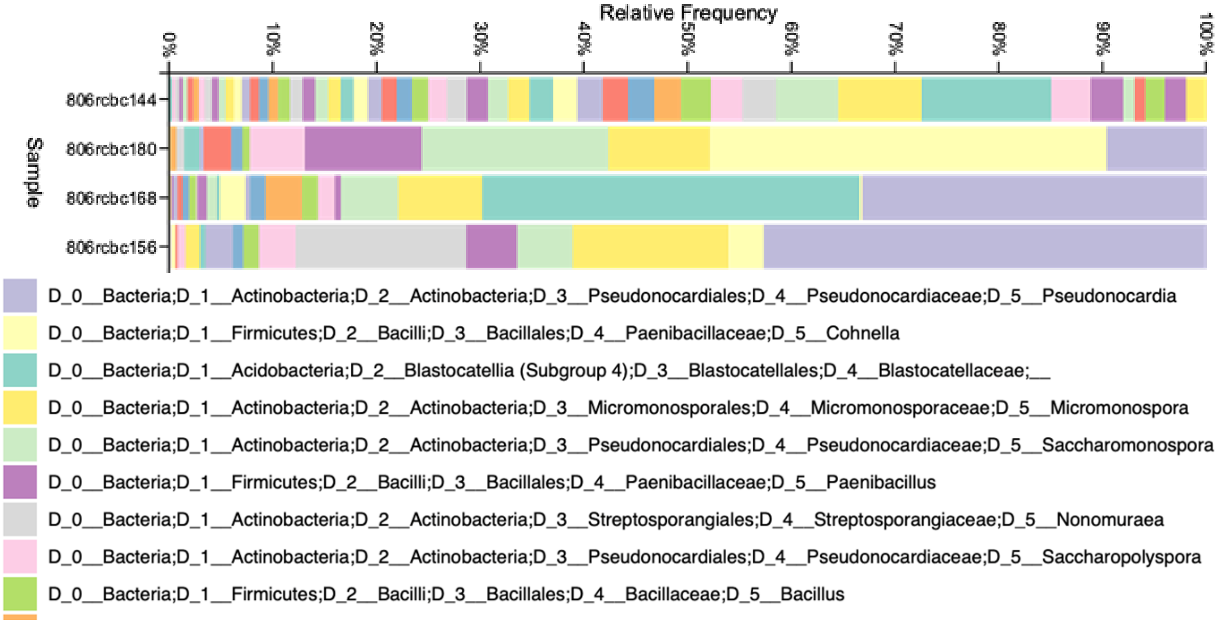

Figure 11-5. DNA sequencing results showing Taxonomy by species.

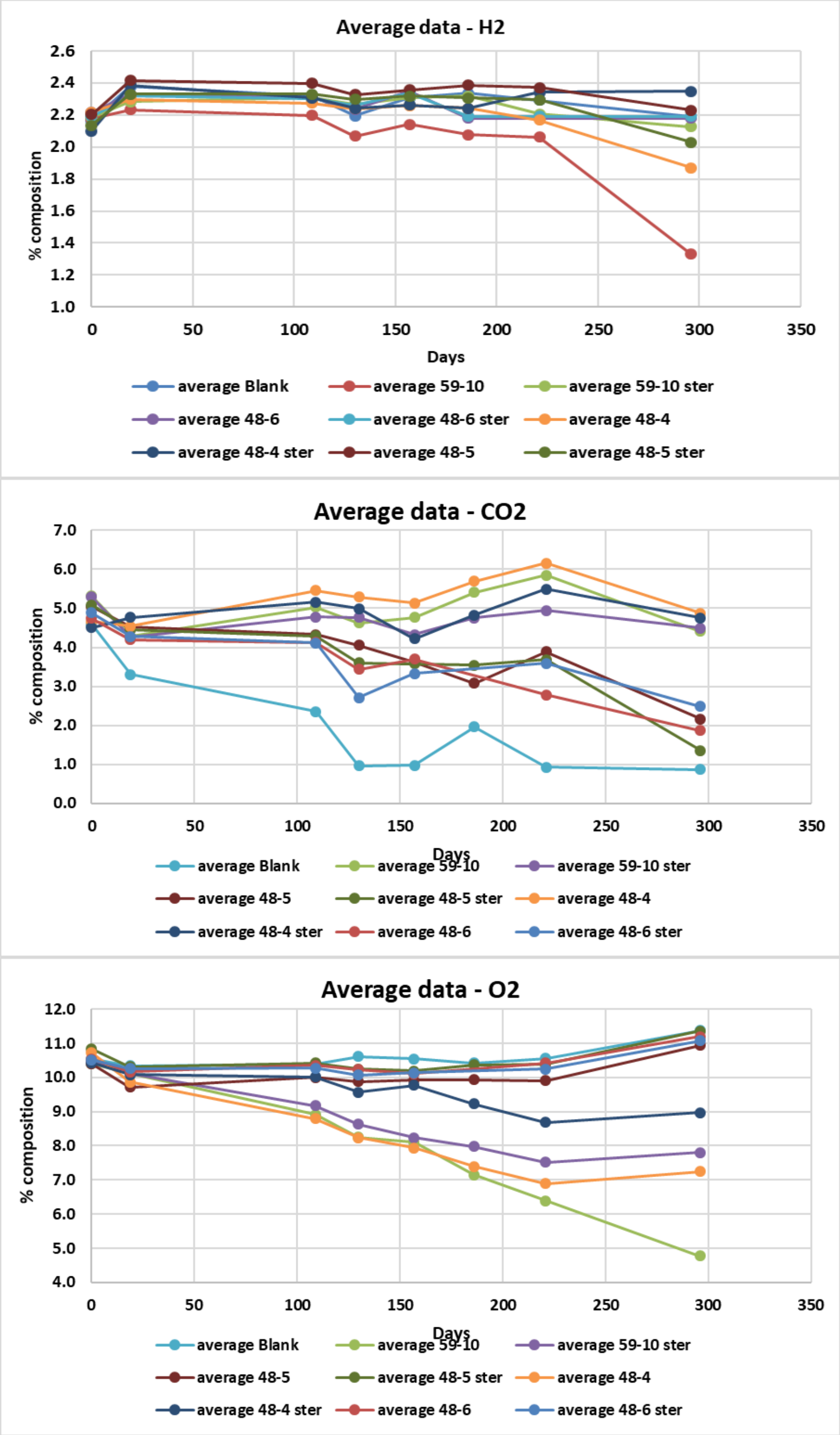

Figure 11-6. Averages of H2, O2, and CO2 concentrations in Experiment 3. H2 is showing some depletion at the 300 day sampling, but activity was much slower to start in this experiment, possibly due to the high solids content in the bottles.

12. MOLECULAR MODELING OF RADIONUCLIDE RETENTION BY BENTONITE

The capability of a bentonite barrier to impede the transport of long-lived radionuclides is an important aspect of the performance evaluation of any storage strategy. A scenario for radionuclide release involves groundwater reaching a corroded canister and mobilizing radionuclides, such as ^{233}U, ^{237}Np, and ^{239}Pu. Thus, knowledge of the aqueous speciation and chemistry of these radionuclides under relevant conditions, their interactions with clay minerals and their mobility within bentonite matrix is critically important for evaluating repository performance. The ultimate goal of this work is to develop the predictive computational model of radionuclide retention in bentonites – relevant for nuclear waste disposal safety assessments. In particular, we proposed to use molecular modeling to parametrize meso- and macroscopic models of radionuclide migration in the clay-barriers, and clay-rich rocks and soils in order to develop a robust field-scale safety assessment model. The molecular modeling offers an alternative route for model parametrization, which does not involve experimental measurement of the toxic radionuclide diffusion.

Overall trends in the speciation of radionuclides in aqueous solution and how their affinity to clay minerals changes with oxidation state and solution pH are relatively well understood (Bradbury and Baeyens 2006, Bradbury and Baeyens 2009). The preference of actinide ions to accumulate in compacted bentonites generally follows their effective charge of their aqueous species. At low pH, the clay edges are positively charged and, therefore electrostatically repel positively charged radionuclide ions. The retention occurs predominantly due to ion-exchange with the counterions on the basal plane of clay particles. The molecular dynamics simulation of Np(V) mobility in the low-charge clay interlayers (Zarzycki, Racette et al. 2020) confirm that the amount of Np uptake decreases and Np mobility increases with an increasing ionic strength due to competition of the background electrolyte cations for the exchange sites in agreement with previous experimental studies by Bradbury et al. (Bradbury and Baeyens 2005, Bradbury and Baeyens 2006).

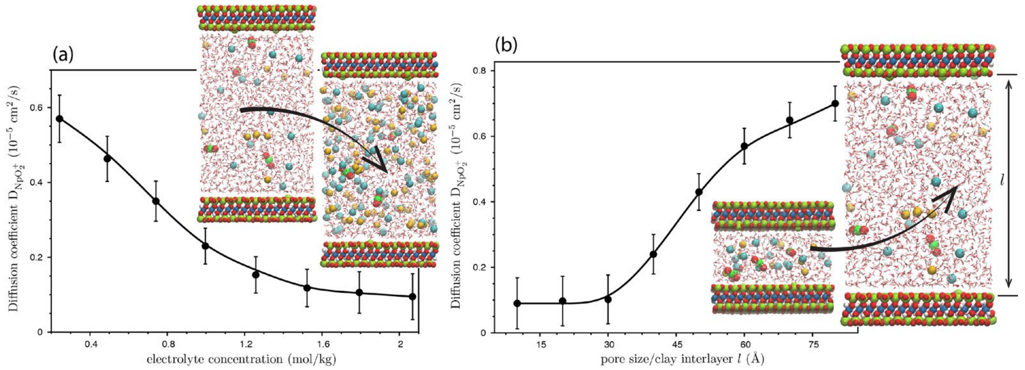

Figure 12-1. Molecular dynamics simulation of Np(V) mobility in clay interlayer (Zarzycki, Racette et al. 2020): effect of electrolyte concentration (a) and clay pore size/swelling state (b).

In Figure 12-1a, we show simulation results of Np(V) mobility in NaCl solution confined between two Na-montmorillonite layers as a function of pore size. As the separation between clay surfaces decreases, the NpO2+ become effectively trapped due to increased salinity, the proximity of surfaces and surface-induced ordering in the aqueous phase. In Figure 12-1b we show simulation results of changes in the Np(V) mobility in the clay pore only due to an increase in the salinity. The decrease in the Np(V) mobility is similar to the one observed if both salinity and confinement are operative. Our results indicate that salinity is a dominant factor affecting Np(V) retention in bentonites in the ionic-exchange regime (i.e., low pH). The ion-ion, ion-surface, and water-structuring effects are also important but as secondary order phenomena.

We extended our molecular modeling efforts by developing force-field interactions for U(VI) species and using molecular dynamics simulation to understand the role of complexation by carbonates, hydroxyls and formation of multicomponent coordination complexes (e.g., calcium carbonyl/hydroxyl uranyl).

12.1 Status of the computational prediction of the retention of multi-nuclear radionuclide complexes by bentonites

We proposed a multiscale computational framework to predict the migration of several actinides as a function of their oxidation state, rock/clay and fluid compositions, pressure, and temperature. The first step in this direction is to develop a molecular-level understanding of multi-nuclear radionuclide complexes by bentonites. This was motivated in part by the difficulties we are facing in measuring radionuclide mobilities in the typical repository conditions.

We have parametrized force-field interaction parameters developed for uranyl complexes, including carbonate-hydroxyl complexes, and combine them with existing force fields for clays and previously developed parameters for neptunium ions. Details of the development procedures and interaction parameter values are described below (see Section 12.1.1)

We have developed a computational framework for modeling retention in diverse systems by implementing a molecular modeling pipeline that takes system composition, pressure, and temperature as an input and generates its molecular representation, runs molecular dynamics simulations and analyzes radionuclide mobilities on the fly. A few examples of molecular dynamics simulations for a system containing uranium and plutonium radionuclides with varying type and amount of electrolyte ions and complexing ligands are shown below (see Section 12.1.2).

12.1.1 Force-Field Development for Uranyl Complexes

In the natural environment, hydroxides and carbonate/bicarbonate ions are the most common complexing ligands. Similarly, to solubility and sorption discussed above, the complexation and complex solubility depend primarily on the actinide oxidation state. For instance, U(IV), Np(IV) hydroxy and carbonate complexes are an order of magnitude less soluble than analogous U(VI) and Np(V) complexes (Ewing, Runde et al. 2010). In principle, complexation by carbonate prevents radionuclides from being retained by bentonites as surface complexes are typically weaker than those formed in bulk. These complexes prefer to remain in the solution, even though they are effectively less mobile than Np(V) or U(VI) ions (Tachi, Nakazawa et al. 2010). To predict radionuclides mobility in the environment, we need to understand complexation and speciation in the aqueous solution and near the mineral. Knowing the energetics and dynamics of sorption and complexation, we more rigorously predict radionuclide mobility in the environment and assess the safety of the geological disposal of radioactive waste.

We used molecular dynamics simulations to examine the effect of complexation and ion-pair formation on radionuclides reactivity and mobility in bentonites. The first step in using classical statistical mechanics simulation methods is to develop an appropriate interaction model – force field, for all species considered, including smectite layers. We used the existing ClayFF (Cygan et al., 2004) force field model for clay solid, and the first-principle quantum chemistry method to developed interaction parameters for actinides and complexing ligands. This procedure is based on the geometry optimization of isolated molecules, ions and ligands followed by the electron density partitioning (Singh and Kollman, 1984; Reed et al. 1985) in order to develop partial charges associated with each interaction site. We used Effective Core Potential (Pepper and Bursten, 1991, Cao et al. 2003, Denning, 2007) approach to take into account relativistic effects and reduce the computational cost associated with a large number of electrons in actinides shells. All calculations were carried out using Density Functional Theory with the hybrid Perdew–Burke–Ernzerhof exchange-correlation functional (Ernzerhof and Scuseria 1999). In order to develop an interaction model that is consistent with ClayFF, we limit intermolecular interactions to the electrostatic and short-range van der Waals forces; the latter was modeled using Lennard-Jones potential. The intramolecular interactions, such as angle bending and bond stretching, were added to uranyl (UO_2^{2+}, Table 12.1), hydroxyl (OH^- , Table 12.2) and carbonate (CO_3^{2-}, Table 12.3) ions. In Figure 12.2 we show a few examples of the coordination complexes we considered during force-field interaction development. In Tables 12.1.-12.3 we listed the interaction parameters we used for modeling uranyl complexes.

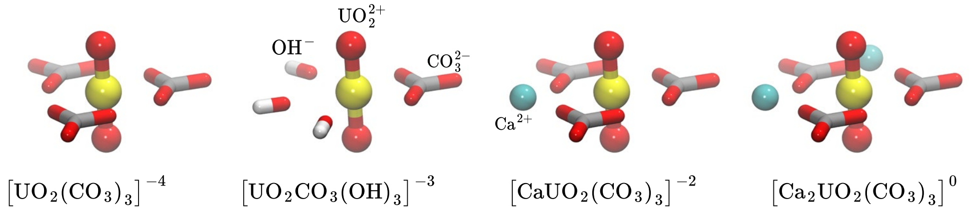

Figure 12-2. Uranyl carbonyl/hydroxyl complexes considered in the molecular modeling of uranyl retention by bentonites in the environmental conditions.

Table 12-1. Force-field parameter values for uranyl ion.

$\mathbf{UO_2^{2+}}$		Lennard-Jones $U(r) = 4\varepsilon\left[\left(\frac{\sigma}{r}\right)^{12} - \left(\frac{\sigma}{r}\right)^{6}\right]$	
Non-bonded interactions	Charge q[e]	σ [nm]	ε [kJ/mol]
U	2.50	0.295	0.530
O	-0.25	0.383	0.057
Bonded interactions			
U-O bond $U(r) = \frac{1}{2}k(r - r_{eq})^2$	r_{eq} =0.176 nm	k= 622294.7 kJ/mol/nm^2	
O-U-O angle $U(\theta) = \frac{1}{2}k(\theta - \theta_{eq})^2$	θ_{eq}= 180	k=198 kJ/mol/rad^2	

Table 12-2. Force-field parameter values for hydroxyl ion.

OH-		Lennard-Jones $U(r) = 4\varepsilon\left[\left(\frac{\sigma}{r}\right)^{12} - \left(\frac{\sigma}{r}\right)^{6}\right]$	
Non-bonded interactions	Charge q[e]	σ [nm]	ε [kJ/mol]
O	-1.201	0.317	0.650
H	0.201	0	0
Bonded interactions			
O-H bond $U(r) = \frac{1}{2}k(r - r_{eq})^2$	r_{eq} =0.098 nm	k= 299490.7 kJ/mol/nm^2	

Table 12-3. Force-field parameter values for carbonate ion.

CO_3^{2-}		Lennard-Jones $U(r) = 4\varepsilon\left[\left(\frac{\sigma}{r}\right)^{12} - \left(\frac{\sigma}{r}\right)^{6}\right]$	
Non-bonded interactions	Charge q[e]	σ [nm]	ε [kJ/mol]
C	1.154	0.340	0.360
O	-1.051	0.296	0.880
Bonded interactions			
C-O bond $U(r) = \frac{1}{2}k(r - r_{eq})^2$	r_{eq} =0.131 nm	k= 533627.36 kJ/mol/nm^2	
O-C-O angle $U(\theta) = \frac{1}{2}k(\theta - \theta_{eq})^2$	θ_{eq}= 120	k= 902.91 kJ/mol/rad^2	
improper periodic dihedral O-O-C-O $U(\phi) = k(1 + \cos(n\phi - \phi_{eq}))$	ϕ_{eq}= 180	k =105.02 kJ/mol n = 2 (multiplicity)	

12.1.1 Bulk and Surface Complexation governs radionuclide retention

The radionuclide mobility in nature is primarily determined by oxidation state, complexation and sorption to the surfaces of naturally occurring minerals/soils or engineered barriers. The radionuclides in the reduced state are generally highly immobile (e.g., $X^{3+/4+}$, where X=U, Np, Pu), whereas in the oxidized state ($XO^{2+/2+}$) they are more soluble and highly mobile. The association of dissolved uranium, plutonium and neptunium with organic and inorganic ligands in solution has a significant impact on its environmental mobility – as it affects their solubility, sorption capacity, and redox equilibrium. Here, we developed a computational framework to study the effects of complexation on radionuclide mobility and retention by smectites.

In Figure 12-3 we show examples of the simulation systems: a pore formed by two parallel clay surfaces with filled by the electrolyte solution containing uranium and plutonium ions and varying types and number of ligands and simple electrolyte ions. In Table 12-4 we listed diffusion coefficients of uranium and plutonium ions in these systems with two types of smectite surfaces that differ in the number of isomorphic substitutions – permanent charge.

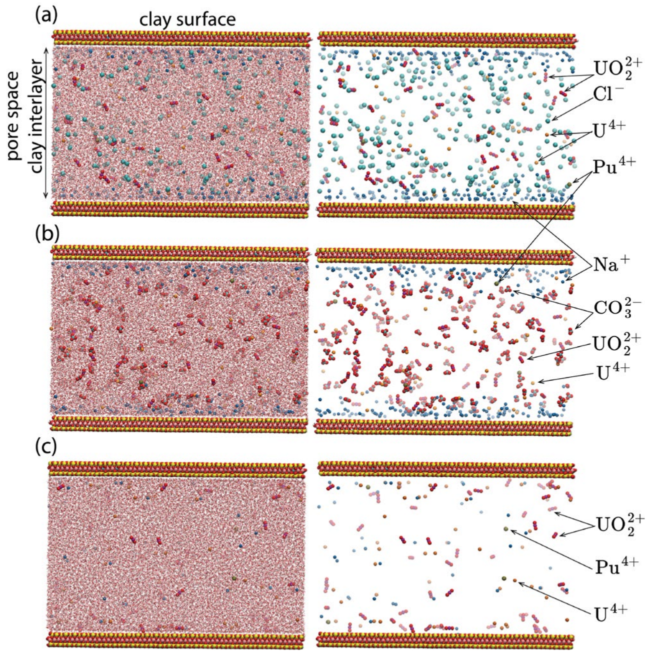

Figure 12-3. Illustration of the molecular models for radionuclide retention by smectite. A montmorillonite clay interlayer filled by electrolyte solution containing various radionuclides (water shown explicitly on the left-hand side). In panel (a) we show an example of a carbonate-free simulation/chloride-rich system. In panel (b) we show an example of a chloride-free/carbonate-rich system. In panel (c) we show an example of anion-free solution with clay counterions partially replaced by radionuclides.

As shown in Table 12-1 the radionuclides mobility decreases with increases clay-surface charge, that is with a number of isomorphic substitutions. If radionuclides replace clay counterions, the mobility decreases even further, by one to two orders in magnitude. Despite identical formal charges on U^{4+} and Pu^{4+} ions, we observe significantly lower mobility of plutonium, evidence for higher affinity of plutonium to smectite surfaces. By comparing diffusion coefficients of chloride-free and carbonate-free solutions, we observe that ion-pair formation between radionuclides and chloride ions increases radionuclide mobility in the solution, but to a much lower extent than in the presence of carbonate ions.

Table 12-4. Solution composition and clay charge effects on radionuclide mobility in the clay interlayer as quantified by the self-diffusion coefficient, D, and its parallel ($\boldsymbol{D_{\parallel}}$) and perpendicular ($\boldsymbol{D_{\perp}}$) to the clay surface components (in 10-5 cm2/s).

	smectite permanent charge due to isomorphic substitutions in the lattice ($Mg^{2+} \rightarrow Al^{3+}$)					
	$\sigma = 0.1$ C/m^2			$\sigma = 0.4$ C/m^2		
Species	$\langle D \rangle$	$D_{\parallel}$	$D_{\perp}$	$\langle D \rangle$	$D_{\parallel}$	$D_{\perp}$
chloride-rich, carbonate-free solution (Figure 12-3a)						
Pu^{4+}	0.28	0.37	0.10	0.09	0.06	0.15
U^{4+}	0.23	0.19	0.30	0.19	0.21	0.16
UO_2^{2+}	0.40	0.43	0.35	0.29	0.33	0.22
carbonate-rich, chloride-free solution (Figure 12-3b)						
Pu^{4+}	0.27	0.39	0.03	0.25	0.33	0.10
U^{4+}	0.16	0.21	0.16	0.20	0.19	0.22
UO_2^{2+}	0.25	0.29	0.19	0.20	0.21	0.17
anion-free solution (Figure 12-3c) clay counterions (Na^+) partially replaced by radionuclides						
Pu^{4+}	0.12	0.12	0.12	0.001	0.001	0.003
U^{4+}	0.11	0.07	0.07	0.03	0.02	0.05
UO_2^{2+}	0.16	0.17	0.14	0.05	0.01	0.14

12.2 Ongoing and planned work

We are currently further developing computational frameworks for predicting radionuclide retention by smectites and mobility in clay pores and interlayers as a function of fluid and solid composition. We plan to extend the interaction parameter library to include some organic ligands commonly encountered in the environment, such as oxalate, malonate, citrate.

We also plan to parametrize mathematical functions describing how fluid properties, such as polarizability and viscosity, are related to the fluid composition and mineral confinement. The fluid polarizability, as measured by the dielectric constant, is one of the most important measures of fluid ability to screen electrostatic interactions. We have recently developed numerical routines to calculate dielectric properties, such as the dielectric relaxation spectra, directly from the atomistic trajectory (Zarzycki and Gilbert 2020). Here, we plan to use the same approach to calculate dielectric properties of complex electrolytes containing various types of radionuclides and complexing ligands trapped by clay surfaces.

Finally, we propose to use molecular simulations to parameterize mathematical representations of transport and thermodynamic properties of radionuclides in the clay matrix (see section 12.2.1). The large-scale models used to assess the safety of given storage scenarios will benefit from using analytical functions for radionuclide retention in the evolving geochemical environment.

12.2.1 Connecting molecular simulations with the field- and macro-scale safety assessment modeling

It is often difficult to experimentally determine the radionuclide migration in clay-rich soil or engineered clay barrier. The radionuclide toxicity requires strict safety protocols, which in turn limits the number of laboratories in which measurements can be carried out as well as the analytical chemistry techniques that can be safely applied. The molecular modeling offers an attractive alternative to the experimental approach. By using molecular modeling, we can estimate transport, speciation, and fluid properties required by the larger scale, continuum radionuclide transport models, and macroscopic/field-scale safety assessment models.

For example, molecular dynamics simulations allow us to estimate radionuclide diffusion coefficient in complex solutions. We plan to carry out a simulation study of diffusion by systematically varying fluid and solid composition in order to get insight into the transport properties' dependence on the system composition, porosity, and connectivity of the clay matrix. For example, as shown in Figure 12-1, variation of Np(V) ion mobility with the pore size or ionic strength (Figure 12-1) are smooth and monotonic; therefore it can be approximated by mathematical functions, such as multidimensional Taylor series or polynomials. One of the tasks we plan to carry out is to develop generalized interpolation polynomial formulas for uranium, plutonium radionuclide mobility as a function of system composition/topology and thermodynamic conditions. For example, the diffusion coefficient can be defined within this mathematical framework as:

$$D_i(X,p,T,\rho,\tau,\ldots) = D_{i,0} + \sum_i \sum_j^{X,p,T,\rho,\tau,\ldots} \sum_n a_{ij} j^n \tag{12.1}$$

where D_i is a diffusion coefficient of *i*-radionuclide in fluid, whose composition is defined by *X*-vector, filling a solid matrix with porosity ρ and tortuosity τ. $D_{i,0}$ represents the *i*-radionuclide diffusion in the diluted aqueous solution at ambient conditions, and polynomial expansion describes how it is altered by the fluid and solid composition, pressure, and temperature. We propose to parametrize analytical expression for transport and retention coefficients as a function of clay pore size, fluid composition using molecular modeling, and next use these functional form in larger-scale mesoscale and macroscale models to assess the safety and evaluate various leaking scenarios. The information flow between nanoscale and macroscale models is shown in Figure 12-4.

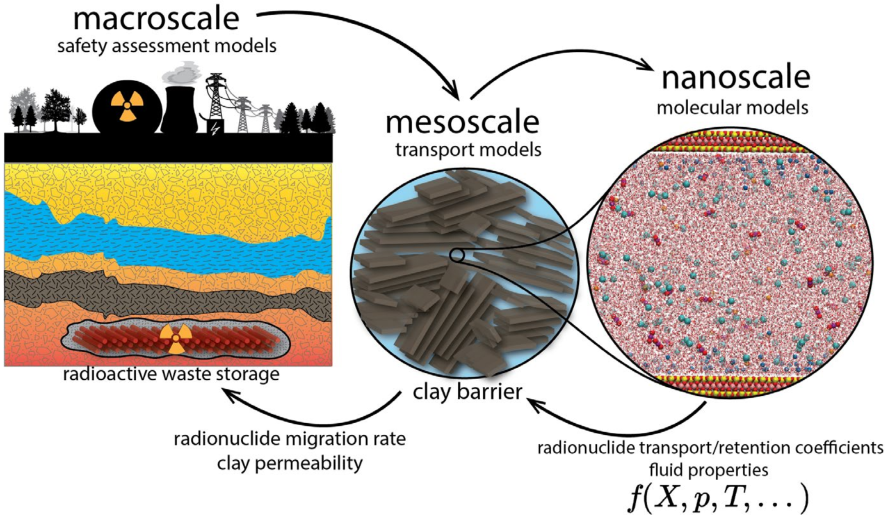

Figure 12-4. Molecular modeling-based parametrization of meso and macroscale models of radionuclide retention, and storage safety.

13. LINKING THM PROCESS MODELS TO GEOLOGIC DISPOSAL SAFETY ASSESSMENT (GDSA)

A schematic of integration between the coupled THM processes models and a repository-scale model for GDSA and PA is shown in Figure 13-1. The GDSA and PA modeling is conducted with the PFLOTRAN code by Sandia National Laboratories. PFLOTRAN has the capability of modeling coupled TH processes and geochemistry, including radionuclide transport in a high-performance computing environment. The idea is to conduct the GDSA modeling of the entire repository, including all emplacement tunnels. In such a large-scale repository model, it will not be possible to model the detailed thermally driven coupled THM processes occurring in the EBS and near-field during the relatively early repository time period of elevated repository temperature.

An initial approach for linking a coupled processes model to the GDSA could be to use detailed coupled THM process models to simulate near field of emplacement tunnels in different parts of a repository, for different FEPs such as a nominal case or cases of extensive gas generation. The output from such modeling to the GDA and PA model would be the following: (1) changes in flow properties (e.g., permeability and porosity) in the near-field, including the buffer and EDZ, and (2) inform PA about local flow created by coupled processes.

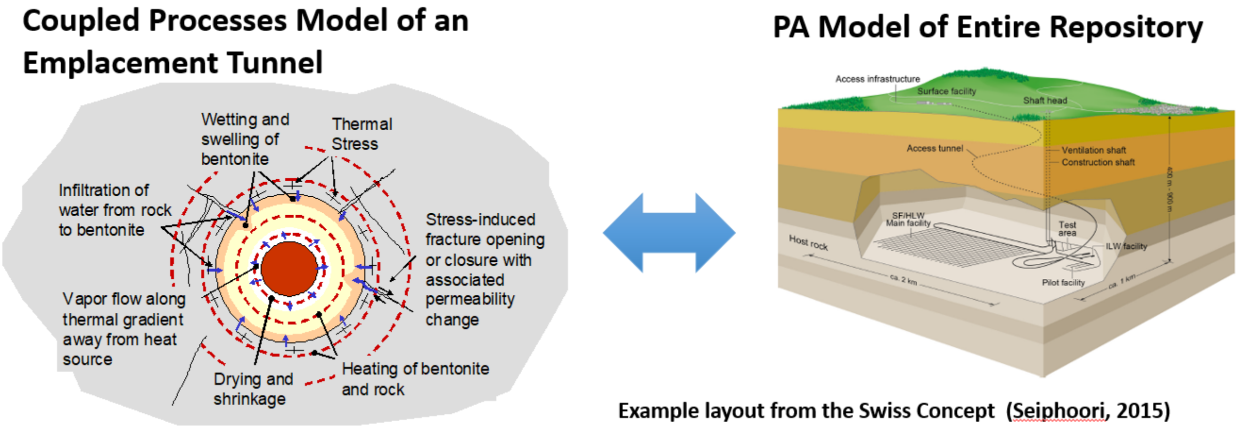

Figure 13-1. Schematic of links between near-field coupled THM processes modeling to repository-scale GDSA and PA models.

Currently, another approach is being developed that would enable inclusion of coupled THM processes into the PFLOTRAN GDSA and PA modeling. This will involve development of an approach to calculate the EDZ permeability evolution as a function of temperature, pressure, and a buffer saturation. The following key observations from the results of modeling of the long-term THM evolution using TOUGH-FLAC (Rutqvist et al., 2014) can be used to develop such an approach:

- The EDZ permeability depends on the effective stress normal to the excavation wall, which is determined by the effective stress of the buffer.
- The effective stress of the buffer can be reasonably modeled using an analytical model, taking into account that the stress depends on the buffer average saturation and buffer temperature.
- The EDZ permeability evolution can be affectively modeled by taking into account the stress tangential to the tunnel opening.

- The tangential stress evolution can be calculated using analytical models, in which the tangential stress depends on pore-elastic and thermos-elastic stresses at the repository level and stress concentrations around the tunnel opening.

Figures 13-2 and 13-3 provide schematics of the conceptual approach, which will be further developed and verified. Figure 13-2 shows the EDZ with different sections that could respond differently as a result of the local stress evolution. In the simplest model, permeability will be determined by the normal stress across the EDZ, which, in turn, is determined by the effective stress within the buffer. The effective stress within the buffer will be determined by the swelling stress during resaturation of the buffer, and, thereafter, the effective stress will be affected by cooling stresses. In a slightly more sophisticated model, the EDZ permeability could depend on three-dimensional stresses. A version of such a model was described by Equation (2.3) in Section 2 of this report. Figure 13-3 shows another view of the link between the detailed THM model and the simplified PFLOTRAN model. In the large-scale PFLOTRAN model, the discretization of the emplacement tunnel is simplified for the purpose of large-scale radionuclide transport simulations. The stress evolution at different EDZ sections in the PFLOTRAN model could be modeled through analytical models, dependent on pressure, temperature and saturation at the different locations in the model (e.g., mid-pillar and buffer).

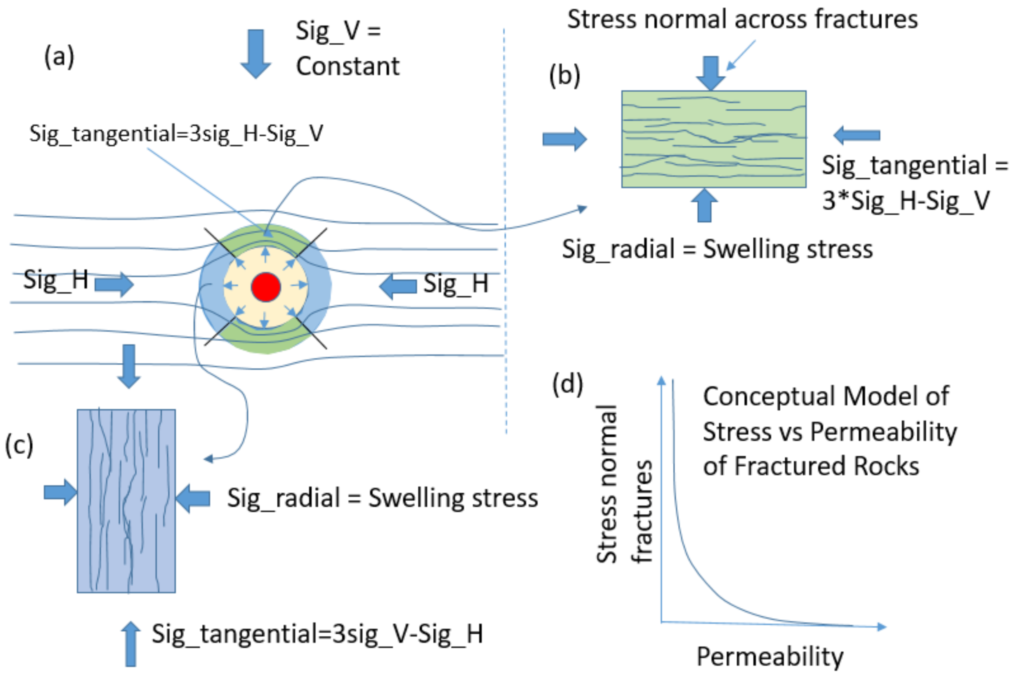

Figure 13-2. Schematic of the EDZ permeability evolution, using a model of an effective stress versus permeability for a fracture rock domain within the EDZ. (a) Different sections of the EDZ evolution on top/bottom and sides of the emplacement tunnel with normal stress from the buffer swelling stress and tangential stress from the horizontal and vertical stress concentrations around the tunnel. (b) EDZ section on the top of the tunnel exposed to radial and tangential stresses. (c) EDZ section on the side of the tunnel. (d) Conceptual model of a normal stress versus permeability for a fracture rocks similar to that shown in (b) and (c).

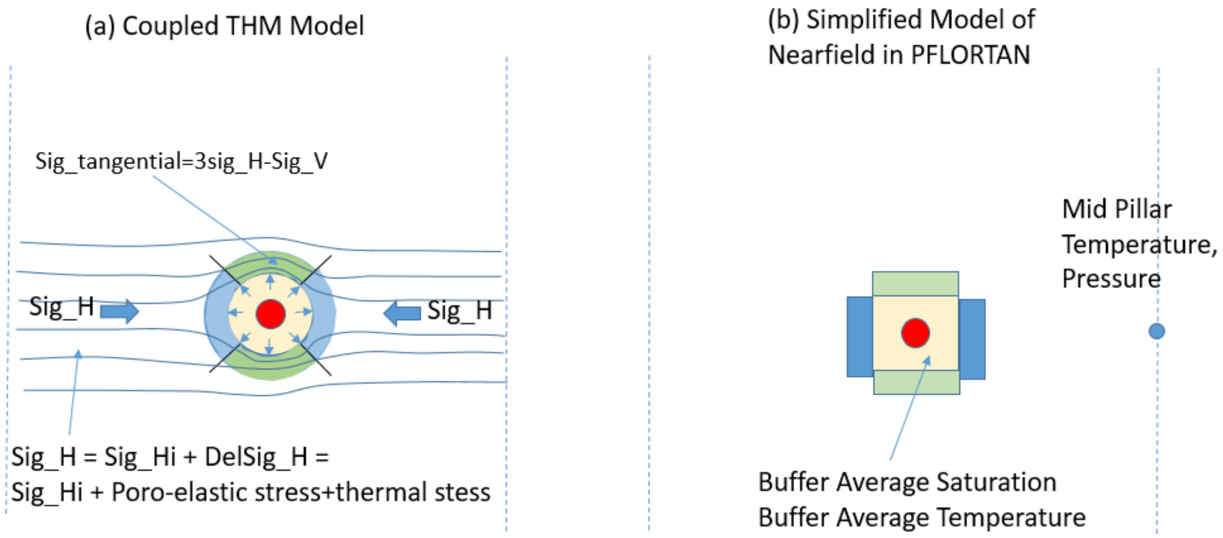

Figure 13-3. Schematic of links between (a) a coupled THM model and (b) PFLOTRAN simplified near field model.

The proposed approach for linking THM process models to GDSA will be further developed and verified during the rest of FY19. This will be done by comparison of a fully coupled THM solution with the simplified approach of a TH model linked to analytical models for stress and permeability changes. Such a simplified model can then be implemented into PFLOTRAN to calculate the evolution of the EDZ permeability.

13.1 Methods

13.1.1 Model geometry

Figure 13-4 shows the geometry and mesh of a hypothetical nuclear waste repository model for the TOUGH-FLAC simulator. The nuclear waste disposal tunnel is located at the center of the model, which is at 500 m deep from the ground surface and 25 m away from the lateral boundaries (i.e., mid-pillar). The inner and outer radius of the canister are 0.35 m and 0.45 m, respectively, whereas the radius of the tunnel is 1.14 m. This model is three dimensional but the plane-strain condition is applied on the out-of-plane direction with the thickness of 1 m. The entire model is discretized into 360 elements (i.e., 248 for rock, 96 for buffer, and 16 for canister) and the size of the mesh is finer around the center of the tunnel than near the model boundaries.

Boundary conditions are also shown in Figure 13-4. Thermo-hydrological boundary conditions are as follows: constant pore pressure and temperature on the top and bottom boundaries, and no fluid or thermal flow along the lateral and canister interior boundaries. Mechanical boundary conditions are as follows: zero displacement perpendicular to the bottom and lateral boundaries (transverse displacements are allowed), and constant pressure on the top and canister interior boundary.

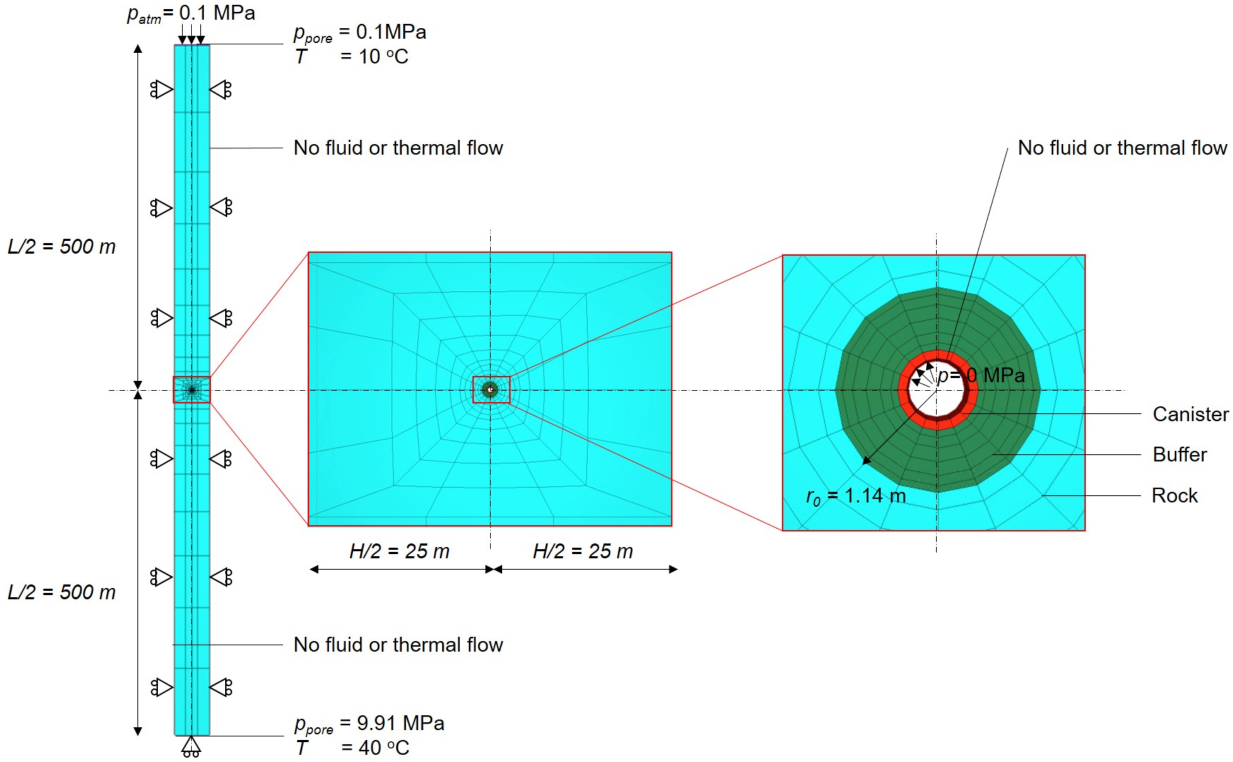

Figure 13-4 The geometry and mesh of the TOUGH-FLAC model.

13.1.2 Material behaviors

13.1.2.1 Thermo-hydrological behaviors

The thermo-hydrological behaviors of the model are simulated by the TOUGH3 simulator. The equation-of-state module #4 (EOS4) is used. In EOS4, the model components are water and air, which can be either in the gas or fluid phase, and the primary variables are gas pressure, gas saturation, and air partial pressure for two-phase conditions, whereas they are gas pressure, temperature, and air partial pressure for single-phase conditions.

Darcy's law is used to simulate the flow of the components. The following relative permeability function (i.e., van Genuchten-Mualem model) is used for the rock:

$$k_{rl} = \begin{cases} \sqrt{S^*}\left(1-\left(1-(S^*)^{\frac{1}{\lambda_k}}\right)^{\lambda_k}\right)^2 & if\ S_l < S_{ls} \\ 1 & if\ S_l \geq S_{ls} \end{cases}$$
$$k_{rg} = \begin{cases} 1-k_{rl} & if\ S_{gr} = 0 \\ \left(1-\hat{S}\right)^2\left(1-\hat{S}^2\right) & if\ S_{gr} > 0 \end{cases} \qquad (13.1)$$

where

$$S^* = \frac{S_l - S_{lr}}{S_{ls} - S_{lr}} \tag{13.2}$$

$$\hat{S} = \frac{S_l - S_{lr}}{1 - S_{lr} - S_{gr}} \tag{13.3}$$

where k_{rl} is relative permeability of the liquid phase, k_{rg} is relative permeability of the gas phase, λ_k is a van Genuchten parameter (in the original notation λ_k is expresses as m), S_l is liquid phase saturation, S_{lr} is residual (i.e., minimum) liquid phase saturation, S_{ls} is saturated (i.e., maximum) liquid phase saturation, and S_{gr} is residual gas phase saturation. It is noted that $0 \leq k_{rl} \leq 1$ and $0 \leq k_{rg} \leq 1$ are applied if calculated relative permeability values are outside these ranges.

The following relative permeability function is used for the buffer:

$$\begin{gathered} k_{rl} = \hat{S}^3 \\ k_{rg} = 1 \end{gathered} \tag{13.4}$$

The following capillary pressure function, given by the van Genuchten model, is used for both rock and buffer:

$$P_{cap} = -P_0 \left((S^*)^{\frac{-1}{\lambda_k}} - 1 \right)^{1-\lambda_k} \tag{13.5}$$

where P_0 is a parameter analogous to the air entry pressure. The maximum capillary pressure value, P_{max}, is specified such that $-P_{max} \leq P_{cap} \leq 0$.

Fourier's law and Fick's law are used to simulate thermal conduction and multi-phase diffusion, respectively.

Table 13-1 shows the thermo-hydrological parameter values (i.e., TOUGH3 input parameter values) employed in this study for the rock, buffer, and canister. It is noted that a smaller residual liquid saturation value for capillary pressure than for relative permeability is used in the rock. This is done to avoid generating infinite capillary pressure when the liquid phase becomes immobile. In addition, all phases are assumed perfectly mobile ($k_{rl} = k_{rg} = 1$) in the canister and identical capillary pressure function and parameter values to those of the buffer are used. This is done to circumvent convergence issues for flow calculation at the buffer-canister interface. Hydrological behavior of the buffer would not be affected by that of the canister as the porosity of the canister is set to a value significantly smaller than that of the rest of the model components.

Table 13-1 Thermo-hydrological parameter values of the model components.

	Rock	Buffer	Canister
Grain density (kg/m^3)	2700	2700	7800
Porosity (-)	0.15	0.41	0.001
Absolute permeability (m^2)	$5\cdot10^{-20}$	$2\cdot10^{-21}$	$2\cdot10^{-21}$
Thermal conductivity (W/(m·°C))	2.2	1.26	12.0
Grain specific heat (J/(kg·°C))	900	800	500
Pore compressibility (1/Pa)	$1\cdot10^{-9}$	$5\cdot10^{-8}$	0
Pore expansivity (1/°C)	0	$1\cdot10^{-4}$	0
Diffusion coefficient for water vapor (m^2/s)	$1.73\cdot10^{-5}$	$1.73\cdot10^{-5}$	$1.73\cdot10^{-5}$
van Genuchten parameter, λ_k (-)	0.41	0.32	0.32
Residual liquid saturation for relative permeability, S_{lr} (-)	0.2	-	-
Residual liquid saturation for capillary pressure, S_{lr} (-)	0.1	0.1	0.1
Saturated liquid saturation, S_{ls} (-)	1.0	1.0	1
Residual gas saturation, S_{gr} (-)	0.01	0	0
Capillary pressure parameter, P_0 (Pa)	$4.76\cdot10^{7}$	$3\cdot10^{7}$	$3\cdot10^{7}$
Maximum capillary pressure, P_{max} (Pa)	$1\cdot10^{8}$	$5\cdot10^{9}$	$5\cdot10^{9}$

13.1.2.2 Mechanical behaviors

Mechanical behaviors are modelled by the FLAC3D simulator in the thermo-hydromechanically (THM) coupled simulation case, whereas they are modelled analytically in the thermo-hydrologically (TH) coupled simulation case, which will be explained in later sections. In either case, the stress-strain relation (i.e., constitutive model) is described in terms of the effective stress, which is defined as follows:

$$\begin{gathered} \sigma'_{ij} = \sigma_{ij} - \alpha_{BW} \cdot p_{pore}\delta_{ij} \\ p_{pore} = max(p_g, p_l) \end{gathered} \tag{13.6}$$

where σ'_{ij} is the effective stress (tensor), σ_{ij} is the total stress (tensor), α_{BW} is the Biot-Willis coefficient, δ_{ij} is the Kronecker delta, p_{pore} is pore pressure, p_g is gas phase pressure, and p_l is the liquid-phase pressure. If the pore space is fully saturated with the liquid phase (i.e., water), pore pressure is the liquid phase pressure, whereas it is the gas phase pressure if the pore space is partially saturated.

The linear isotropic elastic constitutive relation is used to model the mechanical behaviors of the rock and canister. In this case, only two elastic parameters (e.g., Young's modulus and Poisson's ratio) are required. The mechanical behaviors of the buffer are modelled by the Barcelona Basic Model (BBM), which is typically used to model the suction-induced pore collapse of clays. The elastic behavior in the BBM is nonlinear and plastic yielding and plastic hardening/softening are included in the modelling framework of the BBM. The details of the BBM are presented in Alonso et al. (1990) and Rutqvist et al. (2014). The mechanical parameter values used in this study are listed in Table 13-2.

Table 13-2 Mechanical parameter values of the model components.

	Rock	Buffer	Canister
Young's modulus (Pa)	$5.0\cdot10^9$	-	$200\cdot10^9$
Poisson's ratio (-)	0.3	0.4	0.3
Biot-Willis coefficient, α_{BW} (-)	1.0	1.0	1.0
Linear thermal expansion coefficient (1/°C)	$1.0\cdot10^{-5}$	$1.5\cdot10^{-4}$	$1.0\cdot10^{-5}$
Gradient of swelling line for stress, κ_{PS0} (-)	-	0.05	-
Gradient of swelling line for suction, κ_{SP0} (-)	-	0.25	-
Swelling gradient adjusting parameter, α_{PS} (1/Pa)	-	$-3.0\cdot10^{-9}$	-
Swelling gradient adjusting parameter, α_{SS} (1/Pa)	-	0	-
Swelling gradient adjusting parameter, α_{SP} (-)	-	-0.161	-
Reference pressure, p_{ref} (Pa)	-	$0.01\cdot10^6$	-
Gradient of compression line for stress, λ_{PS0} (-)	-	0.15	-
Gradient of compression line for suction, λ_{SP0} (-)	-	0.5	-
Compression gradient adjusting parameter, r_λ (-)	-	0.925	-
Compression gradient adjusting parameter, β_λ (1/Pa)	-	$0.1\cdot10^{-6}$	-
Tensile strength at zero suction, p_{s0} (Pa)	-	0	-
Tensile strength gradient, k_s (-)	-	0.1	-
Tensile strength gradient adjusting parameter, ρ_s (1/°C)	-	0	-
Reference mean net stress, p^c (Pa)	-	$0.5\cdot10^6$	-
Critical state frictional constant, M (-)	-	1.0	-
Pre-consolidation mean net stress, p_0^* (Pa)	-	$12.0\cdot10^6$	-
Porosity (-)	-	0.41	-
Non-associated plastic flow parameter, α_a (-)	-	0.53	-

13.1.1 Simulation stages

13.1.1.1 In situ conditions

The *in situ* conditions prior to the excavation of the nuclear waste disposal tunnel are specified as follows: the temperature is linearly increased with depth from 10°C on the top boundary to 40°C on the bottom boundary, and pore pressure and stresses are also linearly increased with the gradients corresponding to the weight of pore water and rock, respectively. The magnitudes of vertical and horizontal stresses are assumed identical in this study (i.e., isotropic *in situ* stresses). At the *in situ* state, the volume inside the tunnel is assumed to be occupied by rock and no buffer or canister elements are activated.

13.1.1.2 Tunnel excavation stage

The thermo-hydrological part of the tunnel excavation stage is simulated in TOUGH3 as follows: constant pore pressure of 0.1 MPa and constant temperature of 25°C are specified in the buffer and canister elements and the TOUGH3 simulation is run until a steady-state thermal and hydrological flow has been achieved. The steady-state pore pressure and temperature are used as the initial pore pressure (p_{pore0}) and temperature (T_0) in the following canister heating stage.

The mechanical part of the tunnel excavation stage is simulated in FLAC3D as follows: first the stiffness of the buffer and canister elements is set to a value that is smaller by orders of magnitudes than that of the rock so as not to restrict the displacement of the tunnel surface, and then pore pressure and temperature values calculated by TOUGH3 at each converged TOUGH3 simulation step are imported and used as boundary conditions in FLAC3D to compute the corresponding displacements, strains, and stresses in the rock, buffer, and canister. The stress distributions computed by FLAC3D when the steady-state is achieved in TOUGH3 are used as the initial stress values for the THM simulation case of the canister heating stage. For the TH simulation case, on the other hand, the initial stresses after tunnel excavation are calculated analytically as described in the following sections.

13.1.1.3 Canister heating stage

The canister heating stage is simulated by introducing time-varying heat sources in the canister elements in TOUGH3. Figure 13-5 shows the heat rate assigned to the canister elements in TOUGH3. The mechanical parameter values for the buffer and canister are switched from fictitious ones for the excavation stage to the ones listed in Table 13-2. The initial stresses in the buffer and canister are set as follows: $\sigma_{xx} = \sigma_{yy} = \sigma_{zz} = 0.15$ MPa (compression positive) and $\tau_{xx} = \tau_{yy} = \tau_{zz} = 0$ MPa. The initial pore pressure (gas pressure) and temperature are set to 0.1 MPa and 25°C in both the buffer and canister. Finally, the initial gas phase saturation is set to 0.65 in both the buffer and canister. The canister heating stage lasts up to 10^5 years.

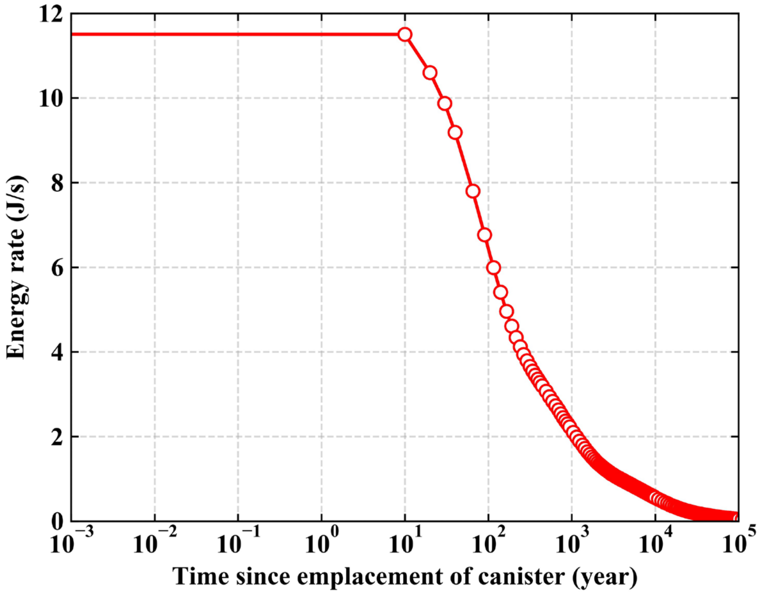

Figure 13-5 Heat rate assigned to the canister elements.

13.1.2 Permeability profiles in rock near the tunnel

In this study, rock permeability near the disposal tunnel is calculated with the following equation:

$$k = (k_r + \Delta k_{max} \exp(\beta_1 \sigma'_m)) \cdot \exp(\gamma \langle \sigma_d - \sigma_{d,crit} \rangle) \quad (13.7)$$

where k is permeability, Δk_{max} is an increment in permeability due to mean effective stress change, β_1 (<0) is a parameter correlating permeability and mean effective stress change, σ'_m is mean effective stress (= mean total stress – pore pressure), γ (>0) is a parameter correlating permeability and deviatoric stress change, σ_d is deviatoric stress (= von Mises equivalent stress), and $\sigma_{d,crit}$ is the critical deviatoric stress value. The $\langle\ \ \rangle$ operator is the MaCaulay brackets, in which $\langle x\rangle = x$ if $x \geq 0$, and $\langle x\rangle = 0$ if $x < 0$. The mean effective stress and deviatoric stress are defined as follows:

$$\sigma'_m = \frac{\sigma'_{xx} + \sigma'_{yy} + \sigma'_{zz}}{3} = \frac{\sigma'_{rr} + \sigma'_{yy} + \sigma'_{\theta\theta}}{3} \tag{13.8}$$

$$\begin{aligned}\sigma_d &= \sqrt{\frac{1}{2}\left(\left(\sigma_{xx} - \sigma_{yy}\right)^2 + \left(\sigma_{yy} - \sigma_{zz}\right)^2 + (\sigma_{zz} - \sigma_{xx})^2 + 6\left(\tau_{xy}^2 + \tau_{yz}^2 + \tau_{xz}^2\right)\right)} \\ &= \sqrt{\frac{1}{2}\left(\left(\sigma_{rr} - \sigma_{yy}\right)^2 + \left(\sigma_{yy} - \sigma_{\theta\theta}\right)^2 + (\sigma_{\theta\theta} - \sigma_{rr})^2 + 6\left(\tau_{ry}^2 + \tau_{y\theta}^2 + \tau_{r\theta}^2\right)\right)}\end{aligned} \tag{13.9}$$

Figure 13-6 shows the absolute permeability profiles in rock around the tunnel after the tunnel excavation stage calculated with Equation 13.7 for the parameter values listed in Table 13-3. The permeability increases near the tunnel because the mean stress decreases due to stress relaxation and deviatoric stress increases simultaneously near the tunnel wall during tunnel excavation. The larger permeability increase in the horizontal direction ($\theta = 0^o$) than in the vertical direction ($\theta = 90^o$) is caused by the greater deviatoric stress above the critical value (= 5 MPa in this study) that is generated in the horizontal direction due to the isotropic *in situ* stress condition assumed in this study. Anisotropic *in situ* stress conditions will affect stress profiles after tunnel excavation significantly, and their effect on permeability will be addressed in future studies. In this study, however, the permeability profiles shown in Figure 13-6 are used as the initial rock permeabilities near the tunnel for the canister heating stage, and the permeability function shown in Equation 13.7 and parameter values listed in Table 13-3 are used to calculate permeability change in rock near the tunnel during the canister heating stage.

Table 13.3 Parameter values for the rock permeability function employed in this study.

Residual permeability, k_r (m^2)	$5\cdot10^{-20}$
Permeability increment, Δk_{max} (m^2)	$1\cdot10^{-17}$
Coefficient for mean effective stress, β_1 (1/Pa)	$-1\cdot10^{-6}$
Coefficient for deviatoric stress, γ (1/Pa)	$3\cdot10^{-7}$
Critical deviatoric stress, $\sigma_{d,\,crit}$ (Pa)	$5\cdot10^{6}$

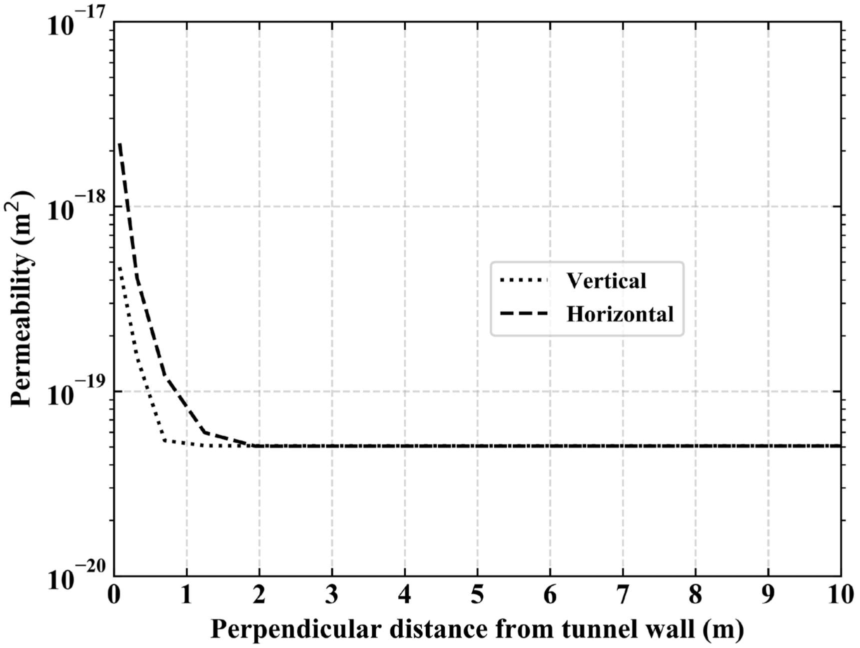

Figure 13-6 Permeability profiles in rock around the tunnel after excavation.

13.1.3 Simulation cases

13.1.3.1 TH simulation case with analytical stress estimation

The primary objective of this study is to estimate mechanically-induced permeability changes in rock around the nuclear waste disposal tunnel only from thermo-hydrological (TH) variables with a reasonable accuracy, so that radionuclide transport can be simulated in the TH code, PFLOTRAN. Permeability in rock with fractures is dependent on stresses, hence stresses have to be estimated first from TH variables, such as pore pressure (i.e., gas pressure), temperature, and suction (i.e., the absolute value of capillary pressure), which are provided from the TOUGH3 simulation. It is noted that compression is taken positive in the following derivation of the stresses.

Buffer stresses

The buffer stress normal to the tunnel surface, p_B, is calculated by the Barcelona Basic Model (BBM) under the assumption that the volume of the buffer (i.e., the space in between the canister and the waste disposal tunnel) remains constant ($d\epsilon_{total} = d\epsilon_{mechanical} + d\epsilon_{suction} + d\epsilon_{thermal} = 0$) and that the strain increments are isotropic with no shear components. The stress-strain relation of BBM is nonlinear, hence the buffer stress has to be updated iteratively as follows:

$$\begin{aligned} p'_{B,i+1} &= p'_{B,i} + \Delta p'_{B,i} \\ \Delta p'_{B,i} &= K'(\Delta\epsilon_s + \Delta\epsilon_{th}) \end{aligned} \tag{13.10}$$

where p'_B is mean effective stress in the buffer, $\Delta p'_B$ is mean effective stress increment in the buffer, K' is the bulk modulus of the buffer, $\Delta\epsilon_s$ is suction-induced volumetric strain increment, and $\Delta\epsilon_{th}$ is thermally-induced volumetric strain increment. The subscript *i* indicates the step number. The bulk modulus and strain increments are calculated as follows:

$$K' = \frac{\upsilon p'_{B,i}}{\kappa_{PS}} \tag{13.11}$$

$$\Delta\epsilon_s = \frac{-\kappa_{SP}}{\upsilon(s_i + p_{atm})}\left(s_{B,i+1} - s_{B,i}\right) \tag{13.12}$$

$$\Delta\epsilon_{th} = 3\alpha_B\left(T_{B,i+1} - T_{B,i}\right) \tag{13.13}$$

where υ is specific volume of the buffer, κ_{PS} is a stiffness coefficient of the buffer against mean effective stress change, κ_{SP} is a stiffness coefficient of the buffer against suction change, p_{atm} is the atmospheric pressure, s_B is suction in the buffer (i.e., the absolute value of capillary pressure), α_B is the linear thermal expansion coefficient of the buffer, and T_B is temperature in the buffer. The stiffness coefficients are suction- and/or mean effective stress-dependent as shown below:

$$\kappa_{PS} = \kappa_{PS0}\left(1 + \alpha_{PS}s_{B,i}\right) \tag{13.14}$$

$$\kappa_{SP} = \kappa_{SP0}\left(1 + \alpha_{SP}\ln\frac{p'_{B,i}}{p_{ref}}\right)\exp\left(\alpha_{SS}s_{B,i}\right) \tag{13.15}$$

where κ_{PS0} is the stiffness coefficient against mean effective stress change at zero suction, κ_{SP0} the stiffness coefficient against suction change at zero mean effective stress and zero suction, p_{ref} is a reference pressure value, and α_{PS}, α_{SP}, α_{SS} are stiffness-adjusting parameters.

Finally, the mean total stress in the buffer is obtained as follows:

$$p_{B,i} = p'_{B,i} + p_{pore,\,i} \tag{13.16}$$

where p_{pore} is pore pressure in the buffer.

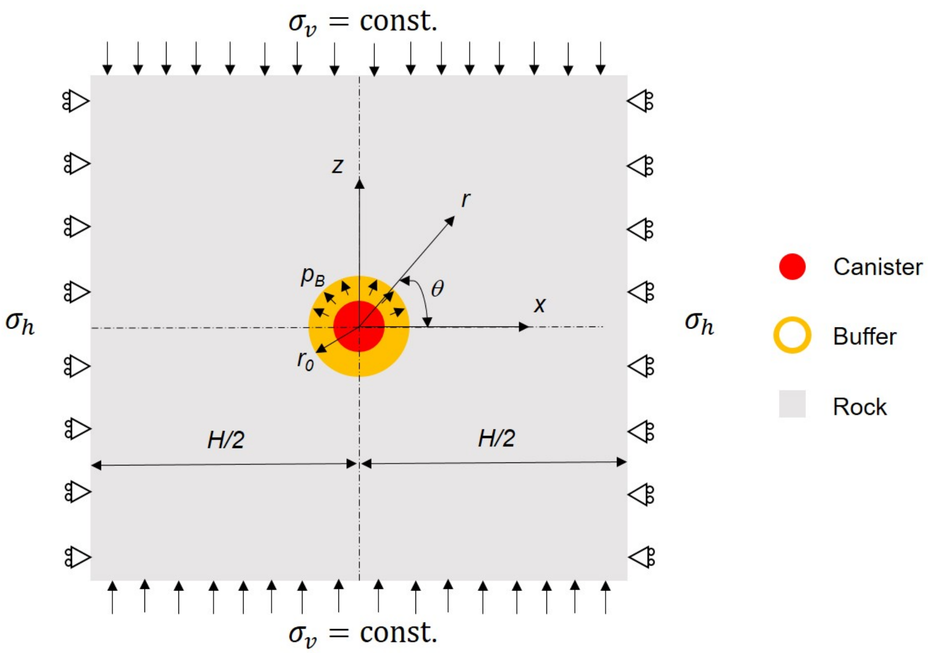

Figure 13-7 Analytical model of a hypothetical nuclear waste repository.

<u>**Rock stresses**</u>

In a hypothetical nuclear waste repository where canisters are deposited in horizontal tunnels with the spacing of H in deep geologic formation, the analytical model domain and boundary conditions can be assumed as shown in Figure 13-7. The horizontal displacement on the lateral boundaries are restrained by assuming the symmetry of the behavior of individual model domains for each disposal tunnel. Constant pressure loads, whose magnitudes are calculated from the self-weight of rock, are specified on the top and bottom boundaries. The gravity is ignored in the model domain. The vertical length of the model is arbitrary but should be sufficiently larger than the diameter of the tunnel.

The total stress on the lateral boundary (i.e., mid-pillar) after the emplacement of the canister is calculated from Hooke's law for linear isotropic elastic material under the plane-strain ($d\epsilon_{H,total} = d\epsilon_{H,mech} + d\epsilon_{H,thermal} = 0$) and zero-lateral strain ($d\epsilon_{h,total} = d\epsilon_{h,mech} + d\epsilon_{h,thermal} = 0$) conditions as follows:

<u>Lateral boundary stress</u>

$$\begin{aligned}\sigma_h = \frac{2\mu}{\lambda + 2\mu}\left(p_{pore}\big|_{r=\frac{H}{2},\theta=0} - p_{pore0}\big|_{r=\frac{H}{2},\theta=0}\right)\\ + \frac{3\lambda\mu + 2\mu^2}{\lambda + 2\mu}2\alpha\left(T\big|_{r=\frac{H}{2},\theta=0} - T_0\big|_{r=\frac{H}{2},\theta=0}\right) + \sigma_{h0}\end{aligned} \tag{13.17}$$

where σ_h is the lateral boundary stress, p_{pore} is pore pressure, T is temperature, σ_{h0}, p_{pore0}, and T_0 are initial lateral boundary stress, pore pressure and temperature, respectively, α is the linear thermal expansion coefficient of rock. The subscript $_{r=\frac{H}{2},\theta=0}$ indicates the specific location of the model from which the pore pressure and temperature values are extracted for use in the equation. The definitions of r, θ, H are provided in Figure 13-7. The parameter λ and μ are the Lamé constants, which are defined as follows:

$$\lambda = \frac{E\nu}{(1+\nu)(1-2\nu)} \qquad \mu = \frac{E}{2(1+\nu)} \tag{13.18}$$

where E is Young's modulus and ν is Poisson's ratio. Stresses in rock are calculated from the Kirsch equations as follows:

Radial stress

$$\begin{aligned}\sigma_{rr} = {} & \frac{\sigma_h - \sigma_{h0}}{2}\left(1-\left(\frac{r_0}{r}\right)^2\right) + \left(\frac{r_0}{r}\right)^2 (p_B - p_{B0}) \\ & + \frac{\sigma_h - \sigma_{h0}}{2}\left(1 - 4\left(\frac{r_0}{r}\right)^2 + 3\left(\frac{r_0}{r}\right)^4\right)\cos 2\theta + \sigma_{rr0}\end{aligned} \tag{13.19}$$

Circumferential stress

$$\begin{aligned}\sigma_{\theta\theta} = {} & \frac{\sigma_h - \sigma_{h0}}{2}\left(1+\left(\frac{r_0}{r}\right)^2\right) - \left(\frac{r_0}{r}\right)^2 (p_B - p_{B0}) \\ & - \frac{\sigma_h - \sigma_{h0}}{2}\left(1 + 3\left(\frac{r_0}{r}\right)^4\right)\cos 2\theta + \frac{E\alpha\left(T - T|_{r=\frac{H}{2},\theta=0}\right)}{(1-\nu)} \\ & + \frac{E\left(p_{pore} - p_{pore}|_{r=\frac{H}{2},\theta=0}\right)}{3K(1-\nu)} + \sigma_{\theta\theta 0}\end{aligned} \tag{13.20}$$

In-plane shear stress

$$\tau_{r\theta} = -\frac{\sigma_h - \sigma_{h0}}{2}\left(1 + 2\left(\frac{r_0}{r}\right)^2 - 3\left(\frac{r_0}{r}\right)^4\right)\sin 2\theta + \tau_{r\theta 0} \tag{13.21}$$

where r_0 is the radius of the tunnel, and σ_{rr0}, $\sigma_{\theta\theta 0}$, $\tau_{r\theta 0}$ are the initial radial, circumferential and in-plane shear stresses. It is noted that the out-of-plane shear stresses $(\tau_{ry}, \tau_{\theta y})$ are assumed to be negligible. The out-of-plane normal stress is calculated from Hooke's law for linear isotropic elastic material under the plane-strain condition $(d\epsilon_{yy,total} = d\epsilon_{yy,mech} + d\epsilon_{yy,thermal} = 0)$ as follows:

Out-of-plane normal stress

$$\begin{aligned}\sigma_{yy} = \frac{\lambda}{2(\lambda+\mu)}\Big((\sigma_{rr}-\sigma_{rr0}) + (\sigma_{\theta\theta}-\sigma_{\theta\theta0}) - 2\big(p_{pore}-p_{pore0}\big) \\ - 2\lambda\alpha(T-T_0)\Big) + (\lambda+2\mu)\alpha(T-T_0) + \big(\sigma_{yy0}-p_{pore0}\big) \\ + p_{pore}\end{aligned} \tag{13.22}$$

where p_{pore} is pore pressure, and p_{pore0} and σ_{yy0} are the initial pore pressure and out-of-plane stress, respectively.

The initial stresses $(\sigma_{h0}, \sigma_{rr0}, \sigma_{\theta\theta0}, \tau_{r\theta0}, \sigma_{yy0})$ are those after the excavation of the nuclear waste disposal tunnel, which are calculated as follows:

Initial lateral boundary stress

$$\begin{aligned}\sigma_{h0} = \frac{2\mu}{\lambda+2\mu}\left(p_{pore0}\big|_{r=\frac{H}{2},\theta=0} - p_{pore,in\,situ}\big|_{r=\frac{H}{2},\theta=0}\right) \\ + \frac{3\lambda\mu+2\mu^2}{\lambda+2\mu}2\alpha\left(T_0\big|_{r=\frac{H}{2},\theta=0} - T_{in\,situ}\big|_{r=\frac{H}{2},\theta=0}\right) + \sigma_{h,in\,situ}\end{aligned} \tag{13.23}$$

Initial radial stress

$$\begin{aligned}\sigma_{rr0} = \frac{\sigma_{h0}-\sigma_{h,in\,situ}}{2}\left(1-\left(\frac{r_0}{r}\right)^2\right) + \left(\frac{r_0}{r}\right)^2\left(p_{B0}-p_{B,in\,situ}\right) \\ + \frac{\sigma_{h0}-\sigma_{h,in\,situ}}{2}\left(1-4\left(\frac{r_0}{r}\right)^2+3\left(\frac{r_0}{r}\right)^4\right)\cos 2\theta + \sigma_{rr,in\,situ}\end{aligned} \tag{13.24}$$

Initial circumferential stress

$$\begin{aligned}\sigma_{\theta\theta0} = \frac{\sigma_{h0}-\sigma_{h,in\,situ}}{2}\left(1+\left(\frac{r_0}{r}\right)^2\right) - \left(\frac{r_0}{r}\right)^2\left(p_{B0}-p_{B,in\,situ}\right) \\ - \frac{\sigma_{h0}-\sigma_{h,in\,situ}}{2}\left(1+3\left(\frac{r_0}{r}\right)^4\right)\cos 2\theta + \frac{E\alpha\left(T_0 - T_0\big|_{r=\frac{H}{2},\theta=0}\right)}{(1-\nu)} \\ + \frac{E\left(p_{pore0}-p_{pore0}\big|_{r=\frac{H}{2},\theta=0}\right)}{3K(1-\nu)} + \sigma_{\theta\theta,in\,situ}\end{aligned} \tag{13.25}$$

Initial in-plane shear stress

$$\tau_{r\theta 0} = -\frac{\sigma_{h0} - \sigma_{h,in\,situ}}{2}\left(1 + 2\left(\frac{r_0}{r}\right)^2 - 3\left(\frac{r_0}{r}\right)^4\right)\sin 2\theta + \tau_{r\theta,in\,situ} \qquad (13.26)$$

Initial out-of-plane normal stress

$$\begin{aligned}\sigma_{yy0} = \frac{\lambda}{2(\lambda+\mu)}\Big(&\left(\sigma_{rr0} - \sigma_{rr,in\,situ}\right) + \left(\sigma_{\theta\theta 0} - \sigma_{\theta\theta,in\,situ}\right) \\ &- 2\left(p_{pore0} - p_{pore,in\,situ}\right) - 2\lambda\alpha\left(T_0 - T_{in\,situ}\right)\Big) \\ &+ (\lambda + 2\mu)\alpha\left(T_0 - T_{in\,situ}\right) + \left(\sigma_{yy,in\,situ} - p_{pore,in\,situ}\right) \\ &+ p_{pore0}\end{aligned} \qquad (13.27)$$

The subscript $_{in\,situ}$ indicates the hydrostatic, geostatic state prior to the excavation of the disposal tunnel. The *in situ* (i.e., geostatic) stresses are calculated as follows:

$$\begin{pmatrix}\sigma_{rr,in\,situ} \\ \sigma_{\theta\theta,in\,situ} \\ \tau_{r\theta,in\,situ} \\ \sigma_{yy,in\,situ}\end{pmatrix} = \begin{pmatrix}\sigma_{xx}\cos^2\theta + \sigma_{zz}\sin^2\theta \\ \sigma_{xx}\sin^2\theta + \sigma_{zz}\cos^2\theta \\ (-\sigma_{xx} + \sigma_{zz})\sin\theta\cos\theta + \tau_{xz} \\ \sigma_{yy}\end{pmatrix} \qquad (13.28)$$

where

$$\begin{pmatrix}\sigma_{xx} \\ \sigma_{zz} \\ \tau_{xz} \\ \sigma_{yy}\end{pmatrix} = \begin{pmatrix}K_0\left(\rho_{rock}\cdot g\cdot(L/2 - z) - p_{pore,in\,situ}\right) + p_{pore,in\,situ} \\ \rho_{rock}\cdot g\cdot(L/2 - z) \\ 0 \\ K_0\left(\rho_{rock}\cdot g\cdot(L/2 - z) - p_{pore,in\,situ}\right) + p_{pore,in\,situ}\end{pmatrix} \qquad (13.29)$$

where ρ_{rock} is the bulk density of rock, g is gravitational acceleration, z is the vertical distance from the center of the tunnel (upward is positive), $L/2$ is the depth from the ground surface to the center of the tunnel, and K_0 is the lateral earth pressure coefficient. The out-of-plane shear stresses (τ_{xy}, τ_{yz}) are assumed to be nonexistent. It is noted that $\sigma_{h,in\,situ}$ is assumed equal to σ_{xx} at the depth of the center of the tunnel as shown below:

$$\sigma_{h,in\,situ} = K_0\left(\rho_{rock}\cdot g\cdot(L/2) - p_{pore,in\,situ}\right) + p_{pore,in\,situ} \qquad (13.30)$$

The *in situ* (i.e., hydrostatic) pore pressure and (i.e., thermostatic) temperature prior to tunnel excavation are calculated as follows:

$$p_{pore,in\,situ} = \rho_{water} \cdot g \cdot (L/2 - z) \tag{13.31}$$

$$T_{in\,situ} = \frac{T_{bottom} - T_{top}}{L}(L/2 - z) + T_{top} \tag{13.32}$$

where ρ_{water} is the density of pore water, and T_{top} and T_{bottom} are static temperature at $z = \frac{L}{2}, -\frac{L}{2}$, respectively.

13.1.3.2 THM simulation case

The thermo-hydromechanical (THM) coupled simulation case is implemented with the TOUGH-FLAC simulator, in order to evaluate the accuracy of stress and permeability estimates calculated in the TH simulation case. The stresses are calculated numerically by FLAC3D and Equation 13.7 is used to compute rock permeability near the tunnel.

13.2 Results

13.2.1 Buffer TH outputs

Figure 13-8 shows the evolution of TH variables (i.e., temperature, pore pressure, saturation, and capillary pressure) in the buffer in the canister heating stage. These outputs are taken from the buffer element at its mid-thickness along the vertical axis ($r = 0.8$ m, $\theta = 90^{\circ}$).

No difference has been found in results between the TH and THM simulation cases, which indicates that the variance in rock permeability between the two cases has negligible effects on the fluid flow and heat transfer in the buffer. The rock permeability variance between the two simulation cases is presented in the following sections.

The maximum temperature in the buffer is approximately 85°C, which is reached between 10 and 100 years since the canister emplacement. Around the same time, the buffer becomes fully saturated with water and pore pressure starts to increase significantly. This is caused by the suction (i.e., capillary pressure)-induced swelling of the buffer; buffer tries to swell upon the imbibition of pore water in the confined space between canister and rock, which results in the compaction of buffer's pore space, which in turn compresses pore fluid and increase its pressure level. Thermal expansion of the pore water in the low permeability buffer (i.e., thermal pressurization) also contributes to this pore pressure buildup. Pore pressure keeps increasing while temperature starts to decrease from its peak value. During this time, the pore pressure buildup is driven by the thermal pressurization of the surrounding rock, where the temperature peak occurs later than the buffer due to slow heat transfer. Pore pressure peaks at 8MPa, which is significantly greater than the hydrostatic pore pressure level of 4.5 MPa at this depth, and it starts to decrease when thermal depressurization starts to occur in the surrounding rock.

These TH outputs in the buffer are used to estimate buffer stresses in the TH simulation case, which are compared against buffer stresses computed in the THM simulation case in the following section.

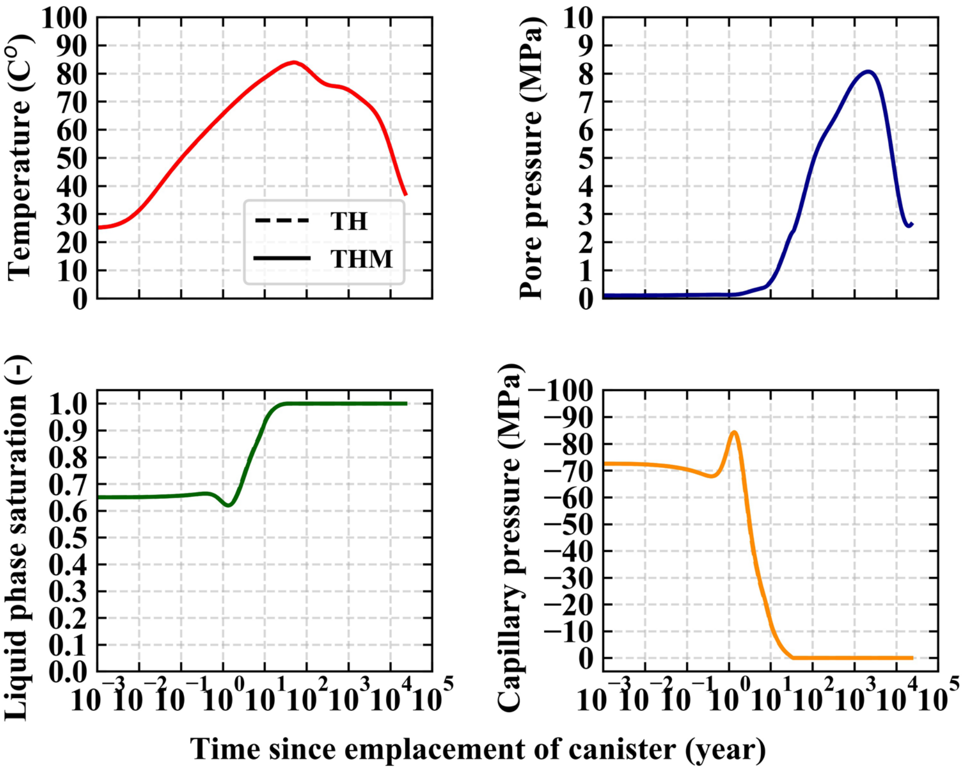

Figure 13-8 The evolution of TH variables--temperature, pore pressure, saturation, and capillary pressure--in the buffer in the canister heating stage.

13.2.2 Buffer stresses

Figure 13-9 shows the evolution of the buffer stresses in the canister heating stage for the TH and THM simulation cases. The match between the TH and THM simulation cases is excellent, validating the analytical solutions for the buffer stresses developed for the TH simulation case. The mean effective stress changes are driven by the suction-induced swelling, and hence they correspond with changes in saturation (and capillary pressure). Thermal expansion and contraction also contribute to the effective stress changes in the buffer but the thermal effect is secondary to the swelling effect. When combined with pore pressure, which renders the mean total stress, the peak buffer stress reaches 12 MPa, which is approximately the same as the *in situ* total stress level at the tunnel depth before excavation.

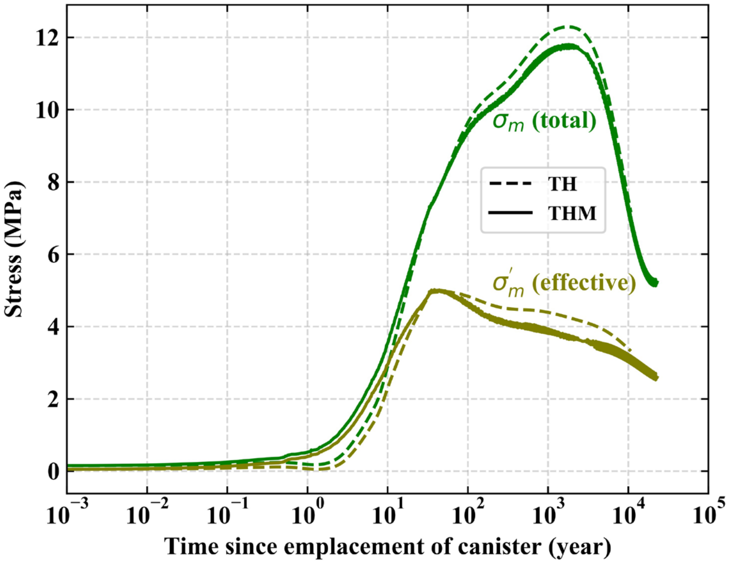

Figure 13-9 The mean total and mean effective stresses in the buffer for the TH and THM simulation cases.

13.2.3 Rock stresses

Rock stresses (i.e., radial effective stress, σ'_{rr}, circumferential effective stress, $\sigma'_{\theta\theta}$, and out-of-plane effective stress, σ'_{yy}) are compared between the TH and THM simulation cases at eight different locations near the tunnel: four locations on the vertical axis (V1, V2, V3, V4) and four locations on the horizontal axis (H1, H2, H3, H4). These locations are shown in Figure 13-10.

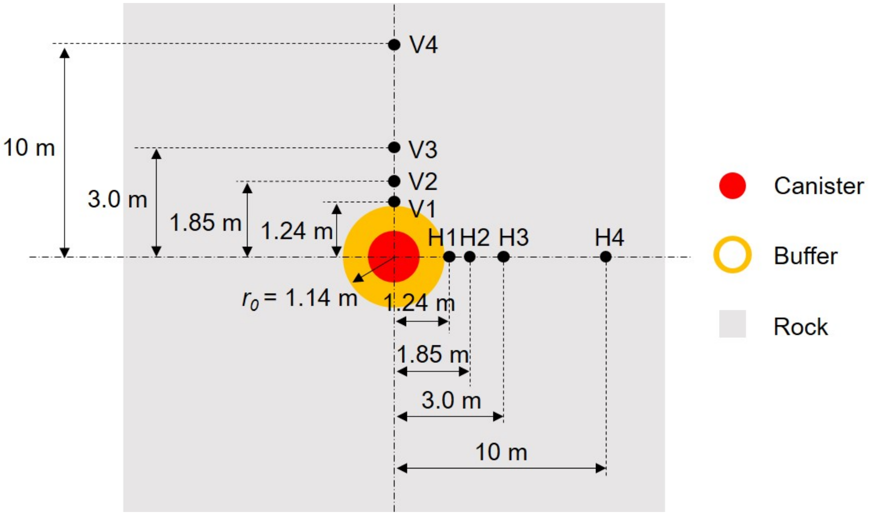

Figure 13-10 Locations in rock where stress data are extracted for comparison.

Figure 13-11 shows the evolution of rock stresses near the tunnel in the canister heating stage. The in-plane shear stress is not shown because its magnitude at these locations are a couple of orders of magnitudes smaller than the other stress levels. The stresses are initially anisotropic near the tunnel wall; the magnitudes of stresses are roughly 15 MPa ($\sigma'_{\theta\theta}$), 8 MPa (σ'_{yy}), and 3 MPa (σ'_{rr}) at V1 in the THM case. This is caused by the cylindrical cavity contraction during the tunnel excavation stage. The tunnel wall relaxes toward the center of the tunnel upon excavation, which reduces the radial stress, while at the same time the tunnel wall compresses in the circumferential direction, which increases the circumferential stress. The cavity contraction effect diminishes as the distance from the tunnel increases and hence the stress state approaches the initial isotropic stress state that is assumed in this study.

The effective stresses are found to increase with time. This trend corresponds with the temperature and buffer stress increase with time. After roughly 10 years, the radial and out-of-plane effective stresses plateau or decrease slightly, whereas the circumferential effective stress decreases significantly at the data points along the horizontal axis (H1, H2, H3, H4). The circumferential stress decreases because of thermally-induced pore pressure buildup while the circumferential total stress (which is vertical total stress developed by rock self-weight at these locations) remains unchanged. The radial and out-of-plane stresses do not decrease as much as the circumferential stress because the total stresses in these directions (*x*- and *y*-axes directions) increase due to the thermal expansion of rock under lateral confinement. These trends more or less hold for the vertical data points (V1, V2, V3, V4) if the radial and circumferential effective stresses are switched in the above explanation. The difference is that the radial effective stress does not decrease significantly near the tunnel wall (V1, V2) like the circumferential effective stress does at the corresponding horizontal data points (H1, H2). This is because the increase in buffer stress offsets the pore pressure buildup in the radial direction near the wall.

Finally, it is found that the match in terms of rock stress levels and their changes with time between the TH and THM simulation cases is excellent, validating the analytical solutions for rock stresses developed for the TH simulation case. An exception is the data point H1 where the initial radial and circumferential stresses are under- and overestimated by roughly 3 MPa, respectively. Possible causes include non-circular tunnel geometry after excavation, inadequate meshing near the tunnel wall, etc. However, the error diminishes after 10 years, after which is of a greater importance to radionuclide transport calculations than the time earlier. Therefore, the initial errors in rock stresses in the TH simulation case are not critical.

Figure 13-12 shows the mean effective and deviatoric stresses in rock. The match between the TH and THM simulation cases is again found excellent. The mean effective stress in the TH case, for example, seems to align perfectly with that in the THM case at all examined data points, whereas the deviatoric stress contains some errors at locations near the tunnel wall (V1, V2, H1, H2) at times earlier than 10 years. This is because the errors in the radial, circumferential, and out-of-plane effective stresses are averaged out in calculating the mean effective stress, whereas the errors are retained in the deviatoric stress calculation. Nevertheless, the errors in the deviatoric stress diminish after 10 years, and hence such errors at early times are not significant for long-term TH simulations of radionuclide transport.

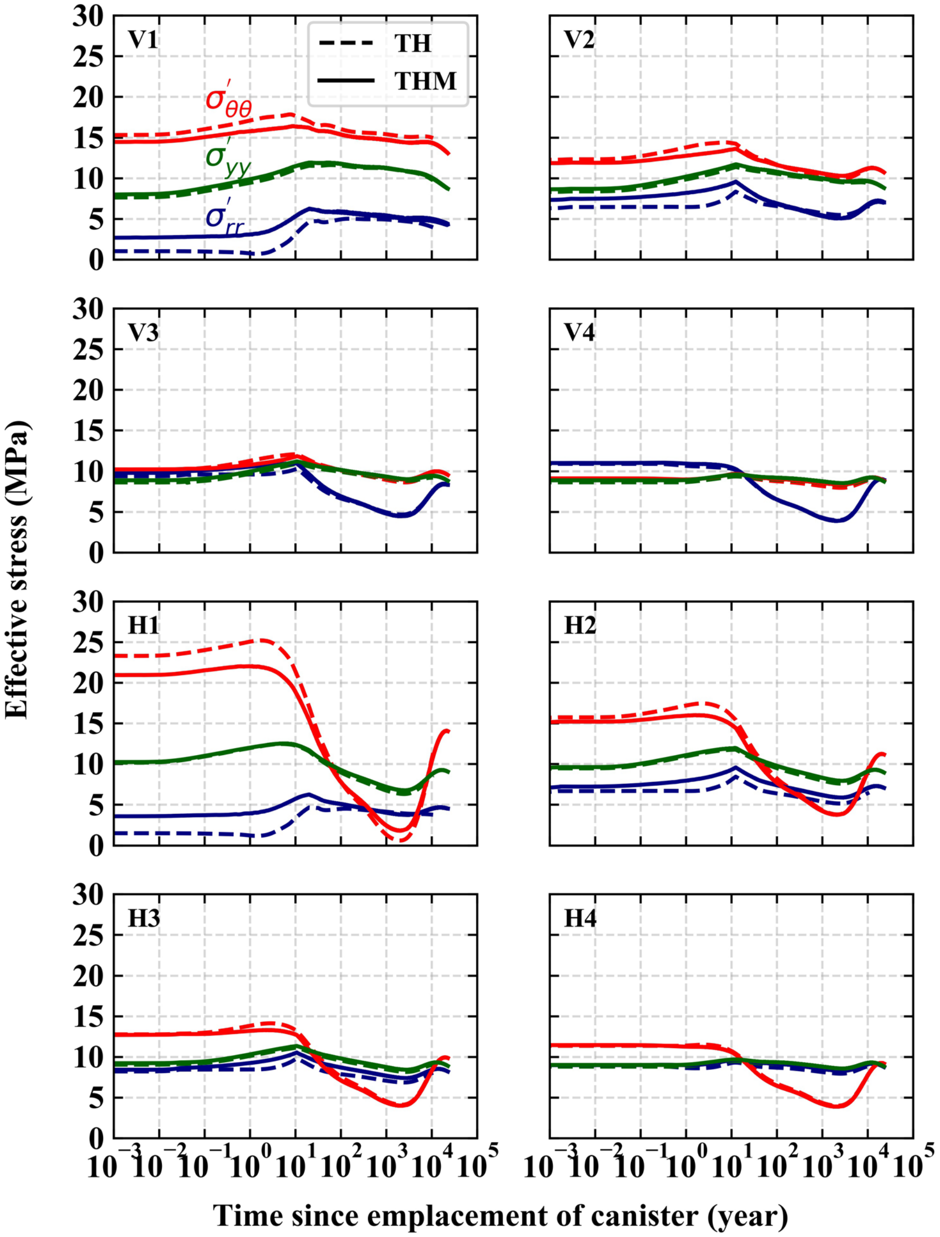

Figure 13-11 Rock stresses near the tunnel in the TH and THM simulation cases.

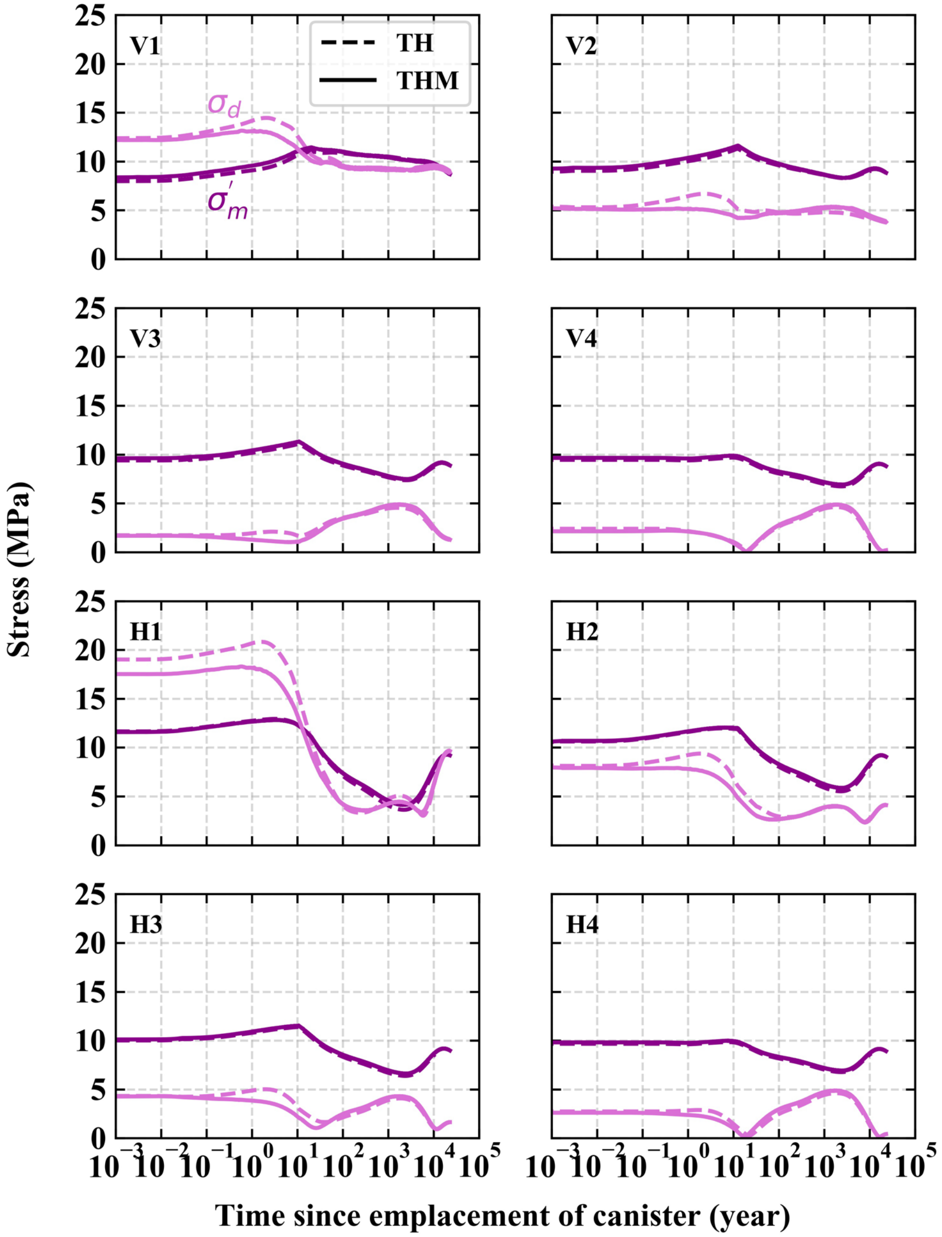

Figure 13-12 Mean effective and deviatoric stresses in the rock near the tunnel in the TH and THM simulation cases.

13.2.4 Rock permeability

Figure 13-13 shows stress-induced permeability changes in rock near the tunnel. It is noted that in these figures the vertical axis is shown in logarithm. Stress-induced permeability changes occur only at locations close to the tunnel wall (V1, V2, H1, H2), which are roughly within twice the radius of the tunnel. At these locations, the initial permeability is higher than the *in situ* rock permeability ($5 \cdot 10^{-20}$ m^2) due mainly to excavation-induced deviatoric stress increase.

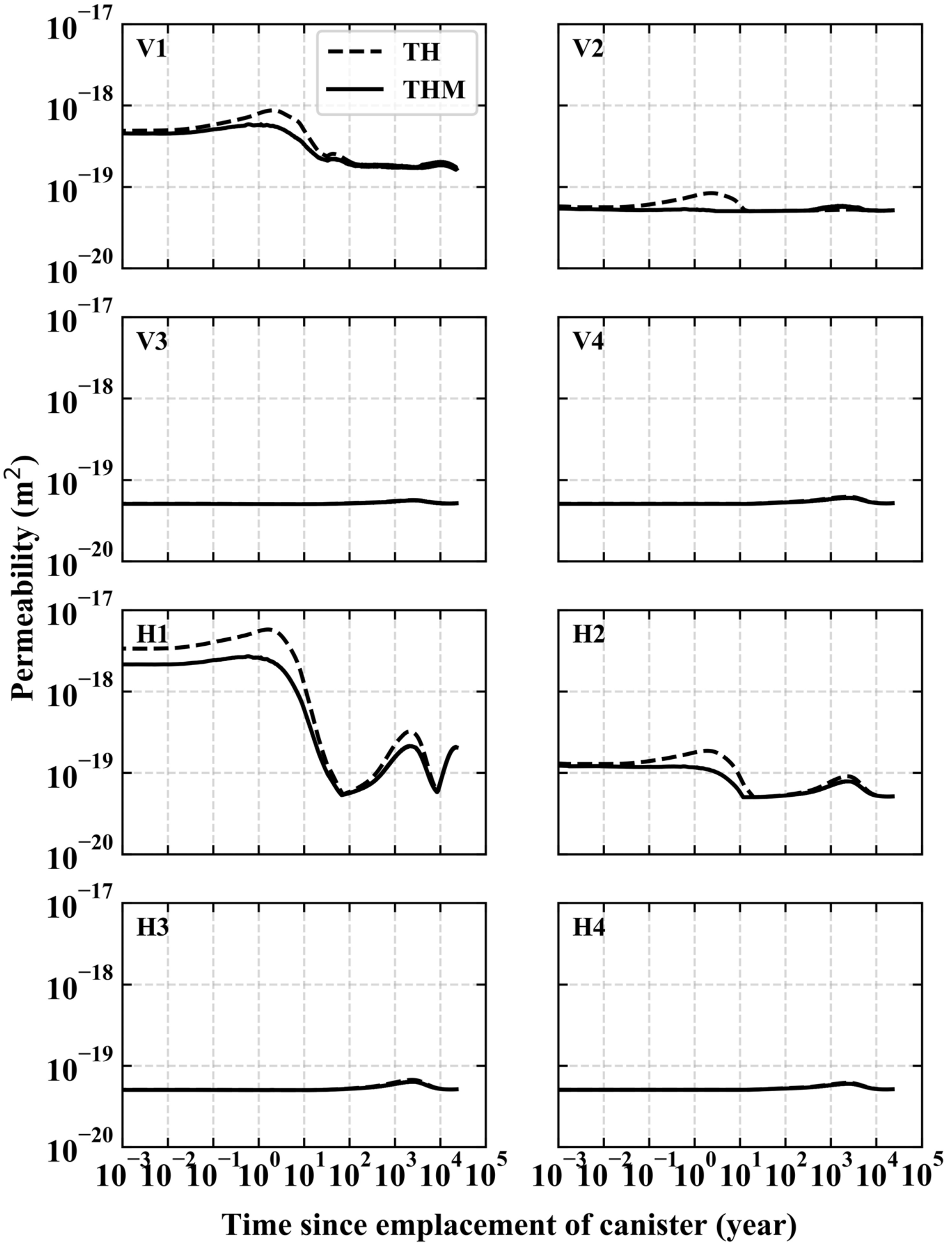

Figure 13-13 Permeability changes in the rock near the tunnel in the TH and THM simulation cases.

Permeability changes are found to be governed by deviatoric stress changes. At the location H1, for example, permeability remains at the initial levels up to roughly 1 year after the emplacement of the canister, after which it decreases more than an order of magnitude toward 100 years. This permeability change is dominated by the decrease in the deviatoric stress level as the effect of mean effective stress decrease, which should have caused an increase in permeability, has been cancelled out. Permeability change after 100 years also corresponds to the changes in the deviatoric stress. The predominant effect of deviatoric stress, however, may be due to the specific parameter values (Table 13-3) that are employed for the permeability function (Equation 12.7), and/or the permeability function itself. Therefore, further studies are necessary to evaluate long-term stress-induced permeability changes in rock near the nuclear waste disposal tunnel.

Finally, the match in rock permeability between the TH and THM simulation cases are adequate, as relatively large errors (maximum error is roughly 100%) are generated near the tunnel wall in the horizontal direction (i.e., H1) at approximately 2 years since canister emplacement. The error is caused by the overestimation of the deviatoric stress in the TH case. The permeability function employed in this study (Equation 13.7) is an exponential function of deviatoric stress above the critical value (5 MPa in this study). As a result, errors in deviatoric stress estimate above 5 MPa are exponentially magnified in the permeability calculation. These errors, however, are not critical as they diminish at roughly 10 years, after which is of particular importance for long-term radionuclide transport simulations.

13.2.5 Rock temperature and pore pressure

Figure 13-14 shows the evolution of temperature and pore pressure in rock near the tunnel. It is found that pore pressure does not vary between the TH and THM simulation cases despite the errors in permeability. Temperature values are also identical between the two cases. This may be because the errors in permeability estimate are small enough not to affect hydrological calculations, but depending on the hydrological parameters of rock (e.g., porosity, relative permeability function, capillary pressure function), pore pressure evolution might be affected by errors in permeability estimate between TH and THM cases. Therefore, the effect of hydrological properties of rock on pore pressure in the TH and THM simulation cases may be addressed in future studies.

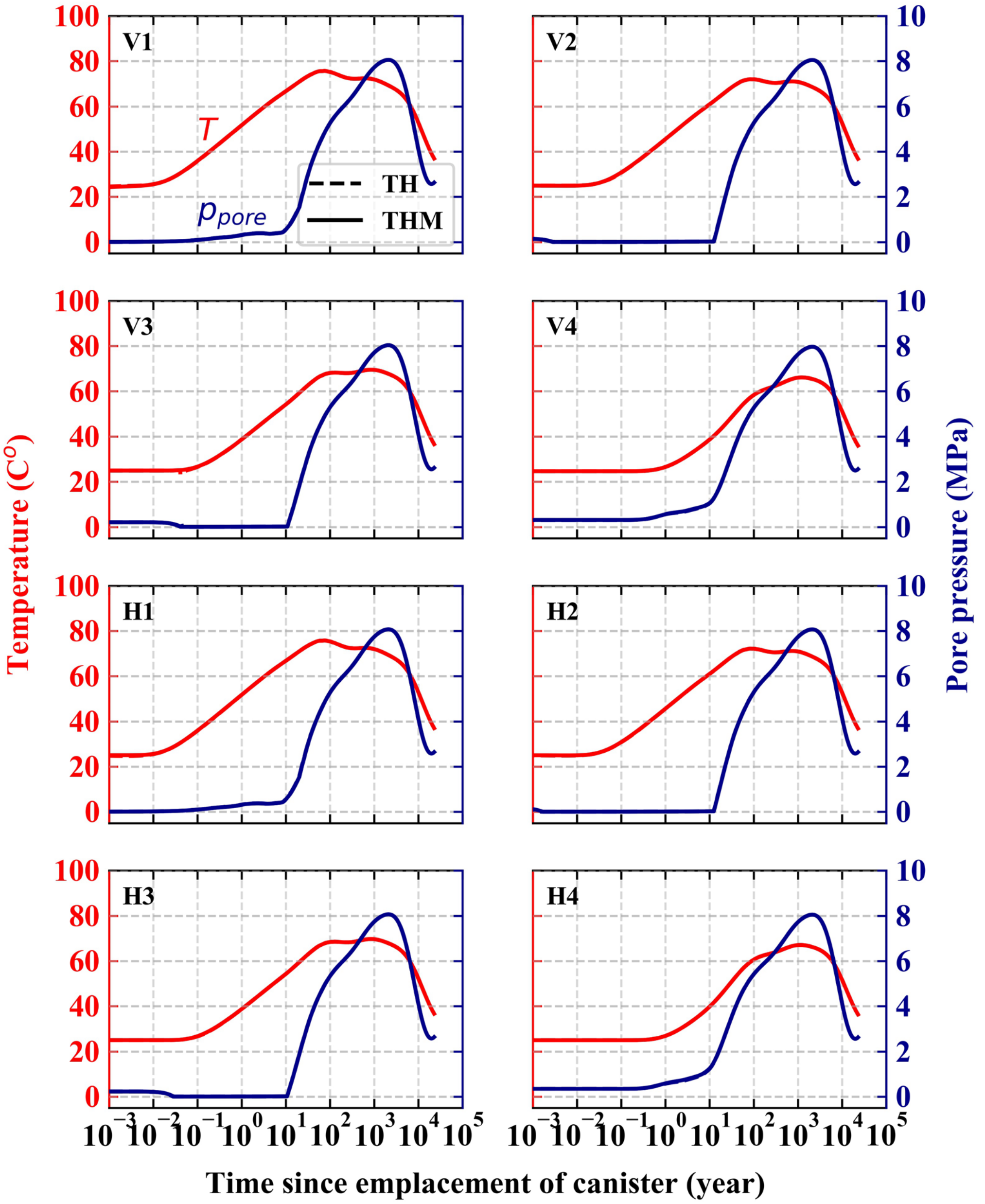

Figure 13-14 Temperature and pore pressure in the rock near the tunnel in the TH and THM simulation cases.

13.3 Summary

The objective of this study is to develop a methodology to estimate stress changes in rock around the nuclear waste disposal tunnel in a simulation where only thermo-hydrological (TH) equations are coupled so as to be able to incorporate stress-induced permeability change into an existing TH simulator for radionuclide transport problems (PFLOTRAN). This year, the methodology has been developed and its validity examined in a numerical simulation of tunnel excavation and canister heating in a hypothetical nuclear waste repository using the TOUGH-FLAC simulator. Results show that the stress estimates obtained in a TH simulation case, where only the TOUGH3 simulator is used, match stress changes calculated directly in a thermo-hydromechanically (THM) coupled simulation case, where the TOUGH-FLAC simulator is used. Only one permeability function of stresses is used to examine the changes in rock permeability around the disposal tunnel, and it is found that the match in permeability values between the TH and THM simulation cases is less satisfactory than that in stress values. This is because the employed permeability function is an exponential function of stresses; small errors in stress values are magnified exponentially in permeability values. Nevertheless, the maximum error in permeability values between the TH and THM cases is roughly 100%, which is not particularly large compared to the range of potential permeability change in rock with fractures, which could be over several orders of magnitudes. In addition, the errors diminish after 10 years since the canister emplacement, after which is a more critical timeframe for radionuclide transport simulations than the time earlier. Therefore, the accuracy of the developed methodology for stress and permeability estimates has been shown adequate. Future studies mentioned below will improve the accuracy and capabilities of the developed methodology, hence they will be addressed in next year to increase the confidence in this methodology so as to be applied in radionuclide transport simulations.

13.4 Future studies

Future studies will include the following:

- Calibration of the parameter values of the permeability function by modelling the tunnel excavation stage of an existing experimental repository, where permeability measurement after the excavation was carried out, to match the calculated and measured permeability distributions around the tunnel.
- Comparison of the results of TH vs. THM modeling with different permeability functions for rock--one that considers effective stresses perpendicular to fracture planes, and the two-parts Hooke's model developed by Liu and Li (2013).
- Sensitivity analysis on the hydrological parameters of rock and the geometry of the repository. In particular, we will simulate the how the rock porosity, relative permeability, and capillary pressure could affect pore pressure estimates in rock in both TH and THM cases, as well as different canister spacing could affect stresses, permeability, and pore pressure estimates.

This page is intentionally left blank.

14. SUMMARY OF FY20 PROGRESS

In FY20, LBNL work on coupled processes in argillite rock has continued with a broad research portfolio, including model developments, validations, and applications, along with fundamental studies of argillite and bentonite-based buffer materials. Below is a brief summary of the different topics:

- Current model developments include moving forward with TOUGH-FLAC, adopting the newly released TOUGH3 and FLAC3D V7 codes, enabling improved performance with parallel processing. Work is underway for improved and more efficient bentonite modeling using the dual-structure (BExM) model. Current TOUGH-RBSN developments include improved modeling of hydromechanical coupling associated with fracturing, as well as anisotropic strength and modulus for argillite.

- TOUGH-FLAC has been validated against major *in situ* heater experiments in argillite at the Mont Terri URL in Switzerland and at the URL in Bure, France. The Mont Terri Full Scale Experiment has been conducted for ~5 years, with heating to temperature of up to 130°C in the buffer. The experiments at the Bure URL have been conducted to study processes of thermal pressurization and associated stress changes causing low permeability of argillite host rocks. For the remainder of FY20, we will participate in DECOVALEX-2023 tasks on Mont Terri Full Scale Experiment as well thermal fracturing task on fracturing due to thermal pressurization at the Bure URL.

- TOUGH-RBSN has been applied to study gas migration as part of the DECOVALEX-2019 Task A. All research teams involved in DECOVALEX-2019 applied the same discrete fracture model for modeling gas migration. In FY20, research also included modeling of gas migration in a rough fracture. For the rest of FY20, as part of DECOVALEX-2023, we will conduct a study of gas migration based on the experimental results obtained from the Large Scale Gas Injection Tests (Lasgit), performed at the Äspö Hard Rock Laboratory.

- In FY20, substantial work has been carried out to study the fracture and fault behavior at the Mont Terri Laboratory. New modeling work have been conducted to understand the mechanisms of fault activation and potential permeability changes. LBNL scientists participated in a DECOVALEX-2019 task on modeling fault activation, which has been completed. Further work will be conducted at Mont Terri to study the long-term sealing.

- The FY20, argillite coupled processes research portfolio also included a continuing research task on the evaluation of coupled microbial-abiotic processes in the EBS and host rock materials. It is focused on consumption of hydrogen gas that could be important in the case of gas generation in the EBS. Preliminary results of laboratory experiments indicate that EBS materials can maintain microbial communities with the potential to metabolize hydrogen.

- In FY20, research also included a task on molecular modeling of radionuclide retention by bentonites. The ultimate goal is to develop the predictive computational model of radionuclide retention in bentonites, which are relevant for nuclear waste disposal safety assessments. At the moment, we are further developing computational frameworks for predicting radionuclide retention by smectites, mobility in clay pores and interlayers as a function of fluid and solid composition. We plan to extend the interaction parameter library to include some organic ligands commonly encountered in the environment, such as oxalate, malonate, citrate. We also plan to parametrize mathematical functions describing how fluid properties, such as polarizability and viscosity, are related to the fluid composition and mineral confinement.

- Finally, as part of LBNL's Argillite R&D work package, LBNL, in collaboration with SNL, is developing approaches for integrating coupled process models into the Geological Disposal Safety Assessment (GDSA) and Performance Assessment (PA). In FY20, LBNL's scientists continued the development and testing of analytical functions of coupled geomechanical responses.

This page intentionally left blank.

15. ACKNOWLEDGEMENTS

This work was supported by the Spent Fuel and Waste Science and Technology Campaign, Office of Nuclear Energy, of the U.S. Department of Energy under Contract Number DE-AC02-05CH11231 with Lawrence Berkeley National Laboratory.

This page is intentionally left blank.

16. REFERENCES

Ajo-Franklin, J.V., Molins, S., and Yang, L. (2017) Coupled Processes in a Fractured Reactive System: A Dolomite Dissolution Study with Relevance to GCS Caprock Integrity, in Caprock Integrity in Geological Storage : Hydrogeochemical and Hydrogeomechanical Processes and their Impact on Storage Security. 2017, Wiley Publishing.

Alonso, E.E., Gens, A., and Josa, A. (1990) A constitutive model for partially saturated soils. Geotechnique. 40: 405-430.

Aoki, K., Seshimo, K., Guglielmi, Y., Nussbaum, C., Shimamoto, T., Ma, S., Yao, L., Kametaka, M., Sakai, T. (2016) Frictional Properties of Main Fault Gouge of Mont Terri, Switzerland. American Geophysical Union, Fall Meeting 2016, abstract #MR41D-2715.

Armand, G., Leveau, F., Nussbaum, C., de La Vaissière, R., Noiret, A., Jaeggi, D., Righini, C. (2014), Geometry and properties of the excavation-induced fractures at the meuse/haute-marne URL drifts. Rock Mechanics and Rock Engineering, 47(1), 21–41. https://doi.org/10.1007/s00603-012-0339-6

Armand, G., Bumbieler, F., Conil, N., de la Vaissière, R., Bosgiraud, J.-M. and Vu, M.-N. (2017) Main outcomes from in situ thermo-hydro-mechanical experiments programme to demonstrate feasibility of radioactive high-level waste disposal in the Callovo-Oxfordian claystone, Journal of Rock Mechanics and Geotechnical Engineering. http://dx.doi.org/10.1016/j.jrmge.2017.03.004

Armstrong, R. T., Evseev, N., Koroteev, D., and Berg, S. (2015) Modeling the velocity field during Haines jumps in porous media, Advances in Water Resources, 77, 57-68.

Asahina, D., and Bolander, J.E. (2011) Voronoi-based discretizations for fracture analysis of particulate materials, Powder Technology, 213, 92–99.

Asahina, D., Houseworth, J.E., Birkholzer, J.T., Rutqvist, J., and Bolander, J.E. (2014) Hydro-mechanical model for wetting/drying and fracture development in geomaterials, Computers & Geosciences, 65, 13–23.

Axen, G.J. (1992) Pore pressure, stress increase, and fault weakening in low-angle normal faulting, J. geophys. Res., 97, 8979–8991. 35.

Berg, S., Ott, H., Klapp, S. A., Schwing, A., Neiteler, R., Brussee, N., Makurat, A., Leu, L., Enzmann, F., Schwarz, J. O., Kersten, M., Irvine, S., and Stampanoni, M. (2013) Real-time 3D imaging of Haines jumps in porous media flow, Proceedings of the National Academy of Sciences of the United States of America, 110(10), 3755-3759.

Biot, M.A., and Willis, D.G. (1957) The elastic coefficients of the theory of consolidation, Journal of Applied Mechanics, 24, 594–601.

Birkholzer, J., Houseworth, J., and Tsang, C. F. (2012) Geologic Disposal of High-Level Radioactive Waste: Status, Key Issues, and Trends, Annual Review of Environment and Resources, Vol 37, 37, 79-+.

Bock, H. (2009) RA Experiment - Updated Review of the Rock Mechanics Properties of the Opalinus Clay of the Mont Terri URL based on Laboratory and Field Testing, Technical Report TR 2008-04, Mont Terri Project Underground Rock Laboratory, c/- Project Manager Christophe Nussbaum, Geotechnical Institute Ltd., Gartenstrasse 13, CH - 3007 Bern / Switzerland.

Booker, J.R., and Savvidou, C. (1985) Consolidation around a point heat source. International Journal for Numerical and Analytical Methods in Geomechanics 9, 173–184.

Bossart, P., Meier, P.M, Moeri, A, Trick, T, and Mayor, J-C. (2002) Geological and hydraulic characterization of the excavation disturbed zone in the Opalinus Clay of the Mont Terri Rock Laboratory. Eng Geol 66, 19–38.

Bossart, P., Trick, T., Meier, P.M., and Mayor, J.-C. (2004) Structural and hydrogeological characterisation of the excavation-disturbed zone in the Opalinus Clay (Mont Terri Project, Switzerland), Applied Clay Science, 26, 429– 448.

Bradbury, M. H. and B. Baeyens (2005) "Modelling the sorption of Mn(II), Co(II), Ni(II), Zn(II), Cd(II), Eu(III), Am(III), Sn(IV), Th(IV), Np(V) and U(VI) on montmorillonite: Linear free energy relationships and estimates of surface binding constants for some selected heavy metals and actinides (vol 69, pg 875, 2005)." Geochimica Et Cosmochimica Acta 69(22): 5391-5392.

Bradbury, M. H. and B. Baeyens (2006) "Modelling sorption data for the actinides Am(III), Np(V) and Pa(V) on montmorillonite." Radiochimica Acta 94(9-11): 619-625.

Bradbury, M. H. and B. Baeyens (2009) "Sorption modelling on illite. Part II: Actinide sorption and linear free energy relationships." Geochimica Et Cosmochimica Acta 73(4): 1004-1013.

Brown, D. (1989) The flow of water and displacement of hydrocarbons in fractured chalk reservoirs., in: Fluid Flow in Sedimentary Basins and Aquifers. J. C. Goff and B. P. Williams, Geological Society London, pp. 201–218.

Cao, X. Y., Dolg, M. and Stoll, H. (2003) "Valence basis sets for relativistic energy-consistent small-core actinide pseudopotentials." Journal of Chemical Physics 118(2): 487-496.

Cappa, F., Guglielmi, Y., Rutqvist, J., Tsang, C-F., and Thoraval, A. (2006) Hydromechanical modeling of pulse tests that measure fluid pressure and fracture normal displacement at the Coaraze Laboratory site, France, Int. J. Rock Mech. Min. Sci., 43(7):1062-1082.

Cappa, F. (2018) Hydromechanical modeling of fluid injection-induced seismicity and aseismic slip into a fault zone in a shale formation at the Mont Terri underground research laboratory, Technical Report. Contrat de recherche: ZFL401-FS

Cappa, F., Guglielmi, Y., Nussbaum, C., and Birkholzer, J. (2018) On the relationship between fault permeability increases, induced stress perturbation, and the growth of aseismic slip during fluid injection, Geophys. Res. Lett., 45. https://doi.org/10.1029/2018GL080233

Chaboche, J.-L. (1992) Damage induced anisotropy: On the difficulties associated with the active/passive unilateral condition. International Journal of Damage Mechanics 1, 148–171.

Christensen, H., and Sunder, S. (2000) Current state of knowledge of water radiolysis effects on spent nuclear fuel corrosion, Nuclear Technology, 131(1), 102-123.

Cihan, A., and Corapcioglu, M. Y. (2008) Effect of compressibility on the rise velocity of an air bubble in porous media, Water Resources Research, 44(4).

Claret, F., Marty, N., and Tournassat, C. (2018) Modeling the Long-term Stability of Multi-barrier Systems for Nuclear Waste Disposal in Geological Clay Formations, Reactive Transport Modeling.

Collins, K., and McGOWN, A. (1974) The form and function of microfabric features in a variety of natural soils.

Corey, A.T. (1954) The Interrelation Between Gas and Oil Relative Permeabilities, Producers Monthly, 38-41.

Coussy, O. (2004) Poromechanics. John Wiley & Sons.

Corkum, A.G., and Martin, C.D. (2007) Modeling a mine-by test at the Mont Terri rock laboratory, Switzerland. International Journal of Rock Mechanics & Mining Sciences 44, 846–859.

Crandall, D., Ahmadi, G. and Smith, D. (2009a) Comparison of Experimental and Numerical Two-Phase Flows in a Porous Micro-Model. The Journal of Computational Multiphase Flows, 2009. 1: p. 325-340.

Crandall, D., Ahmadi, G. and Smith, D. (2009b) Modeling of Immiscible, Two-Phase Flows in a Natural Rock Fracture. Vol. 1. 2009.

Cundall, P. A. (1988) Formulation of a Three-Dimensional Distinct Element Model – Part I: A Scheme to Detect and Represent Contacts in a System Composed of Many Polyhedral Blocks, Int. J.Rock Mech., Min. Sci. and Geomech. Abstr., 25, 107-116 (1988).

Cuss, R.J., Milodowski, A. and Harrington, J.F. (2011), Fracture transmissivity as a function of normal and shear stress: First results in Opalinus Clay. Physics and Chemistry of the Earth, 36(17–18), 1960–1971. https://doi.org/10.1016/j.pce.2011.07.080

Cuss, R.J., Sathar, S. and Harrington, J.F. (2013) Final Report of FORGE WP4.1.2: Validation of critical stress theory applied to repository concepts. British Geological Survey Commissioned Report, CR/13/001. 96pp

Cuss, R.J., Harrington, J.F., Noy, D.J., Graham, C.C., and Sellin, P. (2014) Evidence of localised gas propagation pathways in a field-scale bentonite engineered barrier system; results from three gas injection tests in the Large scale gas injection test (Lasgit). Applied Clay Science, 102, pp.81-92

Cygan, R. T., Liang, J. J. and Kalinichev, A. G. (2004) "Molecular models of hydroxide, oxyhydroxide, and clay phases and the development of a general force field." Journal of Physical Chemistry B 108(4): 1255-1266.

de La Vaissière, R., Armand, G. and Talandier, J. (2014) Excavation damaged zone under imbibition: Evidence of self-sealing into claystone. In Unsaturated Soils: Research and Applications (pp. 1481–1487). CRC Press. https://doi.org/10.1201/b17034-216

de La Vaissière, R., Armand, G. and Talandier, J. (2015) Gas and water flow in an excavation-induced fracture network around an underground drift: A case study for a radioactive waste repository in clay rock. Journal of Hydrology, 521, 141–156. https://doi.org/10.1016/J.JHYDROL.2014.11.067

Denning, R. G. (2007) "Electronic structure and bonding in actinyl ions and their analogs." Journal of Physical Chemistry A 111(20): 4125-4143.

Dieterich, J. H. (1979) Modeling of rock friction experimental results and constitutive equations, J. Geophys. Res., 84, 2161–2168, doi:10.1029/JB084iB05p02161.

Ellis, B., Peters, C., Fitts, J., Bromhal, G., McIntyre, D., Warzinski, R., Rosenbaum, E. (2011) Deterioration of a fractured carbonate caprock exposed to CO2-acidified brine flow. Greenhouse Gases: Sci. Technol. 2011, 1, 248−260.

Ernzerhof, M. and Scuseria, G.E. (1999) "Assessment of the Perdew-Burke-Ernzerhof exchange-correlation functional." Journal of Chemical Physics 110(11): 5029-5036.

Ewing, R. C., W. Runde and T. E. Albrecht-Schmitt (2010) "Environmental impact of the nuclear fuel cycle: Fate of actinides." Mrs Bulletin 35(11): 859-866

Fang, Q.; Boas, and D. A. (2009) Tetrahedral mesh generation from volumetric binary and grayscale images. Proceedings of the 2009 IEEE International Symposium on Biomedical Imaging: From Nano to Macro,

Fang, Y., Elsworth, D., Wang, C., Ishibashi, T. and Fitts, J.P. (2017) Frictional stability-permeability relationships for fractures in shales. Journal of Geophysical Research: Solid Earth, 122(3), 1760–1776. https://doi.org/10.1002/2016JB013435

Fauchille, A. L., Hedan, S., Valle, S., Pret, D., Cabrera, J., and Cosenza, P. (2016) Multi-scale study on the deformation and fracture evolution of clay rock sample subjected to desiccation, Applied Clay Science, 132, 251-260.

Faulkner, D.R. and Rutter, EH. (2001) Can the maintenance of over pressured fluids in large strike-slip fault zones explain their apparent weakness? Geology, 29, 503–506.

Garagash, D.I. and Germanovich, L.N. (2012) Nucleation and arrest of dynamic slip on a pressurized fault, J. geophys. Res., 117, B10310, doi:10.1029/2012JB009209.

Garitte, B., and Gens, A. (2012) TH and THM Scoping computations for the definition of an optimal instrumentation layout in the Full-scale Emplacement (FE) experiment NAGRA NIB 10-34, March 2012.

Garitte, B., Shao, H., Wang, X.R., Nguyen, T.S., Li, Z., Rutqvist, J., Birkholzer, J., Wang, W.Q., Kolditz, O., Pan, P.Z., Feng, X.T., Lee, C., Graupner, B.J., Maekawa, K., Manepally, C., Dasgupta, B., Stothoff, S., Ofoegbu, G., Fedors, R., and Barnichon, J.D. (2017) Evaluation of the predictive capability of coupled thermo-hydro-mechanical models for a heated bentonite/clay system (HE-E) in the Mont Terri Rock Laboratory. Environmental Earth Sciences, 76:64.

Gens, A., and Alonso, E. (1992) A framework for the behaviour of unsaturated expansive clays. Can. Geotech. J. 29, 1013–1032.

Gens, A., Sánchez, M., and Sheng, D. (2006) On constitutive modeling of unsaturated soils. Acta Geotechnica. 1, 137-147.

Gens, A., Sánchez, M., Guimaraes, L.D.N., Alonso, E.E., Lloret, A., Olivella, S., Villar, M.V., and Huertas, F. (2009) A full-scale in situ heating test for high-level nuclear waste disposal: observations, analysis and interpretation. Geotechnique 59, 377–399.

Graupner B., Rutqvist J., and Guglielmi Y. (2020) DECOVALEX-2019 Task B Final Report. Lawrence Berkeley National Laboratory, LBNL-2001263d, 2020.

Greening, C., P. Constant, K. Hards, S.E. Morales, J.G. Oakeshott, R.J. Russell, M.C. Taylor, M. Berney, R. Conrad and G.M. Cook (2015) "Atmospheric Hydrogen Scavenging: from Enzymes to Ecosystems." Applied and Environmental Microbiology 81(4): 1190.

Guglielmi, Y., Cappa, F., and Amitrano, D. (2008) High-definition analysis of fluid induced seismicity related to the mesoscale hydromechanical properties of a fault zone, Geophys. Res. Lett., 35, L06306, doi:10.1029/2007GL033087.

Guglielmi, Y., Cappa, F., Avouac, J.-P., Henry, P., and Elsworth, D. (2015a) Seismicity triggered by fluid injections induced aseismic slip, Science, 348(6240), 1224–1226, doi:10.1126/science.aab0476.

Guglielmi, Y., Elsworth, D., Cappa, F., Henry, P., Gout, C., Dick, P., and Durand, J. (2015b) In situ observations on the coupling between hydraulic diffusivity and displacements during fault reactivation in shales, J. Geophys. Res., 120, doi:10.1002/2015JB012158.

Guglielmi Y. (2016), In-situ clay faults slip hydro-mechanical chat.racterization (FS experiment), Mont Terri underground rock laboratory. Lawrence Berkeley National Laboratory, Report.

Guglielmi Y., Birkholzer J., Rutqvist J., Jeanne P., and Nussbaum C. (2017) Can Fault Leakage Occur Before or Without Reactivation? Results from an in Situ Fault Reactivation Experiment at Mont Terri, Energy Procedia 2017;114:3167-31, https://doi.org/ 10.1016/j.egypro.2017.03.1445

Guglielmi, Y., Nussbaum, C., Jeanne, P., Rutqvist, J., Cappa, F., & Birkholzer, J. (2020a), Complexity of fault rupture and fluid leakage in shale: Insights from a controlled fault activation experiment. Journal of Geophysical Research: Solid Earth, 125, e2019JB017781. https://doi.org/ 10.1029/2019JB017781.

Guglielmi, Y., Nussbaum, C., Rutqvist, J., Cappa, F., Jeanne, P. and Birkholzer, J. (2020b), Estimating perturbed stress from 3-D borehole displacements induced by fluid injection in fractured or faulted shales. Geophys. J. Int. (2020) 221, 1684–1695.

Harrington, J.F., and Horseman, S.T. (1999) Gas transport properties of clays and mudrocks. In: Muds And Mudstones: Physical And Fluid Flow Properties (eds A.C.Aplin, A.J. Fleet, and J.H.S. Macquaker). Geological Society of London, Special Publication No. 158, 107-124.

Harrington, J.F., Milodowski, A.E., Graham, C.C., Rushton, J.C., and Cuss, R.J. (2012) Evidence for gas-induced pathways in clay using a nanoparticle injection technique. Mineralogical Magazine. December 2012, Vol. 76(8), pp.3327-3336. DOI: 10.1180/minmag.2012.076.8.45.

Harrington, J. (2016) Specification for DECOVALEX-2019: Task A: modElliNg Gas INjection ExpERiments (ENGINEER). Ref: BGS-DX-v3.

Harrington, J.F., Graham, C.C., Cuss, R.J., and Norris, S. (2017) Gas network development in a precompacted bentonite experiment: Evidence of generation and evolution, Applied Clay Science, 147, 80–89.

Horseman, S.T., Harrington, J.F., and Sellin, P. (1999) Gas migration in clay barriers. Engineering Geology, Vol. 54, 139-149.

Horseman, S.T., Harrington, J.F., and Sellin, P. (2004) Water and gas flow in Mx80 bentonite buffer clay. In: Symposium on the Scientific Basis for Nuclear Waste Management XXVII (Kalmar), Materials Research Society, Vol. 807. 715-720.

Houseworth, J., Rutqvist, J., Asahina, D., Chen, F., Vilarrasa, V., Liu, H.H., and Birkholzer, J. (2013) Report on International Collaboration Involving the FE Heater and HG-A Tests at Mont Terri. Prepared for U.S. Department of Energy, Used Fuel Disposition Campaign, FCRD-UFD-2014-000002, Lawrence Berkeley National Laboratory.

International Formulation Committee (IFC) (1967) A Formulation of the Thermodynamic Properties of Ordinary Water Substance, IFC Secretariat, Düsseldorf, Germany.

Itasca (2011) FLAC3D V5.0 Fast Lagrangian Analysis of Continua in 3 Dimensions, User's Guide. Itasca Consulting Group, Minneapolis, Minnesota.

Itasca (2018) FLAC3D V6.0 Fast Lagrangian Analysis of Continua in 3 Dimensions, User's Guide. Itasca Consulting Group, Minneapolis, Minnesota.

Itasca, (2016). 3DEC, 3-Dimensional Distinct Element Code. Itasca Consulting Group, Minneapolis, MN.

Jasak, H. (2009), OpenFOAM: Open source CFD in research and industry, International Journal of Naval Architecture and Ocean Engineering, 1(2), 89-94.

Jaeger, J.C., and N.G.W. Cook, (1979), Fundamentals of Rock Mechanics, Chapman and Hall, London, U.K.

Jaeggi and Madaschi, 2017. Technical note TN2017-85: MB-A (Mine-by test in sandy facies) Experiment - Predictive modeling using Code_Aster – model setup and results

Jeanne, P., Guglielmi Y., Rutqvist J., Nussbaum C., and Birkholzer J., (2017), Field characterization of elastic properties across a fault zone reactivated by fluid injection, J. Geophys. Res., 122, doi:10.1002/2017JB014384

Jeanne, P., Guglielmi, Y., Rutqvist, J., Nussbaum, C., and Birkholzer, J. (2018) Permeability variations associated with fault reactivation in a claystone formation investigated by field experiments and numerical simulations. Journal of Geophysical Research, Volume 123, Issue 2, https://doi.org/10.1002/2017JB015149.

Jung, Y., Pau, G. S. H. , Finsterle, S. and Pollyea, R. M. (2017) TOUGH3: A new efficient version of the TOUGH suite of multiphase flow and transport simulators, Comput. Geosci., 108, 2-7.

Khalili, N, and Khabbaz, M.H. (1998) A unique relationship for χ for the determination of the shear strength of unsaturated soils, Géotechnique, 48(2), 681–687.

Kim, J.-S., Kwon, S.-K., Sanchez, M., and Cho, G.-C. (2011) Geological storage of high level nuclear waste, KSCE Journal of Civil Engineering, 15(4), 721-737.

Kim, K., and Lim, Y.M. (2011) Simulation of rate dependent fracture in concrete using an irregular lattice model, Cement and Concrete Composites, 33, 949–955.

Kim, K., Rutqvist, J., Nakagawa, S., and Birkholzer, J. (2017) TOUGH-RBSN simulator for hydraulic fracture propagation within fractured media: Model validations against laboratory experiments, Computers and Geosciences, 108, 72–85

Kim K., Rutqvist J. and Birkholzer J. (2020) Lattice modeling of excavation damage in argillaceous clay formations: Influence of deformation and strength anisotropy. Tunneling and Underground Space Technology, 98, 2020. https://doi.org/10.1016/j.tust.2019.103196.

Kristensson, O., and Åkesson, M. (2008) Mechanical modeling of MX-80 – Quick tools for BBM parameter analysis. Phys Chem Earth, Parts A/B/C. 33, Supplement 1: S508-S515.

Lanyon, G.W., Marschall, P., Trick, T., de La Vaissière, R., Shao, H. and Leung, H. (2014), Self-sealing experiments and gas injection tests in a backfilled microtunnel of the Mont Terri URL. Geological Society, London, Special Publications,400(1), 93–106. https://doi.org/10.1144/SP400.8

Li, B. and Wong, R.C.K. (2016), Creating tensile fractures in Colorado shale using an unconfined fast heating test. Geotechnical Testing Journal, 42(2).

Liu, H.H., Houseworth, J., Rutqvist, J., Li, L., Asahina, D., Chen, F., and Birkholzer, J. (2012) Report on Modeling Coupled Processes in the Near Field of a Clay Repository. Prepared for U.S. Department of Energy, Used Fuel Disposition Campaign, FCRD-UFD-2012-000223, Lawrence Berkeley National Laboratory.

Lloret, A., Villar, M., Sànchez, M., Gens, A., Pintado, X., and Alonso, E. (2003). Mechanical behaviour of heavily compacted bentonite under high suction changes. Geotechnique, 53(1), 27-40.

Lopez-Fernandez, M., Cherkouk, A., Vilchez-Vargas, R., Jauregui, R., Pieper, D., Boon, N., Sanchez-Castro, I. and Merroun, M. L. (2015) "Bacterial Diversity in Bentonites, Engineered Barrier for Deep Geological Disposal of Radioactive Wastes." Microbial Ecology 70(4): 922-93.

Maes, J. (2018) GeoChemFoam User Guide

Marone, C. (1998) Laboratory-derived friction laws and their application to seismic faulting, Ann. Rev. Earth Planet. Sci., 26, 643–696.

Martin C.D., and Chandler N.A. (1994) The progressive fracture of Lac du Bonnet Granite. International Journal of Rock Mechanics and Mining Sciences and Geomechanics Abstract, 31, 643–59.

Martin, C.D., and Lanyon, G.W. (2003) Measurement of in-situ stress in weak rocks at Mont Terri Rock Laboratory, Switzerland. International Journal of Rock Mechanics and Mining Sciences, Volume 40, Issues 7–8, October–December 2003, Pages 1077-1088.

Martino, J.B., and Chandler, N.A. (2004) Excavation-induced studies at the Underground Research Laboratory. International Journal of Rock Mechanics and Mining Sciences, 41, 1413–26.

Mayilraj, S., and Stackebrandt, E. (2014) The Family Paenibacillaceae. In E. Rosenberg, E. F. DeLong, S. Lory, E. Stackebrandt, and F. Thompson (Eds.), The Prokaryotes: Firmicutes and Tenericutes (pp. 267-280). Berlin, Heidelberg: Springer Berlin Heidelberg.

Meier, P.M., Trick, T.H., Blümling, P. and Volckaert, G. (2002) Self-healing of fractures within the EDZ at the Mont Terri Rock Laboratory: results after one year of experimental work. – In: Hoteit, N., Su, K., Tijani, M. and Shao, J.-F. (Eds.): Hydromechanical and thermohydromechanical behaviour of deep argillaceous rocks. –Intern. Workshop, Paris, 11-12 Oct. 2000, p. 267-274, Lisse (Swets and Zeitlinger).

Nguyen, T.S., Börgesson, L., Chijimatsu, M., Hernelind, J., Jing, L., Kobayashi, A., and Rutqvist, J. (2009) A case study on the influence of THM coupling on the near field safety of a spent fuel repository in sparsely fractured granite. Environmental Geology, 57, 1239–1254.

Nussbaum, C., Bossart, P., Amann, F., and Aubourg, C., (2011) Analysis of tectonic structures and excavation induced fractures in the Opalinus Clay, Mont Terri underground rock laboratory (Switzerland), Swiss Journal of Geosciences, 104(2), 187–210. https://doi.org/10.1007/s00015- 011-0070-4

Nussbaum, C., Kloppenburg, A., Caër, T., Bossart, P. (2017) Tectonic evolution around the Mont Terri rock laboratory, northwestern Swiss Jura: constraints from kine-matic forward modelling. Swiss J. Geosci., 110, 39–66. https://doi.org/10.1007/s00015-016-0248-x.

Nutt, M. (2012) Used Fuel Disposition Campaign Disposal Research and Development Roadmap (FCRD-USED-2011-000065 REV1), U.S. DOE Used Fuel Disposition Campaign.

Okabe, A., Boots, B., Sugihara, K., and Chiu, S.N. (2000) Spatial Tessellations: Concepts and Applications of Voronoi Diagrams, 2nd ed., Wiley, NYC, 696 pages.

Orellana, L.F., Scuderi, M. M., Collettini, C., and Violay, M., (2018a) Frictional properties of Opalinus Clay: Implications for nuclear waste storage, J. Geophys. Res, 123. https://doi.org/10.1002/2017JB014931

Orellana, L.F., Scuderi, M.M., Collettini, C., and Violay, M. (2018b) Do scaly clays control seismicity on faulted shale rocks ? Earth Planet Sci Lett., 488, 59-67, doi:10.1016/j.epsl.2018.01.027

Orellana, L. F., Giorgetti, C., and Violay, M., (2019) Contrasting mechanical and hydraulic properties of wet and dry fault zones in a proposed shale-hosted nuclear waste repository. Geophys Res Lett, 46, 1357–1366. doi :10.1029/2018GL080384

Ott, H. and Oedai, S. (2015) Wormhole formation and compact dissolution in single- and two-phase CO2-brine injections. Geophysical Research Letters, 2015. 42(7): p. 2270-2276.

Pedersen, K. (1999) Subterranean microorganisms and radioactive waste disposal in Sweden, Engineering Geology, 52(3-4), 163-176.

Pei, Y., Paton, D.A., Knipe, R.J. and Wu, K. (2015) A review of fault sealing behaviour and its evaluation in siliciclastic rocks. Earth-Science Reviews, 150(July), 121–138. https://doi.org/10.1016/j.earscirev.2015.07.011

Pepper, M. and B. E. Bursten (1991) "The Electronic-Structure of Actinide-Containing Molecules - a Challenge to Applied Quantum-Chemistry." Chemical Reviews 91(5): 719-741.

Plúa, C., Vu, M., Armand, G., Rutqvist, J., Birkholzer, J., Xu, H., Guo, R., Thatcher, K., Bond, A., Wang, w., Nagel, T., Shao, H., and Kolditz, O. (2020) A reliable numerical analysis for large-scale modelling of a high-level radioactive waste repository in the Callovo-Oxfordian claystone. International Journal of Rock Mechanics and Mining Sciences (submitted).

Pruess, K., Oldenburg, C.M., and Moridis, G. (2012) TOUGH2 User’s Guide, Version 2.1, LBNL-43134(revised), Lawrence Berkeley National Laboratory, Berkeley, California.

Raeini, A.Q, Blunt, M. J., and Bijeljic, B. (2012) Modelling two-phase flow in porous media at the pore scale using the volume-of-fluid method, 5653–5668 pp.

Raeini, A.Q., Bijeljic, B., and Blunt, M.J. (2014) Numerical Modelling of Sub-pore Scale Events in Two-Phase Flow Through Porous Media, Transport in Porous Media, 101(2), 191-213.

Reed, A. Weinstock, E., R. B. and Weinhold, F. (1985) "Natural-Population Analysis." Journal of Chemical Physics 83(2): 735-746.

Rinaldi, A.P., and Rutqvist, J. (2019) Joint opening or hydroshearing? Analyzing a fracture zone stimulation at Fenton Hill. Geothermics, 77, 83–98.

Rinaldi A.P., Rutqvist J., Blanco-Martín L., Hu M., and Sentís M.L. (2018) Coupling TOUGH3 with FLAC3D for parallel computing of fluid-flow and geomechanics. Proceedings TOUGH Symposium 2018, Berkeley, California, October 8-10, 2018.

Rice, JR. (1992) Fault stress states, pore pressure distributions, and the weakness of the San Andreas fault, in Fault Mechanics and Transport Properties in Rocks, pp. 475–503, eds Evans, B.&Wong, T.-F., Academic Press.

Rubin, A.M., and Ampuero, J.P. (2005) Earthquake nucleation on (aging) rate and state faults, J. Geophys., Res., 110, B11212, doi:10.1029/2005JB003686.

Rutqvist, J., Noorishad, J., Stephansson, O. and Tsang, C.-F. (1998) Determination of fracture storativity in hard rocks using high pressure testing. Water Resources Research, 34, 2551-2560.

Rutqvist, J., Tsang, C.-F., and Stephansson, O. (2000) Uncertainty in the maximum principal stress estimated from hydraulic fracturing measurements due to the presence of the induced fracture, International Journal of Rock Mechanics and Mining Sciences, 37, 107–120.

Rutqvist, J., Börgesson, L., Chijimatsu, M., Kobayashi, A., Nguyen, T. S., Jing, L., Noorishad, J., and Tsang, C.-F. (2001) Thermohydromechanics of partially saturated geological media – Governing equations and formulation of four finite element models. International Journal of Rock Mechanics and Mining Sciences, 38, 105-127.

Rutqvist, J., Wu, Y.-S., Tsang, C.-F., and Bodvarsson, G. (2002) A modeling approach for analysis of coupled multiphase fluid flow, heat transfer and deformation in fractured porous rock. International Journal of Rock Mechanics and Mining Sciences, 39, 429-442.

Rutqvist, J., and Tsang, C.-F. (2002) A study of caprock hydromechanical changes associated with CO2-injection into a brine formation, Environmental Geology, 42, 296–305.

Rutqvist, J., Börgesson, L., Chijimatsu, M., Hernelind, J., Jing, L., Kobayashi, A., and Nguyen, S. (2009) Modeling of damage, permeability changes and pressure responses during excavation of the TSX tunnel in granitic rock at URL, Canada. Environmental Geology, 57, 1263–1274.

Rutqvist, J. (2011) Status of the TOUGH-FLAC simulator and recent applications related to coupled fluid flow and crustal deformations. Computers and Geosciences, 37, 739–750.

Rutqvist, J., Ijiri, Y, and Yamamoto, H. (2011) Implementation of the Barcelona Basic Model into TOUGH-FLAC for simulations of the geomechanical behavior of unsaturated soils. Computers and Geosciences, 37, 751–762.

Rutqvist, J., Davis, J., Zheng, L., Vilarrasa, V., Houseworth, J., and Birkholzer, J. (2014a) Investigation of Coupled THMC Processes and Reactive Transport: FY14 Progress. Prepared for U.S. Department of Energy, Used Fuel Disposition, FCRD-UFD-2014-000497, Lawrence Berkeley National Laboratory, LBNL-6720E (2014a).

Rutqvist, J., Zheng, L., Chen, F., Liu, H.-H., and Birkholzer, J. (2014b) Modeling of Coupled Thermo-Hydro-Mechanical Processes with Links to Geochemistry Associated with Bentonite-Backfilled Repository Tunnels in Clay Formations. Rock Mechanics and Rock Engineering, 47, 167–186.

Rutqvist, J. (2015) Fractured rock stress-permeability relationships from in situ data and effects of temperature and chemical-mechanical couplings. Geofluids, 15, 48–66.

Rutqvist, J. (2017) An overview of TOUGH-based geomechanics models. Computers and Geosciences, 108, 56–63.

Rutqvist J., Kim K., Xu H., Guglielmi Y., and Birkholzer J. (2018) Investigation of Coupled Processes in Argillite Rock: FY18 Progress. Prepared for U.S. Department of Energy, Spent Fuel and Waste Disposition, SFWD-SFWST-2018-000XXX, LBNL-2001168, Lawrence Berkeley National Laboratory.

Rutqvist J. and Rinaldi A.P. (2019). Fault reactivation and seismicity associated with geologic carbon storage, shale-gas fracturing and geothermal stimulation– Observations from recent modeling studies. Proceedings of 14th Congress of the ISRM, Iguassu Falls, Brazil, Sept 13 - 18, 2019.

Rutqvist J., Graupner B., Guglielmi Y., Kim T., Maßmann J., Nguyen T.S., Park J.W., Shiu W., Urpi L., Yoon J.-S., Ziefle G., and Birkholzer J. (2020) An international model comparison study of controlled fault activation experiments in argillaceous claystone at the Mont Terri Laboratory. International Journal of Rock Mechanics and Mining Sciences (Submitted, April 2020).

Samuelson, J., Elsworth, D., and Marone, C. (2011) Influence of dilatancy on the frictional constitutive behavior of a saturated fault zone under a variety of drainage conditions, J. Geophys. Res., 116, B10406, doi:10.1029/2011JB008556.

Sánchez, M., Gens, A., do Nascimento Guimarães, L., and Olivella, S. (2005) A double structure generalized plasticity model for expansive materials. Int. J. Numer. Anal. Meth. Geomech., 29, 751–787.

Seiphoori, A. (2015) Technical Report 15-05.

Senger, R., and Marschall, P. (2008) Task Force on EBS / Gas Transport in Buffer Material, Nagra Arbeitsbericht NAB 08-24.

Senger R., Romero, E., Ferrari, A., and Marschall, P. (2014) Characterization of gas flow through low-permeability claystone: laboratory experiments and two-phase flow analyses. Norris, S., Bruno, J., Cathelineau, M., Delage, P., Fairhurst, C., Gaucher, E. C., Ho¨hn, E. H., Kalinichev, A., Lalieux, P. and Sellin, P. (eds) Clays in Natural and Engineered Barriers for Radioactive Wast Confinement. Geological Society, London, Special Publications, 400, http://dx.doi.org/10.1144/SP400.15

Singh, U. C. and Kollman, P. A. (1984) "An Approach to Computing Electrostatic Charges for Molecules." Journal of Computational Chemistry 5(2): 129-145.

Smith, D.W., and Booker, J.R., (1993) Green's functions for a fully coupled thermoporoelastic material. International Journal for Numerical and Analytical Methods in Geomechanics 17, 139-163.

Tachi, Y., Nakazawa, T., Ochs, M. , Yotsuji, K., Suyama, T., Seida, Y., Yamada, N. and Yui, M. (2010) "Diffusion and sorption of neptunium(V) in compacted montmorillonite: effects of carbonate and salinity." Radiochimica Acta 98(9-11): 711-718.

Tamayo-Mas, E., Harrington, J.F., Shao, H., Dagher, E.E., Lee, J., Kim, K., Rutqvist, J., Lai, S.H., Chittenden, N., Wang, Y., Damians, I.P., and Olivella, S. (2018) Numerical modeling of gas flow in a compact clay barrier for DECOVALEX-2019, Proceedings of ARMA/DFNE 2018 (DFNE 18-623).

Tsang, C.F., Neretnieks, I., and Tsang, Y. (2015) Hydrologic issues associated with nuclear waste repositories, Water Resources Research, 51(9), 6923-6972.

van Duijn, C., Mikelić, A., Wheeler, M.F., and Wick, T. (2019) Thermoporoelasticity via homogenization:

Modeling and formal two-scale expansions. International Journal of Engineering Science 138, 1–25.

van Genuchten, M.T. (1980) A closed-form equation for predicting the hydraulic conductivity of unsaturated soils. Soil. Sci. Soc. Am. J., 44, 892-898.

Vannucchi, P. (2020) Scaly fabric and slip within fault zones. Geosphere, Vol. 15, Number 2, 342-356.

Viesca, R.C. & Rice, J.R., 2012, Nucleation of slip-weakening rupture instability in landslides by localized increase of pore pressure, J. geophys. Res., 117, B03104, doi:10.1029/2011JB008866.

Vilarrasa, V., Rutqvist, J., Blanco-Martin, L., and Birkholzer, J. (2016) Use of a dual structure constitutive model for predicting the long-term behavior of an expansive clay buffer in a nuclear waste repository.

Villar, M.V. (2017) FEBEX-DP Post-mortem THM/THG Analysis Report. NAGRA, August 2017.

Villar, M.V., Iglesias, R. J., and Luis, G.-S. J. (2020) "State of the in situ FEBEX test (GTS, Switzerland) after 18 years: a heterogeneous bentonite barrier." Environmental Geotechnics 7(2): 147-159.

Wan, J.M., and Wilson, J.L. (1994) VISUALIZATION OF THE ROLE OF THE GAS-WATER INTERFACE ON THE FATE AND TRANSPORT OF COLLOIDS IN POROUS-MEDIA, Water Resources Research, 30(1), 11-23.

Wang, Y. (2011) Research & Development (R&D) Plan for Used Fuel Disposition Campaign (UFDC) Natural System Evaluation and Tool Development, U.S. DOE Used Fuel Disposition Campaign.

Wang, S., et al., (2016) Capillary pressure-saturation relations in quartz and carbonate sands: Limitations for correlating capillary and wettability influences on air, oil, and supercritical CO2 trapping. Water Resources Research, 2016. 52(8): p. 6671-6690.

Watanabe, N., N. Hirano, and N. Tsuchiya (2008), Determination of aperture structure and fluid flow in a rock fracture by high-resolution numerical modeling on the basis of a flow-through experiment under confining pressure, Water Resour. Res., 44, W06412, doi:10.1029/2006WR005411

Witherspoon, P.A., Wang, J.S.Y., Iwai, K., and Gale, J.E. (1980) Validity of cubic law for fluid flow in a deformable rock fracture, Water Resources Research, 16, 1016–1024.

Xu, T. F., Senger, R., and Finsterle, S. (2008) Corrosion-induced gas generation in a nuclear waste repository: Reactive geochemistry and multiphase flow effects, Applied Geochemistry, 23(12), 3423-3433.

Xu, H., Prévost, J.H. (2017) Integration of a continuum damage model for shale with the cutting plane algorithm. International Journal for Analytical and Numerical Methods in Geomechanics, 41(4): 471–487.

Xu, H., Rutqvist, J., Plua, C., Armand, G., and Birkholzer, T. (2020) Modeling of thermal pressurization in tight claystone using sequential THM coupling: benchmarking and validation against in-situ heating experiments in COx claystone. Tunnelling and Underground Space Technology (accepted).

Yielding, G., Freeman, B. and Needham, D.T. (1997) Quantitative fault seal prediction. Bulletin of the American Association of Petroleum Geologists, 81, 897-917.

Yip, M., Mohle, J., and Bolander, J. (2005) Automated modeling of three-dimensional structural components using irregular lattices, Computer-Aided Civil and Infrastructure Engineering, 20, 393–407.

Zarzycki, P. and Gilbert, B. (2020) "Temperature-dependence of the dielectric relaxation of water using non-polarizable water models." Physical Chemistry Chemical Physics.

Zarzycki, P., Racette, J., Tournassat, C., Nagasaki, S., and Gilbert, B. (2020) "Molecular dynamics study of confinement and salinity effect on neptunium (V) mobility in low charge smectite interlayer " Journal of Colloid and Interface Science: in preparation

Zhang C.-L. (2013) Sealing of Fractures in Claystone, Journal of Rock Mechanics and Geotechnical Engineering 5, 214-220.

Zhang C.-L. (2017) Sealing Performance of Fractured Claystone and Clay-Based Materials within the Framework of the German Project THM-TOM and the EC Project DOPAS. Final Report. GRS Report GRS – 451 Gesellschaft für Anlagen- und Reaktorsicherheit (GRS) mbH, Braunschweig.

Zhang, F., Damjanac, B., and Maxwell, S., (2019) Investigating Hydraulic Fracturing Complexity in Naturally Fractured Rock Masses Using Fully Coupled Multiscale Numerical Modeling. Rock Mech. Rock Eng. https://doi.org/10.1007/s00603-019-01851-3

Zheng, L., Rutqvist, J., Steefel, C., Kim, K., Chen, F., Vilarrasa, V., Nakagawa, S., Houseworth, J., and Birkholzer J. (2014) Investigation of Coupled Processes and Impact of High Temperature Limits in Argillite Rock. Prepared for U.S. Department of Energy, Used Fuel Disposition, FCRD-UFD-2014-000493, Lawrence Berkeley National Laboratory, LBNL-6719E.

Zheng, L., Rutqvist, J., Kim, K., and Houseworth, J. (2015) Investigation of Coupled Processes and Impact of High Temperature Limits in Argillite Rock. Prepared for U.S. Department of Energy, Used Fuel Disposition, FCRD-UFD-2015-000362. LBNL-187644, Lawrence Berkeley National Laboratory.

Zheng, L., Kim, K., Xu, H., and Rutqvist, J. (2016) DR Argillite Disposal R&D at LBNL. FCRD-UFD-2016-000437, LBNL-1006013, Lawrence Berkeley National Laboratory.

Zheng L., Kim K., Xu H., Rutqvist J., Voltolini M., and Xiaoyuan C. (2017) Investigation of Coupled Processes and Impact of High Temperature Limits in Argillite Rock: FY17 Progress. Prepared for U.S. Department of Energy, Spent Fuel and Waste Disposition. SFWD-SFWST-2017-000040, LBNL-2001014, Lawrence Berkeley National Laboratory.